Harnessing Cooperative Phenomena in Quantum Emitter Ensembles

Dissertation
zur Erlangung des akademischen Grades
Doctor of Philosophy

eingereicht an der

Fakultät für Mathematik, Informatik und Physik
der Leopold-Franzens-Universität Innsbruck

von

Raphael Holzinger M.Sc.

Betreuer: Univ.-Prof. Dr. Helmut Ritsch
Institut für Theoretische Physik

Innsbruck, Juli 2023

Abstract

An integral part of theoretical quantum optics is devoted to atom-light and atom-atom interactions, at various distances. The fact that atoms (or quantum emitters) in some instances can interact on a long or even infinite range, can lead to the modification of light absorption and emission, which in turn leads to superior optical properties. The field of theoretical quantum optics and specifically the study of emerging collective phenomena in interacting quantum systems is the focus of my research. Here, we employ analytical, as well as extensive numerical tools, in order to investigate various emerging phenomena in the context of long-range and sometimes infinite-range interacting quantum emitters. We exclusively consider open quantum systems, namely systems that can leak energy or information into a coupled system or reservoir, which usually represents the electromagnetic vacuum but can be made of other optical elements such as waveguides or nanophotonic structures. Particularly interesting is the protection of electronic excitations from loss via spontaneous emission. The mechanism for protection stems from the many-body interactions of mesoscopic numbers of quantum emitters. Tailoring interactions, we try to enhance electronic excitation storage and read-out, transport of excitations through arrays of quantum emitters, single photon detection, and entanglement preparation. In addition, we try to extend the understanding of emerging collective quantum many-body phenomena to various quantum technological platforms, such as ultracold atoms in optical lattices, molecules at ambient temperatures, superconducting qubits coupled to optical waveguides or alkaline-earth atoms trapped in tweezer arrays. Collective excitation states of ensembles of quantum emitters possess a wealth of surprising physical properties. Typically, the many-body response of these ensembles leads to delocalized excitations with lifetimes that can vary across many orders of magnitudes. Of particular interest are dark or subradiant states whose long lifetimes can be used to implement extremely efficient quantum memories, lossless transport of photons, and photon-photon gates, to realize future generations of atomic lattice clocks and potentially for improved electromagnetic field sensors. We show, for instance, that subradiant excited states in finite chains of two-level quantum emitters coupled to a one-dimensional reservoir are a resource for superior photon storage and controlled photon manipulation. Typically, states storing multiple excitations exhibit fermionic correlations and are thus characterized by an anti-symmetric wavefunction, which makes them hard to prepare experimentally. We closely collaborated with the Innsbruck-based experimental superconducting qubits group and investigate the possibility to manipulate multiple photons deterministically. This marks an important step in understanding many-body phenomena in quantum emitters and harnessing these phenomena in a controlled fashion. Another quantum

emitter platform that is treated in this thesis includes molecules each featuring multiple vibrational modes. Since molecules possess a strong dipole moment and are typically spaced at nanometer distances, they feature extremely strong dipole-dipole coupling and delocalized excitons that can even prevail at ambient temperatures.

Zusammenfassung

Ein wesentlicher Bestandteil der theoretischen Quantenoptik ist den Atom-Licht- und Atom-Atom-Wechselwirkungen auf unterschiedlichen Entfernungen gewidmet. Die Tatsache, dass Atome (oder Quantenemitter) in einigen Fällen über eine große oder sogar unendliche Reichweite wechselwirken können, kann zu einer Veränderung der Lichtabsorption und -emission führen, was wiederum zu besseren optischen Eigenschaften führt. Der Schwerpunkt meiner Forschung liegt auf dem Gebiet der theoretischen Quantenoptik und insbesondere auf der Untersuchung entstehender kollektiver Phänomene in interagierenden Quantensystemen. Hier nutzen wir sowohl analytische als auch umfangreiche numerische Werkzeuge, um verschiedene auftretende Phänomene im Zusammenhang mit wechselwirkenden Quantenemittern mit groÃer und manchmal unendlicher Interaktionsreichweite zu untersuchen. Wir betrachten ausschließlich offene Quantensysteme, also Systeme, die Energie oder Informationen in ein gekoppeltes System oder Reservoir abgeben können, das normalerweise aus dem elektromagnetischen Vakuum besteht, aber auch aus anderen optischen Elementen wie Wellenleitern oder nanophotonischen Strukturen bestehen kann. Besonders interessant ist der Schutz elektronischer Anregungen vor Verlust durch spontane Emission. Der Schutzmechanismus ergibt sich aus den Wechselwirkungen einer mesoskopischen Anzahl von Quantenemittern. Infolgedessen versuchen wir, die elektronische Speicherung und Auslesung von Anregungen, den Transport von Anregungen durch Arrays von Quantenemittern, die Einzelphotonendetektion und die Herstellung von Verschränkung zu verbessern. Darüber hinaus versuchen wir, das Verständnis neu auftretender kollektiver Quanten-Vielteilchenphänomene auf verschiedene quantentechnologische Plattformen auszudehnen, wie etwa ultrakalte Atome in optischen Gittern, Moleküle bei Umgebungstemperaturen, supraleitende Qubits, die an optische Wellenleiter gekoppelt sind, oder Erdalkaliatome, die in optischen Pinzetten gefangen sind . Kollektive Anregungszustände von Ensembles von Quantenemittern besitzen eine Fülle überraschender physikalischer Eigenschaften. Typischerweise führt die Vielteilchenreaktion dieser Ensembles zu delokalisierten Anregungen, die bei Lebensdauern, die über viele verschiedene Größenordnungen variieren können, durch Dissipation verloren gehen. Von besonderem Interesse sind dunkle oder subradiante Zustände, deren lange Lebensdauer zur Implementierung äußerst effizienter Quantenspeicher, zum verlustfreien Transport von Photonen und Photon-Photon-Gattern, zur Realisierung zukünftiger Generationen von Atomgitteruhren und möglicherweise für verbesserte Sensoren für elektromagnetische Felder genutzt werden kann. Wir zeigen zum Beispiel, dass subradiante angeregte Zustände in endlichen Ketten von Zweiebenen-Quantenemittern, die an ein eindimensionales Reservoir gekoppelt sind, eine Ressource für überlegene

Photonenspeicherung und kontrollierte Photonenmanipulation sind. Typischerweise weisen Zustände, die mehrere Anregungen speichern, fermionische Korrelationen auf und sind daher durch eine antisymmetrische Wellenfunktion gekennzeichnet, was es schwierig macht, sie experimentell vorzubereiten. Wir haben eng mit der in Innsbruck ansässigen Gruppe für experimentelle supraleitende Qubits zusammengearbeitet und untersuchen die Möglichkeit, mehrere Photonen deterministisch zu manipulieren. Dies stellt einen wichtigen Schritt zum Verständnis von Vielteilchenphänomenen in Quantenemittern und zur kontrollierten Nutzung dieser Phänomene dar. Eine weitere Quantenemitterplattform, die in dieser Arbeit behandelt wird, umfasst Moleküle, die jeweils mehrere Vibrationsmoden aufweisen. Da Moleküle ein starkes Dipolmoment besitzen und typischerweise im Nanometerbereich voneinander entfernt sind, weisen sie eine extrem starke Dipol-Dipol-Kopplung und Delokalisierung auf, die sogar bei Umgebungstemperaturen vorherrschen kann.

Danksagung

Zuerst bedanke ich mich bei Prof. Helmut Ritsch für seine ausgezeichnete und langjährige Betreuung, nichtnur wissenschaftlich sondern auch persönlich durfte ich seinen liebenswürdigen Charakter schätzen lernen. Weiters möchte ich mich bei Dr. Claudiu Genes und Dr. Maria Moreno-Cardoner bedanken, mit denen ich bei einigen Projekten zusammenarbeiten durfte.

Ich bedanke mich bei allen aktuellen und ehemaligen Mitgliedern der Forschungsgruppe mit denen ich Wege gekreuzt habe: Sebastian Krämer, Valentin Torggler, Julian Cremer, Wolfgang Niedenzu, Stefan Ostermann, Elias Starchl, David Plankensteiner, Daniela Holzmann, Elvia Colella, Matthias Sonnleitner, Verena Scheil, Laurin Ostermann, Natalia Masalaeva, Farokh Mivehvar, Maxim Laborenz, Arkadiusz Kosior, Julian Moser, Christoph Hotter, Karol Gietka, Martin Fasser und Anna Bychek.

Desweiteren bedanke ich mich bei den administrativen Assistentinnen Nicole Jorda, Birgit Laimer und Elke Stenico für die hochqualifizierte Unterstützung während der Doktorarbeit.

Auch bedanken möchte ich mich bei meinen Kollaboratoren mit denen ich über die Jahre an interessanten Projekten zusammenarbeiten durfte, nämlich, Michael Reitz, Ricardo Gutierrez-Jauregui, Teresa Hönigl-Decrinis, Gerhard Kirchmair, Ana Asenjo-Garcia und Nico S. Bassler.

Zu guter Letzt bedanke ich mich herzlich bei meiner Schwester Eva für ihre Unterstützung und meinen lieben Eltern Maria und Franz für alles.

Contents

1 Introduction

The interaction of several atoms or quantum emitters via the electromagnetic vacuum modes gives rise to a multitude of intriguing phenomena. In particular the modification of the spontaneous emission rate of light of an excited atom which is now modified by the surrounding atoms. Such modifications include the increase or decrease of the photon emission rate of this cooperative ensemble of atoms. These effects are termed superradiance [1, 2] and subradiance and can be understood as the constructive and destructive interference of the light emitted by the individual atoms. On the one hand, superradiance has been studied for a long time and experimentally observed for instance in atomic clouds of atoms [3, 4] due to its strong emission signal. On the other hand, subradiance has always remained more elusive due to its absence of radiation and consequently was hard to measure and only recently experiments showed signatures of subradiance [5]. The central question of this Thesis is how to harness subradiance resulting from the cooperative behavior of quantum emitter arrays and furthermore try to uncover collective phenomena that nature might utilize in order to enhance certain biological functions.

1.1 Light-matter interaction in dense ensembles

Many interesting and useful processes both in nature and in quantum technologies are a consequence of cooperative effects. This means that the behavior of an ensemble of particles or emitters cannot be understood entirely by only looking at the individual emitters as these effects come about by the interaction between them. In quantum optics understanding these phenomena has always been at the forefront of both theory and experiments and in recent years both academia and industry try to find possible applications to exploit quantum effects for near-term devices [6–8]. It is still challenging though to experimentally show the cooperative enhancement gained by interacting quantum emitters. For instance, it was known for many years by theorists that it is possible to perfectly reflect weak incoming light by a two-dimensional ordered array of quantum emitters which is just a single layer thick [9]. Only just recently this was experimentally demonstrated with a 2D array of rubidium atoms trapped in an optical lattice [10] (see Fig. 1.1). Apart from trying to verify the theory with experiments and finding applications, it is equally urgent to understand already existing, though, unexplained phenomena occurring in the natural world. One of the most prominent is the process of photosynthesis, in particular the primary state involving the transfer of photons to particular locations, called reaction centers.

This stage occurs with near unit efficiency, at environmental temperatures, and in variable and noisy environments [11]. Since scientists were not able to reproduce such efficiencies with comparable systems or explain them with conventional, mostly classical models, it was theorized that quantum effects might play a role here. Finding experimental evidence that quantum coherence might be crucial in the transfer process has been hard to find up to now at least in the electronic degrees of freedom. That is why researchers started to look elsewhere, such as the vibrational degrees of freedom, inherent in the individual constituents, namely, molecular pigments [12]. But here again, the conclusion is that cooperative behavior between the vibrations of different molecules is at the core of why nature is so highly efficient at harvesting sunlight. The work presented in this Thesis tries to shed some light on how this can be understood theoretically and hopefully opens possibilities for future research.

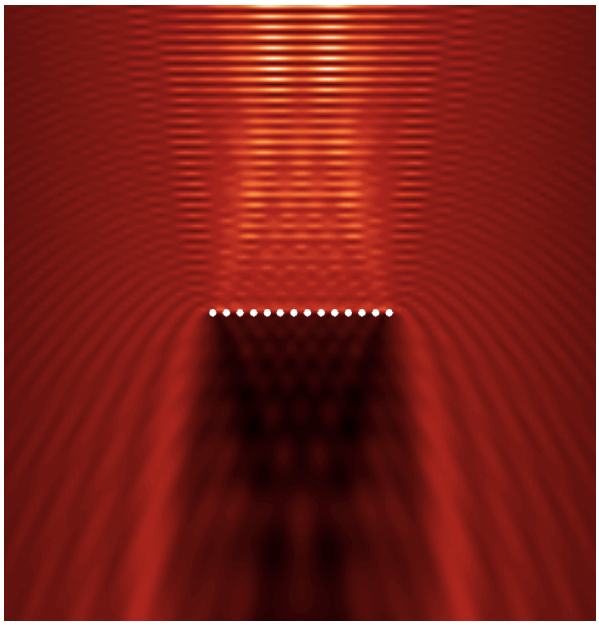

Figure 1.1: Simulation showing the cooperative enhancement of the light−matter interaction strength and the mirror reflection of incoming light (top to down) using an ensemble of ordered quantum emitters. The white dots represent atoms trapped in a 2D array with a nearly perfect reflection of incoming laser light, realizing a mirror with the thickness of a single atom. This was experimentally confirmed recently [10]. The figure was created by the author with the help of [13].

1.2 Outline of this Thesis

The content of this Thesis focuses mainly on three different parts. Part I focuses on emerging collective effects due to interacting quantum emitters in free space. Part II

dives into harnessing the infinite range interaction due to artificial atoms coupled to a waveguide. Lastly, part III treats dipole-dipole interactions with molecular quantum emitters, featuring additional vibrational couplings. These parts are complemented by an introductory chapter that reviews several theoretical concepts, useful to understand the main body of this Thesis. Expert readers can easily skip the introduction to the concepts and directly select an individual chapter for reading. Here follows a succinct summary of each chapter,

- Chapter 2 introduces basic concepts of light-matter interactions, including spontaneous emission of single and many quantum emitters. First, we introduce the basic equations central to this Thesis. Second, various types of quantum emitters are discussed and their advantages and disadvantages are scrutinized. Later we define the basics of open quantum systems based on atomic quantum emitters, artificial atoms coupled to waveguides, and molecules. Finally, we discuss how to gain an improved understanding of quantum emitter ensembles with the help of the collective states picture.
- Chapter 3 investigates how super- and subradiance in two-level emitters can be generalized to multilevel systems with several excited states. We show that for subwavelength arrangements of the emitters, one can realize long-lived subradiant states involving two excitations. Furthermore, possible preparation schemes are discussed, namely probabilistic preparation via a phase-controlled laser pump and dissipative preparation via decay into the subradiant state.
- Chapter 4 shows, that it is possible to realize a source of coherent light with just a handful of quantum emitters. Instead of having a bulky gain medium with an optical resonator, it is possible to create a laser with an ordered array of emitters at a subwavelength spacing. This array is organized in a ring shape and features eigenmodes that exhibit the character of a high-Q resonator, namely a small resonance linewidth. Furthermore, we present that this device can operate without a lasing threshold in a continuous fashion.
- In Chapter 5 we show similarly as in the previous chapter, that subwavelength-spaced quantum emitters can be used to implement nanoscale non-classical light sources. The strong dipole-dipole shifts resulting from the small inter-particle spacings generate a highly nonlinear response strongly suppressing the emission of a second photon. Additionally, we demonstrate, that by extending the quantum emitter array to more than a wavelength, the emitted light can be strongly collimated, thereby creating directional confinement. On top of that, we find that the single photon emission happens at a superradiant rate, namely, faster than from an independent emitter.
- Coming again back to ring geometries, Chapter 6 explores the possibility of enhancing the light absorption capabilities of a single quantum emitter in free space by placing a ring of emitters around it, thereby realizing an antenna effect on the nanoscale. We find that among regular polygons with an identical center

absorbing emitter, a nonagon exhibits a distinct optimum of the absorption efficiency, without the need to detune the central emitter. Only for nine emitters the sum of the coupling strengths of each emitter to all others matches the center to the ring coupling. We also find that for very small structures a quantum treatment predicts an even stronger enhancement for the single photon absorption enhancement than a classical dipole model. Without going too deep, we also connect to natural light-harvesting structures, as in purple bacteria, where chromophoric rings with a 9-fold symmetry are abundant.

- With a change of platform, Chapter 7 explores the controlled preparation and read-out of multi-excitation subradiant states in quantum emitters coupled to one-dimensional waveguides. Since each two-level emitter can only store a single energy quantum, storing multiple excitations requires delocalized states, which typically are hard to prepare with high fidelity. Here we identify a new class of dark states with up to half of the qubits excited. In particular, we suggest an experimental implementation using a 1D waveguide coupled to superconducting transmon qubits.
- Chapter 8 ventures into a treatment of molecular quantum emitters featuring vibrational degrees of freedom additionally. We illustrate a general framework to treat molecules with an arbitrary number of vibrational modes but especially we study the cooperative behavior of an ensemble of diatomic molecules, meaning a single vibrational mode, for the sake of clarity. Molecules are particularly interesting as they usually are spaced at nanometer distances resulting in extremely strong dipole-dipole coupling strength. Here we illustrate the unidirectional transfer of excitation energy between a superradiant state, coupled with free space, and the long-lived subradiant state, highly protected from radiative decay. We show that this process occurs for a particular molecular aggregate, namely the H-aggregate where the symmetric state is energetically the highest eigenstate of the system. Furthermore, we look at ring geometries with a higher number of molecules and the possibility of coherent light emission.
- Continuing with the insights gained from the previous chapter 9 we proceed to tread molecular aggregates in more detail. Using a quantum optics framework we try to understand the dynamics describing an effect known in quantum chemistry as Kasha's rule. Studying the absorption spectrum of deeply subwavelength molecular aggregates, one can observe that the dominant resonance peak can be shifted with respect to a single molecule (monomer) and the fluorescence peak can be shifted as well or be strongly suppressed. Here we try to illuminate these facts with our quantum optics framework and derive scaling laws for this behavior as a function of the number of molecules and number of vibrational couplings.
- Lastly, in Chapter 10 we come back to general quantum emitters neglecting the direct inclusion of vibrational couplings. Although this could in principle be simulated via individual dephasing of each quantum emitter. We investigate

the general optical properties of stacked rings of quantum emitters with various relative positions and orientations. Inspired by natural light-harvesting antennas in purple bacteria, which involve three stacked rings with 9 chromophores each, we also present the optical properties with our dipole model using the real physical parameters.

Finally, we summarize the main conclusions of this Thesis and give some outlook for future research directions and open questions.

2 Fundamental concepts

The goal of this chapter is to provide a compact overview of the most important theoretical foundations and concepts that are utilized in the main part of this Thesis.

2.1 Single quantum emitters

Many excellent literature references treat two-level quantum emitters [14–16] and here we just give a quick overview of the definition that are fundamental to the following chapters. In the sections that follow we assume for the sake of clarity that the quantum emitters are at zero temperature, except in a few cases where it is explained. This results in a reduction of decoherence and fewer unwanted decay channels. One of the central goals of quantum optics is to increase the coupling of light with atoms or quantum emitters. However, in free space, the interaction between photons and atoms is often too small to obtain efficient quantum control using light. For an ideal two-level atom, the optical cross-section is given by $\sigma_{\text{scat}} = 3\lambda_0^2/(2\pi)$, where $\lambda_0 = 2\pi c/\omega_0$ is the resonant wavelength and the transition frequency between the ground and excited state is given by ω_0. Simultaneously, the minimal area to which a light beam can be focused down is limited by the diffraction, $A_{\text{eff}} \sim \lambda_0^2$. This gives a fundamental limit on the likelihood that an atom in free space absorbs a photon. This probability $P = \sigma_{\text{scat}}/A_{\text{eff}}$ for state-of-the-art technologies is on the order of $P \sim 0.1$. There have been many improvements and ingenious inventions to improve this probability, such as using optical cavities, waveguides, or nanophotonic structures. Partly this Thesis takes different approaches and takes inspiration from nature which implements biological antennae made up of chromophores that augment absorption centers. Further details on this topic follow in the chapters below.

A two-level system features a ground state $|g\rangle$ and an excited state $|e\rangle$ which can be reached from the ground state through a dipole-allowed transition. We exclude the possibility that the electron can go anywhere else except these two levels and the basis follows the completeness relation $|g\rangle\langle g| + |e\rangle\langle e| = I_2$, where I_2 is the identity in the two-dimensional Hilbert space. The two terms can also be seen as projectors on the ground and excited state respectively. The ladder operators that bring the system up and down are defined as

$$\hat{\sigma} = |g\rangle\langle e|, \quad \hat{\sigma}^\dagger = |e\rangle\langle g|. \tag{2.1}$$

Remembering basic quantum physics courses we know that the dipole moment operator $\hat{d} = -e\hat{r}$ does not have matrix elements on the individual orbitals such that $\langle g|\hat{d}|g\rangle = 0$

and $\langle e|\hat{d}|e\rangle = 0$. We then can write the basis decomposition of the dipole moment operator as

$$\hat{d} = |g\rangle d_{\mathrm{ge}}\langle e| + |e\rangle d_{\mathrm{ge}}^{*}\langle g|, \quad d_{\mathrm{ge}} = \langle g|\hat{d}|e\rangle. \tag{2.2}$$

Now we let the two-level system interact with an electromagnetic field $\hat{E}$ which could also be time-dependent and write the total Hamiltonian as

$$\hat{\mathcal{H}}/\hbar = \omega_e \hat{\sigma}^{\dagger}\hat{\sigma} + \omega_g \hat{\sigma}\hat{\sigma}^{\dagger} + (\hat{\sigma} d_{\mathrm{ge}} \cdot \hat{E}^{\dagger} + \hat{\sigma} d_{\mathrm{ge}}^{*} \cdot \hat{E}), \tag{2.3}$$

where $\omega_0 = \omega_e - \omega_g$ from above. This is the basic formalism for a single two-level system at zero temperature without additional degrees of freedom and is easily generalized to the many emitter cases [17]. In the sections below we will discuss the process of spontaneous emission from the excited state to the ground state.

2.1.1 Molecules

In this section we generalize the two-level emitter model introduced above to molecular emitters featuring vibrational degrees of freedom due to relative nuclear motion. For simplicity and the sake of clarity we take a molecule with a single relative nuclear coordinate, meaning, a diaatomic molecule featuring two nuclei [18, 19].

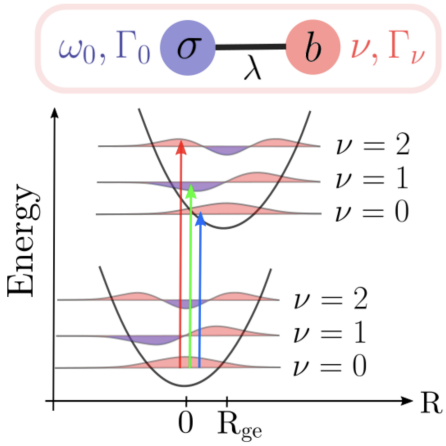

Figure 2.1: The potential energy landscape in a diatomic molecule approximated by harmonic potentials with two electronic energy levels. The two potentials are displaced by R_{ge} and the optical transition with frequency ω_0 and linewidth Γ_0 is coupled to a single vibrational mode with frequency ν and linewidth Γ_ν and Huang-Rhys factor λ.

To include the electronic-vibrational coupling we take a single nuclear coordinate R into account. Since we want to have non-zero vibrational coupling we assume that, along the nuclear coordinate, the minima for ground (coordinate R_g, state vector

$|g\rangle$) and excited (coordinate R_e and state vector $|e\rangle$) electronic orbitals are different, illustrated in Fig. 2.1. The total molecular Hamiltonian describing both electronic and vibrational dynamics can be written as

$$\mathcal{H}_{\text{mol}} = \left[\omega_0 + \frac{\hat{P}^2}{2\mu} + \frac{1}{2}\mu\nu^2\left(\hat{R} - R_e\right)^2\right]\sigma^\dagger\sigma + \left[\frac{\hat{P}^2}{2\mu} + \frac{1}{2}\mu\nu^2\left(\hat{R} - R_g\right)^2\right]\sigma\sigma^\dagger, \quad (2.4)$$

with $\mu = m/2$ being the effective mass (m is the mass of a single nucleus). The kinetic and potential energies are written in terms of the position $\hat{Q}$ and momentum operators $\hat{P}$ representing the nuclear coordinate, with commutator $[\hat{Q}, \hat{P}] = i\hat{I}$. Introducing oscillations around the minima $\hat{Q} = \hat{R} - R_{\text{g}}$, we can rewrite $\hat{R} - R_{\text{e}} = \hat{Q} + R_{\text{g}} - R_{\text{e}} =: \hat{Q} - R_{\text{ge}}$ and arrive at

$$\mathcal{H}_{\text{mol}} = \frac{\hat{P}^2}{2\mu} + \frac{1}{2}\mu\nu^2\hat{Q}^2 + \omega_0\sigma^\dagger\sigma - \mu\nu^2\hat{Q}R_{\text{ge}}\sigma^\dagger\sigma + \frac{1}{2}\mu\nu^2R_{\text{ge}}^2\sigma^\dagger\sigma, \quad (2.5)$$

where ν is the frequency of the vibrational mode, in a harmonic approximation. The momentum and position operators can be written in terms of bosonic operators $\hat{Q} = q_{\text{zpm}}(b^\dagger + b)$, $\hat{P} = ip_{\text{zpm}}(b^\dagger - b)$ as well. As is the case for the quantum harmonic oscillator, the bosonic operators here satisfy the commutation relation $[b, b^\dagger] = 1$ and the zero-point motion and momentum are defined as $q_{\text{zpm}} = 1/\sqrt{2\mu\nu}$ and $p_{\text{zpm}} = \sqrt{\mu\nu/2}$. Using these expressions the above Hamiltonian can be rewritten to yield the well-known Holstein Hamiltonian for a single diatomic molecule [20]

$$\mathcal{H}_{\text{mol}} = (\omega_0 + \lambda^2\nu)\sigma^\dagger\sigma + \nu b^\dagger b - \lambda\nu(b^\dagger + b)\sigma^\dagger\sigma. \quad (2.6)$$

The dimensionless vibronic coupling strength λ is given by $\lambda = \mu\nu R_{\text{ge}}q_{\text{zpm}}$, where λ^2 is the so called Huang-Rhys factor. Typically values for the Huang-Rhys factor range between $\sim 0.01 - 1$. Now, we show how the Holstein Hamiltonian can be cast into diagonal form and how laser light is absorbed by a molecule. To this end we make a unitary transformation, also called polaron transformation $\mathcal{U}^\dagger = |g\rangle\langle g| + \mathcal{D}^\dagger|e\rangle\langle e|$ with the displacement operator $\mathcal{D} = e^{-i\sqrt{2}\lambda p} = e^{\lambda(b^\dagger - b)}$. In the new basis, the Holstein Hamiltonian obtains the form $\tilde{\mathcal{H}}_{\text{mol}} = \mathcal{U}^\dagger\mathcal{H}_{\text{mol}}\mathcal{U} = \omega_0\sigma^\dagger\sigma + \nu b^\dagger b$ and with eigenstates $|g; n\rangle$ and $|e; n\rangle$. The eigenstates in the original basis can be found by reversing the polaron transformation $|g; n\rangle$ and $\mathcal{D}|e; n\rangle$. Now we introduce a coherent laser drive of the form $\mathcal{H}_\ell = i\eta(\sigma^\dagger e^{-i\omega_\ell t} - \sigma e^{i\omega_\ell t})$, which in the polaron-transformed basis is then expressed as $\tilde{\mathcal{H}}_\ell = i\eta(\sigma^\dagger\mathcal{D}^\dagger e^{-i\omega_\ell t} - \sigma\mathcal{D}e^{i\omega_\ell t})$. One can now look at the transition probabilities between the energy levels, induced by the laser drive. We assume an initial state $|g; 0\rangle$ in the displaced basis and compute the probability of exciting the system to state $|e; n\rangle$,

$$P_{\text{abs}}(n) = |\langle e; n|\sigma^\dagger\mathcal{D}^\dagger|g; 0\rangle|^2 = e^{-\lambda^2}\frac{\lambda^{2n}}{n!}, \quad (2.7)$$

which is a Poissonian distribution leading to the so-called Franck-Condon principle for molecular transitions.

For dissipative radiative processes, we notice that the collapse operator in the Lindbladian is also transformed to $\sigma\mathcal{D}$ such that radiative decay follows the same distribution for transitions of the electronic state $|e;0\rangle$ to $|g;n\rangle$. Note, that even though the zero phonon line (ZPL) ($n = 0 \leftrightarrow n = 0$) by itself can be quite weak, it can be strongly enhanced by different means. One way is to resonantly couple the ZPL to a mode of a cavity, which can tilt the branching ratio in favor of the ZPL via the Purcell enhancement. Of course, the presence of vibrations and subsequent weakening of the bare transition might appear as a limitation for conventional quantum optics which prefers resonant couplings and control. However, it can also be used as a resource as for instance the existence of many vibrational levels and decay channels might aid the fast transfer between various delocalized states at a rate much faster than via coherent electronic excitation transfer only [12, 21, 22]. When tackling a system involving many molecules such as in large biomolecular ensembles, e.g. light-harvesting complexes in purple bacteria [23], the dimension of the whole system can become rather involved and unsolvable. One simplification we are making most throughout this thesis is that the electronic degrees of freedom of each emitter or molecule can be reduced to just two levels. As we later show this can be simplified even further by assuming that just a single excitation is present in the system, neglecting all possibilities that the system can host two or more excitations. With that assumption, the system size grows linearly with N, the number of emitters. However, vibrational degrees of freedom present an additional increase in the system dimension. Realistically each molecule can host dozens of vibrational modes each haven multiple vibronic excitations, which would render again the system unsolvable. But it turns out that for many cases in low-temperature limits taking a single excitation per vibrational mode is sufficient and for obtaining qualitative conclusions it is even sufficient to take only a single vibrational mode per molecule, see Fig. 2.1. Generally in a low excitation limit for both vibrations and electronic excitations the whole system size grows only as $N \times M$ where N is the number of molecules and M the number of vibrational modes per molecule and consequently a mesoscopic number of molecules can be simulated.

2.2 Long-range interactions on various platforms

There are a multitude of possible quantum emitters appearing in nature and are utilized in laboratories around the world, each having its advantages and disadvantages, in this section we discuss a handful of the most common ones and also show some of their properties in Fig. 2.2. Generally, we are interested in emitters that possess the ability to interact with neighboring emitters, preferably on a long range, beyond nearest-neighbors. Quantum control of neutral atoms has led to remarkable breakthroughs over the decades but their interaction is generally limited to local collisions. However, non-local interactions and entanglement of distant quantum emitters promise to lead to new breakthroughs, which is why figuring out ways to engineer and control such long-range interactions is one of the most urgent challenges in quantum physics

nowadays.

Atoms and molecules in free space with an induced transition dipole moment and/or permanent dipole moments are prime candidates for interacting over a long range since the dipole-dipole interaction includes terms scaling with the distance as $\sim 1/r$ and $\sim 1/r^3$. They feature a large range of transition frequencies and linewidths with many possible transitions to choose from.

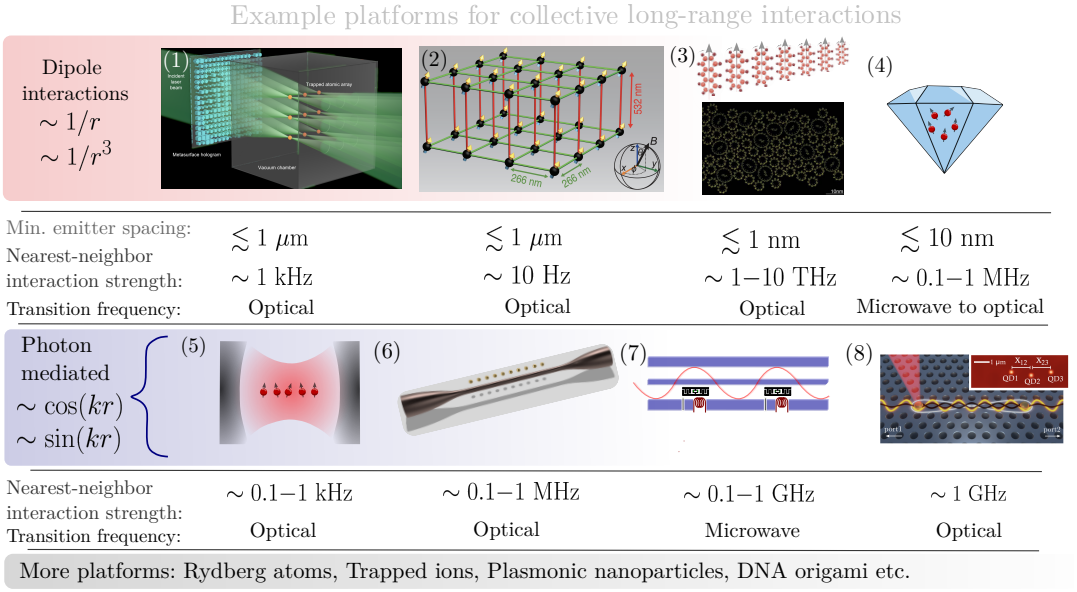

Figure 2.2: Examples of quantum emitter platforms, that are readily utilized to study collective long-range interactions. (1) Atoms trapped in a metasurface holographic optical trap. Image courtesy [24]. (2) Image courtesy [25]. (3) Molecular aggregates assembled or naturally occurring in ring-shaped geometries inside light-harvesting complexes. Image courtesy [26]. (4) Nitrogen-vacancy centers inside a single diamond crystal. (5) Atoms trapped inside an optical cavity. (6) Atoms trapped along a nanophotonic fiber. (7) Superconducting transmons capacitively coupled to a 1D transmission line. (8) Semiconductor quantum dots coupled to a nanophotonic structure with a hexagonal defect pattern. Image courtesy [27].

Even though current techniques enable cooling down molecules to ultracold temperatures, it is still a major challenge due to the complexity of the molecular internal structure introduced by its rotational and vibrational degrees of freedom. At the same time, these additional degrees of freedom, combined with the control accessible via optical trapping technologies and the long-range interaction introduced by the electronic transition, offer a lucrative perspective for their utilization in near-term quantum technologies. In particular, we will show how the vibrational modes can help

mediate between collective electronic states that would otherwise be inaccessible by external light sources. In paramagnetic atoms, permanent magnetic dipole moments can be found with an interaction range that exceeds the nearest neighbor. For instance, it was shown, that erbium atoms tightly trapped in a 3D optical lattice can be used to explore many-body problems such as the extended Bose-Hubbard model. Yet another group of quantum emitters that can exhibit direct long-range interactions are Rydberg atoms. These are atoms in a largely excited state with their valence electrons that orbit hundreds of Angstrom away from the nucleus. The subsequent large electric dipole moment scales with $\sim n^4$, where n is the principal quantum number. The range of interaction can be of the order of 10 μm. Rydberg atoms are currently trapped with optical tweezers or optical lattices with a high degree of control. One disadvantage is the finite lifetime of the Rydberg states in the order of ~ 100 μs, which can be circumvented via Rydberg dressing techniques. Apart from direct dipole-dipole couplings, long-range interactions can also be mediated via engineered photon reservoirs.

One such reservior is an optical fiber with atoms trapped nearby. In principle, the fiber mediates infinite periodic interactions between the atoms making them particularly interesting for long-range studies, and the input- and output fields can be read out easily at the ends of the fiber. A major obstacle is the low ratio of the atomic decay into the fiber versus decay into free space, which for state-of-the-art experiments is of the order of ~ 0.1. Another platform is photonic crystals with periodic defects or holes that provide control over the dispersion of the guiding modes. In this way, interactions can be engineered although the interaction range scales as $\sim e^{-r}$, but still beyond nearest-neighbor interaction is possible. Our last but prime example of infinite-range photon-mediated interactions is optical cavities. Depending on the quality of the cavity mirrors, the photons make numerous round-trips and interact with all emitters inside the cavity, and in consequence can significantly increase the atom-light interaction time. Additionally, optical lattices can be incorporated introducing short-range interaction as well making the by far best and most explored platform to date.

2.3 Ensemble of interacting quantum emitters

2.3.1 Master equation for spontaneos emission

In this section, we briefly outline the approximations used to derive the master equation, the theoretical starting point for most of the work presented in this Thesis. The derivation follows from a system of quantum emitters coupled linearly to a bath formed of harmonic oscillators [28–30]. We take as an initial state, the density operator in the full Hilbert space of an ensemble of the two-level systems in contact with infinitely many electromagnetic modes. The evolution of the bath and system is described by

the total Hamiltonian ($\hbar = 1$)

$$\begin{aligned}
\mathcal{H} &= \mathcal{H}_\mathrm{b} + \mathcal{H}_\mathrm{s} + \mathcal{H}_\mathrm{int}\,, \\
\mathcal{H}_\mathrm{b} &= \sum_s \int_0^\infty d\omega \omega b_s^\dagger(\omega) b_s^\dagger(\omega)\,, \\
\mathcal{H}_\mathrm{int} &= \sum_{n,s} \int d\omega \lambda_{n,s}(\omega) \left(b_s(\omega) + b_s^\dagger(\omega)\right)\left(\hat{\sigma}_n + \hat{\sigma}_n^\dagger\right)\,,
\end{aligned} \tag{2.8}$$

where $b_s(\omega)$ are bosonic annihilation operators for bath modes of frequency ω with polarization s. The coupling strength $\lambda_{n,s}(\omega)$ generally depends on the field amplitude evaluated at the emitter position x_n. This rather general coupling can accurately describe atoms coupled to a 3D electromagnetic environment under the electric dipole approximation [30] or artificial atoms coupled to a transmission line [31] for instance. We restrict to the two-level approximation with system operators $\hat{\sigma}_n$ and the system Hamiltonian is

$$\mathcal{H}_\mathrm{s} = \sum_n \omega_0 \sigma_n^\dagger \sigma_n\,. \tag{2.9}$$

In an interaction picture, after a unitary transformation with respect to the free Hamiltonians $\mathcal{H}_\mathrm{b}$ and $\mathcal{H}_\mathrm{s}$ the density operator for bath plus system $\rho(t) = \rho_s(t) \otimes \rho_b(t)$ follows the von Neumann equation $i\dot{\rho} = [\tilde{\mathcal{H}}_\mathrm{int}, \rho]$. After formal integration, this differential equation gives rise to an integral equation

$$\dot{\rho}_s = i \int_0^t d\tau [\tilde{\mathcal{H}}_\mathrm{int}(t), [\tilde{\mathcal{H}}_\mathrm{int}(\tau), \rho_s(t)]] \tag{2.10}$$

where the bath variables have been traced out to obtain the density matrix of the ensemble ρ_s. In writing the above master equation we have also assumed that the system and bath are uncorrelated at an initial time, namely

$$\rho(0) = \rho_s(0) \otimes \rho_b(0) \tag{2.11}$$

This equation describes the self-consistent evolution of the quantum system and the environment (bath) and it considers correlations that arise between the two. The description can be simplified for a large bath weakly coupled to the emitters $\omega_0 \gg \lambda_{n,s}(\omega_0)$ and with a smooth frequency spectrum around the emitter resonance frequency. The integral equation above is a non-Markovian master equation and can only be recursively solved. To arrive at a Markovian master equation, we have to substitute τ by $t - \tau$ in the integrand which keeps the integration bounds unchanged. Thus, we can see the parameter τ as showing how far we go backward in time to account for memory effects over which correlations with the bath remain relevant. Under the Markov approximation, these memory effects are short-lived and therefore the correlations decay very quickly. In this limit, we can extend the upper bound of the integration to infinity, and obtain a Markovian master equation. In other words, this approximation neglects the correlations that arise between field and bath and sets

the correlation time of the environment as the shortest time-scale of the system [28]. As an example for atoms with optical frequencies, the correlation time with the bath is on the order of femtoseconds, on the other hand, the lifetime of the optical transition is on the order of nanoseconds or more. The resulting master equation with diagonal Lindblad term has the general form

$$\begin{aligned}\dot{\rho}(t) = &-i[\mathcal{H}, \rho_s(t)] \\ &+ \sum_{k,\omega} \frac{\gamma_k(\omega)}{2}\Big(2A_k(\omega)\rho_s A_k(\omega)^\dagger - A_k(\omega)^\dagger A_k(\omega)\rho_s - \rho_s A_k(\omega)^\dagger A_k(\omega)\Big),\end{aligned} \tag{2.12}$$

where this is evaluated usually around the emitter transition frequency, i.e. $\omega = \omega_0$ and A_k are general collapse operators acting on the system. In the next sections, we show its form for specific baths where this equation can be written explicitly with analytic expression which is not possible for environments with arbitrary boundary conditions and one has to resort to numerical tools.

Free space

The photon-mediated interactions between closely spaced emitters are described by the electromagnetic Green's tensor, stemming from Maxwell's equations in classical electrodynamics. Usually, the mediating environment is provided by a dielectric medium with an arbitrary geometry, for which there is no analytic expression of the Green's tensor and it has to be calculated numerically, provided that the boundary conditions are known and the medium is fairly homogenous. This allows to obtain effective couplings between the quantum emitters which give rise to collective frequency shifts and modified decay rates into the medium, which will be described in more detail below. On the other hand, if the reservoir with which the emitters are in contact is given by free space and to which they can decay with rate Γ_0, the Green's function can be brought into analytic form and the interaction terms in the Hamiltonian and Lindbladian are given in terms of it. In other words, the collective coupling rates J_{ij} and Γ_{ij} are given as the real and imaginary part of the overlap of the transition dipole of the ith atom with the electric field emitted by the jth atom, i.e.

$$J_{ij} = -\frac{3\pi\Gamma_0}{k_0}\mathrm{Re}\Big(\boldsymbol{d}_i^* \cdot \boldsymbol{G}\left(\boldsymbol{r}_i - \boldsymbol{r}_j, \omega_0\right) \cdot \boldsymbol{d}_j\Big), \tag{2.13a}$$

$$\Gamma_{ij} = \frac{6\pi\Gamma_0}{k_0}\mathrm{Im}\Big(\boldsymbol{d}_i^* \cdot \boldsymbol{G}\left(\boldsymbol{r}_i - \boldsymbol{r}_j, \omega_0\right) \cdot \boldsymbol{d}_j\Big). \tag{2.13b}$$

In the above, $\boldsymbol{G}\left(\boldsymbol{r}, \omega_0\right)$ is the electromagnetic Green's tensor of a dipole source in free-space [32] which is given explicitly by

$$\boldsymbol{G}\left(\boldsymbol{r}, \omega_0\right) \cdot \boldsymbol{d} = \frac{e^{ik_0 r}}{4\pi r}\Big[\left(\hat{\boldsymbol{r}} \times \boldsymbol{d}\right) \times \hat{\boldsymbol{r}} + \left(\frac{1}{k_0^2 r^2} - \frac{i}{k_0 r}\right)\left(3\hat{\boldsymbol{r}}\left(\hat{\boldsymbol{r}} \cdot \boldsymbol{d}\right) - \boldsymbol{d}\right)\Big], \tag{2.14}$$

where $r = |\boldsymbol{r}|$ and $\hat{\boldsymbol{r}} = \boldsymbol{r}/r$ is the position unit vector and $k_0 = \omega_0/c$. The dipole orientation is encoded in $\boldsymbol{d}$ and can be real for linear polarized dipoles or complex for circularly polarized dipoles.

The electric field that is generated by an ensemble of dipole emitters can be calculated [33, 34] as

$$\boldsymbol{E}^{+}(\boldsymbol{r}) = \frac{|\boldsymbol{d}|k_0^2}{\epsilon_0} \sum_i \boldsymbol{G}\left((\boldsymbol{r} - \boldsymbol{r}_i, \omega_0) \cdot \boldsymbol{d}\, \sigma_i^{-}\right., \tag{2.15}$$

for the positive frequency component, assuming identical dipole orientations and where ϵ_0 is the dielectric constant in free space. This just constitutes the electric field generated by an ensemble of N atoms at the position $\boldsymbol{r}$ in the vacuum and the radiated field intensity at this position is given by

$$I(\boldsymbol{r}) = \langle \boldsymbol{E}^{+}(\boldsymbol{r}) \boldsymbol{E}(\boldsymbol{r}) \rangle. \tag{2.16}$$

The nearest neighbor coherent interaction shows a $1/r^3$ dependence while the dissipative interaction follows a $1/r$ dependence, as a function of r, the separation.

As an example to simplify matters for emitters polarized perpendicular to the emitter plane in the far field, we use the fact that the Green's tensor becomes approximately independent of the relative emitter position ($|\boldsymbol{r} - \boldsymbol{r}_i| \gg \lambda_0$) and the dipoles appear as being in the same spot. In our case of identical two-level emitters polarized in z-direction distributed in the xy-plane, the Green's tensor simplifies to

$$\boldsymbol{G}\left(\boldsymbol{r} - \boldsymbol{r}_i, \omega_0\right) \cdot \boldsymbol{d} \approx \frac{e^{ikr}}{4\pi r} \hat{e}_z \Big(1 - \frac{1}{k_0^2 r^2} - \frac{i}{k_0 r}\Big), \tag{2.17}$$

which in the far-field can be approximated by $\hat{e}_z e^{ikr}/4\pi r$, therefore only a $1/r$ term survives at large distance.

Waveguide medium

As a second example of a possible reservoir to which two-level emitters can couple, we discuss the one-dimensional single-mode waveguide. Let us consider a linear chain of N emitters resonantly coupled to the modes of a single-mode waveguide. Each emitter has again two internal states $|e_m\rangle$ and $|g_m\rangle$ separated by a transition frequency ω_0 and is characterized by its position x_m along the waveguide. As opposed to the decreased interaction over distance in free-space the waveguide mediates the emitter-emitter interactions over an infinite range. Spontaneous emission into the waveguide occurs at rate Γ_0 and assuming that ω_0 is well below the cutoff frequency of the waveguide, the time evolution for the emitter density matrix of the array $\hat{\rho}$ has the form [35, 36] $\dot{\hat{\rho}} = -i\left(\hat{\mathcal{H}}_{\text{eff}}\hat{\rho} - \hat{\rho}\hat{\mathcal{H}}_{\text{eff}}^{\dagger}\right) + \sum_{m,n} \Gamma_{m,n} \hat{\sigma}_m \hat{\rho} \hat{\sigma}_n^{\dagger}$, where $\hat{\mathcal{H}}_{\text{eff}}$ is the collective Hamiltonian

($\hbar = 1$)

$$\hat{\mathcal{H}}_{\text{eff}} = \sum_{m,n=1}^{N} \Big(J_{m,n} - i\frac{\Gamma_{m,n}}{2} \Big) \hat{\sigma}_m^\dagger \hat{\sigma}_n \,, \tag{2.18}$$

composed of lowering operators $\hat{\sigma}_m = |g_m\rangle\langle e_m|$ and crucially of the periodic infinite range coherent and dissipative interaction terms

$$J_{m,n} = (\Gamma_0/2) \sin k_0 |x_m - x_n| \tag{2.19}$$

and

$$\Gamma_{m,n} = \Gamma_0 \cos k_0 |x_m - x_n|, \tag{2.20}$$

respectively. The interaction strength is determined by the individual decay rate Γ_0 while the effective emitter separation by $k_0 = \omega_0/c$, the wavevector of the guided mode on resonance with the emitters. This allows to create scenarios which would not be possible for emitters in free space. For instance for emitter separations $d = n\lambda_0$ with n being a whole positive number, the coherent exchange rates $J_{m,n}$ are zero and there is only collective dissipation $\Gamma_{m,n} = \Gamma_0$ for all n, m. In this so-called "mirror configuration", in the single excitation manifold, there is only one bright state, $|\Psi_S^{(1)}\rangle = \sum_m^N \hat{\sigma}_m^\dagger |G\rangle/\sqrt{N}$ where $|G\rangle = |g\rangle^{\otimes N}$, and $(N-1)$ perfectly dark states of exactly zero decay rate. This is the ideal realization of the Dicke model, where only the symmetric mode with decay rate $N\Gamma_0$ exists. It should be noted, that in experimental realizations dephasing, imperfections, and decoherence into free-space lead to a deviation from the idealized case as there will be coupling between different eigenmodes and $J_{nm} \neq 0$.

2.4 Collective excitations

In this section, we show how transforming the system of coupled quantum emitters into a collective basis can lead to a better understanding of the underlying physics. To this end, we choose emitters arranged in a ring geometry for the sake of clarity but the same analysis applies to all ordered emitter arrays in one to three dimensions. Furthermore, we restrict ourselves initially to the single excitation which means that we can analytically diagonalize the system and analyze the eigenvalues qualitatively. Also throughout this section we assume that all emitters are linear polarized perpendicular to the plane, $\vec{d} = (0, 0, 1)^T$.

2.4.1 Single excitation manifold

In this section, we want to showcase the usefulness of the collective basis and take two-level emitters in a ring geometry for simplicity, since one can write the eigenmodes and eigenvalues analytically even for finite system sizes [37]. In such a case we can neglect

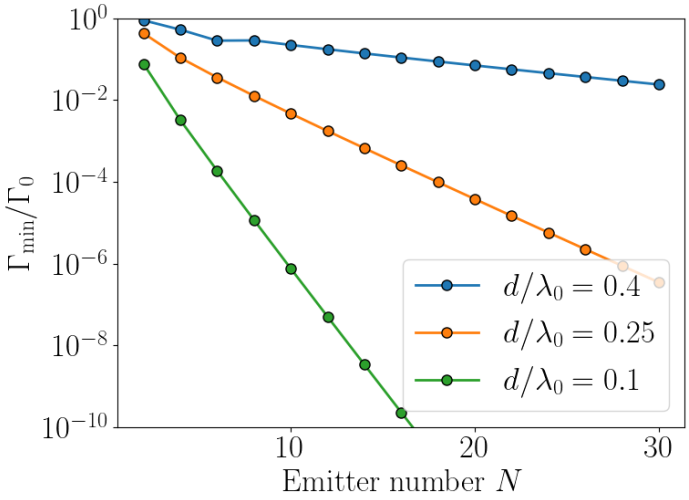

Figure 2.3: Scaling of the smallest decay rate of the single-excitation eigenstates in a ring of emitters as a function of the emitter number. The inter-emitter spacing d substantially changes the scaling but for fixed distances, the smallest decay rate is exponentially suppressed, i.e. $\Gamma_{\min}/\Gamma_0 \sim e^{-N}$.

the recycling term, the first term in the Lindbladian. This term keeps track of the change in the ground state population. Now the problem can be analytically understood from the properties of the eigenstates of an effective Hamiltonian, containing the remaining two parts of the Lindblad expression. The non-hermitian Hamiltonian is given by

$$\mathcal{H}_{\text{eff}} = \sum_{ij}^{N} \left(J_{ij} - i\frac{\Gamma_{ij}}{2} \right) \hat{\sigma}_i^\dagger \hat{\sigma}_j \tag{2.21}$$

For a single ring, where the dipole orientations preserve the rotational invariance, the collective eigenmodes of the effective Hamiltonian are perfect spin waves given by $|\Psi_m\rangle = \hat{S}_m^\dagger |g\rangle$, with

$$\hat{S}_m = \frac{1}{\sqrt{N}} \sum_{j=1}^{N_R} e^{im\varphi_j} \hat{\sigma}_j, \tag{2.22}$$

where $|g\rangle$ denotes all emitters in the ground state. Here $\varphi_j = 2\pi j/N$ is the angle associated with the position of emitter j along the ring and $m = 0, \pm 1, \cdots, \lceil \pm (N-1)/2 \rceil$ is the angular momentum of the collective mode. The associated energy shifts and decay rates of these spins waves are given by $J_m = \sum_j e^{im\varphi_j} J_{1j}$ and $\Gamma_m = \sum_j e^{im\varphi_j} \Gamma_{1j}$ respectively. For instance, the mode with $m = 0$ is fully symmetric upon exchange of emitters and for very small emitter spacings has a decay rate $\propto N\Gamma_0$, while the

remaining $N-1$ collective modes have vanishingly small decay rates. In Fig. 2.3 we show the scaling of the smallest decay rate as a function of the emitter number N. Although it significantly depends on the inter-emitter spacing d it shows an exponential suppression, $\Gamma_{\mathrm{min}}/\Gamma_0 \sim e^{-N}$. The analytic form of the eigenvalues indexed by the angular momentum number m also allows us to plot them as an energy band as shown in Fig. 2.4. For a single ring, this generates a dispersion curve with superradiant ($\Gamma_m > \Gamma_0$) eigenmodes inside a region enclosed by $\pm 2d$, whereas modes outside this region are subradiant and get more subradiant at the edge of the energy band. For small inter-emitter spacings the most subradiant, long-lived mode is exactly at the edge of the band, at $m = \pm(N-1)/2$ for odd N. Generally, these states are preferential for single photon storage but are notoriously hard to access and control. Only states inside the enclosed grey region can be directly excited by external light but decay back to ground state at a fast rate excluding them as candidates for photon storage. Similarly, excitation transport over a long range also needs protection from radiative decay at least as long as the transport time [38]. We will show in later chapters about molecules, that vibrations can be a resource to create a unidirectional flow of energy from the energetically higher-lying superradiant states into the lower-lying subradiant states.

2.4.2 Superradiant burst from a fully inverted ensemble

Dipole emitters in close proximity alter their radiative environment and collectively interact with light. For fully-inverted emitters, meaning all are in the excited state, at a single spatial location, this leads to the emission of a short pulse of light that initially rises in intensity. This stands in contrast to the exponential decay of independent emitters, which exhibit a monotonic emission rate. The superradiant process or Dicke superradiance [2], occurs because atoms synchronize as they decay, locking in their phase and emitting at an increasing rate. Although this scenario appears to be superficial and unattainable, it has been realized in various platforms such as optical cavities or waveguides where the condition of emitters at a point is met by the confined optical field and the infinite periodicity of the emitter-emitter interaction along the cavity or waveguide field. In these highly symmetric conditions, emitters are indistinguishable from each other and only a linear number of symmetric states participate in the dynamics. Here we describe the dynamics of a collection of N identical two-level systems interacting via a shared electromagnetic field. The emitters are again arranged in a ring with dipole orientations perpendicular to the ring plane. Since the system is fully inverted initially we are not able to analytically diagonalize the whole system. Still, we can bring the Lindbladian into a diagonal form by transforming into the collective spin basis,

$$\dot{\rho} = -i[\mathcal{H}, \rho] + \sum_{\nu=1}^{N} \frac{\Gamma_\nu}{2}\Big(2\hat{\mathcal{O}}_\nu \rho \hat{\mathcal{O}}_\nu^\dagger - \hat{\mathcal{O}}_\nu^\dagger \hat{\mathcal{O}}_\nu \rho - \rho \hat{\mathcal{O}}_\nu^\dagger \hat{\mathcal{O}}_\nu\Big). \tag{2.23}$$

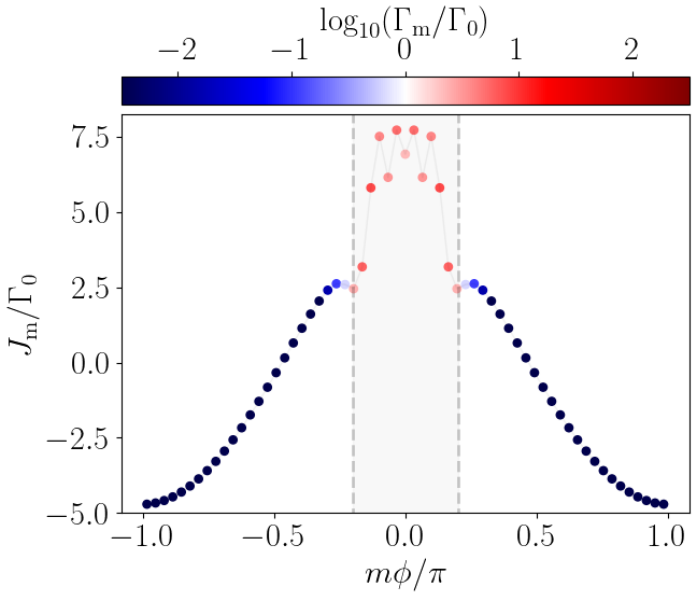

Figure 2.4: Eigenvalues for a ring of 61 two-level emitters with dipole orientations perpendicular to the ring plane organized in an energy band. The decay rates are color coded and show a super- to subradiant crossover at $m\phi/\pi = \pm 2d$, where $\phi = 2\pi/N$. Eigenmodes beyond this crossover are extremely subradiant as their emission is exponentially suppressed perpendicular along the ring. The dipole orientation is such, that the symmetric $m = 0$ state is energetically higher relative to the subradiant modes. For in-plane dipole orientation, the $m = 0$ mode would be at the bottom of the energy band. Here m is the angular momentum number with $m \in [-(N-1)/2, ..., (N-1)/2]$.

The collective jump operators $\hat{\mathcal{O}}_\nu$ are acting with rate Γ_ν and for subwavelength spacings there are only a small number of them that are non-negligible. In fact, it was shown in previous work [39] that the variance of these collective decay rates predicts whether a superradiant burst will take place. The condition for superradiance to occur reads $\mathrm{var}(\{\Gamma_\nu\}/\Gamma_0) > 1$ but is only valid for an initially fully inverted ensemble. On the other end, subradiance emerges simultaneously but in the long time limit, only a small fraction of the initial excitations remain, see Fig. 2.5. The subradiance can be explained by the fact, that some of the excited state population gets more and more sucked into subradiant decay channels where $\Gamma_\nu \ll \Gamma_0$ where the decay process is radically slowed down. The subradiant tail was experimentally shown recently for a cloud of rubidium atoms confined in an optical cavity [40]. These processes are usually highly probabilistic and harder to control than single-photon processes which already have many applications in quantum technologies. This makes this part of quantum

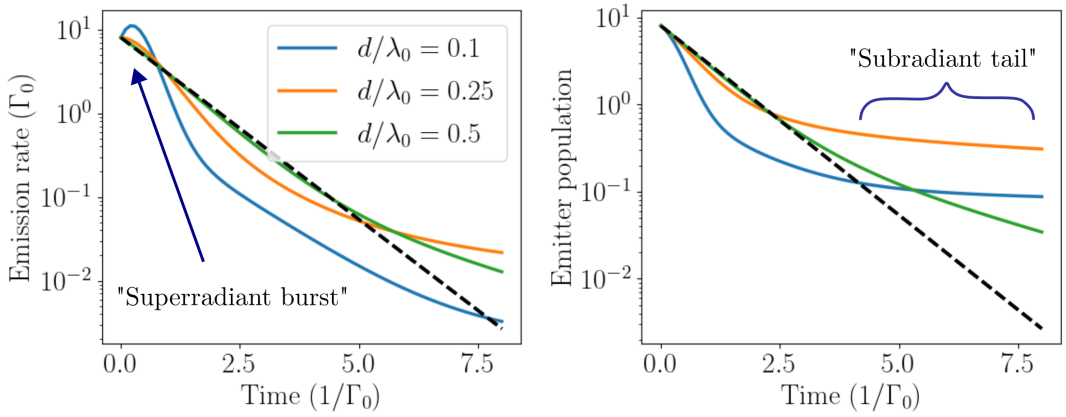

Figure 2.5: Multi-emitter decay is determined by the distance between emitters and their dipole orientation. 8 inverted emitters placed at a subwavelength spacing $d < \lambda_0$ interact with each other and decay collectively via the emission of a burst of light. In contrast, atoms that are far separated ($d \to \infty$) emit as single entities, in the form of an exponentially decaying pulse (black dashed line). For extended finite emitter numbers, there is a critical distance at which the crossover between a superradiant burst and monotonically decreasing emission occurs.

optics, namely many-body phenomena extremely interesting and challenging research topics with potentially huge advancements throughout the field.

3 Publication

Europhysics Letters **128**(4), (2020)

Subradiance in Multiply Excited States of Dipole-Coupled V-Type Atoms

R. Holzinger[1], L. Ostermann[1] and H. Ritsch[1]

[1]*Institut für Theoretische Physik, Universität Innsbruck, Technikerstrasse 21, A-6020 Innsbruck, Austria*

We generalize the theoretical modeling of collective atomic super- and subradiance to the multilevel case including spontaneous emission from several excited states towards a common ground state. We show that in a closely packed ensemble of N atoms with $N-1$ distinct excited states each, one can find a new class of non-radiating dark states, which allows for long-term storage of $N-1$ photonic excitations. Via dipole-dipole coupling only a single atom in the ground state is sufficient in order to suppress the decay of all $N-1$ other atoms. By means of some generic geometric configurations, like a triangle of V-type atoms or a chain of atoms with a $J=0 \to J=1$ transition, we study such subradiance including dipole-dipole interactions and show that even at finite distances long lifetimes can be observed. While generally hard to prepare deterministically, we identify various possibilities for a probabilistic preparation via a phase controlled laser pump and decay.

doi: 10.1209/0295-5075/128/44001

3.1 Introduction

Quantum fluctuations in the electromagnetic vacuum field inevitably lead to energy dissipation from excited atomic states via the spontaneous emergence of photons [41] known as spontaneous emission. In a quantum electrodynamics treatment the probability for this process and its corresponding decay rate $\Gamma = \omega_0^3 \mu^2/(3\pi\epsilon_0\hbar c^3)$ was first derived by Weiskopf and Wigner [42]. It is proportional to the third power of the transition energy between the excited and lower lying state as well as to the square of the transition dipole moment between those two states.

As there is only one electromagnetic vacuum, atoms in close proximity will experience correlated fluctuations inducing cooperative effects in their dissipative behavior. By means of constructive as well as destructive interference of the emerging photons the collective spontaneous emission rates are drastically modified as a function of distance [43–46]. A strongly increased spontaneous emission is dubbed 'superradiance' while a decreased rate is referred to as 'subradiance' [47].

Due to the quantum nature of atomic excitations, they can be delocalized and distributed over an entire atomic ensemble, exhibiting highly multi-partite entanglement [48–50]. Well known examples are the single-excitation Bell states of two atoms [51, 52], the W-state [53, 54] and many others.

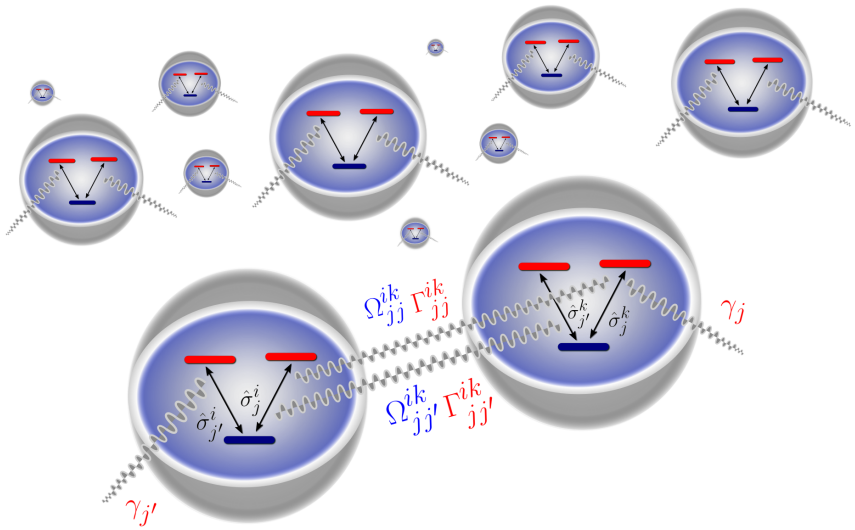

Figure 3.1: *Model.* We consider a collection of N identical multilevel atoms separated by a finite distance, which are coupled to the quantized electromagnetic vacuum field. Each atom i features $N-1$ excited states $|e_j\rangle$ with independent transitions to a common ground state $|g\rangle$, represented by σ^i_j. The collective decay rates are given by $\Gamma^{ik}_{jj'}$, whereas the collective energy shifts are written as $\Omega^{ik}_{jj'}$. The individual spontaneous emission rate for transition j in all atoms is γ_j.

Depending on the geometry of the atomic ensemble as well as on the local phase difference of the excitation amplitudes between the atoms, such delocalized excitation states can feature either super- or subradiance. For instance, for two closely spaced atoms ($d \ll \lambda_0 = 2\pi c/\omega_0$), the symmetric Bell state $|+\rangle = (|eg\rangle + |ge\rangle)/\sqrt{2}$ is superradiant, while its asymmetric analogue $|-\rangle = (|eg\rangle - |ge\rangle)/\sqrt{2}$ is strongly subradiant and decouples from the radiation field completely at distances close to zero [2]. This leads to the term 'dark state'. Because of the fact that their lifetime is often orders of magnitude longer than typical experimental cycles, those dark states are a valuable resource in quantum information storage and processing [55, 56].

While subradiant states of dense atomic ensembles are easy to identify theoretically [57,58], they have been quite elusive and hard to find in concrete experiments [5,59], with directional emission patterns as one of the signatures of destructive interference leading to subradiance [60]. Besides the influence of motion and various dephasing mechanisms, it was recently pointed out, that the complex level structure of typical atoms beyond a two-level approximation will often prevent the appearance of perfectly dark states [61]. In particular, for excited atomic states, which can decay to different lower states via more than one decay channel, the observation of subradiance is much more challenging. It can be easily shown that for a system of two Λ-type atoms no dark state can be found, as both decay channels need to be blocked via interference, which cannot be achieved simultaneously. However, in earlier work [61] we could show that an ensemble of N N-level atoms with and $N-1$ independent decay channels from the excited state to $N-1$ different ground states, a unique perfectly dark state, can be identified. This completely anti-symmetric dark state has remarkable entanglement and symmetry properties making it a promising candidate for quantum information applications.

In this paper, we investigate a related system, namely the inverted energy level configuration involving N atoms where one ground state is coupled to $N-1$ excited states $|i\rangle = |s_i\rangle = |e_i\rangle$. Each upper state can decay independently to a common ground state $|0\rangle = |s_0\rangle = |g\rangle$. Again the totally anti-symmetric state is a dark state of a similar form

$$|\psi_{\mathrm{d}}^N\rangle = \frac{1}{\sqrt{N!}} \sum_{\pi \in S_N} \mathrm{sgn}(\pi) \bigotimes_i |s_{\pi(i)}\rangle. \tag{3.1}$$

Here the sum runs over all permutations π of N elements. Using a spatially symmetric configuration of three atoms we will show below, that this N-level state of N atoms is subradiant as well as an eigentstate of the Hamiltonian.

3.2 Model

Let us consider a collection of N identical V-level type atoms at fixed positions $\{\vec{r}_i\}_{i=1}^N$. Each atom features $N-1$ excited states $\{|e_j\rangle\}_{j=1}^{N-1}$ at energies ω_j with dipole coupling to a common ground state $|g\rangle$ via a transition dipole moment of $\vec{\mu}_j$.

The combined Hamiltonian of the atoms and the electromagnetic field is given by

$$H = H_{\mathrm{A}} + H_{\mathrm{F}} + H_{\mathrm{int}} \tag{3.2}$$

with the atomic part $H_{\mathrm{A}} = \sum_{i=1}^{N} \sum_{j=1}^{N-1} \omega_j \sigma_j^{i+} \sigma_j^{i-}$ and the field $H_{\mathrm{F}} = \sum_{\vec{k},\lambda} \omega_k a_{\vec{k},\lambda}^{\dagger} a_{\vec{k},\lambda}$.

The interaction between the atoms and the field in dipole approximation is then

$$H_{\mathrm{int}} = -\sum_{i=1}^{N} \sum_{j=1}^{N-1} \left(\vec{\mu_j^i} \sigma_j^{i+} \cdot \vec{E}\left(\vec{r}_i\right) + \mathrm{h.c.} \right), \tag{3.3}$$

where $\vec{E}\left(\vec{r}_i\right)$ is the quantized electromagnetic field. When particularizing to $N = 3$ below, we will consider a situation where the transition dipole matrix elements inside each atom are mutually orthogonal and real, that is

$$\mu_j^i \cdot \mu_{j'}^i = 0. \tag{3.4}$$

After tracing out the electromagnetic field modes in a standard quantum optics fashion assuming the field in its vacuum state [46, 62–64] the system dynamics can be described by the master equation

$$\dot{\rho} = i\left[\rho, H\right] + \mathcal{L}\left[\rho\right] \tag{3.5}$$

with the effective Hamiltonian including dipole-dipole interaction

$$H = \sum_{i=1}^{N} \sum_{j=1}^{N-1} \omega_j \sigma_j^{i+} \sigma_j^{i-} + \sum_{i \neq k}^{N} \sum_{j,j'}^{N-1} \Omega_{jj'}^{ik} \sigma_j^{i+} \sigma_{j'}^{k-} \tag{3.6}$$

and the Liouvillian in Lindblad form

$$\mathcal{L}\left[\rho\right] = \sum_{i,k}^{N} \sum_{j,j'}^{N-1} \Gamma_{jj'}^{ik} \left(2\sigma_j^{i-} \rho \sigma_{j'}^{k+} - \sigma_j^{i+} \sigma_{j'}^{k-} \rho - \rho \sigma_j^{i+} \sigma_{j'}^{k-} \right), \tag{3.7}$$

where $\sigma_j^{i\pm}$ denotes the rising (lowering) operator of the j-th transition in the i-th atom.

The coherent part of the dipole-dipole interaction induces energy shifts (see Fig. 4.1) due to the couplings

$$\Omega_{jj'}^{ik} = \frac{3\sqrt{\gamma_j \gamma_{j'}}}{2} \left[\left(\vec{\mu}_j^i \cdot \vec{\mu}_{j'}^k \right) P_R\left(k_0 r_{ik}\right) - \left(\vec{\mu}_j^i \cdot \vec{r}_{ik} \right) \left(\vec{\mu}_{j'}^k \cdot \vec{r}_{ik} \right) Q_R\left(k_0 r_{ik}\right) \right], \tag{3.8}$$

while the incoherent collective dissipation is characterized by

$$\Gamma_{jj'}^{ik} = \frac{3\sqrt{\gamma_j \gamma_{j'}}}{2} \left[\left(\hat{\mu}_j^i \cdot \hat{\mu}_{j'}^k \right) P_I\left(k_0 r_{ik}\right) - \left(\hat{\mu}_j^i \cdot \hat{r}_{ik} \right) \left(\hat{\mu}_{j'}^k \cdot \hat{r}_{ik} \right) Q_I\left(k_0 r_{ik}\right) \right]. \tag{3.9}$$

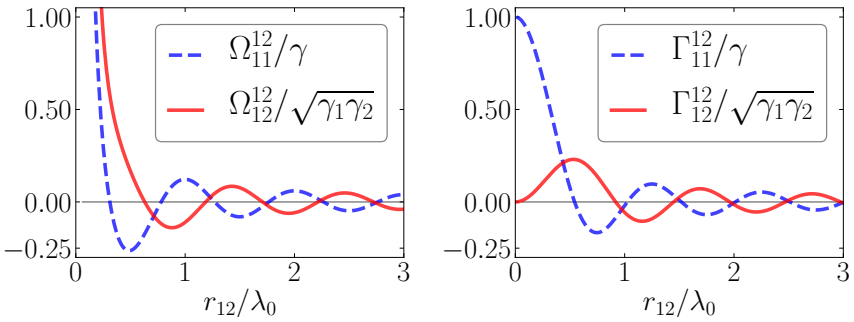

Figure 3.2: *Collective Couplings.* Coherent and dissipative dipole-dipole coupling coefficients as a function of the interatomic distance with $\theta_1 = \pi/4$, $\theta_2 = 3\pi/4$ for $\phi = 0$ (see Fig. 3.3). The blue dashed lines represent the coupling of two neighbouring and parallel dipole moments whereas the red lines represent couplings of orthogonal dipole moments which appear due to their indirect interaction via the same vacuum field.

Furthermore, for brevity we have introduced the functions

$$P_R(\xi) = \frac{\cos\xi}{\xi} - \frac{\sin\xi}{\xi^2} - \frac{\cos\xi}{\xi^3}, \tag{3.10}$$

$$P_I(\xi) = \frac{\sin\xi}{\xi} + \frac{\cos\xi}{\xi^2} - \frac{\sin\xi}{\xi^3}, \tag{3.11}$$

$$Q_R(\xi) = \frac{\cos\xi}{\xi} - 3\frac{\sin\xi}{\xi^2} - 3\frac{\cos\xi}{\xi^3}, \tag{3.12}$$

$$Q_I(\xi) = \frac{\sin\xi}{\xi} + 3\frac{\cos\xi}{\xi^2} - 3\frac{\sin\xi}{\xi^3}, \tag{3.13}$$

where $r_{ik} = |\vec{r}_i - \vec{r}_k|$ represents the interatomic distance between atom i and atom k, and $k_0 = \omega_0/c$ with $\omega_0 = \left(\omega_j + \omega_{j'}\right)/2$ and $\Gamma_{jj'}^{ii} = \gamma_j = 2\mu_j^2{\omega_j}^3/\left(3\epsilon_0 c^3\right)$ is the spontaneous emission rate of a single atom on the j-th transition. The couplings for the energy shifts as well as the collective decays are plotted in Fig. 3.2 as a function of the interatomic distance, whereas varying the dipole moment orientations leads to oscillations of various amplitudes (see Fig. 3.3). The terms Γ_{12}^{12} and Ω_{12}^{12} are dipole-dipole cross coupling coefficients, which couple dipoles even though they are orthogonal. [46].

3.3 Equilateral Triangle: Analytical Treatment

For three 3-level atoms placed at the corners of an equilateral triangle with dipole orientations chosen such that the configuration features a C_3 symmetry (see Fig. 3.3), the states $|\Psi_d^3\rangle$ and $|\Psi_{sr}^3\rangle$ are both eigenstates of the Hamiltonian from eq. (6.10) whose energies can be calculated explicitly. For three V-type atoms $|\Psi_d^3\rangle$ is given by

$$|\Psi_d^3\rangle = \frac{1}{\sqrt{6}}\{|e_1e_2g\rangle + |ge_1e_2\rangle + |e_2ge_1\rangle - |e_1ge_2\rangle - |e_2e_1g\rangle - |ge_2e_1\rangle\}, \tag{3.14}$$

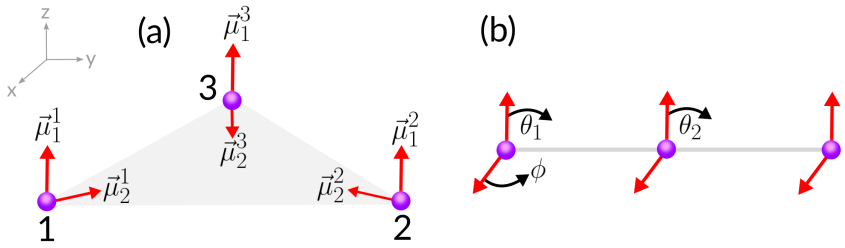

Figure 3.3: *Geometries.* We consider (a) an equilateral triangle and (b) a linear chain of three 3-level atoms. Here $\vec{\mu}_j^i$ represents the dipole orientation of the j-th transition in atom i.

whereas in the superradiant analogue $|\Psi_{sr}^3\rangle$, which is comprised of the exact same bare states, all signs are positive. Clearly, the dynamics of any eigenstate of the Hamiltonian is restricted to the decay towards other eigenstates $|\psi_{\text{eig}}\rangle$ induced by the Liouvillian, i.e. $\dot{\rho}_{\text{eig}} = \mathcal{L}[\rho_{\text{eig}}]$ with $\rho_{\text{eig}} = |\psi_{\text{eig}}\rangle\langle\psi_{\text{eig}}|$. The corresponding rates can be found by calculating the overlap with all other states. The decay and feeding rates for a certain selection of states are shown in Fig. 3.11. Explicitly, the decay rate for the eigenstate $|\psi_{\text{eig}}\rangle$ is given by $\langle\psi_{\text{eig}}|\,\mathcal{L}[\rho_{\text{eig}}]\,|\psi_{\text{eig}}\rangle$.

We find that the lowest lying energy state in the double excitation manifold corresponds to the antisymmetric dark state $|\Psi_d^3\rangle$, while the highest energy state is the superradiant state. With a more and more pronounced subradiance in $|\Psi_d^3\rangle$ at decreasing interatomic distances, also its feeding rate from higher lying states decreases, which culminates in a decoupling from all other states and the electromagnetic field. In particular, for the equilateral triangle configuration, the lower an eigenstate lies energetically, the smaller its decay rate, as can be seen for selected states in Fig. 3.11. A full account of all coupling and feeding rates is available in the supplementary information [65]. Also note that all feeding and decay rates to and from a particular state sum up to zero.

3.4 Numerical Diagonalization for three and more Atoms

For the case of $N \geq 3$ atoms we analyze the scaling of the decay rates as a function of the interatomic distance for increasing atom numbers and different geometries.

In Fig. 3.5(a) the simple case of two two-level atoms is shown, where the sub- and superradiant decay rates oscillate around the independent decay rate Γ with an amplitude decreasing with the interatomic distance, such that the super- and subradiant state switch their roles at each node. The black dashed curve corresponds to the lowest decay rate at any given distance and is generalized to more involved configurations in Fig. 3.5(b).

In Fig. 3.5 it can be seen, that the lowest collective decay rate for the $(N-1)$-

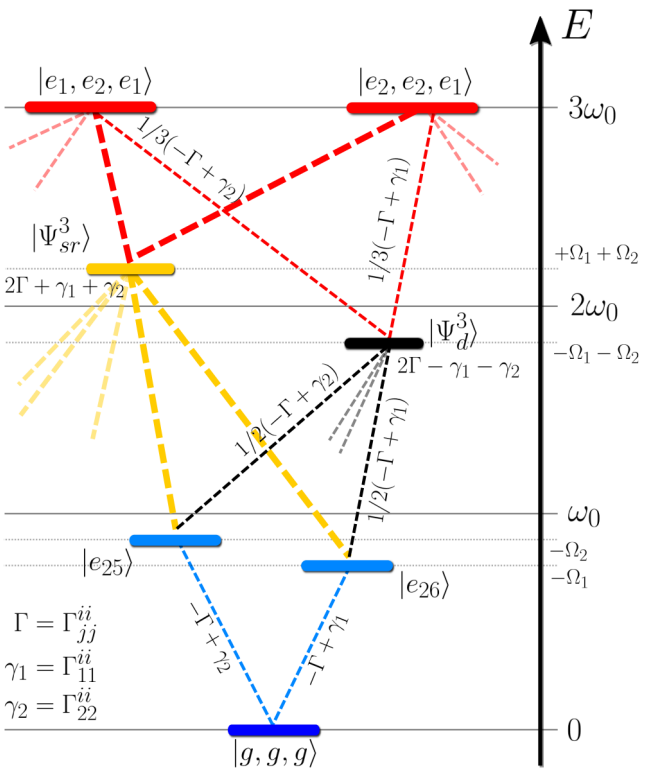

Figure 3.4: *Decay Cascade.* After diagonalizing the Hamiltonian for the equilateral triangle configuration of three 3-level atoms with symmetric dipole orientations we show the decay cascade for selected eigenstates (the full cascade can be found in the supplement [65]). We define $\gamma_1 \equiv \frac{3}{2}\Gamma P_I(k_0 r)$ and $\gamma_2 \equiv -\frac{3}{4}\Gamma P_I(k_0 r) + \frac{9}{8}\Gamma Q_I(k_0 r)$ and Γ represents the spontaneous emission rate of a single V-type atom with degenerate excited states. Additionally, the collective energy shifts in the respective excitation manifolds are shown with $\Omega_k \equiv \Omega^{ii}_{kk}$ and ω_0 being the energy between ground and excited states.

excitation manifold for N atoms goes to zero only if the interatomic distances approach zero, if all dipole transition moments are orthogonal to the plane of the atomic ensemble. For the equilateral triangle with symmetric dipole orientations and for $N \geq 4$ atoms with more than two transitions this is not possible anymore and the minimal decay rate is Γ.

3.5 Dark State Preparation

In most geometric configurations apart from the equilateral triangle the anti-symmetric state $|\psi^3_d\rangle$ is not an exact eigenstate of the Hamiltonian from Eq. (6.10) Yet, its

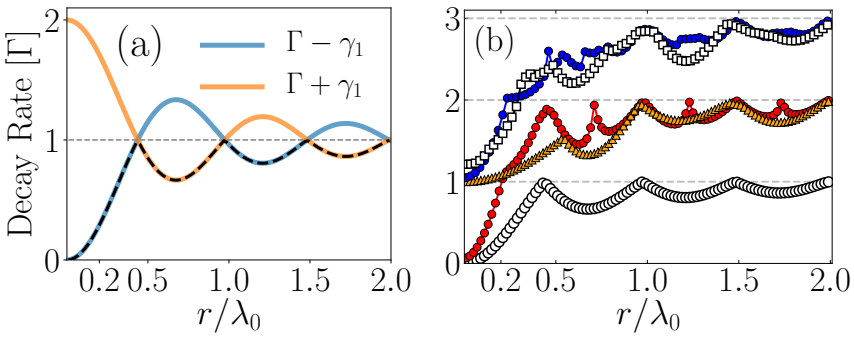

Figure 3.5: *Decay Rates.* (a) Sub- and superradiant decay rates for two dipoles as a function of the interatomic distance, where $\gamma_1 = \frac{3}{2}\Gamma P_I(k_0 r)$ and the black dashed line indicates the lowest decay rate at any given distance. (b) Lowest decay rates in the $(N-1)$ excitation manifold for N N-level emitters as a function of the interatomic distance, with the white circles corresponding to two 2-level atoms, the red circles to three 3-level V-type atoms in a linear chain, the orange triangles to an equilateral triangle, the blue circles to four 4-level V-type atoms in a chain and the white squares to four atoms in a square.

subradiant property will prevail as shown for a linear chain in Fig. 3.6. The state $|\Psi_{\text{unp}}\rangle = (|e_1 e_2\rangle + |e_2 e_1\rangle)/\sqrt{2} \otimes |g\rangle$ denotes a product state with atoms 1 and 2 entangled and exhibits subradiance as well. Generally, subradiance becomes particularly apparent at small atomic distances, where the derivative of the incoherent coupling with respect to r is almost zero. At finite distances $|\psi_d^3\rangle$ can couple to to other states and will therefore decay as shown in 3.6. Naturally, this means that it can be populated via decay from a higher lying state, which in this case are all triply excited states. A typical case where the dark state becomes populated by photon emission for a three qutrit chain prepared in a totally inverted state, $|e_1, e_2, e_1\rangle$, is demonstrated in Fig. 3.8. Note that there are, in fact, eight different possibilities for triply excited states, i.e. $|e_i, e_j, e_k\rangle$ with $i, j, k \in \{1, 2\}$, which lead to similar results. In Fig. 3.8 it can be seen, that the dark state can acquire a significant population, even via purely dissipative preparation, by choosing an appropriate geometric configuration. On the other hand, the feeding rate for the dark state becomes smaller with decreasing distances as it starts to decouple from the electromagnetic field. As we have seen above, after an initial build-up of population in the dark state, the remainder of the population mostly ends up in the ground state. Hence, one can think of reusing the atoms in the ground state in order to further increase the occupation of the dark state. For this purpose , the preparation of the dark state $|\Psi_d^3\rangle$ or its superradiant analogue $|\Psi_{sr}^3\rangle$ can be facilitated by a continuous pump laser. It turns out that using different excitation phases for each atom can strongly improve the efficiency of this process, although this might be challenging to implement in practice. We include a continuous pump in our

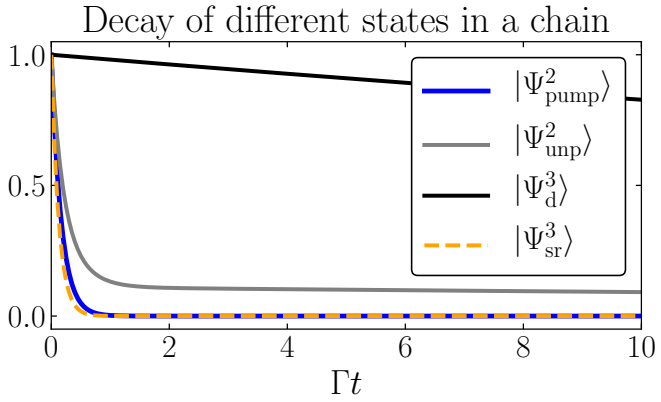

Figure 3.6: *Decay.* Population during decay for different doubly excited states in a linear chain of V-type atoms at $\lambda_0/50$ separation. The black line corresponds to the dark state $|\Psi^3_d\rangle$, the yellow dashed line to the superradiant state $|\Psi^3_{sr}\rangle$, the grey line to an unpolarized product state $1/\sqrt{2}(|e_1e_2\rangle - |e_2e_1\rangle)\otimes|g\rangle$ and the blue line to $1/\sqrt{2}(|e_1e_2\rangle - |e_2e_1\rangle)\otimes|e_1\rangle$, where all three atoms are initially excited.

model by adding the term $H_{\text{pump}} = \sum_{i=1}^{3}\sum_{j=1}^{2}\eta_i(\sigma_j^i + \sigma_j^{i\dagger})$ to the Hamiltonian with $\eta_1 = \eta$, $\eta_2 = \eta e^{i\varphi_1}$ and $\eta_3 = \eta e^{i\varphi_2}$, assuming that all atoms are driven with the same strength η. In our example the atoms are initialized in the ground state, $|ggg\rangle$, and we look at the population of the dark state after a given laser illumination time. In Fig. 3.9 the preparation probabilities for $|\Psi^3_d\rangle$ in a linear chain and for its superradiant analogue $|\Psi^3_{sr}\rangle$ in an equilateral triangle are shown as a function of the laser phase using a constant pump amplitude of $\eta = 8.5\Gamma$ at an interatomic distance of $\lambda_0/50$ in both cases. For the linear chain it can be seen, that for instance if atom 2 and 3 are driven by phases $\varphi_1 = \pi/2$ and $\varphi_2 = \pi$ relative to atom 1, the preparation probability for $|\Psi^3_d\rangle$ reaches 20%. The state will still decay, but with a small rate, as given in Fig. 3.6. In contrast, setting $\varphi_1 = 0$ and $\varphi_2 = 0$ in the equilateral triangle results in a preparation probability of 30% for $|\Psi^3_{sr}\rangle$. We find a surprisingly high preparation probability after a time evolution of $\Gamma t = 0.3$.

Now, we include different phases for different transitions by writing our pump Hamiltonian as $H_{\text{pump}} = \sum_{i=1}^{3}\sum_{j=1}^{2}\eta_j^i(\sigma_j^i + \sigma_j^{i\dagger})$. Figure 3.10 (a) shows the preparation probability for $|\Psi^3_d\rangle$ for a range of different phases, where for instance for $\varphi_1 = \varphi_2 = 7/10\pi$ a maximum of $\approx 24\%$ is reached after $\Gamma t = 0.3$. In Fig. 3.10 (b) we compare the time evolution of a pulsed laser with a continuous drive. Both cases lead to the same maximal value after $\Gamma t = 0.3$, but, after turning off the laser the dissipative dynamics lead to larger preparation probabilities shortly after that. Only for times longer than $\Gamma t = 1.5$ the laser driven system dominates the preparation probability. Specifically, for the case of pulsed lasing in Fig. 3.10 (b) the first peak corresponds to a preparation probability of 24% and the second peak to 15%, both within an evolution

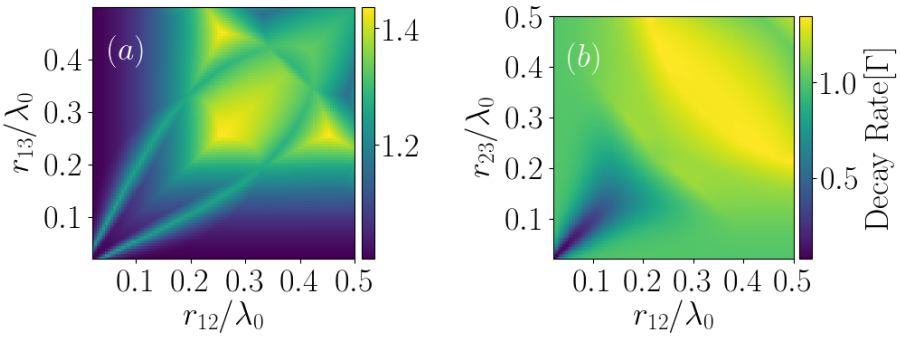

Figure 3.7: *Lowest Decay Rates.* The lowest decay rates (a) for three 3-level V-type atoms in a triangle configuration for eigenstates in the two-excitation manifold for different distances between atoms 1,2 and atoms 1,3 respectively and (b) in a chain of atoms for different distances between atoms 1,2 and atoms 2,3 where all transitions are orthogonal to the direction of the chain are shown.

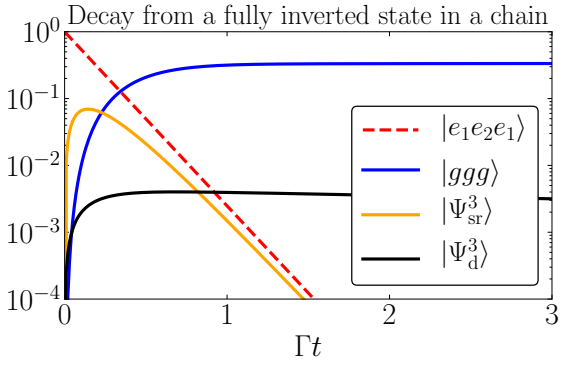

Figure 3.8: *Inverted Decay.* Occupation probabilities during a purely dissipative preparation of different typical states of three V-type atoms in a linear chain with interatomic distance $\lambda_0/20$. The red dashed line represents the inverted initial state, the orange line the superradiant state $|\Psi^3_{sr}\rangle$, the blue line the ground state fraction during the decay and the black line the dark state $|\Psi^3_d\rangle$ fraction during the decay process.

time of $\Gamma t = 1$.

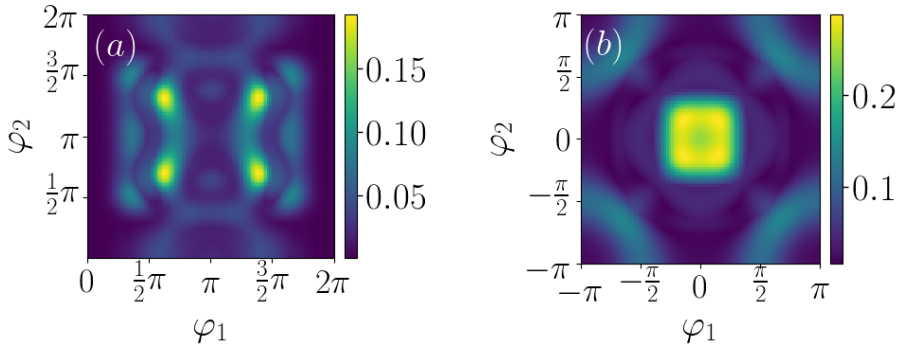

Figure 3.9: *Continous Laser Pump.* (a) Preparation probability of the dark state $|\Psi_d^3\rangle$ in a linear chain starting from $|g,g,g\rangle$ with interatomic separation $r = \lambda_0/50$, laser pumping strength $\eta = 8.5\Gamma$ and laser phases $e^{i\varphi_1}$ and $e^{i\varphi_2}$ for atoms 2 and 3 on both transitions with respect to atom 1 after $\Gamma t = 0.3$. (b) Probabilities for the superradiant state $|\Psi_{sr}^3\rangle$ in an equilateral triangle with the same parameters as in (a) where a maximum of $\approx 30\%$ is obtained for phases $(\varphi_1, \varphi_2) = (\pm\pi/3, \pm\pi/3)$.

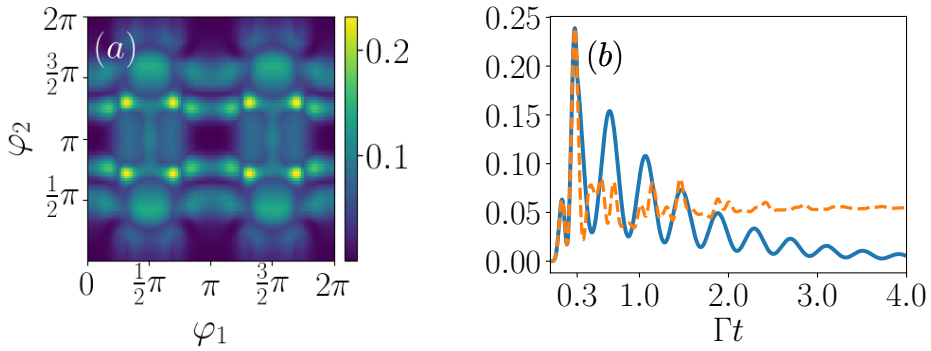

Figure 3.10: *Pulsed Laser.* (a) Preparation probability of the dark state $|\Psi_d^3\rangle$ in a linear chain starting from $|g,g,g\rangle$ with interatomic separation $r = \lambda_0/50$, laser pumping strength $\eta = 10\Gamma$ and laser phases $\eta_j^1 = \eta$,$\eta_1^2 = \eta e^{i\varphi_1}$,$\eta_1^3 = \eta e^{2i\varphi_1}$ and $\eta_2^3 = \eta_2^2 = \eta e^{2i\varphi_2}$. (b) Probability for $|\Psi_{\mathrm{d}}^3\rangle$ with the parameters from (a) and phases $\varphi_1 = \varphi_2 = 7/10\pi$ where the preparation probability is maximal. The orange dashed line corresponds to continuous lasing throughout the time evolution and the blue line to a laser pulse for a time of $[\Gamma t = 0.3]$.

3.6 Conclusions

We have generalized the concept of subradiance to multilevel emitters with several excited atomic levels decaying via independent decay channels towards a common ground state. In these systems the most subradiant states are completely anti-symmetric and maximally entangled. In contrast to ensembles of two-level emitters this multilevel type of dark states can hold several excitation quanta without decay. Hence detection could be facilitated by non-classical photon correlations at long time delays.

Entangled subradiant states have promising applications in quantum information processing and optical lattice clocks [66, 67], amongst other key quantum technologies, where longer coherence times and a better understanding of energy level shifts induced via dipole-dipole interactions are crucial for improved accuracies. States that do not decay as they decouple from the radiation field in turn are hard to access in order to prepare them directly. Yet, a probabilistic preparation can be achieved via spontaneous emission from higher lying states or in a much more efficient way by the application of laser pulses with spatial phase control. Future work in this lines of studies will include coupling to a cavity field and analyzing the emission and absorption behaviour of multiple V-type emitters via an input/output formalism as in [68]. Another direction is to investigate possible waveguiding effects with the above model in the second excitation manifold as was done for the single excitation manifold in [69] for two-level emitters and for emitters with multiple levels in the ground and excited state.

Acknowledgements

Financial support for this publication has been provided by the European Research Commission through the Quantum Flagship project iqClock (R. H. and H. R.) as well as by the Austrian Science Fund FWF through project P29318-N27 (L. O.).

3.7 Supplemental Material

3.7.1 Decay Cascade For Three 3-level Emitters

By considering

$$\langle\psi|\,\mathcal{L}[|\psi_d^3\rangle\,\langle\psi_d^3|]\,|\psi\rangle \quad \text{and} \quad \langle\psi|\,\mathcal{L}[|\psi_{sr}^3\rangle\,\langle\psi_{sr}^3|]\,|\psi\rangle \tag{3.15}$$

where $|\psi\rangle$ are all the lower lying eigenstates into which the superradiant and subradiant state decays, we obtain the decay rates into the respective states. For $|\psi\rangle = |\psi_d^3\rangle$ or $|\psi\rangle = |\psi_{sr}^3\rangle$ we obtain the total decay rate.

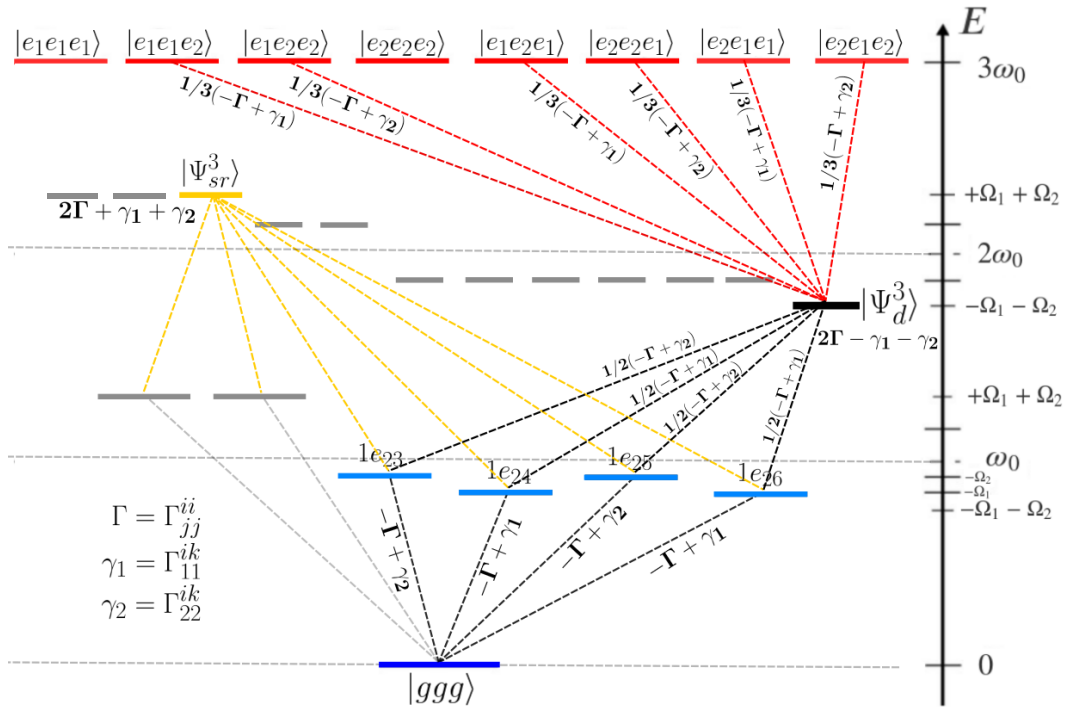

Figure 3.11: All 27 eigenstates for the equilateral triangle with eight fully inverted states corresponding to all permutations of $|e_i, e_j, e_k\rangle$ with $i, j, k \in \{1, 2\}$, twelve eigenstates in the double excitation manifold, six eigenstates in the single excitation manifold and one ground state with no excitations. As in the main text, we define $\gamma_1 \equiv \frac{3}{2}\Gamma P_I(k_0 r)$ and $\gamma_2 \equiv -\frac{3}{4}\Gamma P_I(k_0 r) + \frac{9}{8}\Gamma Q_I(k_0 r)$ with Γ being the spontaneous emission rate of a single 3-level V-type atom on both transitions, assuming degeneracy.

Whereas for

$$\langle\psi^3_d|\,\mathcal{L}[|e_i e_j e_k\rangle\langle e_i e_j e_k|]\,|\psi^3_d\rangle \quad \text{and} \quad \langle\psi^3_{sr}|\,\mathcal{L}[|e_i e_j e_k\rangle\langle e_i e_j e_k|]\,|\psi^3_{sr}\rangle\,, \tag{3.16}$$

where $i, j, k = 1, 2$ and $e_i e_j e_k$ are the 8 possible inverted states which can feed the Super- and Subradiant states, we obtain the feeding rates. From the decay rate of the dark state we see that in the limiting case of infinitely close atoms, the decay could become even zero and the state would be indeed stationary under the Liouvillian superoperator. As is demonstrated in the main text, for the triangle it approaches 1Γ for infinitesimal distances and zero for the linear chain.

4 Publication

Physical Review Letters **124**(253603), (2020)

Nanoscale Coherent Light Source

R. Holzinger[1], D. Plankensteiner[1], L. Ostermann[1] and H. Ritsch[1]

[1]*Institut für Theoretische Physik, Universität Innsbruck, Technikerstrasse 21, A-6020 Innsbruck, Austria*

A laser is composed of an optical resonator and a gain medium. When stimulated emission dominates mirror losses, the emitted light becomes coherent. We propose a new class of coherent light sources based on wavelength sized regular structures of quantum emitters whose eigenmodes form high-Q resonators. Incoherent pumping of few atoms induces light emission with spatial and temporal coherence. We show that an atomic nanoring with a single gain atom at the center behaves like a thresholdless laser, featuring a narrow linewidth. Symmetric subradiant excitations provide optimal operating conditions.

DOI: 10.1103/PhysRevLett.124.253603

4.1 Introduction

Conventional lasers consist of an optical cavity filled with a gain medium, typically comprised by an ensemble of energetically inverted emitters amplifying the light field via stimulated emission. Pioneering experiments have realized lasers with the most minimalistic gain medium yet, a single atom [70–77]. Corresponding theoretical quantum models have already been studied extensively for several decades [78–81]. Standard models of a single-atom laser still feature a macroscopic optical resonator supporting the corresponding laser light mode. Technically, the noise of the cavity mirrors is a substantially limiting factor for the frequency stability of a laser. This can be reduced when working in the bad cavity regime, such that the coherence is stored in the atomic dipoles rather than the light field. In such superradiant lasers [82–86] the properties of the emitted light are governed by the gain medium rather than the resonator.

In this work we go one step further removing the cavity altogether and consider a nano-scale system where atomic quantum emitters provide for the necessary gain while simultaneously acting as a resonator. Thus, in principle, the size of the entire setup can be reduced to even below the order of the laser wavelength. Such a device is characterized solely by the spectral properties of the atoms. As discovered recently,

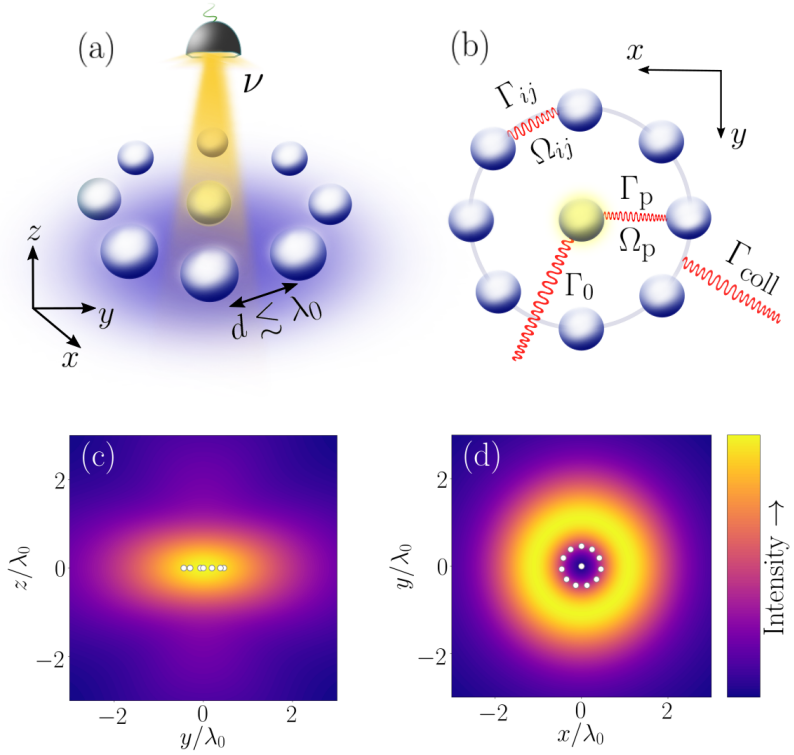

Figure 4.1: *Coherent Light Emission from a Partially Pumped Atomic Array.* (a) A ring of atoms with an additional atom in its center incoherently pumped with a rate ν. (b) The atoms decay at a spontaneous decay rate Γ_0 and are collectively coupled to the center atom with dispersive coupling Ω_p and dissipative coupling Γ_p, respectively. In turn, the ring atoms have couplings Ω_{ij} and Γ_{ij} amongst each other. The symmetric excitation exhibits a collective decay rate Γ_coll. (c) The field intensity generated in the steady state according to eq. (5.4) for a ring of $N = 11$ atoms in the xz-plane with $y = 2.5\lambda_0$ and interatomic distance $d = \lambda_0/5$ and pumping rate $\nu = 0.1\Gamma_0$. (d) The field intensity in the xy-plane with $z = 2.5\lambda_0$.

tailored dipole-coupled atomic arrays possess collective eigenmodes with a very long lifetime demonstrating analogous characteristics to a high-Q optical cavity mode [37,87]. Such arrangements could be implemented, e.g. by means of optical tweezers [88–90] or superconducting qubit setups operating in the microwave regime [91]. We study the

prospects of implementing a minimalistic sub-wavelength sized laser by incoherently pumping some of the dipoles in such a nano array. As our generic setup we consider a single atom placed in the center of a small ring comprised of identical emitters. The collective coupling to the other emitters in the ring is mediated by virtual photon exchange through the electromagnetic vacuum [43, 75, 92]. The collective eigenmodes of the outer ring take on the role of a resonator mode.

We show that such a minimal model constitutes a steady-state coherent light source with a spectral linewidth well below the single atom decay rate. Therefore, it can be viewed as a minimal implementation of a laser. Depending on the number of atoms and the configuration of the array, the collective nature of the dipole-dipole couplings leads to strong quantum correlations within the atoms and an inherent emission of a coherent field. Optimal operation is achieved when the collective state in the ring atoms features a single subradiant excitation only.

4.2 Model

We consider N identical two-level atoms with excited state $|e\rangle$ and ground state $|g\rangle$ each, separated in frequency by ω_0 and arranged in a ring geometry at an interatomic distance of $d\lambda_0 = 2\pi c/\omega_0$. An additional gain atom is placed in the center of the ring as depicted in Fig. 4.1a and is assumed to be pumped to its upper level incoherently at a rate ν (after having eliminated auxiliary levels). The corresponding raising (lowering) operators of the ith atom are $\sigma_i^{\pm}$ for $i \in \{1, 2, \ldots, N, p\}$ (the index p corresponds to the central, pumped atom). The excited state is subject to spontaneous emission with a rate Γ_0. All transition dipoles $\boldsymbol{\mu}_i$ are chosen such that they point in z-direction. At the considered distances, the fields emitted by each of the atoms interfere resulting in effective dipole-dipole interactions [43], so that the atomic ring acts like a resonator [37] coupled to the gain atom in its center. Using standard quantum optical techniques [62] we obtain a master equation for the internal dynamics of the emitters, $\dot{\rho} = i\,[\rho, H] + \mathcal{L}_\Gamma\,[\rho] + \mathcal{L}_\nu\,[\rho]$, where the Lindblad term describing the incoherent pumping of the central atom is given by $\mathcal{L}_\nu\,[\rho] = \frac{\nu}{2}\left(2\sigma_\mathrm{p}^+\rho\sigma_\mathrm{p}^- - \sigma_\mathrm{p}^-\sigma_\mathrm{p}^+\rho - \rho\sigma_\mathrm{p}^-\sigma_\mathrm{p}^+\right)$. The corresponding Hamiltonian in a frame rotating at the atomic transition frequency ω_0 is

$$H = \sum_{i,j:i\neq j} \Omega_{ij}\sigma_i^+\sigma_j^-, \tag{4.1}$$

while the Lindblad operator accounting for collective spontaneous emission reads

$$\mathcal{L}_\Gamma\,[\rho] = \sum_{i,j} \frac{\Gamma_{ij}}{2}\left(2\sigma_i^-\rho\sigma_j^+ - \sigma_i^+\sigma_j^-\rho - \rho\sigma_i^+\sigma_j^-\right). \tag{4.2}$$

The collective coupling rates Ω_{ij} and Γ_{ij} are given as the real and imaginary part of the overlap of the transition dipole of the ith atom with the electric field emitted by the jth atom [93]. The emitted electric field $\boldsymbol{E}^+(\boldsymbol{r})$ can be used to compute the field

intensity as [93], i.e.

$$I(\boldsymbol{r}) = \left\langle \boldsymbol{E}^{+}(\boldsymbol{r})\boldsymbol{E}^{-}(\boldsymbol{r}) \right\rangle , \tag{4.3}$$

The steady-state intensity is shown in Fig. 4.1c and Fig. 4.1d for typical operating conditions.

4.3 Continuous Collective Emission

Our goal is to find operating regimes where the system emits coherent light with a narrow linewidth. As the configuration is symmetric with respect to the coupling of the ring atoms to the gain atom in the center, we can expect the ring atoms to be driven into a symmetric excitation state given as

$$|\psi_{\mathrm{sym}}\rangle = \frac{1}{\sqrt{N}} \sum_{j=1}^{N} \sigma_j^{+} \, |g\rangle^{\otimes N} . \tag{4.4}$$

In accordance with standard laser theory we will target parameters for which a symmetric excitation of the ring atoms constitutes a good cavity, i.e. the radiative loss is sufficiently small. To this end, we study the stationary populations of different eigenstates of our Hamiltonian from Eq. (5.2) during a time evolution starting from the ground state as depicted in Fig. 4.2a.

Indeed, as shown in Fig. 4.2, we find that the two eigenstates involving the symmetric single-excitation state in the ring are occupied predominately at all times (except for the ground state). These states are given by

$$|\Psi_i\rangle = a_i \, |g\rangle^{\otimes N} \otimes |e\rangle + b_i \, |\psi_{\mathrm{sym}}\rangle \otimes |g\rangle , \tag{4.5}$$

for $i \in \{1, 2\}$, where a_i and b_i depend on the particular geometry with $|a_i|^2 + |b_i|^2 = 1$.

Note that the gain atom can only emit one photon into the ring at a time. Hence, the single-excitation manifold dominates the dynamics even for pump rates substantially larger than the single-atom decay rate. This is shown in Fig. 4.2b, where we plot the occupation probability of different eigenstates at steady state as a function of ν.

The fact that the ring does indeed form a resonator can be seen more clearly as follows. Let us assume that only the symmetric state in the ring is populated. Thus, we can rewrite the Hamiltonian in the subspace spanned by the ground and excited state of the gain atom in the center, as well as the ground state of the ring and its symmetric state obtaining [93]

$$H_{\mathrm{sym}} = \Omega_{\mathrm{sym}} \sigma_{\mathrm{sym}}^{+} \sigma_{\mathrm{sym}}^{-} + \sqrt{N} \Omega_{\mathrm{p}} \left(\sigma_{\mathrm{sym}}^{+} \sigma_{\mathrm{p}}^{-} + \mathrm{H.c.} \right) , \tag{4.6}$$

where $\Omega_{\mathrm{sym}} = \sum_{j=2}^{N} \Omega_{1j}$ is the dipole energy shift of the symmetric state. Written like this, the Hamiltonian resembles the Jaynes-Cummings Hamiltonian with the ring

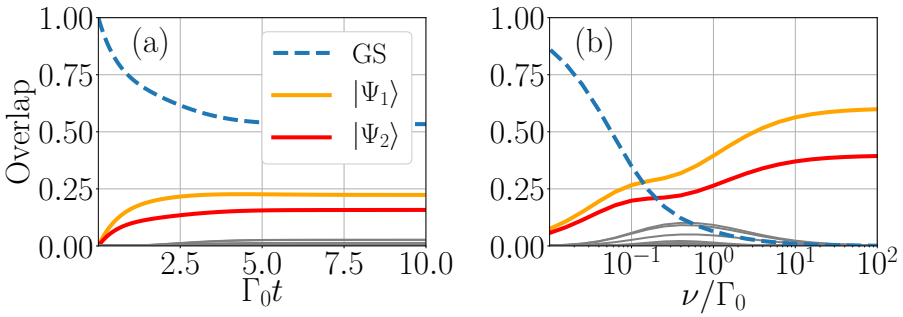

Figure 4.2: *Dissipative System Dynamics.* (a) Time evolution of the population of the eigenstates of the Hamiltoniann from eq. (5.2)]for $N = 5$ ring atoms with an interatomic distance $d = \lambda_0/2$ and an incoherent pump rate $\nu = \Gamma_0/2$ starting from the ground state. The state $|\Psi_{1,2}\rangle$ feature a large contribution from the symmetric state of the ring atoms $|\psi_{\text{sym}}\rangle$ and show significantly higher populations than all other excited eigenstates (gray lines) at all times. (b) Stationary population of the eigenstates for different pump rates. We can see that even for large pump rates $\nu > \Gamma_0$ the symmetric single-excitation states dominate.

taking on the role of the cavity mode. In this sense, the symmetric subspace lowering operator $\sigma^-_{\text{sym}} = |g\rangle^{\otimes N} \langle\psi_{\text{sym}}| \otimes 1_{\text{p}}$ can be interpreted as the photon annihilation operator of our "cavity". The coupling between the gain atom and the cavity is then determined by Ω_{p}. If we neglect the dissipative coupling between the central atom and the atoms forming the ring, i.e. $\Gamma_{\text{p}} = 0$, we can rewrite the decay of the system as $\mathcal{L}[\rho] = \mathcal{L}_\nu[\rho] + \mathcal{L}_0[\rho] + \mathcal{L}_{\text{sym}}[\rho]$, with

$$\mathcal{L}_0[\rho] = \frac{\Gamma_0}{2}\left(2\sigma^-_{\text{p}}\rho\sigma^+_{\text{p}} - \sigma^+_{\text{p}}\sigma^-_{\text{p}}\rho - \rho\sigma^+_{\text{p}}\sigma^-_{\text{p}}\right), \tag{4.7a}$$

$$\mathcal{L}_{\text{sym}}[\rho] = \frac{\Gamma_{\text{sym}}}{2}(2\sigma^-_{\text{sym}}\rho\sigma^+_{\text{sym}} - \sigma^+_{\text{sym}}\sigma^-_{\text{sym}}\rho - \rho\sigma^+_{\text{sym}}\sigma^-_{\text{sym}}).$$

Minimizing the decay rate of the ring atoms is important, but in order to build up population within the ring we need an efficient coupling to the gain atom as well. In analogy to the Jaynes-Cummings model we thus define a cooperativity parameter [93] $C := N\Omega_{\text{p}}^2/(\Gamma_0\Gamma_{\text{sym}})$. An efficient coherent coupling of the ring atoms to the gain atom is achieved when $C > 1$. As we can see in Fig. 4.4b, we reach this limit at extremely small distances or at a distance where Γ_{sym} is minimal (see Fig. 4.3). The cooperativity becomes large at $d < 0.1\lambda_0$ since for $d \to 0$ the coherent coupling diverges. Yet, this is also the limit where the energy difference Ω_{sym} is large, which detunes the ring atoms from the gain atom. Furthermore, as we will show later, due to the superradiant loss of the ring in this limit the emitted light features thermal

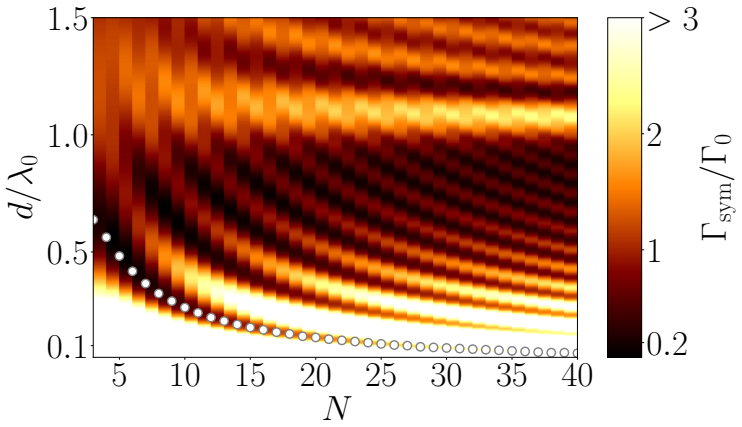

Figure 4.3: *Super- and Subradiance of the Symmetric State.* The decay rate of the symmetric state Γ_{sym} as a function of the atom number in the ring and their interatomic distance. The white dots highlight specific interatomic distances where the decay of the symmetric state is the smallest (subradiant).

statistics rather than coherence. Consequently, we find that the optimal parameter regime indeed lies where the ring atoms show a subradiant behaviour, i.e. at the points highlighted in Fig. 4.3. As seen in Fig. 4.4a, the dissipative coupling of the central

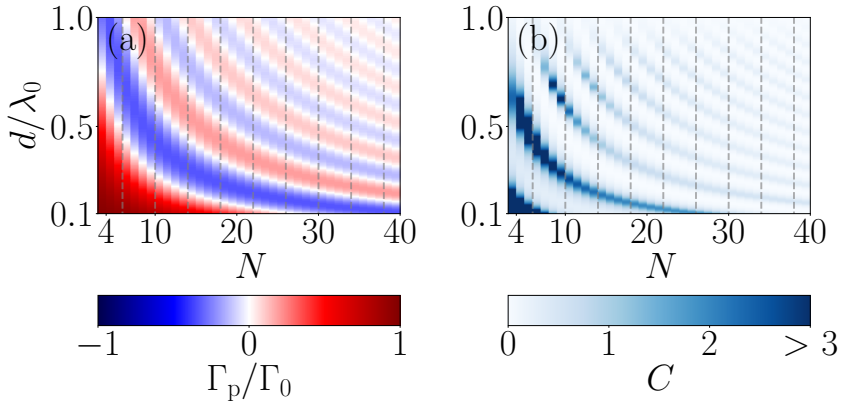

Figure 4.4: *Coupling of the Central Gain Atom to the Outer Ring.* (a) The dissipative coupling Γ_{p} between the central atom and the ring atoms is plotted as a function of the atom number N and the inter-atomic distance d. One can see that it becomes negligible at the points where $|\psi_{\mathrm{sym}}\rangle$ is subradiant. (b) Cooperativity C for different distances and atom numbers. The cooperativity is large when $d \to 0$ due to the divergent behavior of Ω_{p}, or when Γ_{sym} is small.

atom vanishes at points where the symmetric state shows suppressed spontaneous emission (see Fig. 4.3). Hence, the loss during the excitation transport from the gain medium to the ring is reduced as well.

4.4 Photon Statistics and Spectral Properties

We have now identified a regime where our system resembles the typical setup of a single-atom laser. In order to study the statistical properties of the emitted light we calculate the normalized second-order correlation at zero time delay $g^{(2)}(0)$ of the electric field intensity. In the far-field $r \gg \lambda_0$, where the intensity correlation function becomes independent of the position [93] and is given by

$$g^{(2)}(0) = \frac{\sum_{ijkl} \left\langle \sigma_i^+ \sigma_j^+ \sigma_k^- \sigma_l^- \right\rangle}{|\sum_{mn} \left\langle \sigma_m^+ \sigma_n^- \right\rangle|^2}. \tag{4.8}$$

Coherent light exhibits a Poissonian statistic implying $g^{(2)}(0) = 1$ [62,94]. Therefore, an operation in the previously identified parameter regimes leads to the emission of coherent light. In addition , we calculate the amount of emitted light, i.e. $I_{\text{out}} := \sum_{ij} \Gamma_{ij} \left\langle \sigma_i^+ \sigma_j^- \right\rangle$. In Fig. 4.5a we can see that points of coherent light emission where $g^{(2)}(0) = 1$ are achieved along a curve strongly resembling the optimal subradiance parameters shown in Fig. 4.3. The points where $g^{(2)}(0) = 0$ correspond to the situation where the gain atom decouples from the cavity atoms, since then only the single atom in the center can emit light. And, because it is not possible for a single atom to emit more than one photon at a time, we observe anti-bunching. However, this regime does not coincide with "lasing" since the ring atoms are not occupied. Simultaneously, the intensity shown in Fig. 4.5b is small, but still finite when the emitted light is coherent. This is because coherences can only build up when the loss from the atoms in the ring is sufficiently low (Γ_{sym} is small), which also reduces the amount of light emitted. In order to analyze the emitted light in more detail, we compute its spectral linewidth. Therefore, we calculate the emission spectrum by means of the Wiener-Khinchin theorem [93, 95]. It is given as the Fourier transform of the first-order coherence function, $g^{(1)}(\tau) := \sum_{i,j} \left\langle \sigma_i^+(\tau) \sigma_j^- \right\rangle$. The spectrum has a Lorentzian shape, thus we compute the linewidth $\Delta\nu$ as the full width at half maximum (FWHM). In Fig. 4.5c, we show the linewidth as a function of N and the interatomic distance d. Once again, we find that the linewidth is small ($\Delta\nu < \Gamma_0$) at the points where the symmetric state is subradiant. It can be seen that in order to maintain coherent light emission the interatomic distances need to become smaller for an increasing number of atoms in a ring of constant radius.

Note, that in order to treat larger atom numbers in the above calculations we have truncated the Hilbert space at the second-excitation manifold [93]. Since the

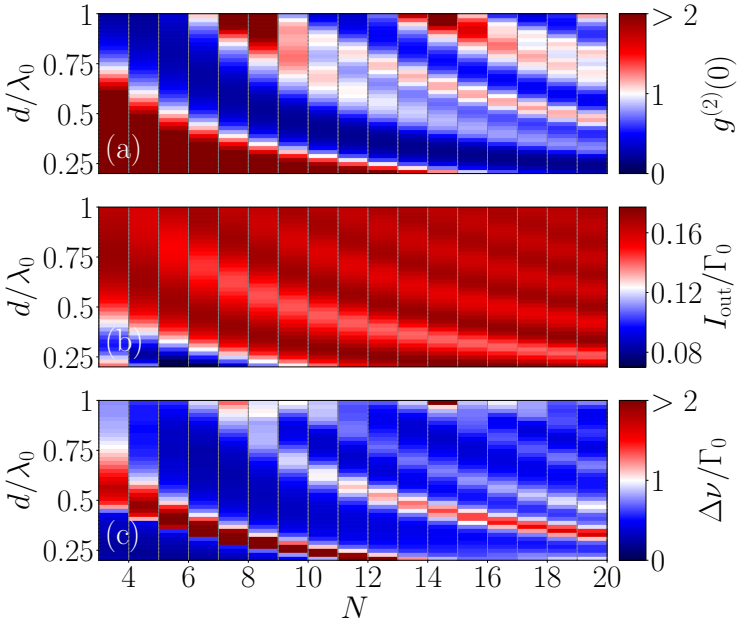

Figure 4.5: *Intensity and Statistics of the Emitted Light.* (a) Steady-state second-order correlation as a function of the ring atom number and atom spacing. For each atom number N there are specific interatomic distances d where the emitted light changes from thermal-like light emission (red), passing over regions of Poissonian statistics (white), to sub-Poissonian properties (blue). (b) The radiated intensity I_{out} for the same parameter region. Where $g^{(2)}(0) = 1$ the intensity is maximal, regardless of the atom number. (c) The spectral linewidth $\Delta\nu$ for the same parameters. It reduces to well below Γ_0. The pump rate was $\nu = 0.1\Gamma_0$.

single-excitation subspace usually dominates [as shown in Fig. 4.2], neglecting any state containing more than two excitations is well justified.

4.5 Threshold-Less Behavior

In standard lasing models, coherent output light is achieved from a certain input power threshold on. Above threshold, the intensity of the emitted light increases drastically. In an effort to identify such a threshold in our setup, we compute the properties of the output light as a function of the pump strength of the gain atom.

The system does not exhibit a threshold. Such a threshold-less behavior has been observed in single-atom lasing setups [71]. As we can see in Figs. 4.6a and 4.6b, the output intensity grows as soon as the pump rate becomes nonzero, rather than requiring a sufficiently large pump rate. At the same time, the photon statistics of

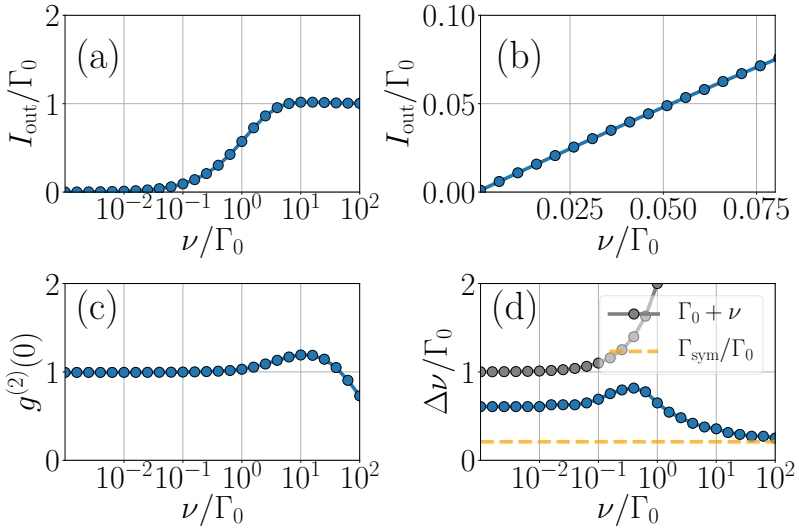

Figure 4.6: *Threshold-Less Coherent Light Emission.* (a) I_{out} as a function of the pump rate ν for $N = 5$, $d = \lambda_0/2$ exhibiting maximum from $\nu \approx 4\Gamma_0$ onwards. (b) A zoom in to the weak pump region shows the immediate onset of the intensity I_{out} at small ν. (c) The second-order correlation $g^{(2)}(0)$ in steady state is 1 for finite, but small ν. (d) The radiative linewidth $\Delta\nu$ (blue) in the steady state stays well below the pump broadened linewidth $\Gamma_0 + \nu$ of a single emitter (gray), and approaches the decay rate Γ_{sym} of the symmetric state (yellow, dashed line).

the emitted field are Poissonian, i.e. $g^{(2)}(0) = 1$, for arbitrarily low pumping rates (see Fig. 4.6c). The only point at which the photon statistics change is when the pump rate becomes large, $\nu \sim 10\Gamma_0$, such that the emitted light starts to reproduce the thermal statistics of the input field. It can also be seen in Fig. 4.6a that above this point the output intensity is actually reduced. As one would expect, the linewidth of the emitted field is small ($\Delta\nu < \Gamma_0$) as long as the light is coherent (see Fig. 4.6d). When the incoherent pumping rate ν is increased, states outside the symmetric subspace are occupied, which leads to a slight increase in the linewidth. However, by increasing ν further, the linewidth decreases again and approaches Γ_{sym} as the central atom decouples from the ring atoms the light is emitted from the ring in the subradiant symmetric state.

4.6 Conclusions

We predict that a continuously pumped single atom surrounded by a nano-ring of identical atoms could act as a minimal, sub-wavelength sized implementation of a laser. Under suitable operating conditions the system will emit spatially and temporarily

coherent light with Poisson statistics. Our analysis reveals a close analogy to the Jaynes-Cummings model, where the outer ring atoms take on the role of a high-Q cavity mode with the central atom providing for gain. The system works best when driven into a collective subradiant state with a single excitation. In this limit, spontaneous emission is suppressed and the operation strongly resembles the behavior of a threshold-less laser [96]. While the implementation of such a system in a pure form could be envisioned in optical tweezer arrays of neutral atoms [88], analogous setups based on quantum dots have been implemented and are already operational in the pulsed excitation regime [97].

Let us note here that there are no principal lower physical limits on the size of the system apart from the technical implementation of the structure and its pumping. Hence, very high density arrays of such lasers on a surface are possible.

Acknowledgements

We acknowledge funding from the European Union's Horizon 2020 research and innovation program under Grant Agreement No. 820404 iqClock (R. H., D. P. and H. R.) as well as from the Austrian Science Fund under project P29318-N27 (L. O.). The numerical simulations were performed with the open-source framework QuantumOptics.jl [13] and the graphs were produced with the open-source library Matplotlib [98].

4.7 Supplemental Material

4.7.1 Symmetric Subspace

As mentioned in the main text, during the whole time evolution and for any incoherent pumping rate ν the ring is mainly in the symmetric state. This allows us to restrict ourselves to a subspace within the single-excitation manifold where either the central atom is excited or the symmetric state of the ring is populated. The Hilbert space is spanned by these two states and the ground state of the system, i.e.

$$\Big\{|\phi_1\rangle, |\phi_2\rangle, |\phi_3\rangle\Big\} \equiv \Big\{|\psi_{\mathrm{sym}}\rangle \otimes |g\rangle, |g\rangle^{\otimes N} \otimes |e\rangle, |g\rangle^{\otimes N} \otimes |g\rangle\Big\}. \tag{4.9}$$

Within this subspace the nonzero matrix elements of the Hamiltonian are given by

$$\langle\phi_1|H|\phi_1\rangle = \Omega_{\mathrm{sym}}, \tag{4.10a}$$

$$\langle\phi_1|H|\phi_2\rangle = \sqrt{N}\Omega_{\mathrm{p}}. \tag{4.10b}$$

In turn, this allows us to rewrite the Hamiltonian in this basis as

$$H_{\mathrm{sym}} = \Omega_{\mathrm{sym}}\sigma^{+}_{\mathrm{sym}}\sigma^{-}_{\mathrm{sym}} + \sqrt{N}\Omega_{\mathrm{p}}\left(\sigma^{+}_{\mathrm{sym}}\sigma^{ge}_{\mathrm{p}} + \mathrm{H.c.}\right), \tag{4.11}$$

where the subspace lowering operator is given by

$$\sigma^{-}_{\mathrm{sym}} = |g\rangle^{\otimes N} \langle\psi_{\mathrm{sym}}| \otimes 1_p. \tag{4.12}$$

If there is only a single excitation present in the system the Lindblad operator accounting for the collective spontaneous emission can be rewritten as

$$\mathcal{L}_\Gamma[\rho] = \sum_{i,j} \frac{\Gamma_{ij}}{2} \left[\sigma_i^{eg}\sigma_j^{ge}, \rho\right], \tag{4.13}$$

where the atomic density matrix in the steady state will live in the symmetric subspace, such that

$$\rho \propto \sum_{i,j}^{2} |\phi_i\rangle \langle\phi_j| . \tag{4.14}$$

Applying the Lindblad superoperator will yield the decay rates Γ_{p}, Γ_{sym} and Γ_0 for $i \neq j$, $i,j = 1$ and $i,j = 2$, respectively. The collective decay Γ_{p} between the central atom and the ring atoms will be approximately zero for the distances where $g^{(2)}(0) = 1$ and can be neglected as is discussed in the main text. The ring features the collective decay $\Gamma_{\mathrm{sym}} = \langle\psi_{\mathrm{sym}}|\mathcal{L}_\Gamma[\rho]|\psi_{\mathrm{sym}}\rangle$ and the central atom independent spontaneous emission Γ_0 with the decay operators $\sigma^{-}_{\mathrm{sym}}$ and σ^{-}_{p} respectively. Therefore the Lindblad term can be split into

$$\mathcal{L}_\Gamma[\rho] = \mathcal{L}_{\Gamma_{\mathrm{sym}}}[\rho] + \mathcal{L}_{\Gamma_0}[\rho]. \tag{4.15}$$

This leads to a form of the Hamiltonian and Master equation which resembles the Jaynes-Cummings model, where the good cavity is given by the subradiant symmetric state of the ring atoms.

The definition of the cooperativity parameter can be understood as follows. As can be seen in H_{sym}, the coupling coefficient between the central atom and one of the ring atoms is given by $\sqrt{N}\Omega_{\mathrm{p}}$, whereas the spontaneous decay into the vaccum modes for the center atom is simply Γ_0. As analyzed in the main text, the ring atoms are predominately in the symmetric state with a collective decay rate Γ_{sym} for the parameters where the symmetric state is maximally subradiant. Interpreting the ring in the symmetric state as a cavity and the center atom as the gain medium leads to the definition of the cooperativity parameter C.

4.7.2 Truncating the Hilbert Space at Low Excitation

Concerning the scaling behaviour of the system a mean field treatment even with the inclusion of correlations to second order is not sufficient since the properties of the steady state strongly depend on correlations of higher orders in particular $g^{(2)}(0)$

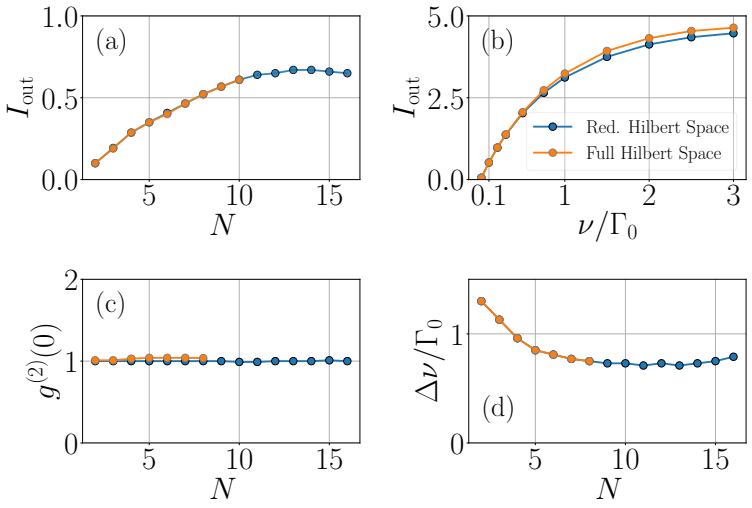

Figure 4.7: (a) Scaling behaviour of I_{out} in the steady state as a function of the atom number in the ring, where the interatomic distance for each N is chosen along the white circles in fig. 3 of the main text and the incoherent pumping rate $\nu = 10^{-1}\Gamma_0$. (b) Comparison of the Master equation with the cut-off at the second excitation manifold as a function of the incoherent pumping rate ν for $N = 8$ atoms in the ring. (c,d) The intensity correlation function $g^{(2)}(0)$ and the linewidth $\Delta\nu$ as a function of N for a pumping rate $\nu = 10^{-1}\Gamma_0$ and an interatomic distance $\lambda_0/2$ between neighbouring atoms.

involves products of four operators. In order to analyze the scaling behaviour for a larger number of emitters in the ring we restrict the system to two excitations. This cut-off can only be a good approximation to the full model for small enough incoherent pumping rates ν. In fig. 4.7b the output intensity I_{out} in the steady state of the reduced Hilbert space is compared to the full model for eight atoms in the ring and a good agreement can be found for $\nu \leq \Gamma_0$. For I_{out}, the intensity correlation function $g^{(2)}(0)$ and the linewidth $\Delta\nu$ in fig. 4.7acd the pumping rate is $10^{-1}\Gamma_0$ and the interatomic distances are chosen along the white circles in fig. 3. The linewidth $\Delta\nu$ is well below Γ_0 with $N \geq 4$ emitters in the ring and for distances d where $g^{(2)}(0) \approx 1$ but reaches a minimum which is above $\Gamma_0/2$.

4.7.3 Computing the Spectrum

The spectrum we use in order to compute the linewidth via its FWHM is given by the Fourier Transform of the first-order correlation function. Similarly to the second-order correlation function, in the far-field this expression becomes independent

of the geometry and is given by

$$g^{(1)}(\tau) = \sum_{i,j} \langle \sigma_i^+ \sigma_j^- \rangle. \tag{4.16}$$

The spectrum can then be computed via [95] as

$$S(\omega) = 2\Re\left\{ \int_0^\infty d\tau e^{-i\omega\tau} \sum_{i,j} \langle \sigma_i^+(\tau) \sigma_j^- \rangle \right\}. \tag{4.17}$$

5 Publication

Applied Physics Letters **119**(024002), (2021)

Nanoscale continuous quantum light sources based on driven dipole emitter arrays

R. Holzinger[1], M. Moreno-Cardoner[1] and H. Ritsch[1]

[1]*Institut für Theoretische Physik, Universität Innsbruck, Technikerstrasse 21, A-6020 Innsbruck, Austria*

Regular arrays of two-level emitters at distances smaller than that of the transition wavelength collectively scatter, absorb, and emit photons. The strong inter-particle dipole coupling creates large energy shifts of the collective delocalized excitations, which generates a highly nonlinear response at the single and few photon level. This should allow us to implement nanoscale non-classical light sources via weak coherent illumination. At the generic tailored examples of regular chains or polygons, we show that the fields emitted perpendicular to the illumination direction exhibit a strong directional confinement with genuine quantum properties as antibunching. For short interparticle distances, superradiant directional emission can enhance the radiated intensity by an order of magnitude compared to a single atom focused to a strongly confined solid angle but still keeping the anti-bunching parameter at the level of $g^{(2)}(0) \approx 10^{-2}$.

DOI: 10.1063/5.0049270

5.1 Introduction

A coherently driven single two-level quantum emitter is well known to radiate nonclassical light, which shows perfect anti-bunching [99–101] as well as squeezing [102,103]. It is, however, very difficult to efficiently harness these properties directly. Usually it requires complex optical elements such as high-Q cavities, high aperture lenses [104,105] or tailored optical structures [106]. Using larger ensembles of identical emitters increases the radiative output power but the nonclassical properties typically average out to create narrow band radiation but with close to thermal statistics [107, 108]. For small interparticle dipole interactions in a dilute gas, the dynamics of the whole

ensemble in the low excitation regime then can be mapped to an effective harmonic oscillator using the Holstein Primakoff transformation [109, 110].

However, recent experimental advances allow implementing and controlling precise arrays of individual quantum emitters at very close distances on the wavelength scale [111–114]. Here, collective radiation effects as sub- and super-radiance play a central role and exhibit a wealth of new physical phenomena [1, 2, 5, 115]. These unusual radiative properties of sub-wavelength structures of dipole coupled quantum emitters have recently been studied theoretically in great detail in various contexts [9, 50, 57, 58, 61, 116–137]. This leads to several suggestions for novel platforms for light matter coupling surpassing current limitations of quantum information protocols [58, 87, 138], precision spectroscopy [67, 139] or opto-mechanics [140, 141]. Some first experimental confirmations of such collective effects were also experimentally observed, where superradiance proved more accessible [3, 59] than subradiance [5, 142].

Recently we have predicted that a ringlike sub-wavelength structure with a single atom pumped at its center providing for gain can be tuned to emit spatially and temporarily coherent light [143]. Using other operating parameters the system is also predicted to generate non-classical light with strong photon anti-bunching. In closely related foundational work it was pointed out that scattering a simple plane wave off a regular dipole array with strong dipole-dipole interaction is already sufficient to tailor the quantum statistical properties of the scattered photons [144, 145]. The emerging non-clasical radiative properties here can strongly vary depending on whether the excitation frequency is tuned to superradiant or subradiant collective excitations. Here we extend such studies to explore the potential of ordered structures of dipolar quantum emitters as the basis to implement minimal non-classical light sources. In particular we study how size, geometric shape of the structure and the orientation and polarization of the individual dipoles can be used to tailor the spatial and temporal distribution of the scattered radiation as well as its genuine quantum properties. As has been seen even for a single atom [108,146,147], quantum properties of the scattered radiation depend on the emission direction. In larger ensembles this can be tailored to direct a large fraction of the emission towards a small angle, still keeping its special quantum statistical properties. This could e.g. point towards a high flux directional single photon source of subwavelength dimensions. Note that the commonly used classical coupled dipole model [148] is not sufficient to account for and describe these special radiation properties, as the origin is tied to the restriction of excitations to low energy manifolds due to the strongly varying collective exciton shifts. This suppression of multiple excitations could also be at the heart of recent observations of antibunching in biological light harvesting structures [149]. For the sake of simplicity we will mainly focus on the two cases of an ordered linear string or a regular polygon of dipoles. This work is organized as follows. After an introduction and short review of our quantum coupled dipole model we study the spatial distribution of the emitted radiation as a function of size of the linear chain of emitters and relate it to the directional $g^{(2)}(0)$-function. In the final part we then concentrate on the non-classical aspects of the photon statistics which is closely tied to the strong nonlinear suppression of the

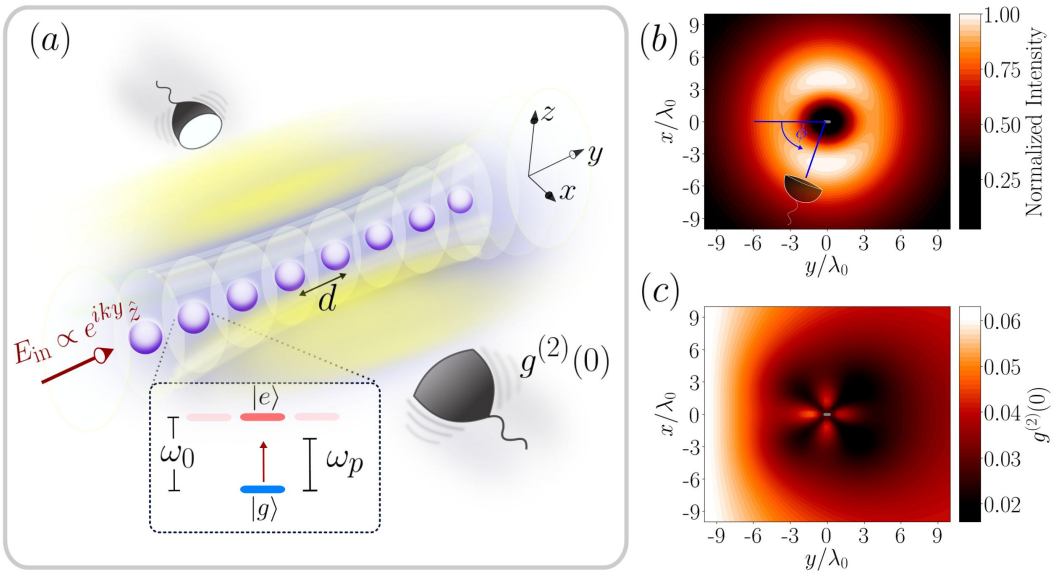

Figure 5.1: (a) Schematics of the system: An ordered chain of quantum emitters with transition frequency ω_0 and spontaneous emission rate Γ_0 is trapped along the y-axis with lattice constant d and transition dipole moment pointing in the z-direction. A coherent drive of frequency ω_p with polarization parallel to the atomic one propagates along the y-axis with Rabi frequency Ω_p. In this configuration the emitters can be treated as being two-level. The scattered light by the array is detected in the far field at a plane of constant z. (b) The normalized electric field intensity distribution of the steady state for a chain of $N = 22$ quantum emitters with $d = \lambda_0/60$, where λ_0 is the emitter transition wavelength. The laser is tuned to the most superradiant single excitation state with a driving rate $\Omega_p = \Gamma_0$. The detector position is given by $(r \sin\phi, -r\cos\phi, z = 5\lambda_0)$, with the azimuthal angle ϕ indicated in the figure. The preferred angle is in the direction of maximal scattering which simultaneously does not coincide with the laser beam direction. (c) The bunching parameter $g^{(2)}(0)$ for the same parameters as in (b) evaluated in the plane with constant $z = 5\lambda_0$.

ensemble excitations to the second and third excitation manifolds. In the supplement we discuss 2D geometries, which can confine the emission in two dimensions towards implementing higher collection efficiencies.

5.2 Model

We consider N identical two-level atoms with excited state $|e\rangle$ and ground state $|g\rangle$ each, separated in frequency by ω_0 with an inter-atomic distance $d\lambda_0 = 2\pi c/\omega_0$. The

emitters are coherently pumped by a laser at rate Ω_p, polarization $\boldsymbol{\epsilon}_p$ and detuning Δ_p with respect to ω_0. The corresponding raising (lowering) operators of the ith atom are $\sigma_i^{+(-)}$ for $i \in \{1, 2, \ldots, N\}$, its dipole moment is denoted by $\boldsymbol{\mu}_i$, with corresponding dipole moment orientation $\hat{\boldsymbol{\mu}}_i = \boldsymbol{\mu}_i/\mu$ and strength μ identical for all the emitters, and the positions are fixed at $\boldsymbol{r}_i$. The excited state is subject to spontaneous emission with rate $\Gamma_0 = \mu^2\omega_0^3/3\pi\hbar\epsilon_0 c^3$. At the considered distances, the fields emitted by each of the atoms interfere resulting in effective dipole-dipole interactions [43]. Using standard quantum optical techniques [62] we obtain a master equation for the internal dynamics of the emitters, $\dot{\rho} = -\frac{i}{\hbar}[\mathcal{H}, \rho] + \mathcal{L}_\Gamma[\rho]$, where the photonic part has been traced out in the Born-Markov approximation. The corresponding Hamiltonian in a frame rotating at the atomic transition frequency ω_0 is $\mathrm{H} = \sum_j \Delta_p \sigma_j^+\sigma_j^- + \sum_{i,j:i\neq j} \Omega_{ij}\sigma_i^+\sigma_j^- + +\Omega_p\boldsymbol{\epsilon}_p \cdot \sum_j \hat{\boldsymbol{\mu}}_j \left(e^{-i\boldsymbol{k}\cdot\boldsymbol{r}_j}\sigma_j^+ + e^{i\boldsymbol{k}\cdot\boldsymbol{r}_j}\sigma_j^-\right)$, where we have assumed that the incident field is a plane wave with wave-vector $\boldsymbol{k}$ ($|\boldsymbol{k}| \approx 2\pi/\lambda_0$), while the Lindblad operator accounting for collective spontaneous emission reads

$$\mathcal{L}_\Gamma[\rho] = \sum_{i,j} \frac{\Gamma_{ij}}{2}\left(2\sigma_i^-\rho\sigma_j^+ - \sigma_i^+\sigma_j^-\rho - \rho\sigma_i^+\sigma_j^-\right). \tag{5.1}$$

The collective coupling rates Ω_{ij} and Γ_{ij} are given respectively by the real and imaginary parts of the overlap between the transition dipole moment of the ith atom and the electromagnetic field created by the jth atom, i.e. $\Omega_{ij} = -(3\pi\Gamma_0/k_0)\mathrm{Re}[G_{ij}]$ and $\Gamma_{ij} = (6\pi\Gamma_0/k_0)\mathrm{Im}[G_{ij}]$, with $G_{ij} = \hat{\boldsymbol{\mu}}_j \cdot \boldsymbol{G}(\boldsymbol{r}_{ij}, \omega_0) \cdot \hat{\boldsymbol{\mu}}_i$, and $\boldsymbol{G}$ is the Green's tensor in free space. When acting on an oscillating unit dipole at the origin, this is given by

$$\boldsymbol{G}(\boldsymbol{r}, \omega_0) \cdot \hat{\boldsymbol{\mu}} = \frac{e^{ik_0 r}}{4\pi r}\Big[(\hat{\boldsymbol{r}} \times \hat{\boldsymbol{\mu}}) \times \hat{\boldsymbol{r}} + \Big(\frac{1}{k_0^2 r^2} - \frac{i}{k_0 r}\Big)(3\hat{\boldsymbol{r}}(\hat{\boldsymbol{r}} \cdot \hat{\boldsymbol{\mu}}) - \hat{\boldsymbol{\mu}})\Big]. \tag{5.2}$$

Here, $\hat{\boldsymbol{r}} = \boldsymbol{r}/|\boldsymbol{r}|$ is the unit vector in the direction where the Green's tensor is evaluated and $k_0 = \omega_0/c$ is the wave-number of the emitted light by the dipole. After solving for the atomic density matrix the electric field generated at position $\boldsymbol{r}$ can be found from a generalized input-output relation which in the absence of external fields is given by [58, 127]

$$\hat{\boldsymbol{E}}^+(\boldsymbol{r}) = \mu_0\omega_0^2 \sum_{j=1}^{N} \boldsymbol{G}(\boldsymbol{r} - \boldsymbol{r}_j, \omega_0) \cdot \boldsymbol{\mu}_j \sigma_j^-. \tag{5.3}$$

The field intensity can then be evaluated from the emitted electric field operator $\boldsymbol{E}^+(\boldsymbol{r})$ at position $\boldsymbol{r}$:

$$\mathcal{J}(\phi) = \left\langle \hat{\boldsymbol{E}}^+(\boldsymbol{r}(\phi))\hat{\boldsymbol{E}}^-(\boldsymbol{r}(\phi)) \right\rangle. \tag{5.4}$$

We will consider a one-dimensional chain of atoms coherently driven by a plane wave propagating along the chain axis, defined as the y-axis. The atomic and field polarizations are parallel along the z-axis. To separate the scattered quantum light

from the driving laser light, the detector is placed along the $x-$direction as seen in Figs. 5.1(a) and (b). The external field will be on resonance with the most superradiant collective mode in order to maximize the photon emission rate. For typical operating conditions, we show in Fig. 5.1(b) the emitted steady state light intensity pattern of an atomic chain with 22 emitters. In order to evaluate the directional intensity, and similar to [150–153], we will consider the total light intensity covered by a detector of angular width $\Delta\phi = 0.01\pi$ in the far field, and calculate the average value of $\mathcal{J}(\phi)$ over the emission angle $\Delta\phi$.

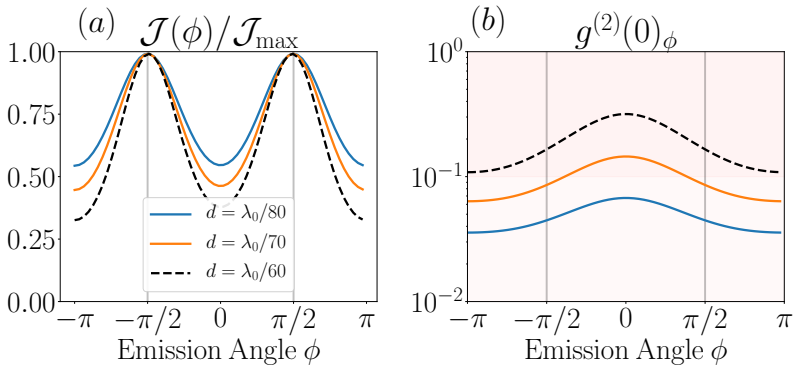

Figure 5.2: *Steady State Emission.* (a) Far field intensity distribution versus azimuthal angle ϕ (normalized with respect to its maximum value over ϕ) and (b) bunching parameter $g^{(2)}(0)|_\phi$, for a linear chain of $N = 30$ emitters linearly polarized in z direction with different values of the lattice constant d. The geometry is the same as in Fig. 5.1, but with the detector placed at $(r\sin\phi, -r\cos\phi, 0)$ and $r = 100\lambda_0$. (a) Shows that maximal emission occurs perpendicular to the chain for all lattice constants. This enables separation of the incoming and scattered fields in real space and minimizes its interference. In (b) a photon bunching parameter of $g^{(2)}(0)|_\phi \leq 0.1$ is achieved for a small enough lattice spacing in the direction perpendicular to the chain. The vertical lines at $\pm\pi/2$ indicate the angles of maximal scattering.

In addition, one can also obtain from Eq. (5.9), normalized (zero-time delay) second-order correlation functions, defined as

$$g^{(2)}(0)\Big|_\phi = \frac{\langle \hat{\boldsymbol{E}}^+(\boldsymbol{r})\hat{\boldsymbol{E}}^+(\boldsymbol{r})\hat{\boldsymbol{E}}^-(\boldsymbol{r})\hat{\boldsymbol{E}}^-(\boldsymbol{r})\rangle}{|\langle \hat{\boldsymbol{E}}^+(\boldsymbol{r})\hat{\boldsymbol{E}}^-(\boldsymbol{r})\rangle|^2}, \tag{5.5}$$

and which is shown in Fig. 5.1(c) in the xy-plane for a constant z. For the same geometry as in Fig. 5.1, we evaluate in Fig. 5.2 the emitted light intensity and the correlation function $g^{(2)}(0)|_\phi$ in the far field ($|\boldsymbol{r}| = r \gg \lambda_0$), as a function of the azimuthal angle ϕ which is defined in the plane containing the array (see Fig. 5.1). We choose a coherent external field with pumping rate $\Omega_p = \Gamma_0$ and again tuned

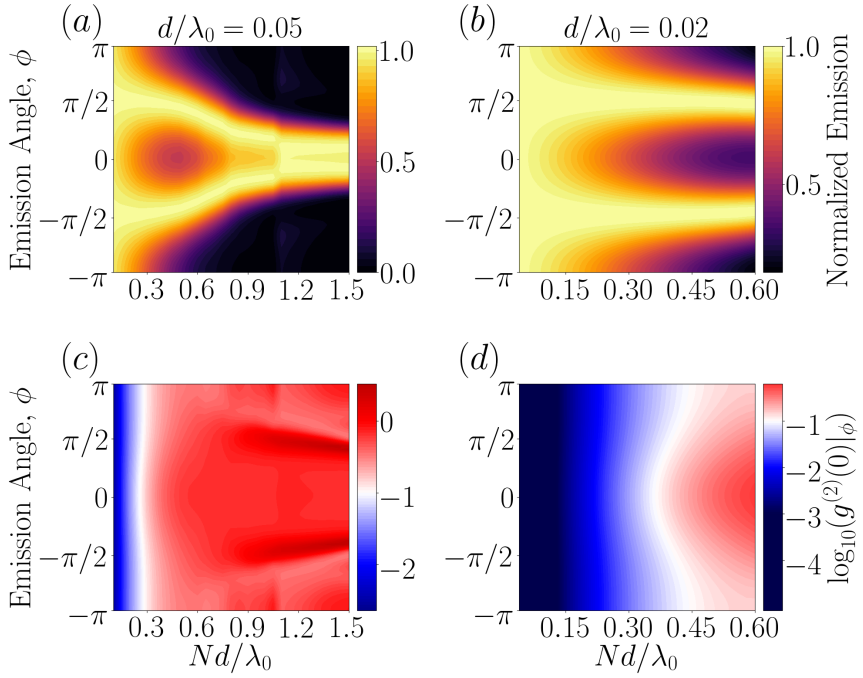

Figure 5.3: Normalized scattered field intensity distribution (with respect to its maximum value over ϕ for each value of the chain length) and photon bunching parameter $g^{(2)}(0)|_\phi$ calculated for the steady state and in the far field ($r = 100\lambda_0$), as a function of the emission angle ϕ and total chain length Nd/λ_0. The two panels are for $d/\lambda_0 = 0.05$ and $d/\lambda_0 = 0.02$, as indicated. The laser and detector position parameters are identical to Fig. 5.2. For long enough chains $Nd\lambda_0$ the scattered field concentrates around the perpendicular direction to the chain ($\phi = \pm\pi/2$). Taken together, (b) and (d) show that it is possible to achieve directional emission perpendicular to the laser beam direction with a photon bunching of $g^{(2)}(0)|_\phi \leq 0.1$ for a lattice spacing $d = 0.02\lambda_0$.

to the most superradiant single excitation eigenmode of the chain. In Fig. 5.2(a) the directional emission is normalized by the maximal emission $\mathcal{J}_{\max}$ over the angle ϕ. The different lines correspond to various lattice constants d. In Fig. 5.2(b) the $g^{(2)}(0)|_\phi$ function has values ≤ 0.1 in the direction of maximal emission for $d \leq \lambda_0/70$ with the emission exhibiting two emission maxima perpendicular to the laser beam direction ($\phi = 0$).

In order to analyze the dependence of the directional emission on the total chain length, we have evaluated in Figs. 5.3(a) and (b) the directional emission $\mathcal{J}(\phi)$ (normalized by its maximum value) and in Figs. 5.3(c) and (d) the two-photon

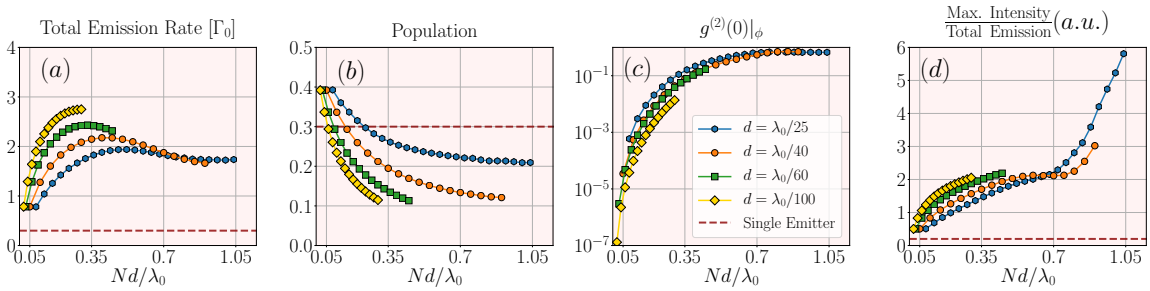

Figure 5.4: The steady state of a coherently driven linear chain of emitters with different lattice constants d for the same geometry and parameters as in Fig 1. In (a) and (b) the total photon emission rates and the emitter populations are shown respectively and show an increasing superradiant emission rate for decreasing d. (c) Photon correlations $g^{(2)}(0)|_\phi$ are measured in the direction of maximal emission in the far field ($r = 100\lambda_0$) and which is as seen in Figs. 1-3 perpendicular to the chain and laser beam in x direction for a total chain length of $Nd0.35\lambda_0$. A bunching parameter of $g^{(2)}(0)|_\phi \leq 0.1$ in combination with directional perpendicular emission with respect to the lasing direction is reached for sufficiently small lattice constants d. (d) The maximal intensity in the xy plane as can be seen in Figs. 1-3 divided by the total emission rate. The sudden increase of the peak intensity for a total chain length $0.7\lambda_0$ originates from the merger of the two emission peaks as seen in Fig. 5.3 (a) which turns the perpendicular emission into a reflection in the laser beam direction. In comparison the dashed line shows the steady state values for a single emitter coherently driven with a rate $\Omega_p = \Gamma_0$ with the emission being uniform in the xy-plane without directionality. Note that in the case of maximal emission in two directions (see Fig. 1 (a) and (b)) the maximal intensity is calculated for one of the maxima.

correlation function $g^{(2)}(0)$ characterizing bunching in the system, for fixed lattice constant d and an increasing number of emitters. As it has been previously shown, the emission becomes highly directional for increasing chain lengths, both when targeting superradiant [144, 145, 154–157] and subradiant [58] eigenmodes. Instead, the anti-bunching is reduced as the length chain increases, but at constant length chain it is always enhanced by reducing d. Directional photon statistics of this kind have been recently observed for two emitters by varying the detector position [108]. Therefore, these results suggest that it is possible to obtain highly directional anti-bunched light by decreasing the lattice constant d, and keeping the total length chain large enough compared to λ ($Nd\lambda/3$). To see how general these results are, we have also analyzed other geometries in the supplemental material. In particular, we have considered a scheme consisting of two coupled rings of linearly polarized emitters, for

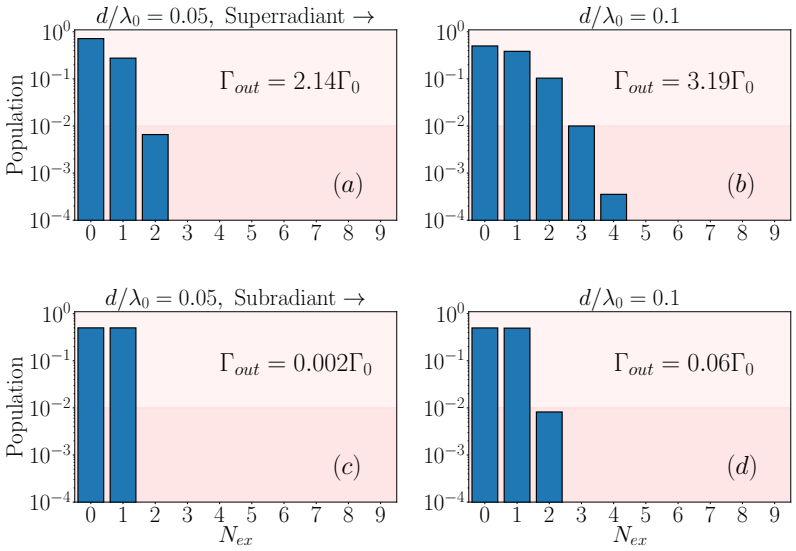

Figure 5.5: Excitation energy distribution in steady state for a coherently driven linear chain of 9 emitters along the y direction each linear polarized in z direction with the linear polarized drive along the chain direction and pump amplitude $\Omega_p = \Gamma_0$. The x axis denotes the excitation manifolds which are proportional to the output electric field (see Eq. 5.9). For (a) and (b) in the first row the laser is tuned to resonance with the maximally superradiant single excitation eigenstate while for (c) and (d) in the second row we target the most subradiant single excitation state in a steady state operation with their respective photon emission rates $\Gamma_{\rm out}$ shown in each figure. Note very strong (nonlinear) suppression of higher excitation numbers for short inter-particle distances. The red horizontal shades are guides for the eyes only.

which it is also possible to obtain strongly directional anti-bunched scattered light. We now evaluate in Fig. 5.4(a) and (b) the total photon emission rate and excited state population respectively, for the above system geometry, as a function of the length chain Nd and for different lattice spacings. The total excited level population of the steady state is given by $\langle \hat{n}_{\rm ex} \rangle = \sum_{j=1}^{N} \langle \sigma_j^+ \sigma_j^- \rangle$ whereas the photon emission rate is $\Gamma_{\rm out} = \sum_{ij}^{N} \Gamma_{ij} \langle \sigma_i^+ \sigma_j^- \rangle$, which reduces to $N\Gamma_0$ for N identical initially fully inverted two-level emitters. For a steady state which consists only of a superposition of the ground state and a single excitation in the mode m, the total emission rate is given by $\Gamma_m \langle n_{\rm ex} \rangle$, where Γ_m is the collective decay rate of the mode m. On the other hand, a single dipole in free space coherently driven by a laser at rate Ω_p and detuning Δ_p (with respect to the atomic transition frequency) has an effective decay rate of $\Gamma_0 \Omega_p^2 / (4\Delta_p^2 + \Gamma_0^2 + 2\Omega_p^2)$, which can be derived by solving the atomic master

equation in the steady state. The effective rate saturates at $\Gamma_0/2$ for $\Omega_p \gg \Gamma_0$, which constitutes the maximum steady state emission rate of a single coherently driven two level emitter. The total photon emission rate of closely spaced quantum emitters as e.g. in Fig. 5.1(a) can be many times that value, as shown in Fig. 5.4(a). In the same figure, we show in panel (c) the two-photon correlation evaluated in the direction of maximal emission. Finally, in panel (d) we have plotted the maximal intensity in the $xy-$plane normalized by the total emission, which is a figure of merit for the directionality of the emitted light. To increase the total photon emission rate it is reasonable to increase the number of emitters, but as already previously discussed this leads to a higher $g^{(2)}(0)$ in the direction of maximal emission. However, as it can be clearly seen in 5.4(c), by decreasing the lattice spacing for a given chain length, the $g^{(2)}(0)$ in the direction of maximal emission is decreasing as well. The smallest lattice separation of $d = \lambda/100$ shows the highest total emission rate and maximum renormalized intensity, indicating that a larger amount of the totally emitted light is concentrated in the emission peak(s). The sudden increase in the ratio in (d) for a chain length of $0.7\lambda_0$ originates from the merger of two emission peaks into one, which is reflected back into the laser beam direction as seen in Fig. 5.3(a). The decrease of the emitter population plotted in Fig. 5.4(b) with increasing emission rate shows the increasing superradiance of the targeted eigenmode of the chain which possesses a decay rate of $\approx N\Gamma_0\langle n_{\mathrm{ex}}\rangle$ for $d \leq \lambda_0/100$. On the other hand the decrease of the total emission rate for increasing chain length is due to less emitter population in the superradiant mode. Fig. 5.4 shows that both a directional emission and a bunching parameter $g^{(2)}(0) \leq 0.1$ in the direction of maximal emission can be achieved for lattice spacings of $d \approx \lambda_0/100$ as the chain length exceeds $\lambda_0/3$. The dashed lines in Fig. 5.4 show the case of a single emitter coherently driven with a rate $\Omega_p = \Gamma_0$. The $g^{(2)}(0)$ function is zero in this case but the small emission rate and absence of emission peaks in the xy-plane renders the efficient collection of the scattered light less favorable. Although the distances between the emitter are out of reach for optical tweezers and lattices at present, recently [158] superradiant and subradiant states in single nanocuboids at room temperature have been observed. Here the lattice constants of the nanocube can be adjusted and the spacing between the interacting dipoles can be below $\lambda_0/100$.

5.3 Photon statistics

In the following, we will discuss photon statistics in terms of the occupations in the various excitation manifolds since we have eliminated the photonic modes during the derivation of the atomic master equation, however, the output intensity is proportional to the atomic raising/lowering operators weighted by the Green's tensor. In Fig. 5.5 it can be seen that single photon states of high quality can be obtained at $d \leq \lambda_0/10$ for a laser tuned both to the superradiant (in Fig. 5.5(a,b)) and subradiant (in Fig. 5.5(c,d)) eigenmode of the chain. The geometry is identical to the previous examples with the

laser driving the chain from the y direction at a rate $\Omega_p = \Gamma_0$. For the subradiant case in Fig. 5.5 (c) the total emission rate for a linear chain of 9 emitters at a spacing of $0.05\lambda_0$ shows that a steady state occupation of 50% in the single excitation manifold is reached. The total emission rate indicates a lifetime 500 times longer than that of a single excited emitter. The statistics in Fig. 5.5 are obtained by continuous laser driving in the steady state and if the laser is tuned to the most subradiant eigenmode of the chain the emitter population levels out at 50% as for a chain emission rate of $\ll \Gamma_0$ a pumping rate of $\Omega_p = \Gamma_0$ resembles the case of a single strongly driven emitter. In this regime the chain prepared in the subradiant collective mode behaves like a single strongly driven emitter which reaches a excited state occupation of 0.5 in the steady state. In the supplement we demonstrate an efficient way to prepare a subradiant eigenmode via a laser pulse. Pulsed on-demand production of photon number states is proposed in [159] with a single multi-level atom in a cavity.

5.4 Conclusions

We have shown that the collective excitations in regular sub-wavelength structures of dipolar quantum emitters can behave like a designer two-state atom [160] with a strongly enhanced effective dipole moment and a tailorable spatial radiation pattern. When illuminated with weak coherent light their strong nonlinear response at the single or few photon level leads to directional emission of strongly anti-bunched light without the help of any additional optical elements. While we restricted ourselves here to the most simple generic cases of regular chains, more general structures can be envisaged for specific applications and in particular as the basis of minimalist nanoscale single photon sources. We highlight these surprising features for the generic examples of a regular polygon with titled polarization and interacting regular polygons which are partially pumped in the supplement. Even at fairly high excitation powers, in strongly interacting configurations the second excitation manifold is only very weakly excited, which might be a hint on the origin of anti-bunching found in bio-molecular dipole configurations [149]. Interestingly, as shown in the supplement for a ring with slightly tilted dipoles, besides the spatial dipole arrangement, polarization can be an efficient tool to separate excitation light and emitted photons in addition to directional spatial filtering. Note that while atoms in tweezers might be the most straightforward test bed for these ideas, alternatives used synthetic molecules [160], nanocuboids [158] at room temperatures or quantum dot nano-structures [161] and should largely exhibit similar physics as long as the couplings are comparable with environmental decoherence effects.

Acknowledgements

We thank David Plankensteiner for helpful discussions and acknowledge funding from the Austrian Science Fund (FWF) doctoral college DK-ALM W1259-N27 (R. H.), and the European Unions Horizon 2020 research and innovation program under the Marie Sklodowska-Curie grant agreement No. 801110 and the Austrian Federal Ministry of Education, Science and Research (BMBWF) (M.M.-C.). It reflects only the authors view and the Agency is not responsible for any use that may be made of the information it contains. Numerical simulations were performed with the Julia programming language including the QoJulia.org quantum optics package [13].

5.5 Supplementary Material

5.5.1 Green's Tensor and effective Model

The electric field generated by an ensemble of atoms is mediated by the electromagnetic Green's tensor, moreover in the weak excitation limit the Hamiltonian can be rewritten in a form which allows for analytic solutions of its eigenvalue equation. These steps are described below for the special case of an infinite chain. For a finite chain the procedure is only valid approximately because of its open boundaries at the ends of the chain but for an infinite chain it becomes accurate and as investigated previously [58, 162] 1D atomic arrays behave like a quantum waveguide and support guided modes that do not decay into free space. The Green's tensor in free space acting on an oscillating unite dipole is given by

$$\boldsymbol{G}(\boldsymbol{r},\omega_0)\cdot\hat{\boldsymbol{\mu}} = \frac{e^{ik_0 r}}{4\pi r}\Big[(\hat{\boldsymbol{r}}\times\hat{\boldsymbol{\mu}})\times\hat{\boldsymbol{r}} + \Big(\frac{1}{k_0^2 r^2} - \frac{i}{k_0 r}\Big)(3\hat{\boldsymbol{r}}(\hat{\boldsymbol{r}}\cdot\hat{\boldsymbol{\mu}}) - \hat{\boldsymbol{\mu}})\Big]. \tag{5.6}$$

Here, $\hat{\boldsymbol{r}} = \boldsymbol{r}/|\boldsymbol{r}|$ is the unit vector in the direction where the Green's tensor is evaluated, $k_0 = \omega_0/c$ is the wavenumber of the emitted light by the dipole and $\hat{\boldsymbol{\mu}} = \boldsymbol{\mu}/|\boldsymbol{\mu}|$ is the unit dipole orientation. The coherent and dissipative interaction rates between emitter i and j read

$$\Omega_{ij} = -\frac{3\pi\Gamma_0}{k_0}\mathrm{Re}\{\hat{\boldsymbol{\mu}}_i^*\cdot\boldsymbol{G}(\boldsymbol{r}_i-\boldsymbol{r}_j,\omega_0)\cdot\hat{\boldsymbol{\mu}}_j\}, \tag{5.7}$$

$$\Gamma_{ij} = -\frac{3\pi\Gamma_0}{k_0}\mathrm{Im}\{\hat{\boldsymbol{\mu}}_i^*\cdot\boldsymbol{G}(\boldsymbol{r}_i-\boldsymbol{r}_j,\omega_0)\cdot\hat{\boldsymbol{\mu}}_j\} \tag{5.8}$$

where $\hat{\boldsymbol{\mu}}_i$ is the unit dipole moment associated with the transition of atom i. The single atom spontaneous emission rate is given by $\Gamma_0 = \omega_0^3|\boldsymbol{\mu}|^2/3\pi\epsilon_0\hbar c^3$. As described in the main text after solving for the atomic density matrix the electric field generated at position $\boldsymbol{r}$ can be obtained from a generalized input-output relation [58], which in the absence of external fields is given by

$$\hat{\boldsymbol{E}}^+ = \mu_0\omega_0^2\sum_{j=1}^{N}\boldsymbol{G}(\boldsymbol{r}-\boldsymbol{r}_j,\omega_0)\cdot\hat{\boldsymbol{\mu}}_j\sigma_j^-. \tag{5.9}$$

To obtain this equation the Markovian approximation has been made, therefore retardation effects arising from the physical sepration between the quantum emitters can be ignored. As long as the ensemble stays within the length scales of ≈ 1 meter this assumption is well founded. [36,163,164] We will consider the weak excitation limit in which only the single-excitation manifold is significantly occupied and neglecting external driving fields for the moment. In this case the recycling term which is the first term in the Lindblad expression can be neglected. This term accounts for the change in the ground state population. Then, the system can be fully understood from the properties of the eigenstates of an non-Hermitian Hamiltonian that reads (setting $\hbar = 1$) $\mathcal{H} = \omega_0 \sum_{i=1}^{N} \sigma_i^+ \sigma_i^- + \mathcal{H}_{\text{eff}}$ with

$$\begin{aligned} \mathcal{H}_{\text{eff}} &= -\mu_0 \omega_0^2 \sum_{i,j=1}^{N} \hat{\boldsymbol{\mu}}_i^* \cdot \boldsymbol{G}(\boldsymbol{r}_i - \boldsymbol{r}_j, \omega_0) \cdot \hat{\boldsymbol{\mu}}_j \sigma_i^+ \sigma_j^- \\ &= \sum_{i,j=1}^{N} \Big(\Omega_{ij} - i\frac{\Gamma_{ij}}{2}\Big) \sigma_i^+ \sigma_j^-, \end{aligned} \tag{5.10}$$

where $\Omega_{ii} = 0$, as it only leads to a finite global energy shift in the Hamiltonian for identical emitters. This model will now be used to to investigate the properties of a linear chain of atoms in free space without external driving.

For an infinite chain that extents along the y direction the eigenstates of $\mathcal{H}_{\text{eff}}$ are spin waves with a well defined wave vector $k_y \in [-\pi/d, \pi/d]$. The collective spin operators $\hat{S}_{k_y}^\dagger = 1/\sqrt{N} \sum_j e^{ik_y y_j} \sigma_j^+$ satisfy the eigenvalue equation $\mathcal{H}_{\text{eff}} \hat{S}_{k_y}^\dagger |g\rangle^{\otimes N} = \omega_{k_y} \hat{S}_{k_y}^\dagger |g\rangle^{\otimes N}$, where y_j is the position along the chain of emitter j and $|g\rangle^{\otimes N}$ the total ground state of the sytem. The complex eigenvalues read

$$\omega_{k_y} = \omega_0 - \frac{3\pi\Gamma_0}{k_0} \hat{\boldsymbol{\mu}}^* \cdot \tilde{\boldsymbol{G}}(k_y) \cdot \hat{\boldsymbol{\mu}}, \tag{5.11}$$

assuming all quantum emitters have the same unit dipole moment $\hat{\boldsymbol{\mu}}$. The imaginary part of ω_{k_y} corresponds to the decay rate of the spin wave, and its real part accounts for the frequency shift with respect to the bar atomic frequency ω_0. In the above equation $\tilde{\boldsymbol{G}}(k_y) = \sum_j e^{-ik_y y_j} \boldsymbol{G}(y_j, \omega_0)$ is the discrete Fourier transformation of the vacuum Green's tensor.

Fig. 1(a) shows the real and imaginary part of ω_{k_y} as well as the light line beyond which ($k_y > k_0 = \omega_0/c$) the spin wave mode becomes extremely subradiant as opposed to modes inside the light line ($k_y < k_0$) which acquire a finite life time and some even become superradiant. In fact for the special case of infinitesimal emitter distances there will be $N - 1$ subradiant states and a single superradiant state. It is the superradiant mode closest to the lower energy band of Fig. 1(a) which we address with a coherent driving laser such that the detuning Δ_l in the main text is on resonance with said mode. For guidance a chain of 50 emitters is shown vs. a chain of 5 emitters with a single

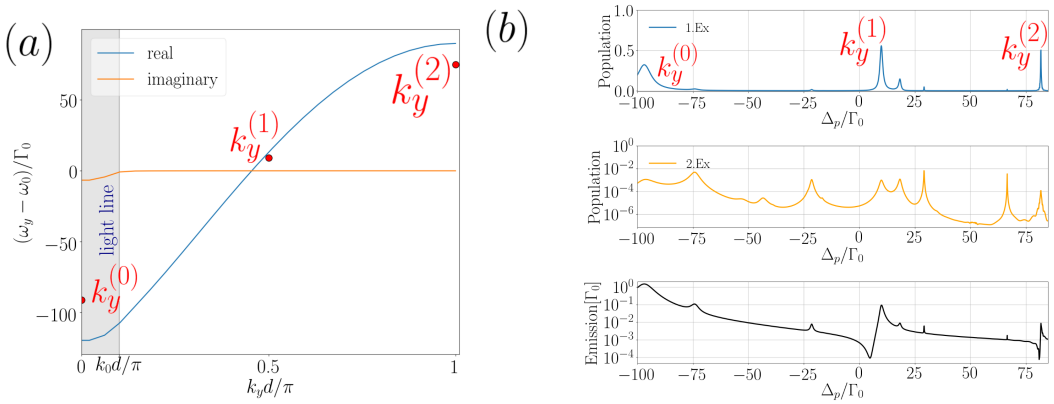

Figure 5.6: *Energy Band.* In (a) the continuous lines represent a chain of $N = 50$ emitters whereas the dots indicate the real part of $(\omega_y - \omega_0)/\Gamma_0$ of a 5 emitter chain. Since the dispersion relation is symmetric around the y-axis the first Brillouin-Zone is shown only for wavenumbers $k_y \in [0, \pi/d]$. The spacing is $d/\lambda_0 = 0.05$ and all emitters are linearly polarized along the chain. (b) shows the steady state populations and total emission rate of a 5 emitter chain driven coherently from the z-direction. The x axis shows the laser detuning with respect to the single atom transition frequency ω_0. Resonances at the single-excitation eigenenergies are clearly visible and show significant populations in the steady state and note that the linewidths of the resonances is given by the decay rates of the targeted modes.

collective mode $k_y^{(0)}$ inside the region enclosed by the light line and two subradiant modes outside of it. Due to the finiteness of the system the solution is only approximate but still a qualitative picture can be extracted as there is a clear connection between the energy band and the scattered light observed in Fig. 1(b). As the laser is tuned to the frequency corresponding to the mode $|\Psi_{k_y^{(0)}}\rangle = 1/\sqrt{N}\sum_j e^{-ik_y^{(0)} y_j}\sigma_j^+|g\rangle^{\otimes N}$ superradiant emission ($> \Gamma_0$) is observed in the steady state total emission rate with vanishing populations in the higher excitation manifolds. The same holds for the subradiant modes where the population is saturating at 1/2 excitations. Note that the emission rate for $k_y^{(2)}$ amounts to $\Gamma_0/100$ in the steady state corresponding to a 100 fold increased lifetime of the stored energy compared to independent emitters. As one increases the number of emitters in the chain these effects increase significantly with the most subradiant mode's decay rate scaling with N^{-3} for large N [58]. As discussed in the main text for the superradiant mode to show strong anti-bunching in the scattered light the chain length should not exceed the wavelength λ_0 of the emitted light of a single atom.

5.5.2 Pulsed preparation of a subradiant state

In Fig. S5.7 we show the pulsed preparation of a subradiant single excitation eigenmode of a linear chain of 12 emitters. In Fig. 5 of the main text it is shown that a steady state operation leads to a 50% occupation of the first excitation manifold but as we show in Fig. S5.7(b-d) the occupation can reach near unity if the pulse duration, amplitude and detuning are optimal. The emitters are linear polarized in z direction and the chain extents along y with lattice constant $d = \lambda_0/20$ and with a linear polarized laser pulse propagating along the chain. The Hamiltonian in Eq. 1 of the main text will now have a time dependence as follows

$$\mathcal{H}(t) = \sum_j^N \Delta_p \sigma_j^+ \sigma_j^- + \sum_{i,j:i\neq j}^N \Omega_{ij} \sigma_i^+ \sigma_j^- + \Omega_p(t) \boldsymbol{\epsilon}_p \cdot \sum_j^N \hat{\boldsymbol{\mu}}_j \left(e^{-i\boldsymbol{k}\cdot\boldsymbol{r}_j} \sigma_j^+ + e^{i\boldsymbol{k}\cdot\boldsymbol{r}_j} \sigma_j^- \right), \tag{5.12}$$

where $\Omega_p(t) = \tilde{\Omega}_p e^{-(t-t_0)^2/\tau^2}$ is a laser pulse with amplitude $\tilde{\Omega}_p$, a full width half maximum of the pulse duration of τ and peak at t_0. In Fig. S5.7(b) the case of a laser pulse with $\tau = 25\Gamma_0$, $\Omega_p = \Gamma_0$ and $t_0 = 50\Gamma_0$ is plotted. The laser is now tuned to the most subradiant single excitation eigenmode of the chain. In (a) the normalized intensity distribution is plotted at $\Gamma_0 t = 150$ and shows that the chain radiates only at the ends with a emission rate of $10^{-3}\Gamma_0$ as is shown in (c). The distribution of the emitter population in the individual excitation manifolds in (d) at $\Gamma_0 t = 150$ shows that the chain stores nearly a single excitation which decreases at a rate of $10^{-3}\Gamma_0$. Experimentally verifying the preparation of subradiant states has always been a challenge and this should only illustrate the preparation with a minimal amount of elements.

5.5.3 Nano-Rings

As another example of ordered arrays the ring provides closed boundary conditions, namely rotation symmetry thereby allowing for an explicit calculation of eigenmodes. [165] As in the case of the chain the Hamiltonian can be cast into a non Hermitian form where the complex eigenvalues read

$$\omega_m = \omega_0 - \frac{3\pi\Gamma_0}{k_0} \hat{\boldsymbol{\mu}}^* \cdot \tilde{\boldsymbol{G}}(m) \cdot \hat{\boldsymbol{\mu}}, \tag{5.13}$$

where $\tilde{\boldsymbol{G}}(m) = \sum_{jl} e^{-im(\varphi_l - \varphi_j)} \boldsymbol{G}(\boldsymbol{r}_l - \boldsymbol{r}_j, \omega_0)$ is again the discrete Fourier transformation of the Green's tensor for the ring. The angle associated with position $j \in (1, ..., N)$ is denoted by $\varphi_j = 2\pi(j-1)/N$ and $m = 0, \pm 1, \pm 2, ..., \lceil \pm (N-1)/2 \rceil$ corresponds to the angular momentum of the mode. [165, 166] The collective energy shifts and emission rates of the mode are given by the real part $\Omega_m = \mathrm{Re}\{\omega_m\}$ and

the imaginary part $\Gamma_m = \mathrm{Im}\{\omega_m\}$ of the eigenvalue ω_m. From Eq. 5.13 it is easy to see that the eigenvalue spectrum will be symmetric under the exchange $m \leftrightarrow -m$, meaning, $\omega_m = \omega_{-m}$. Relevant for the present case is the superradiant $m = 0$ mode which is non-degenerate and will be targeted by a coherent pump of rate $\Omega_p = \Gamma_0$. The corresponding eigenstate has the form

$$|\Psi_{m=0}\rangle = \frac{1}{\sqrt{N}} \sum_{j=1}^{N} \sigma_j^+ |g\rangle^{\otimes N} \tag{5.14}$$

with a superradiant emission rate $\Gamma_{\mathrm{sup}} = \sum_{j=1}^{N} \Gamma_{1j}$ and eigenenergy $\omega_0 + \sum_{j=2}^{N} \Omega_{1j}$ which has the same form as the eigenenergies of the hermitian Hamiltonian which is used for the simulations. Note that for infinitesimal emitter spacing the ensemble approaches the Dicke Limit [2] for which the superradiant mode decays with rate $N\Gamma_0$. Now we will investigate a coherently driven ring of emitters of separation $d = 0.03\lambda_0$ each having linear polarization in z direction with a linear polarized laser propagating in the y direction with a pumping rate $\Omega_p = \Gamma_0$ (see Eq. 1 in the main text). Fig. S3(a) shows the normalized intensity distribution in the steady state for $N = 4$ emitters in the ring and features a uniform ring shaped emission into the xy-plane. Now in (b) a second identical undriven ring is placed at a $\pi/4$ angle w.r.t. the first ring with a separation between the two rings centers of $0.7\lambda_0$. The resulting steady state emission shows strong directionality in the xy-plane in a direction which is not interfering with the laser's direction. The 1D plot in (c) shows the corresponding emission peaks in the far field and (d) the bunching parameter $g^{(2)}(0)$ as a function of the emission angle ϕ in the xy-plane. A bunching parameter of < 0.1 can be observed in the direction of maximal emission coinciding exactly with the global minima of the $g^{(2)}(0)$ function which would constitute a good single photon source. Finally in (e) the scaling behaviour is plotted when the emitter number in the undriven ring is varied leaving all other parameters fixed including the distance between the two ring centers. The steady state total emission rate remains roughly constant with a small variation at $N = 4$. This is expected as the driven ring's emitter number remains constant and which is the source of the emission or scattered light. The bunching parameter on the other hand shows strong variations of two orders of magnitude as the second ring's emitter number is changed. The ratio between the maximal emission in the xy-plane and the the total emission in (d) is increasing with increasing emitter, therefore more light is concentrated in the direction of maximal emission. Simultaneously a bunching parameter $g^{(2)}(0) \approx 10^{-4}$ is reached which would constitute an almost perfect source of single photons. Although driving only one of the rings might be a challenge experimentally the small bunching parameter in combination with the strong directionality as seen in Fig. S3(b,c) and a total emission rate of $> \Gamma_0$ in this system seems to be an interesting avenue for future experimental and theoretical studies.

5.5.4 Tilted Polarization

To drive only one of the rings in the previous example might prove experimentally difficult. By again considering the same geometry as in Fig. S3 but adding a small x component of $\epsilon = 0.1$ to the polarization of the left ring and the laser being circular polarized as $(\hat{x}, i\hat{y}, 0)^T/\sqrt{2}$ and propagating along the z direction. With a pumping rate of $\Omega_p = 20\Gamma_0$ the laser beam will only drive the left ring which still has a dipole-dipole interaction with the second ring. The normalized steady state emission for $N = 14$ emitters per ring is plotted in Fig. S4 (b) and shows strong directionality in the xy-plane. In (a) the steady state total emission rate as a function of the emitter number per ring is shown in a, whereas in (c) and (d) the bunching parameter $g^{(2)}(0)$ in the direction of maximal emission and the ratio between maximal emission and total emission in the xy-plane are plotted. At $N = 14$ the whole system shows a total emission rate approximately 7 times larger than that of a single emitter which is $\Gamma_0/2$, a bunching parameter $g^{(2)}(0) \approx 0.03$ and increasingly more light concentrated in the direction of maximal emission. In effect the tilted polarization of the driven ring converts the circular polarized laser light into highly antibunched linear polarized light in a continuous manner.

5.5.5 Spatial Disorder Effects

In Fig. S5.10 we plot in (a) the total emission rate and in (b) the bunching parameter $g^{(2)}(0)$ in the direction of maximal emission as a function of the emitter number in a linear chain along y for different degrees of spatial disorder. Each emitter is linear polarized in z direction and the linear polarized driving laser propagates along the chain direction with rate $\Omega_p = \Gamma_0$. The laser is tuned to the most superradiant single excitation state for each N where $\epsilon = 0$. This means that the positional disorder also induces some detuning between the laser frequency ω_p and the targeted eigenmode of the disordered chain. We consider a classical disorder, where each emitter is randomly displaced around its initial position in the xy plane by a value between $[-d\epsilon, d\epsilon]$. We plot the total emission rate and the bunching parameter after averaging over 100 disorder realizations. The chain lies along y and the disorder for each emitter is in x and y direction. Evidently in the presence of significant fluctuations of $\epsilon/d = 0.1$ the total emission rate is substantially decreased and the bunching parameter increased on the other hand moderate disorder has only small effects on both values. In the case of subradiance it was shown that moderate disorder has relatively little influence on the decay rate of the most subradiant eigenmode. [167]

5.5.6 Truncated Model

Throughout this work a truncated Hilbert space is used for most simulations by which the full quantum model is restricted only up to two excitations. In this way it is still possible to calculate second order correlations in normal order of the form

$\langle \hat{\sigma}_i^+ \hat{\sigma}_j^+ \hat{\sigma}_k^- \hat{\sigma}_l^- \rangle$ and investigate larger system sizes with finite computational resources. In order to calculate the occupation in a given excitation manifold we have diagonalized the given Hamiltonian and summed up the projections of the steady state density matrix on the respective eigenstates. For instance in the first excitation manifold are N eigenstates, so the population is given by $\sum_{j=1}^{N} \langle \psi_j | \rho_{ss} | \psi_j \rangle$, where $|\psi_j\rangle$ denote the N single excitation eigenstates and ρ_{ss} is the density matrix for the emitters in the steady state. There are $N(N-1)/2$ eigenstates carrying two excitations and so forth with all excitation manifolds adding up to 2^N states.

In Fig. S5 the full quantum model is compared to the truncated model for a linear chain of 5 emitters both for in population and total emission rate versus pumping rate Ω_p. A good approximation to the full model for small enough coherent pumping rates $\Omega_p \leq \Gamma_0$ can be found. The vanishing population in the third excitation manifold of the full model shows that the truncated model describes the system sufficiently well from a physics viewpoint.

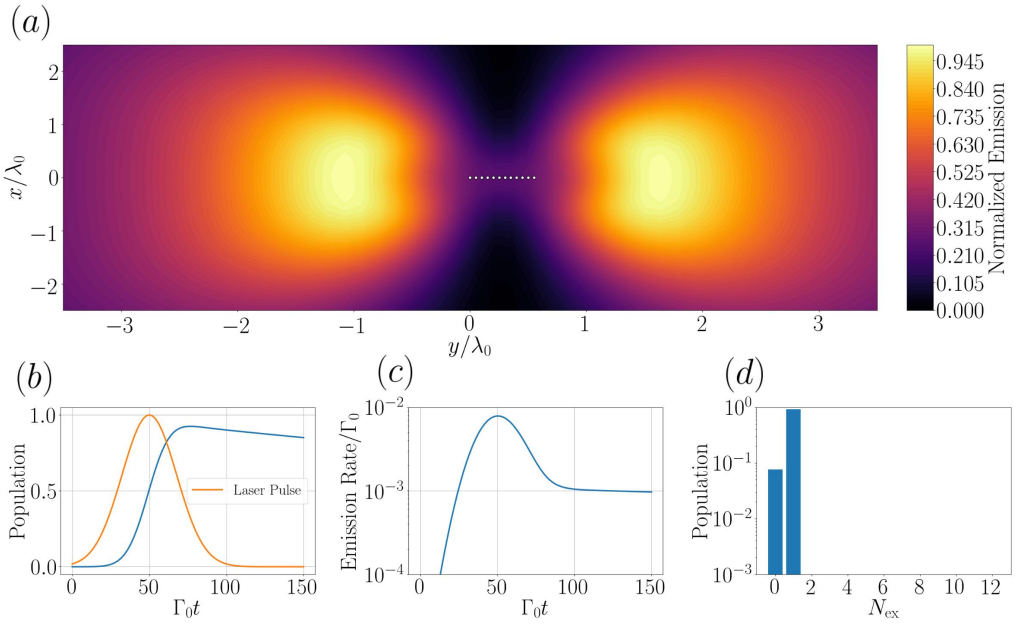

Figure 5.7: *Subradiance.* The linear chain of 12 quantum emitters along the y direction each linearly polarized in z direction with spacing $d = \lambda_0/20$. For optimal subradiant state preparation a laser pulse propagating along the chain is chosen with amplitude $\tilde{\Omega}_p = \Gamma_0$ and FWHM of the pulse duration of $\tau = 25\Gamma_0$. The laser is linear polarized and tuned to the most subradiant single excitation eigenmode of the chain. In (a) the normalized intensity distribution at $\Gamma_0 t = 150$ in the xy plane is shown with a cut at $z = 20d$. The emission rate in (c) shows that the chain radiates weakly only at its ends with a rate $10^{-3}\Gamma_0$. In (b) the laser pulse and the emitter population of the chain are plotted with the chain population reaching almost unity. (d) shows the distribution of the population in the individual excitation manifolds at $\Gamma_0 t = 150$. Only the total ground state and the first excitation manifold are populated showing that a single excitation is stored in the chain which radiates at a rate $10^{-3}\Gamma_0$.

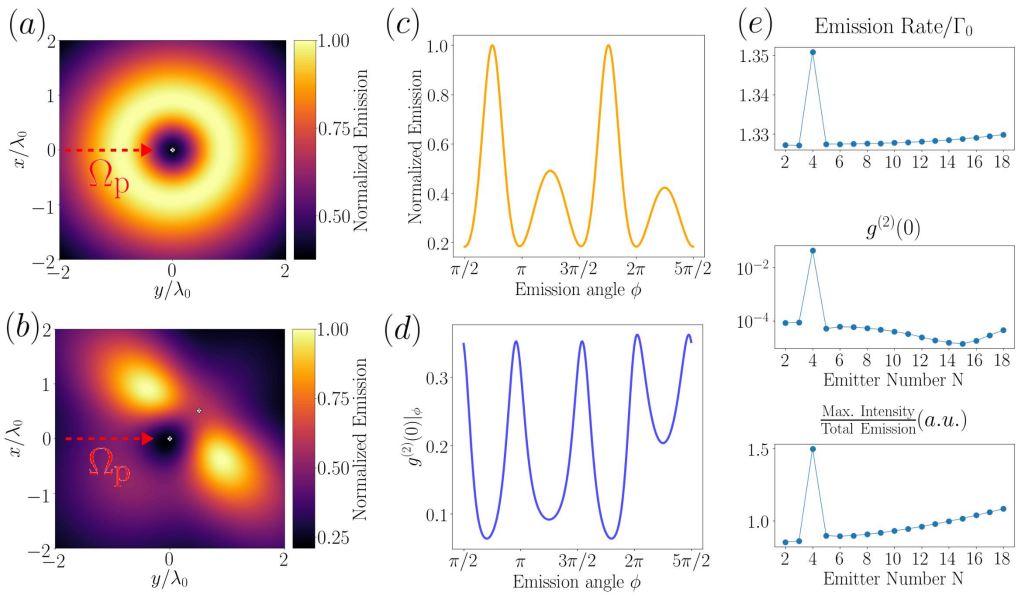

Figure 5.8: *Nano Ring.* (a) A single ring of emitters ($N = 4$) is continuously driven by a linear polarized laser from the y direction with driving rate $\Omega_p = \Gamma_0$. The emitters are linear polarized in z direction with a separation $d = 0.03\lambda_0$. The laser is tuned to the most superradiant single excitation eigenmode of the ring which is given by $\omega_0 + \sum_{j=2}^{N} \Omega_{1j}$ but steady state emission shows no directionality in the xy-plane. (Cut in $z = 1.5\lambda_0$) In (b) a second identical undriven ring is placed at an $\pi/4$ angle to the first ring with the centers of the rings being $0.7\lambda_0$ apart and the steady state showing strong directional emission in a direction which is not interfering with the laser beam direction. The intensity maxima in (b) are shown in (c) as a function of the emission angle ϕ (xy-plane) and (d) shows correspondingly a low bunching parameter $g^{(2)}(0) < 0.1$ in the directions of maximum emission. Scaling behaviours as a function of the undriven ring emitter number are plotted in (e) for the total emission rate, $g^{(2)}(0)$ in the direction of maximum emission and the ratio between maximal emission and total emission in the steady state. The emitter number of the driven ring is fixed at $N = 4$ and the distance between the ring centers is fixed at $0.7\lambda_0$ as is the emitter spacing $d = 0.03\lambda_0$. For an increasing emitter number in the undriven ring, more light is concentrated in the direction of maximal emission with a $g^{(2)}(0) \leq 10^{-3}$ as seen in (e), constituting a nearly perfect directional single photon source.

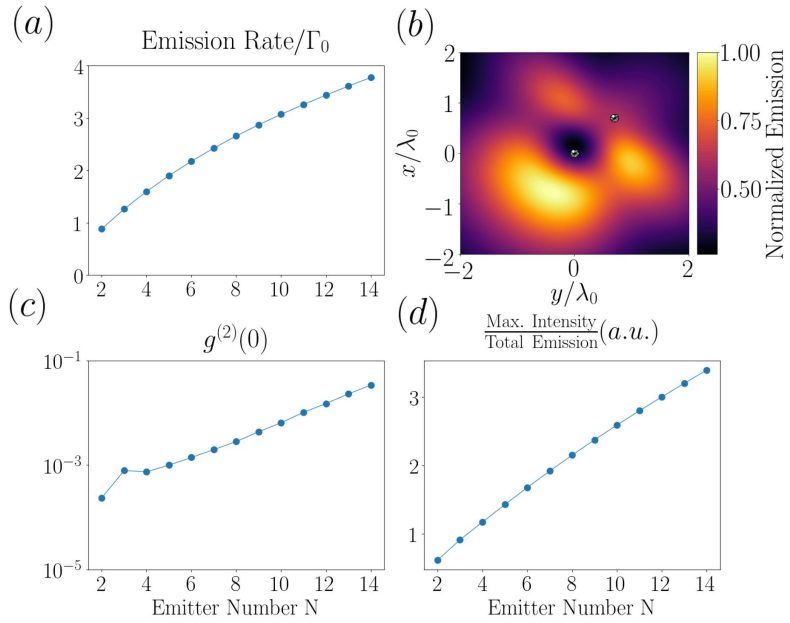

Figure 5.9: *Tilted Polarization.* Taking the same arrangement as in Fig. S3 with $d = 0.02\lambda_0$ but adding a small component of $x = 0.1$ to the dipole orientations ($\hat{\boldsymbol{\mu}} = (0, 0, 1)^T$) of the emitters in the driven ring on the left. The laser beam propagates in the z-direction with a rate $\Omega_p = 20\Gamma_0$ and a circular polarization $(\hat{x}, i\hat{y}, 0)^T/\sqrt{2}$. In (b) the normalized steady state emission rate in the xy-plane is shown for $N = 14$ emitters per ring (Cut in $z = 1.5\lambda_0$). The total emission rate, the bunching parameter and the ratio between maximal emission and total emission in the steady as a function of the emitter number per ring are shown in (a), (c) and (d) respectively. A single ring of such small scale with transversally polarized emitters would emit into the whole xy plane equally but the presence of a second identical undriven ring directs the emission into a particular direction.

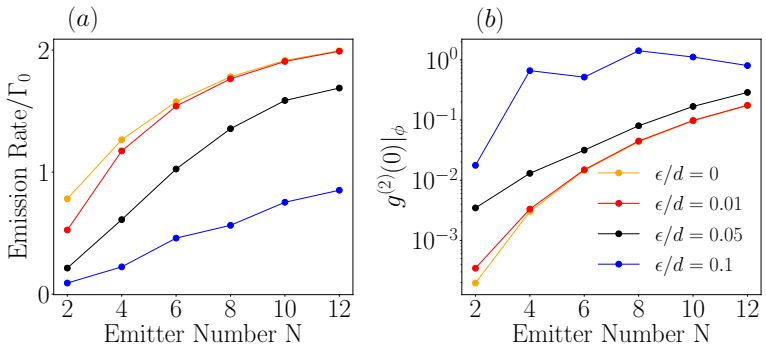

Figure 5.10: Influence of positional disorder ϵ for a linear chain in (a) the steady state emission rate and (b) bunching parameter $g^{(2)}(0)$ in the direction of maximal emission. The continuous lines are guides for the eye showing the dependence on the emitter number N. For a chain along y, each emitter is displaced in x and y by a random value between $[-d\epsilon, d\epsilon]$. We average over 100 random configurations for each value of ϵ. For all plots, $d = \lambda_0/40$.

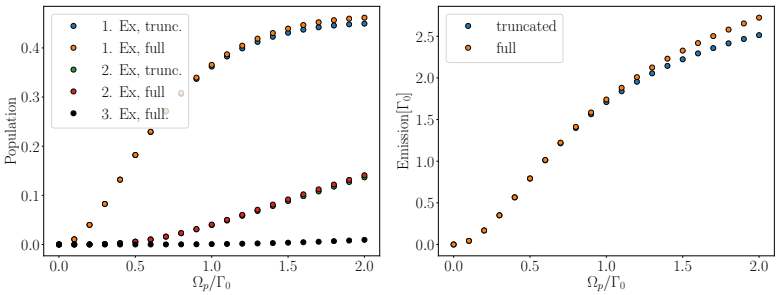

Figure 5.11: A comparison of the full quantum model with the truncated model is shown in the steady state for a 5 emitter chain along y with spacing $d/\lambda_0 = 0.05$ and the emitters linearly polarized in z direction. The laser is again tuned to the most superradiant single excitation eigenmode and propagates along the chain direction. The truncation includes only up to two excitation but it is seen that the third excitation manifold in the full model is almost negligible and the total emission rate shows good agreement up to a coherent driving rate of Γ_0 both for the steady state population and the total emission rate.

6 Publication

Optics Express **30**(10779-10791), (2022)

Efficient nano-photonic antennas based on dark states in quantum emitter rings

M. Moreno-Cardoner[1], R. Holzinger[1] and H. Ritsch[1]

[1]*Institut für Theoretische Physik, Universität Innsbruck, Technikerstrasse 21, A-6020 Innsbruck, Austria*

Nanoscopic arrays of quantum emitters can feature highly sub-radiant collective excitations with a lifetime exponentially growing with emitter number. Adding an absorptive impurity as an energy dump in the center of a ring shaped polygon allows to exploit this feature to create highly efficient single photon antennas. Here among regular polygons with an identical center absorbing emitter, a nonagon exhibits a distinct optimum of the absorption efficiency. This special enhancement originates from the unique emergence of a subradiant eigenstate with dominant center occupation. Only for nine emitters the sum of coupling strengths of each emitter to all others matches the center to the ring coupling. Analogous to a parabolic mirror the antenna ring then concentrates incoming radiation at its center without being significantly excited itself. Similar large efficiency enhancements, which even prevail for broadband excitation, can also be engineered for other antenna sizes by tailoring the frequency and magnitude of the central absorber. Interestingly, for very small structures a quantum treatment predicts an even stronger enhancement for the single photon absorption enhancement than a classical dipole model. As natural light harvesting structures are often based on ring shaped structures, the underlying principle might be exploited there as well.

DOI: 10.1364/OE.437396

6.1 Introduction

Collective radiation effects such as sub- and super-radiance [1, 2, 5, 115] in sub-wavelength structures of dipole coupled quantum emitters create growing widespread

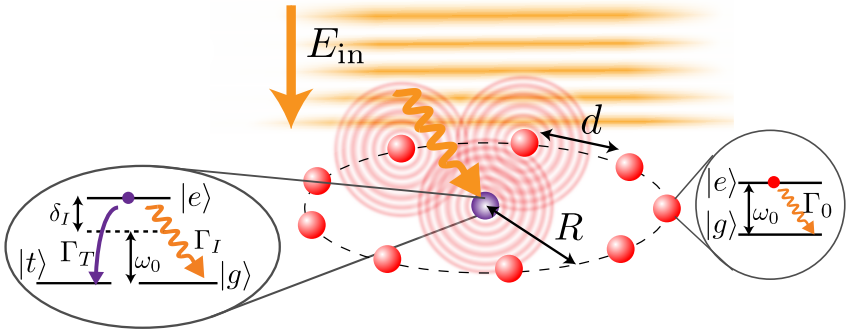

Figure 6.1: Scheme of an antenna in form of a regular polygon of N two-level emitters of radius R and distance d coupled to a central impurity which decays from state $|e\rangle$ either to state $|g\rangle$ at rate Γ_I or to an auxiliary state $|t\rangle$ via an extra irreversible channel at rate Γ_T. The impurity $|g\rangle$-$|e\rangle$ transition is detuned from the antenna atoms by δ_I. The whole system is uniformly driven.

interest [9,50,57,58,61,116–136,168] as recent experimental advances allow implementing and controlling precise arrays of individual quantum emitters at close distance e.g. in uniformly filled optical lattices [111–114], optical tweezers arrays, microwave coupled superconducting q-bits [169–171] or solid-state quantum dots [172,173].

Ordered dipole arrays create novel platforms for enhanced atom-light coupling surpassing current limitations of quantum information protocols [58,87,138], precision spectroscopy [67,139] or opto-mechanics [140,141]. Moreover they represent a genuine test bed for fundamental studies of quantum many body states of light and matter [132,139,174,175]. Nature is abundantly engineering complex sub-wavelength scale structures of optical dipoles in common light harvesting complexes [160,176–181].

Among various designs, arrays forming regular polygons with sub-wavelength interparticle distance (referred here as nanorings) exhibit exceptional radiative properties [58,143,165,182–184]. On the one hand they support extremely subradiant guided modes with a loss exponentially decreasing with atom number [58], allowing for efficient energy transport within a single ring [183] or between two neighboring rings [165,184]. On the other hand they possess collective eigenmodes with a tightly confined field in a sub-wavelength region near their center. Adding gain at the ring center, such nano-rings as optical resonators allow to create coherent laser-like nanoscopic light sources [143].

Here we exhibit how such a ring structure can act like a parabolic mirror antenna [185,186] concentrating incoming radiation in a sub-wavelength volume at its center and strongly enhancing the single photon absorption cross section by placing an impurity there, way beyond the single atom value. Surprisingly one finds that antenna rings of $N = 9$ dipoles with an equal center dipole exhibit a distinctively superior performance compared to other antenna atom numbers in several respects. Let us note here, that

ring structures in a common form of bacterial light harvesting complexes called LHC2 often appear with 9-fold rotational symmetry, but are comprised of several concentric rings [160, 176–180, 187–193]. Interesting previous results show that the dynamics of excitation energy transfer between concentric rings at room temperature are indeed improved by coherence or quantum mechanical coupling between the chromophores forming the ring [189–193].

Analysing the collective eigenmodes reveals a first hint for the astonishing superiority of a nine-atom ring with a central impurity. Only for $N = 9$ we find an extremely subradiant mode with the central emitter as the most strongly excited component. Similar sub-radiant states can also be engineered for other ring emitter numbers, when one precisely optimizes their center impurity dipole moment and transition frequency. As a key property, despite being strongly subradiant, these collective states still sufficiently couple to a perpendicular incident plane wave. At resonance, the high-Q center field enhancement of the dark mode creates a large steady state excitation of the central emitter so that the energy can be efficiently absorbed.

Importantly, throughout the absorption process the ring atoms are only weakly excited and will hardly dissipate or re-emit energy. The mechanism resembles a generalized form of cavity anti-resonance spectroscopy with the ring acting as enhancement cavity [194]. Interestingly, the collection efficiency enhancement is even much larger, if the incoming field does not directly excite the central absorber, but only couples to the antenna ring. Any irreversible non-radiative decay from the excited state of the central emitter slowly but efficiently extracts the collected energy without re-emission into free space. Hence the system is a minimalist model for a light-harvesting complex build of a ring shaped antenna and a central absorber as energy dump [160, 176, 180, 181, 195].

6.2 The model

We model our generic antenna as a regular polygon of N equal point-like two-level emitters with dipole moment $\wp_i = \wp$ at distance d with radius R. At its center we add an extra dipole (referred to as "impurity"), with a transition of polarization strength $\wp_I = \sqrt{\Gamma_I/\Gamma_0}\ \wp$ detuned from the antenna atoms by δ_I. Energy loss is modelled by an additional incoherent decay channel to an auxiliary state $|t\rangle$ at rate Γ_T (see Fig. 6.1). All emitters (including the impurity) are interacting via vacuum mediated dipole-dipole interactions which in the Born-Markov approximation leads to the master equation (in the frame rotating at ω_0) [43]:

$$\dot{\rho} = -i[\hat{H}, \rho] + \mathcal{L}[\rho] \quad , \quad \hat{H} = \sum_{i \neq j} J_{ij} \hat{\sigma}_i^{eg} \hat{\sigma}_j^{ge} - \delta_I \hat{\sigma}_I^{ee}, \tag{6.1}$$

$$\mathcal{L}[\rho] = \frac{1}{2} \sum_{i,j} \Gamma_{ij} \left(2\hat{\sigma}_j^{ge} \rho \hat{\sigma}_i^{eg} - \hat{\sigma}_i^{eg} \hat{\sigma}_j^{ge} \rho - \rho \hat{\sigma}_i^{eg} \hat{\sigma}_j^{ge} \right), \tag{6.2}$$

where $\hat{\sigma}_j^{ge}$ ($\hat{\sigma}_j^{eg}$) is the lowering (raising) operator between excited and ground state of emitter j. The dispersive and dissipative couplings are $J_{ij} = \mathrm{Re}\mathcal{G}_{ij}$ and $\Gamma_{ij} = -2\mathrm{Im}\mathcal{G}_{ij}$, with $\mathcal{G}_{ij}$ being the dipole-dipole coupling matrix, which is proportional to the free space Green's tensor, and it can be written as:

$$\mathcal{G}_{ij} = \frac{3\Gamma_0}{4k_0^3 r^3 \wp^2} e^{ik_0 r} \wp_i^{\alpha,*} \wp_j^{\beta} \left[\left(1 - ik_0 r - k_0^2 r^2\right) \delta_{\alpha\beta} + \left(-3 + 3ik_0 r + k_0^2 r^2\right) \frac{\mathbf{r}_\alpha \mathbf{r}_\beta}{r^2} \right].$$

$\mathbf{r} = \mathbf{r}_i - \mathbf{r}_j$ is the vector connecting dipoles i and j, whose $\alpha-$component and modulus is denoted by $\mathbf{r}_\alpha$ and $r = |\mathbf{r}|$ and $\wp_i^\alpha$ is the $\alpha-$component of the vector polarization of emitter i. $k_0 = \omega_0/c$ is the transition wave-number and $\Gamma_0 = |\wp|^2 k_0^3/3\pi\epsilon_0$ the spontaneous emission rate of a single ring emitter. In the low intensity limit the observables are described by the non-Hermitian effective Hamiltonian $\hat{H}_{\text{eff}} = \sum_{ij} \left(J_{ij} - i\frac{\Gamma_{ij}}{2}\right) \hat{\sigma}_i^{eg} \hat{\sigma}_j^{ge}$. The remaining terms in Eq.(7.10) describe corrections of higher order in pump intensity.

6.3 Sub-radiant modes in the ring-impurity system

A sub-wavelength ring of emitters exhibits extremely subradiant excitation modes whose field vanishes at the center [165] and thus they are decoupled from the center impurity. However, in presence of the impurity one finds a new class of subradiant states with large center occupation and strong coupling to the symmetric bright mode of the outer ring (antenna). When the antenna is excited the center impurity oscillates with opposite phase and almost perfectly cancels the total emitted field creating a so called anti-resonance [194]. The large excitation weight of the central emitter in combination with the suppressed decay here is the key to low loss energy transfer and large absorption cross-section.

For concreteness and simplicity we restrict ourselves to the symmetric case where all emitters are circularly polarized in the ring plane. Nevertheless, equivalent phenomena appear in more general polarization configurations [184], where all emitters equally couple to the central impurity. Within the single excitation subspace the center only couples to the unique symmetric antenna mode (represented by $S^\dagger = N^{-1/2} \sum_{j=1}^N \hat{\sigma}_j^{eg}$), and $\hat{H}_{\text{eff}}$ reads:

$$\hat{H}_{\text{eff}} = -\left(\delta_I + i\frac{\Gamma_I}{2}\right) \hat{\sigma}_I^{ee} + \left(J_R - i\frac{\Gamma_R}{2}\right) S^\dagger S + \sqrt{\frac{N\Gamma_I}{\Gamma_0}} \left(J - i\frac{\Gamma}{2}\right) \left[S^\dagger \hat{\sigma}_I^{ge} + S\hat{\sigma}_I^{eg}\right], \tag{6.3}$$

J_R and Γ_R are the collective frequency shift and decay rate of the symmetric ring mode [165]. Here we omitted the other eigenmodes of the ring decoupled from the center since they are irrelevant to the impurity dynamics. The ring-impurity's dispersive and dissipative couplings are given by $J = \mathrm{Re}\ \mathcal{G}$ and $\Gamma = -2\mathrm{Im}\ \mathcal{G}$, with

$$\mathcal{G} = \frac{3\Gamma_0}{8k_0^3 R^3} e^{ik_0 R} \left[-1 + ik_0 R + k_0^2 R^2\right]. \tag{6.4}$$

Note that the effective field the symmetric ring mode creates at the impurity position corresponds to a single dipole with dipole moment $\sqrt{N}\wp$. Hence the system is formally equivalent to two coupled emitters of unequal dipole moments. The effective ring dipole is detuned from the impurity by $J_R + \delta_I$. A study of this equivalent toy system is given in [196].

For a single excitation, the collective eigenmodes of the ring-impurity system and the corresponding decay rates and frequency shifts can be obtained by diagonalizing the 2×2 matrix resulting from projecting Eq.(6.3) into the subspace spanned by $\{|R\rangle, |I\rangle\}$, with $|R\rangle = S^\dagger |g\rangle$ and $|I\rangle = \hat{\sigma}_I^{eg} |g\rangle$. Fig. 10.2 shows the decay rate $\Gamma_{\min}$ and impurity occupation weight $\langle \hat{\sigma}_I^{ee} \rangle$ respectively, for the most subradiant eigenmode in the case where ring and impurity emitters are identical ($\delta_I = 0$ and $\Gamma_I = \Gamma_0$), as a function of emitter number N and ring size. As central result of this work we find that in the sub-wavelength regime ($\lambda_0/d5$) an extremely dark mode with suppressed decay rate $\Gamma_{\min}/\Gamma_0 10^{-3}$ emerges exclusively when the ring contains exactly $N = 9$ emitters.

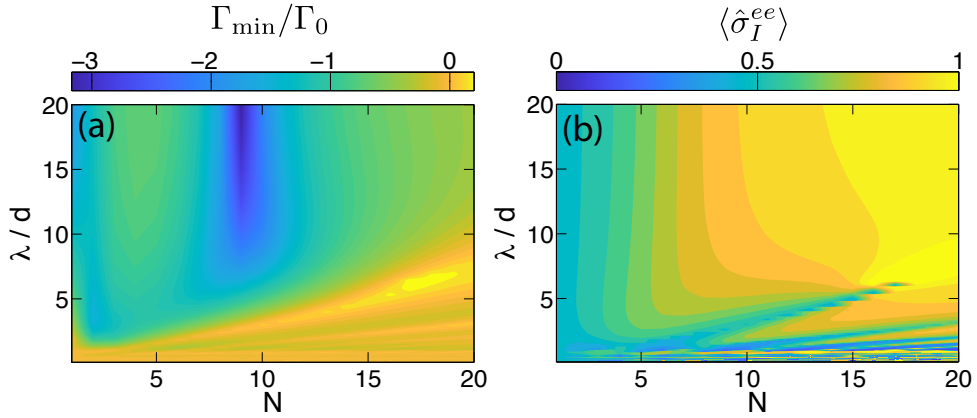

Figure 6.2: Eigenstate properties of the coupled ring-impurity system. (a) Collective decay rate $\Gamma_{\min}$ (in units of Γ_0) and (b) impurity excited state population $\langle \hat{\sigma}_I^{ee} \rangle$, of the most subradiant state emerging in the coupled ring-impurity system, plotted versus N and λ/d. The figure shows that at sufficiently large value of λ/d a very subradiant state for $N = 9$ ring emitters exists, whose impurity excited state population is large.

Its appearance can be understood in the two effective dipoles model, as a subradiant state arises when two dipoles have similar magnitude but opposite phase (singlet configuration) so that their radiated far fields cancel. For a generic state of the form $|\Psi\rangle = \alpha |R\rangle + \beta |I\rangle$ this implies $\beta \approx -\alpha\sqrt{N/\Gamma_I}$. In general, however, such a state is not an energy eigenmode. In the sub-wavelength regime ($\lambda/R \gg 1$), where $\Gamma_R \approx N\Gamma_0$ and $\Gamma \approx \Gamma_0$, this state is only an eigenmode if:

$$J_R + \delta_I \approx J(N - \Gamma_I/\Gamma_0). \tag{6.5}$$

For identical emitters ($\delta_I = 0$ and $\Gamma_I = \Gamma_0$) this reduces to $J_R \approx (N-1)J$. Hence all emitters including the central one experience virtually the same total interaction strength with all others. Indeed we find that the closest integer value N satisfying this condition is $N = 9$ as for the most subradiant mode. This reflects a special geometric property of the nonagon (regular polygon with $N = 9$ sides), where the sum of the inverse cubic distances $1/r_{ij}^3$ to all other N-1 corners is closest to $(N-1)/R^3$, i.e., the scaling of the near field dipole-dipole interaction.

Based on this general principle it is straightforward to induce a similar dark mode for other values of N by suitable tuning of the impurity parameters δ_I or Γ_I to fulfill Eq.(6.5). At small values of λ/d the system properties are very sensitive to δ_I and Γ_I and this estimate only yields almost optimal values. In general, the effective polarization strengths $\sqrt{N}\alpha$ and $\sqrt{\Gamma_I}\beta$ associated with the ring and impurity components of the eigenmode are complex values and a minimal decay rate requires a very small imaginary part and a relative phase close to π. This ensures that short range interactions between the two dipoles do not contribute to the free space energy loss. We show in Fig. 10.3 the minimum collective decay rate of the coupled system corresponding to $\Gamma_I = \Gamma_0$ when optimizing over the detuning δ_I, as a function of N and λ/d.

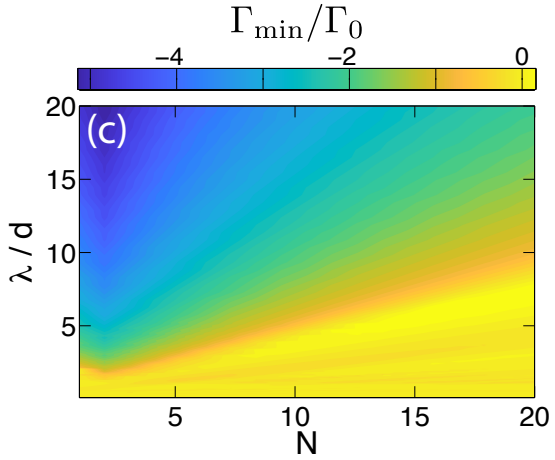

Figure 6.3: Decay rate (in units of Γ_0 and in log-scale) of the most subradiant mode of the coupled ring-impurity system, as a function of N and λ/d, when optimized over the impurity detuning δ_I (see also Fig. 10.9 for comparison with the corresponding cross-section).

6.4 Absorption cross section

Let us now study the light absorption of this special dark resonance by adding an incoherent decay at rate Γ_T from the excited state of the center to an auxiliary state $|t\rangle$

(see Fig. 6.1). This implements a sink extracting energy without back-action and could represent irreversible conversion of photons into chemical energy at the reaction center. In an atom based setup extra atoms coupled to the central atom via a dipole moment component orthogonal to the antenna dipoles could extract excitations [197]. For superconducting q-bits one could use a tiny antenna close to the center q-bit [169,198]. Mathematically we simply add a loss term $\mathcal{L}_T[\rho] = \Gamma_T \left[\hat{\sigma}^{te}\rho\hat{\sigma}^{et} - (1/2)\left\{\hat{\sigma}^{ee},\rho\right\}\right]$ in the master equation.

Absorption efficiency is quantified by the cross section $\sigma_{\rm abs}$, which represents the effective area for which an incident photon triggers an absorption event. The relative rate of absorbed versus incident photons per area A then is $\sigma_{\rm abs}/A = dn_{\rm abs}/dn_{\rm in}$. In contrast to total scattering or light extinction often used (e.g. [176,199]), our definition of $\sigma_{\rm abs}$ includes both, the probability of scattering a photon by the system and its subsequent transfer to the auxiliary impurity state. Note that the resulting cross section here can exceed the resonant single emitter scattering cross-section $\sigma = 6\pi/k_0^2$.

The rate of effectively absorbed photons is $dn_{\rm abs}/dt = \Gamma_T \langle\hat{\sigma}_I^{ee}\rangle$. When all emitters are driven by a perpendicularly propagating coherent field of frequency ω_L (detuning $\delta = \omega_L - \omega_0$), whose Rabi frequency is $\Omega(\mathbf{r}_i) = \Omega$, we add the term $\hat{H}_{\rm in} = -\delta\sum_i \hat{\sigma}_i^{ee} + \sum_i [\Omega(\mathbf{r}_i)\hat{\sigma}_i^{eg} + h.c.]$ in Eq.(10.1). In this case the incident photon rate is $dn_{\rm in}/dt = 4\Omega^2 k_0^2 A/6\pi\Gamma_0 = (4\Omega^2/\Gamma_0)(A/\sigma)$, leading to $\sigma_{\rm abs}/\sigma = \Gamma_T\Gamma_0\langle\hat{\sigma}_I^{ee}\rangle/4\Omega^2$. Here the absorption efficiency is compared to a single emitter weakly driven on resonance with spontaneous emission rate Γ_0 including the additional decay channel at rate Γ_T. In steady state we have: $\sigma_{\rm abs,c}^{\rm single} = \sigma\Gamma_0\Gamma_T/(\Gamma_0+\Gamma_T)^2$, i.e. the product of the probabilities for first scattering a photon and subsequently absorbing it, with maximum value $\max(\sigma_{\rm abs,c}^{\rm single}) = \sigma/4$ for $\Gamma_T = \Gamma_0$.

For a very low-intensity coherent field we get:

$$|\Psi\rangle = |g\rangle - i\sum_\nu \frac{1}{\nu-\delta}\,|\nu\rangle\left\langle\nu^T\right\rangle\Omega + O(\Omega^2/\Gamma_0^2), \tag{6.6}$$

where $|\nu\rangle$ are the eigenmodes of the system with complex eigenvalues $\nu = \omega_\nu - i\Gamma_\nu/2$ and $|\Omega\rangle \equiv \sum_i \Omega(\mathbf{r}_i)\hat{\sigma}_i^{eg}|g\rangle$. In general excitations of dark modes with long lifetime are strongly suppressed due to the small overlap with propagating field modes. However, resonant enhancement due to the extremely small dark state damping still yields a large absorption cross sections. For an energetically well resolved eigenmode $|\nu_0\rangle$ with a decay rate smaller than its frequency difference to nearby modes, the absorption cross section is dominated by a single term:

$$\frac{\sigma_{\rm abs}}{\sigma} \approx \frac{\Gamma_T\Gamma_0}{\Omega^2\Gamma_{\nu_0}^2}\,|\langle I\rangle\,\nu_0|^2\cdot\left|\left\langle\nu_0^T\right\rangle\Omega\right|^2. \tag{6.7}$$

It surpasses a single atom if $\Gamma_{\nu_0}/2 < |\langle I\rangle\,\nu_0|\cdot\left|\left\langle\nu_0^T\right\rangle\Omega\right|/\Omega$, i.e. the decay rate of the eigenmode has to be small but contain a large impurity occupation weight to compensate for the smaller overlap with incoming radiation. In Fig. 10.4(a) we show for $N = 9$ (identical emitters case) as a function of λ/d and detuning $\delta = \omega_L - \omega_0$ of the

external coherent drive, the absorption cross section $\sigma_{\rm abs}$ in units of $\max(\sigma_{\rm abs,c}^{\rm single}) = \sigma/4$. This shows that a narrow resonance where the absorption is greatly enhanced emerges for $\lambda/d5$, corresponding to the frequency of the dark mode previously discussed. In Fig. 10.4(b) we then plot $\sigma_{\rm abs}$ versus λ/d and N, when the external drive detuning is tuned to the dark mode. In the deep sub-wavelength regime ($\lambda/d5$) a distinct maximum cross-section arises for $N = 9$ emitter antennae and the regions of maximal absorption correspond to those with minimum collective decay.

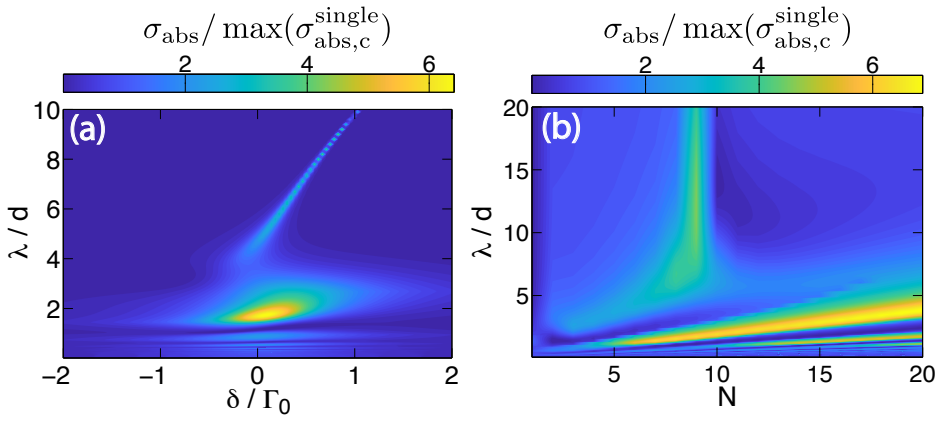

Figure 6.4: Absorption cross-section $\sigma_{\rm abs}$ (in units of maximal single atom absorption cross section $\max(\sigma_{\rm abs,c}^{\rm single}) = \sigma/4$) of the coupled ring-impurity system illuminated by a weak coherent circularly polarized field. (a) $\sigma_{\rm abs}$ versus external field detuning δ and λ/d for $N = 9$. For small enough rings ($\lambda/d \gg 1$) the system is a frequency-selective antenna with resonantly enhanced absorption cross-section, corresponding to the dark eigenmode and which can be tuned via the system parameters. (b) $\sigma_{\rm abs}$ versus N and λ/d for resonant light with the subradiant eigenmode. A maximum in the absorption occurs exactly where the collective mode is most subradiant (see for comparison Figure 2 (a)).

As said, a similar dark mode can be accessed for different values of N by tuning the impurity parameters Γ_I and δ_I, which yields an enhanced absorption cross section as shown in Fig. 10.5(a) and (b), where we plot $\sigma_{\rm abs}$ versus N and δ_I (at fixed $\Gamma_I = \Gamma_0$), or Γ_I (at fixed $\delta_I = 0$), for $\lambda/d = 20$. Finally, in Fig. 10.9 we depict $\sigma_{\rm abs}$ as a function of N and λ/d for optimal δ_I, showing that enhanced absorption $\sigma_{\rm abs}$ with respect to the single emitter case can be achieved for an arbitrary value of $N \geq 3$ by tuning the impurity parameters.

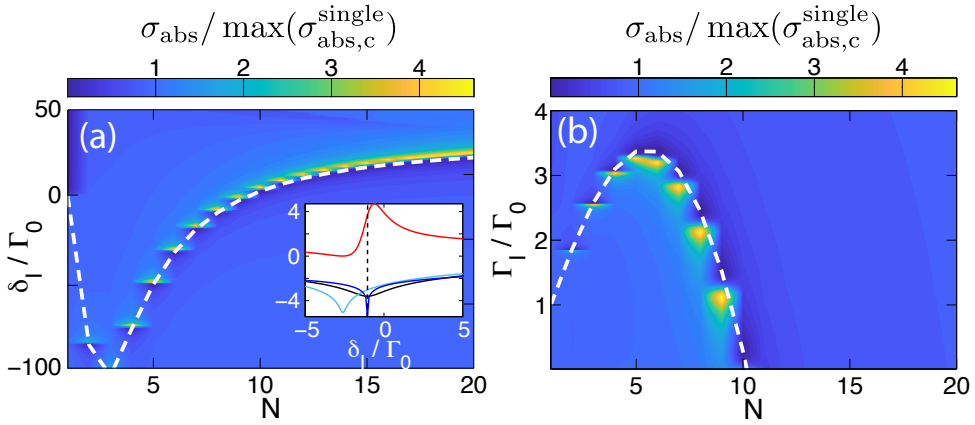

Figure 6.5: Effect of impurity detuning δ_I and decay Γ_I in the coupled ring-impurity system. Absorption cross section $\sigma_{\rm abs}$ (in units of maximal single atom absorption cross section $\max(\sigma^{\rm single}_{\rm abs,c}) = \sigma/4$) versus N and (a) δ_I at fixed $\Gamma_I = \Gamma_0$, and (b) Γ_I at fixed $\delta_I = 0$, for $\lambda_0/d = 20$. The dashed white lines are Eq.(6.5). Inset: $\sigma_{\rm abs}$ for $N = 9$ (red line), dark mode decay rate (log-scale, black line), effective dipole moment $|\wp_{\rm eff}|^2$ (cyan line) and $\mathrm{Im}[\wp_{\rm eff}]$ (blue line, log-scale), for comparison. $\sigma_{\rm abs}$ is very sensitive to the detuning δ_I with a sharp maximum near the minimum of $\mathrm{Im}[\wp_{\rm eff}]$.

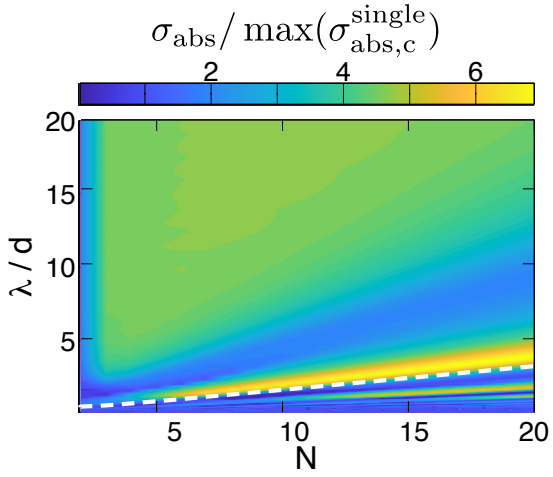

Figure 6.6: Absorption cross-section $\sigma_{\rm abs}$ (in units of maximal single atom absorption cross section $\max(\sigma^{\rm single}_{\rm abs,c}) = \sigma/4$) versus N and λ/d optimized as function of δ_I at fixed $\Gamma_I = \Gamma_0$. The dashed white line represents $\lambda/R = 1$. For optimal δ_I enhanced absorption with respect to the single atom case occurs for $N \geq 3$ at $\lambda/R \geq 1$.

6.5 Enhancement of incoherent light absorption

So far we dealt with spatial and temporal coherent input radiation with well defined intensity as it occurs for incoming laser light. Of course this is far from the conditions present for thermal radiation sources, where only spatial and not temporal coherence is present. It is, however, straightforward to generalize our absorption model to account for a spectral bandwidth of the incoming light. Actually in the very large bandwidth limit one simply has to replace the coherent driving amplitude by a temporally incoherent but spatially coherent field. Mathematically this just amounts to add the excitation rates in form of an extra Liouvillian term:

$$\mathcal{L}_{\rm inc}[\rho] = \epsilon[\hat{R}^\dagger_{\mathbf{k}}\rho\hat{R}_{\mathbf{k}} - (1/2)\{\hat{R}_{\mathbf{k}}\hat{R}^\dagger_{\mathbf{k}}, \rho\}], \tag{6.8}$$

with $\hat{R}_{\mathbf{k}} = \sum_j e^{i\mathbf{k}\mathbf{r}_j}\hat{\sigma}^{ge}_j$ added to the master equation. For low-intensity radiation impinging perpendicular to the ring ($\mathbf{k} = 0$ and $\epsilon \ll \Gamma_0$) in Fig. 10.10 we show $\sigma_{\rm abs}$ in units of $\sigma^{\rm single}_{\rm abs,inc} = \sigma\Gamma_T/(\Gamma_0 + \Gamma_T)$, corresponding to a single emitter. In Fig. 10.10(a), where $\sigma_{\rm abs}/\sigma^{\rm single}_{\rm abs,inc}$ is plotted versus Γ_T and N for $\lambda/d = 40$, we see that this ratio again attains a maximum for $N = 9$ in the small $\Gamma_T \ll \Gamma_0$ regime. In addition, a broad maximum centered around $N = 9$ arises for fast center loss $\Gamma_T/\Gamma_0 \sim 10^3$. Again a choice of $N = 9$ seems optimal. Note that nature is partly using 9-fold symmetry but the construction involves a much more complex and intricate structure for each element [200, 201] involving transfer between different rings [184, 202].

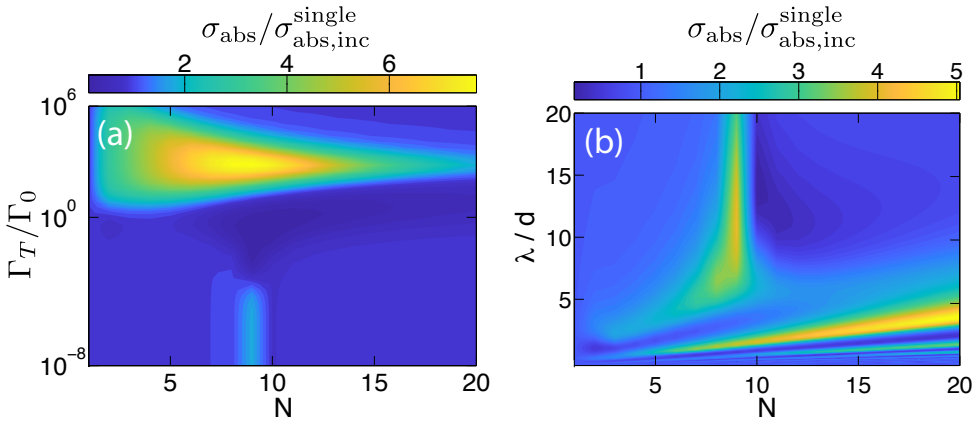

Figure 6.7: Absorption cross-section $\sigma_{\rm abs}$ (in units of $\sigma^{\rm single}_{\rm abs,inc} = \sigma\Gamma_T/(\Gamma_0 + \Gamma_T)$, corresponding to the absorption cross section of a single emitter weakly incoherently driven) in the coupled ring-impurity system for an incoherent weak pump. (a) $\sigma_{\rm abs}$ versus N and Γ_T/Γ_0, at fixed $\lambda/d = 40$, and (b) versus N and λ/d, at fixed $\Gamma_T/\Gamma_0 = 10^{-4}$. An enhancement in absorption with respect to the single emitter case is found for $N = 9$ at sufficiently small Γ_T/Γ_0 and large λ/d.

6.6 Semi-classical coupled dipole model

As we have seen above the enhancement is close tied to a very dark collective eigenstate of the system with ample weight on the center dipole. As it has been argued that the most dark states are entangled [50, 203], one can ask whether our results hold in the case of classical dipole arrays. To this end we can simply apply a mean-field type of approximation to the quantum description, representing atomic operators by their mean values and study the differences to the quantum model, where we restricted the Hilbert space to the single or the two excitation manifold. In this classical limit we get simple coupled c-number Bloch equations for each dipole and the center impurity. For symmetry reasons the expectation values for all ring atoms follow the same time evolution, so that finally we end up with a rather small finite closed set of differential equations:

$$\begin{aligned}
\dot{\langle\sigma_I^{ee}\rangle} &= -2\Omega\Im\{\langle\sigma_I^{ge}\rangle\} + (iJ-\Gamma/2)\sqrt{N}\langle\sigma_I^{ge}\rangle\langle S\rangle^* - (iJ+\Gamma/2)\sqrt{N}\langle S\rangle\langle\sigma_I^{ge}\rangle^* \\
&\quad - (\Gamma_0+\Gamma_T)\langle\sigma_I^{ee}\rangle \\
\dot{\langle\sigma_I^{ge}\rangle} &= -(i\delta_I+\Gamma_I/2+\Gamma_T/2)\langle\sigma_I^{ge}\rangle + i\Omega(2\langle\sigma_I^{ee}\rangle-1) + 2(iJ+\Gamma/2)\sqrt{N}\langle S\rangle\langle\sigma_I^{ee}\rangle \\
&\quad - (iJ+\Gamma/2)\sqrt{N}\langle S\rangle \\
\dot{\langle S\rangle} &= -(iJ_{\mathrm{R}}+\Gamma_{\mathrm{R}}/2)\langle S\rangle - \sqrt{N}(iJ+\Gamma/2)\langle\sigma_I^{ge}\rangle - i\sqrt{N}\Omega.
\end{aligned} \tag{6.9}$$

These equations can be readily solved for the steady state and we can then extract the effective cross section exactly as in the quantum model above with the initial values given by $(\langle\sigma_I^{ee}\rangle, \langle\sigma_I^{ge}\rangle, \langle S\rangle) = (0,0,0)$. Fig. 6.8 compares the classical approximation with the quantum model with the Hilbert space truncated to either one or two excitations. In Fig. 6.8 (a) the quantum description leads to a significantly larger absorption cross section compared to the classical description and the same holds for Fig. 6.8 (b) when the coherent driving rate Ω becomes sufficiently large but still orders of magnitude below the single atom saturation power.

Interestingly in the case of very close dipoles, larger differences appear and the quantum model always predicts a superior cross section by looking at a cut along the $N = 9$ line. Note that for very small diameters $\lambda/d > 8$ in the sub-wavelength region the quantum model predicts a significantly larger absorption cross section. In this regime, the energy shifts get more important than the modifications of the decay properties. One might speculate that this makes coherence more robust, increasing the absorption efficiency.

6.7 Conclusions

A sub-wavelength regular nonagon of dipoles has a built in geometric symmetry allowing for the existence of unique subradiant eigenstates with a high center population weight,

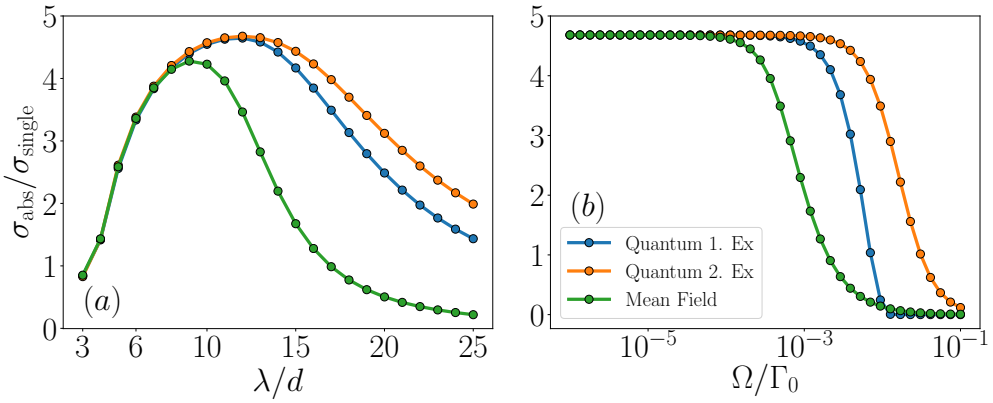

Figure 6.8: Effective absorption cross section in the steady state of the coupled ring-impurity system as a function of emitter distance and driving rate in the ring for the quantum model and the classical approximation (mean-field) corresponding to a coupled dipole model. (a) Absorption cross section as function of the interatomic emitter distance in the $N = 9$ ring for a coherent pumping rate $\Omega/\Gamma_0 = 5 \times 10^{-4}$ with detuning $\Delta = -\Re\{\lambda_{Dark}\}$, trapping rate $\Gamma_T = -2\Im\{\lambda_{Dark}\}$ for the impurity in the center and all emitters circularly polarized. (b) For $d = \lambda/12$ and $N = 9$ the mean field approximation is compared to the quantum model (one and two-excitation truncated states as indicated in the label) for increasing coherent driving rates Ω for the same Δ and Γ_T as in (a). The lines are only guides to the eye.

if one adds an additional equivalent centered absorber acting as an energy dump. This special property enhances absorption of light for weak uniform illumination not only in the case of resonant enhancement for spectral narrow radiation but it also appears for broadband incoherent light. Actually the absorption enhancement is even much stronger when only the antenna dipoles are selectively illuminated, while the center impurity is shielded. While such selective illumination seems hard to implement technically, a dynamical mechanism switching the center dipole on and off or shift its frequency should induce a similar effect. Note that comparable enhancements can also be engineered for other antenna sizes and geometries if one optimizes the center impurity strength and resonance frequency.

Interestingly, a classical mean field description reproduces these results well for larger ring dimensions and atom numbers, while the strongest enhancement at sub-wavelength distances appears only in a quantum treatment. Preliminary studies beyond weak field illumination also reveal a suppression of absorption of a second photon as long as the system is in the excited state. This will presumable suppress the g2 intensity correlation function of the emitted fluorescence as has recently also

been found in related studies [144, 204]

In practise, such dark state nano-ring antenna configurations inspired by natural ring structures should find applications in nanoscale single photon detection or even spectroscopy. Operated in reverse these structures act as coherent light nano-sources [143] or even non-classical single photon sources [204].

Let us finally remark, that while this effect appears not to be directly exploited in single natural LHC2 molecules, already the more complex form of of LHC1 is composed of a ring structure with a reactive center, where the proposed mechanism could be at work and in particular in combined LHC2-LHC1 compounds [176]. As these whole structures are very well below a wavelength in size, even thermal light will couple directly to collective delocalized excitations as starting point of light absorption. Clearly, light to chemical energy conversion in a thermal environment with a complex reaction center is a way more complex process. Nevertheless, it is hard to imagine that the ring symmetry found in many biological realizations is not used [202] and a pure coincidence.

Acknowledgments

We thank David Plankensteiner, Claudiu Genes and Laurin Ostermann for helpful input and are grateful to Darrick E. Chang for illuminating insight and ideas related to this work. We are indebted to Charles Adams for critical reading and suggestions to improve title and presentation of this work. We acknowledge funding from the Austrian Science Fund (FWF) doctoral college DK-ALM W1259-N27 (R. H.), and the European Unions Horizon 2020 research and innovation program under the Marie Sklodowska-Curie grant agreement No. 801110 and the Austrian Federal Ministry of Education, Science and Research (BMBWF) (M.M.-C.). It reflects only the authors view and the Agency is not responsible for any use that may be made of the information it contains. Numerical simulations were performed with the Julia programming language including the QoJulia.org quantum optics package [13].

6.8 Supplemental material

6.8.1 Simplified model based on an effective dipole to replace the ring

A regular polygon of antenna emitters with a single center dipole as excitation receiver as discussed above constitutes a highly symmetric arrangement. Hence, as it has been seen and used in previous work [165], rotation symmetry allows for an explicit calculation of eigenmodes for a simplified treatment. Nevertheless the resulting full description still is quite complex and requires a large Hilbert space. Thus the key physics is not always very easy to extract and analyze.

Here we will thus reduce the system to the minimal nontrivial size. For this we use only two effective dipoles, an antenna dipole μ_a with a large dipole moment proportional to the square root of the number of ring atoms representing the ring and a weak receiver dipole $\mu_c = \mu$ at distance R with an extra loss channel to represent the reaction center with corresponding energy extraction. Hence mathematically we end up with single two-level emitter for the ring and an Λ-type level system for the center. Interestingly we will see, that still a great deal of the essential physics that we found above, can be analyzed in such a oversimplified form.

As we will deal with spatially uniform and weak excitation fields, they will almost exclusively couple to the dominant symmetric mode and excitation is limited to the single excitation manifold in the ring. Hence we replace the ring of N emitters, with a dipole moment μ and decay rate Γ each, by a single effective antenna with N-fold dipole moment $\mu_a = \sqrt{N_a}\mu$ placed at a small distance R to the center dipole with moment $\mu_c = \mu$. Both dipoles are modeled as two-level systems $(|0\rangle, |1\rangle)$ with a circular polarized transition dipole moment and closely related transition frequency. The center atom is modeled as a three level Λ system, where spontaneous emission from the excited level on a second independent transition towards an additional state $|T\rangle$ mimics the receivers energy absorption. The dipole-dipole interaction is then determined by two parameters characterizing the effective dipole-dipole interaction with real part $\Omega(R)$ and imaginary part $\Gamma(R)$.

The simplified Hamiltonian of our system thus reads:

$$H = \hbar\omega_c\sigma_c^+\sigma_c^- + \hbar\omega_a\sigma_a^+\sigma_a^- + \hbar\omega_l P_l + \hbar\Omega(R)(\sigma_a^+\sigma_c^- + \sigma_a^-\sigma_c^+) \tag{6.10}$$

with $\omega_l, \omega_c, \omega_a$ denoting the energies of the auxiliary loss level, center atom and antenna atom respectively and P_l the Projector on the loss level. Note that for the corresponding full geometry the respective energies and coherent shifts are given by $\omega_a = \Omega_{\text{sym}}$ and $\Omega(R) = \sqrt{N}\Omega_{ac}$ with $\Omega_{\text{sym}} = \sum_{i\neq c}\Omega_{ic}$ being the Eigenenergy of the symmetric state in the ring. The spontaneous decay rates of the two dipoles is then related by $\Gamma_a = N^2\Gamma_c$. At very close (sub-wavelength) distance we have:
$\Gamma \approx \sqrt{(\Gamma_a\Gamma_c)} = N\Gamma_c$ and $\Omega \ll \Gamma$. Thus collective spontaneous decay including incoherent pumping is described by the Liouvillian

$$\begin{aligned} L\rho = \sum_{ij\in\{a,c\}} &\frac{\Gamma_{ij}}{2}\Big(2\sigma_i^-\rho\sigma_j^+ - \{\sigma_i^+\sigma_j^-, \rho\}\Big) + \frac{\Gamma_l}{2}\Big(2\sigma_l^-\rho\sigma_l^+ - \{\sigma_l^+\sigma_l^-, \rho\}\Big) \\ &+ \frac{\nu_{ij}}{2}\Big(2\sigma_i^+\rho\sigma_j^- - \{\sigma_i^-\sigma_j^+, \rho\}\Big). \end{aligned} \tag{6.11}$$

$$\text{with } \Gamma = \begin{bmatrix} \Gamma_a & \Gamma_{ac}(R) \\ \Gamma_{ac}(R) & \Gamma_c \end{bmatrix} \text{ and } \nu = \begin{bmatrix} \nu_a & \nu_{ac} \\ \nu_{ac} & \nu_c \end{bmatrix}.$$

The two single excitation eigenstates of H, denoted as

$$|\pm\rangle = (|01\rangle \pm |10\rangle)/\sqrt{2}, \tag{6.12}$$

have energies $E_\pm = \hbar(\omega \pm \Omega)$. While for N=1 the energy eigenstates directly correspond to the most dark and bright superposition states with respect to decay, for $N > 1$ the states $|\pm\rangle$ are not eigenstates of the decay matrix Γ. The most bright $|B\rangle$ and dark states $|D\rangle$ are given by

$$|B\rangle = (c_- |10\rangle + |01\rangle)/\mathcal{N}_- \tag{6.13}$$

$$|D\rangle = (c_+ |10\rangle + |01\rangle)/\mathcal{N}_+. \tag{6.14}$$

where $c_\pm = (\Gamma_a - \Gamma_c \mp \sqrt{\Gamma_a^2 - 2\Gamma_a\Gamma_c + \Gamma_c^2 + 4\Gamma_{ac}})/2\Gamma_{ac}$ and $\mathcal{N}_\pm$ is a normalisation constant. Hence, for a large effective antenna ring atom number N, where $c_+ \ll 1$, the dark state $|D\rangle$ carries most excitation within the center atom. Hence it possesses a large decay rate to the target loss state $|T\rangle$ without much loss to free space. This properties play a key role in the absorption and energy loss dynamics of our coupled toy system as outlined below.

In order to study the light absorption in the system we can prepare it in state $|G\rangle = |00\rangle$ and simply calculate the population transfer to the final state $|T\rangle$ for various excitation an decay scenarios for a given short illumination time. Let as first start with incoherent excitation in the weak excitation regime. Here we look at three generic cases of excitation, but pumping (a) only the strong effective dipole or (b) only the center (weak) dipole and alternatively (c) collective driving of both dipoles simultaneously. Typical absorption cases are shown in Fig.6.10. We clearly see that increasing the dipole moment of the antenna dipole leads to much faster population accumulation in the center absorber = receiver atom. At the same time we note that for increased relative strength of the antenna the difference between collective pumping of both dipoles or only exciting the large antenna dipole diminishes. When we relax the energy resonance condition between antenna and receiver dipole, we see pronounced differences between the three cases. In particular for selective incoherent pumping of the antenna the energy transfer to the center is resonantly enhanced at suitable receiver atom energy shift. Here the range of useful detunings gets larger with closer spacing of the receiver to the antenna. Note that as we simply assume incoherent antenna excitation the observed resonance is connected to resonant energy transfer and not to selective excitation. As expected, a more complex and interesting behavior appears for driving with a coherent field with tunable frequency. Again we study the population transferred to the center trap state after a given illumination time as function of the excitation laser frequency for different effective ring dipole strengths and the two cases of antenna or collective excitation. We see two absorption maxima at the energies of the two coupled eigenstates $|\pm\rangle$. The magnitude, splitting and width of the component increases with antenna dipole magnitude. We see that a larger antenna dipole moment leads to a strongly broadened absorption line with a reduced maximum. Note that in course of this transfer the antenna dipole is only weakly excited and population dominantly accumulates in the dark state. Interestingly,

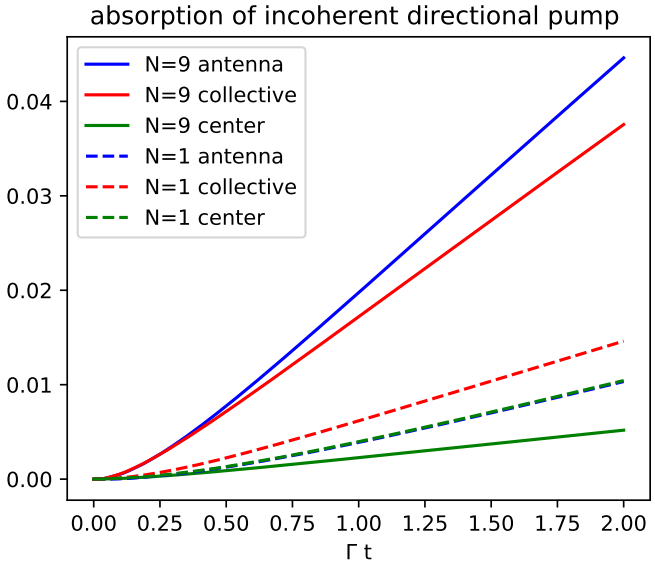

Figure 6.9: Target state population as function of time Γt for incoherent collective excitation of the effective antenna atom only, the center atom only or both, where the ring is replaced by an effective single dipole of strength $\mu_{eff} = 1 * \mu$ (dashed lines) and strength $\mu_{eff} = \sqrt{9}\mu$ (solid lines). For pump and impurity loss rate we have chosen $\nu = 0.01\Gamma$ and $\Gamma_T = 3\Gamma$.

the total area of the spectrum increases with growing antenna dipole moment up to a value of about $N \approx 10$. Hence a nine atom ring as it appears in biological structures seem to be close to the optimum for a given amount of material. We see that a larger antenna dipole significantly enhances the final trap state population. This enhancement is surprisingly stable against laser phase fluctuations (laser bandwidth). While for small antenna dipoles selective pumping of the antenna only clearly is favorable, the difference gets smaller for larger antenna dipoles. Again a value of $N = 9$ already captures most of the enhancement and further increase of the antenna dipole only adds minor gain. Let us remark here that for collective coherent driving, secondary absorption maxima appear at larger distances of about $R \approx 0.75\lambda$.

Finally we come back to the large bandwidth driving limit, where we can replace coherent excitation simply by transition rates. Again we compare antenna and collective excitation and vary the distance. We see that for equal excitation rates, transfer is strongly enhanced at short distances and unequal dipole moments. Similar as above, antenna only driving is generally more effective but the difference gets insignificant at about $N \approx 10$ ring dipoles. Hence overall, splitting a light absorbing structure into a strong antenna system and a dedicated energy receiver, as also seems present in biological systems, has several generic benefits.

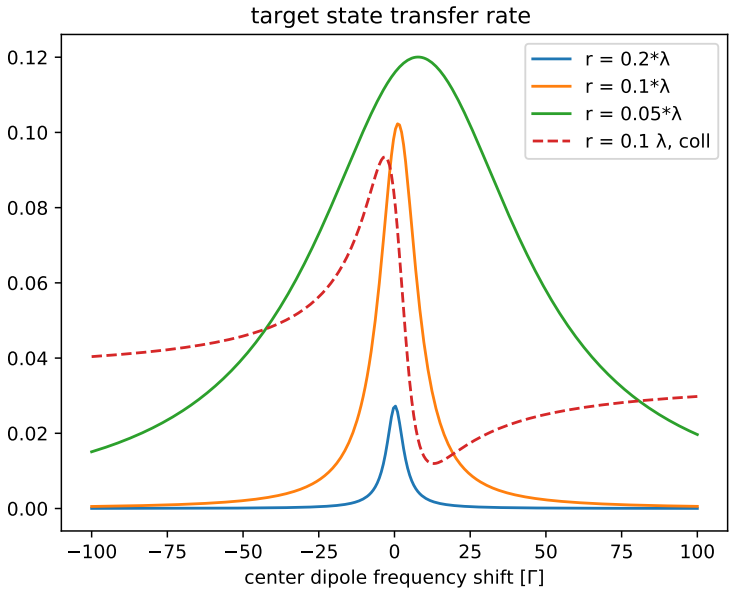

Figure 6.10: Target state population transfer rate as function of relative center dipole resonance frequency shift for weak incoherent antenna atom excitation and effective dipole strength of $\sqrt{9}\mu$ (solid lines) for three dipole distances $r = (0.2, 0.1, 0.05)$. We see a strong increase of the resonant transfer for shorter antenna - receiver distances. For comparison collective pumping of both dipoles at the intermediate distance shows regions of enhancement and suppression of transfer efficiency (dashed line).

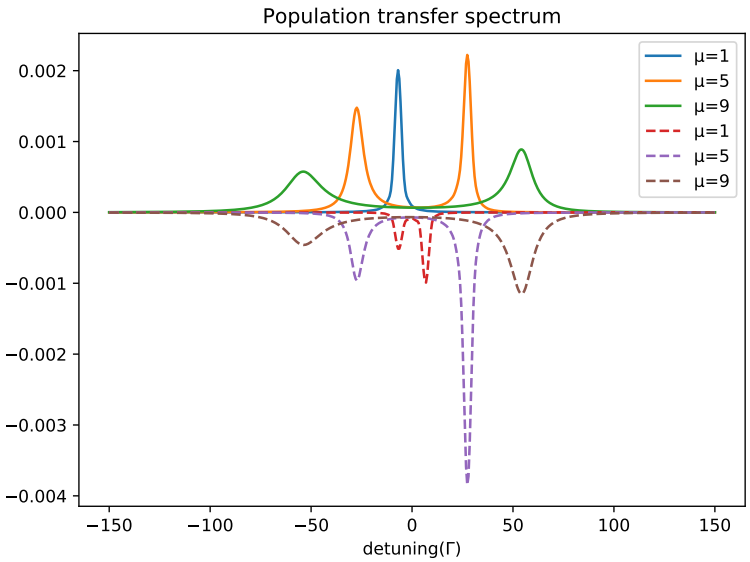

Figure 6.11: Frequency dependence of coherent pump induced population transfer to target state for collective excitation (solid lines) and selective antenna excitation (dashed lines plotted with sign changed for better visibilty) for different effective antenna dipole moments.

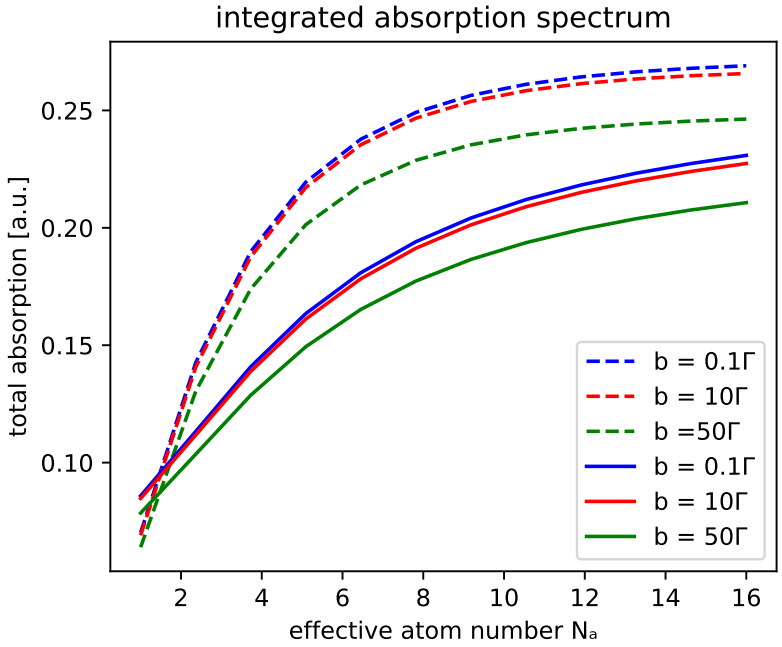

Figure 6.12: Integrated area of absorption spectrum [a.u.] as function of antenna dipole moment μ for different laser bandwidths comparing antenna pumping (dashed lines) and collective pumping (solid lines). We used $\Gamma_T = \Gamma$ and $\Omega = 0.1\Gamma$.

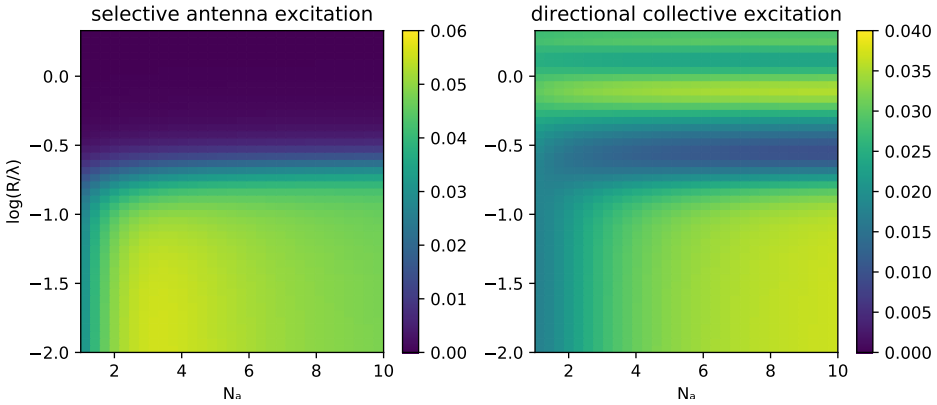

Figure 6.13: Fraction transferred to target state after a fixed short illumination time for incoherent broadband light as function of antenna dipole moment μ and antenna to absorber distance comparing selective antenna pumping (left) and collective pumping (right)

7 Publication

Physical Review Letters **129**(253601), (2022)

Control of Localized Single- and Many-Body Dark States in Waveguide QED

R. Holzinger[1], R. Gutierrez-Jauregui[3], T. Hönigl-Decrinis[2], G. Kirchmair[2], A. Asenjo-Garcia[3] and H. Ritsch[1]

[1]*Institut für Theoretische Physik, Universität Innsbruck, Technikerstrasse 21, A-6020 Innsbruck, Austria*
[2]*Institute for Quantum Optics and Quantum Information of the Austrian Academy of Sciences, Technikerstrasse 21, A-6020 Innsbruck, Austria*
[3]*Department of Physics, Columbia University, New York, NY 10027, USA*

Subradiant states in a finite chain of two-level quantum emitters coupled to a one-dimensional reservoir are a resource for superior photon storage and their controlled release. As one can maximally store one energy quantum per emitter, storing multiple excitations requires delocalized states, which typically exhibit fermionic correlations and anti-symmetric wavefunctions, thus making them hard to access experimentally. Here we identify a new class of quasi-localized dark states with up to half of the qubits excited, which only appear for lattice constants of an integer multiple of the wavelength. These states allow for a high-fidelity preparation and minimally invasive read out in state-of-the-art setups. In particular, we suggest an experimental implementation using a coplanar waveguide coupled to superconducting transmon qubits on a chip. With minimal free space and intrinsic losses, virtually perfect dark states can be achieved for a low number of qubits featuring fast preparation and precise manipulation.

DOI: 10.1103/PhysRevLett.129.253601

7.1 Introduction

Collective excitation states of ensembles of quantum emitters possess several surprising and long-sought physical properties. Typically, excitations are delocalized and lost dissipatively to the environment at rates that vary over many orders of magnitude. Of

particular interest are states with long lifetimes. These dark—or subradiant—states can be used to implement extremely efficient quantum memories [205, 206], lossless transport of excitations [207, 208], photon-photon gates [209], future generations of atomic lattice clocks [210, 211] and improve quantum sensing. Recently, applications towards building superior single photon antennas [212] or nanoscopic coherent or non-classical light sources based on dark resonances have been proposed [213]. In most cases, studies and experiments on subradiance focus on manipulating a single excitation only, i.e., they limit their scope to the lowest Dicke manifold [213–225]. Many-body multiple excitation subradiant states have attracted some interest only recently, but in general the preparation and manipulation of such states remains challenging as they are typically very delocalized. One option is to use more complex atomic emitters with several internal excited states. This allows to store several photons in a dark subspace, but they are tied to multipartite entanglement, which is fragile in general [226–231]. For a chain of qubits coupled to a waveguide, dark states within the two-excitation manifold have been classified into fermionic, dimerized or edge states among others [232–246]. Experimental preparation and control of such states remains challenging and only quite recently the two-excitation manifold was probed experimentally with superconducting transmon qubits [247].

In this work, we theoretically predict a new type of many-body dark states for arrays of qubits coupled to a 1D bath. These states emerge when the lattice constant is an integer of the guided mode wavelength and are distinguished by strongly localized excitations. The states are built from antisymmetric superpositions of symmetric states, whose decay into the bath is forbidden due to destructive interference [35]. For instance, we find that a large fraction $2(N-3)/(N-2)$ of two excitations stored in an N qubit array settles in just two qubits, while a small fraction spreads along the remaining qubits to inhibit decay [see Fig. 10.1(c)]. We show below an analytical description for these states and characterize their spatial correlations. We study spectral signatures of photon transport in the presence of these states. From these findings, we propose a realistic protocol to store and release microwave photons in a controlled fashion. Our work should lead to multiple opportunities within atomic physics and quantum optics, such as multi-photon memories for quantum repeaters, and unlock rich phenomena in ordered systems of long-range interacting quantum emitters, both in the linear and quantum many-body regimes. We also note that the high-fidelity preparation protocol presented here may inspire experimental confirmation and further the understanding of many-body subradiant states.

7.2 Model

Consider an array of N qubits resonantly coupled to the modes of a waveguide as illustrated in Fig. 10.1. Each qubit has two internal states $|e_m\rangle$ and $|g_m\rangle$ separated by a transition frequency ω_0 and is characterized by its position x_m. The waveguide mediates the qubit-qubit interactions and acts as a source of dissipation. With the

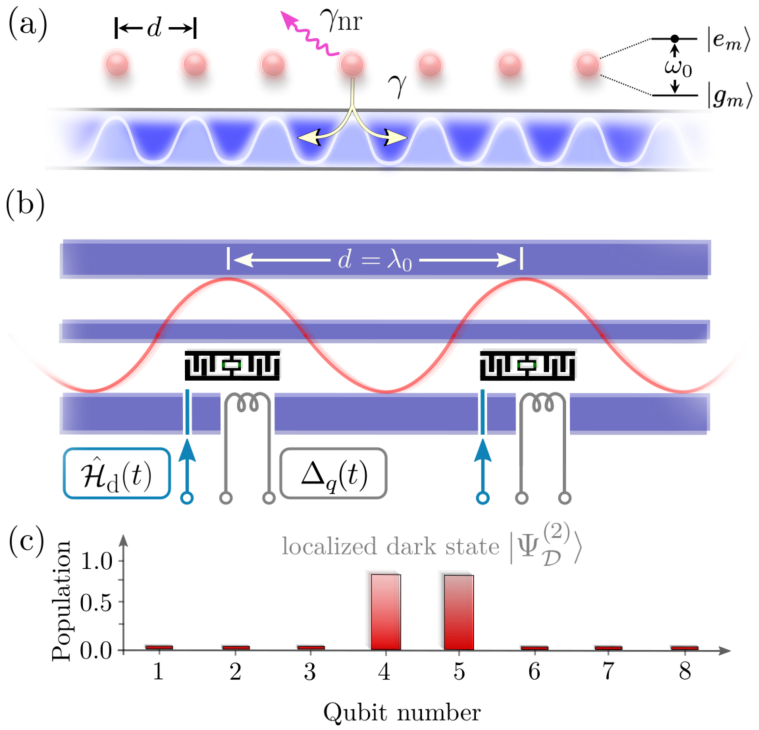

Figure 7.1: (a) Schematics of a regular chain of qubits coupled to a 1D waveguide with photon-mediated interactions determined by the single-qubit decay rates γ. For qubits separated by integer multiples of the wavelength λ_0, a degenerate family of non-radiative dark states forms, which are only subject to very small free space decay and non-radiative losses $\gamma_{\rm nr}$. (b) Waveguide QED realization with superconducting circuits: transmons (in black) are coupled to a coplanar waveguide (in blue). The individual qubit frequencies and thus effectively their distance d can be tuned in-situ via flux-bias lines. For the preparation and read-out of dark states, local driving pulses $\hat{\mathcal{H}}_{\rm d}(t)$ and local detuning control $\Delta_{\rm q}(t)$ are applied via separate control lines. (c) Distribution of the excited state population for $N = 8$ qubits for a localized two-excitation dark state $|\Psi^{(2)}_{\mathcal{D}}\rangle$ as described by Eq. (7.7). Two qubits store a large fraction $2(N-3)/(N-2)$ of the excitation energy.

inclusion of spontaneous emission into the waveguide and assuming that ω_0 is well below the cutoff frequency of the waveguide, the master equation for the density operator of the array $\hat{\rho}$ reads [35, 36] $\dot{\hat{\rho}} = -i\left(\hat{\mathcal{H}}_{\rm eff}\hat{\rho} - \hat{\rho}\hat{\mathcal{H}}^{\dagger}_{\rm eff}\right) + \sum_{m,n}\gamma_{m,n}\hat{\sigma}_m\hat{\rho}\hat{\sigma}^{\dagger}_n$, where $\hat{\mathcal{H}}_{\rm eff}$ is the collective Hamiltonian ($\hbar = 1$)

$$\hat{\mathcal{H}}_{\rm eff} = \sum_{m,n=1}^{N}\left(J_{m,n} - i\frac{\gamma_{m,n}}{2}\right)\hat{\sigma}^{\dagger}_m\hat{\sigma}_n\,, \tag{7.1}$$

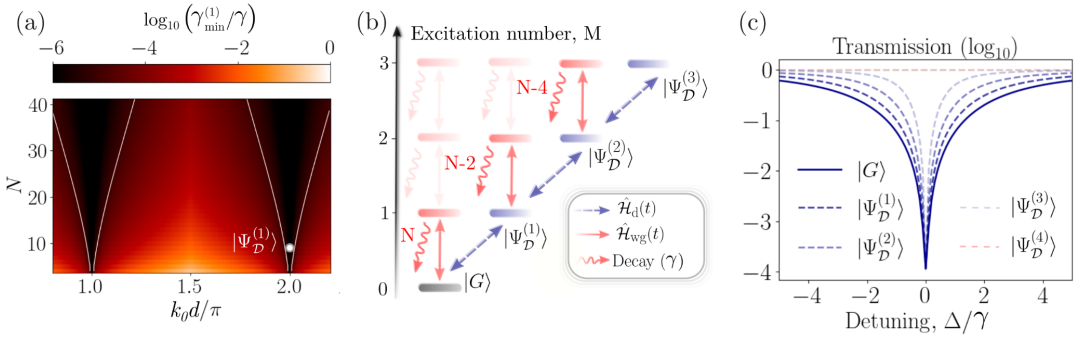

Figure 7.2: (a) Minimal decay rate $\gamma^{(1)}_{\rm min}$ within the single-excitation manifold as a function of qubit number and separation d for lossless qubits with $\gamma_{\rm nr} = 0$. Continuous white lines enclose regions of strong collective subradiance, where $\gamma^{(1)}_{\rm min}/\gamma \leq 10^{-5}$. The example of Eq. (7.3) is indicated with a white dot for $N = 8$ qubits. (b) Assuming M qubits are driven individually, we show the energy level diagram indicating the route towards dark state preparation and probing with coupling to $|\Psi^{(M)}_{\mathcal{D}}\rangle$ facilitated by a coherent drive $\hat{\mathcal{H}}_{\rm d}(t)$. Once $|\Psi^{(M)}_{\mathcal{D}}\rangle$ is prepared a second field sent through the waveguide, as described by $\hat{\mathcal{H}}_{\rm wg}(t)$ in Eq. (7.6), transfers the state outside the dark manifold, from where it decays with rate $(N-2M)\gamma$. (c) Weak field waveguide transmission as a function of probe frequency tuned across the single qubit resonance frequency ω_0 for a 8-qubit chain in the ground state (solid line) and the single- to four-excitation dark states (dashed lines). The blockade window decreases from the linewidth $N\gamma$ of the symmetric single-excitation state towards $(N-2M)\gamma$ for the M-excitation dark state and disappears for the four-excitation dark state showing complete transmission.

composed of lowering operators $\hat{\sigma}_m = |g_m\rangle\langle e_m|$ and interaction terms $J_{m,n} = (\gamma/2)\sin k_0|x_m - x_n|$ and $\gamma_{m,n} = \gamma\cos k_0|x_m - x_n|$. The interaction is weighted by the individual decay rate γ while the qubit separation by $k_0 = \omega_0/c$, the wavevector of the guided mode on resonance with the qubits. For qubit separation $d = n\lambda_0$ with $n \in \mathbb{N}^+$, the coherent exchange rates $J_{m,n}$ are zero and there is only collective dissipation $\gamma_{m,n}$.

We are interested in localized dark states $|\Psi^{(M)}_{\mathcal{D}}\rangle$ storing M excitations. To construct such states, we divide the chain into two parts of M and $N-M$ qubits, respectively. The precise position of the qubits is not relevant for this division and without losing generality we define the collective operators $\mathcal{S}_1 = \sum_{j=1}^{M}\hat{\sigma}_j/\sqrt{M}$ and $\mathcal{S}_2 = \sum_{j=M+1}^{N}\hat{\sigma}_j/\sqrt{N-M}$ to act over each part. The effective Hamiltonian for

$d = n\lambda_0$ within this division reads

$$\hat{\mathcal{H}}_{\text{eff}} = -\frac{iM\gamma}{2}\mathcal{S}_1^\dagger\mathcal{S}_1 - \frac{i(N-M)\gamma}{2}\mathcal{S}_2^\dagger\mathcal{S}_2 - i\Gamma(\mathcal{S}_1^\dagger\mathcal{S}_2 + \mathcal{S}_2^\dagger\mathcal{S}_1). \tag{7.2}$$

The last term shows that the symmetric superpositions of the two parts are dissipatively coupled by the enhanced rate $2\Gamma = \sqrt{M(N-M)}\gamma$. A similar division can be done for odd multiples of $\lambda_0/2$ separations with the symmetric operators now replaced with anti-symmetric operators, having alternate signs between consecutive qubits. The division is a formal one, but our results can be generalized to non-identical couplings as shown in the Supplementary Information. In particular, if we assume that the first qubits decay with a rate γ_1 while the remaining decay with γ_2 the localization is enhanced. That is, a higher fraction of the excited state population is concentrated in the first qubits. The effects of impurities as non-radiative energy loss γ_{nr} and dephasing γ_ϕ are also explored in the SI.

Single Excitation.— Qubits decay into the waveguide via collective channels determined by the eigenstates of the effective Hamiltonian. The decay rates depend on qubit number N and lattice spacing d, as shown in Fig. 7.2(a) for the slowest decay rate of a single excitation. While in general this rate is suppressed with increasing qubit number – following a N^{-3} scaling [233] – this is not the case for spacing $k_0 d = n\pi$. In the so-called "mirror configuration" (with $d = n\lambda_0$), there is only one bright state, $|\Psi_{\mathcal{S}}^{(1)}\rangle = \sum_j^N \hat{\sigma}_j^\dagger|G\rangle/\sqrt{N}$ where $|G\rangle = |g\rangle^{\otimes N}$, and $(N-1)$ perfectly dark states of exactly zero decay rate. Leveraging the degeneracy of the dark manifold, one can build highly-localized dark states. Consider the state

$$|\Psi_{\mathcal{D}}^{(1)}\rangle = \frac{1}{\sqrt{N}}\Big(\sqrt{N-1}\hat{\sigma}_1^\dagger - \mathcal{S}_2^\dagger\Big)|G\rangle, \tag{7.3}$$

composed of the normalized sum of $|\Psi_m\rangle = 1/\sqrt{2}(\hat{\sigma}_1^\dagger - \hat{\sigma}_m^\dagger)|G\rangle$ states, which span the $N-1$ dark subspace. The operator $\mathcal{S}_2$ is defined in the model section. The dark state displays the unique feature that a large fraction $\langle\hat{\sigma}_1^\dagger\hat{\sigma}_1\rangle = 1 - 1/N$ of the excited state population is concentrated in the first qubit. By increasing the system size, the excitation is mostly stored in the first qubit while being protected from decay by a vanishing amount spread in the remaining qubits. The absence of coherent exchange interaction is crucial in so far as it would introduce unwanted couplings between bright and dark states.

7.3 Dark state preparation and probing

The choice to store an excitation in the first qubit is not unique and any other qubit is equally valid [248]. The dark state $|\Psi_{\mathcal{D}}^{(1)}\rangle$, however, can be efficiently prepared by introducing an external coherent drive on resonance with qubits and localized on the first qubit. This pulsed drive couples to the chain via $\hat{\mathcal{H}}_{\text{d}}(t) = \Omega_{\text{d}}(t)(\hat{\sigma}_1^\dagger + \hat{\sigma}_1)$ where

$\Omega_\mathrm{d}(t)$ is a time-dependent Rabi frequency. It connects the ground state to both bright and dark states with asymmetrical coupling strengths

$$\langle \Psi_{\mathcal{S}}^{(1)} | \hat{\mathcal{H}}_\mathrm{d}(t) | G \rangle = \Omega_\mathrm{d}(t) \sqrt{1/N}, \tag{7.4}$$

$$\langle \Psi_{\mathcal{D}}^{(1)} | \hat{\mathcal{H}}_\mathrm{d}(t) | G \rangle = \Omega_\mathrm{d}(t) \sqrt{1 - 1/N}, \tag{7.5}$$

thus coupling to the dark state with high fidelity in the $N \gg 1$ limit. The drive not only prepares single-excitation dark states but also connects dark states along the excitation ladder through paths illustrated in Fig. 7.2(b). These paths continue until half of the qubits are excited and there are no more dark states [240]. To probe the

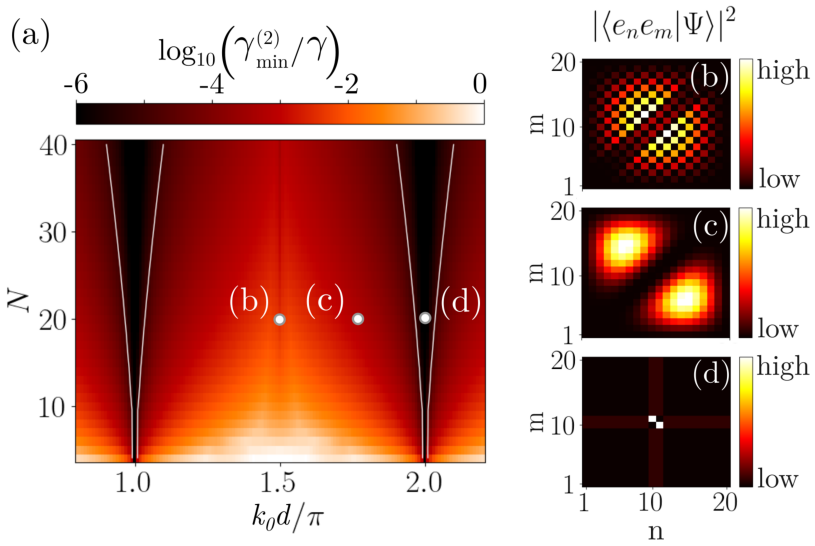

Figure 7.3: (a) Minimal decay rate $\gamma^{(2)}_{\mathrm{min}}$ within the second excitation manifold as a function of chain size N and qubit separation d. The continuous white lines enclose the regions where $\gamma^{(2)}_{\mathrm{min}}/\gamma \leq 10^{-5}$. The subradiant states generally exhibit non trivial spatial correlations $|\langle e_n e_m|\Psi\rangle|^2$, which renders them challenging to access. For $k_0 d = (2n+1)\pi/2$ with $n \in \mathbb{N}$ a checkerboard pattern emerges in (b) whereas in (c) a typical fermionic occupation is shown, which is shared by most subradiant states. In (d) the dark state $|\Psi^{(2)}_{\mathcal{D}}\rangle$, of Eq. (7.7), is shown for $k_0 d = 2n\pi$ with two excitations localized in the center of the array.

dark states we use a second, weak driving field ($\Omega_\mathrm{wg}(t)/\gamma \ll 1$). The field propagates along the waveguide and couples to the qubits through

$$\hat{\mathcal{H}}_\mathrm{wg}(t) = \sum_{j=1}^{N} \left(\Delta_\mathrm{wg} \hat{\sigma}_j^\dagger \hat{\sigma}_j + \Omega_\mathrm{wg}(t)(\hat{\sigma}_j^\dagger + \hat{\sigma}_j) \right). \tag{7.6}$$

Notice there is no phase pick-up between the qubits due to the $n\lambda_0$ separation. This probe connects dark and bright states through paths shown in Fig. 7.2(b). It then

opens a window into the dark states by measuring the field $\hat{E} = \hat{E}_{\rm in} + i\sqrt{\gamma/2}\sum_j \hat{\sigma}_j$ composed from the superposition of probe and fields scattered into the waveguide. Figure 7.2(c) shows the transmission $\langle \hat{E}^\dagger \hat{E}\rangle / \langle \hat{E}_{\rm in}^\dagger \hat{E}_{\rm in}\rangle$ for different initial states. An 8-qubit chain is probed by a rectangular waveguide pulse of duration $t\gamma = 50$ during which the transmitted field is recorded using the master equation accounting for multiple excitations [214]. We begin with N qubits in the ground state where the transmission linewidth is $N\gamma$, corresponding to the symmetric state $|\Psi_{\mathcal{S}}^{(1)}\rangle$ excited by the probe. For the qubits prepared in the Mth excitation dark state the transmission linewidth is reduced to $(N-2M)\gamma$ [248]. For a single excitation, with $N <= 3$, the probe excites $\hat{\mathcal{H}}_{\rm wg}(t)|\Psi_{\mathcal{D}}^{(1)}\rangle \propto |\Psi^{(2)}\rangle$, with $|\Psi^{(2)}\rangle \propto ((N-2)\sigma_1^\dagger - \sqrt{N-1}\mathcal{S}_2^\dagger)\ \mathcal{S}_2^\dagger|G\rangle$. For $M = N/2$ the waveguide drive is orthogonal to the dark state and therefore renders the system completely transparent. In this way the two-excitation manifold is utilized to escape the decoherence-free subspace and probe the preparation of the dark state [247]. Note that we assume the ideal case without imperfections and positional disorder, which would lead to a finite lifetime of the dark state and a higher overall transmission, treated in the SI [248].

7.4 Multiple Excitations

The localized dark states for multiple excitations are written explicitly in the SI [248]. For simplicity, we focus on the two-excitation subspace of Eq. (7.2), where the Hilbert space is spanned by states $|e_n e_m\rangle = \hat{\sigma}_n^\dagger \hat{\sigma}_m^\dagger |G\rangle$. In general, the most superradiant two-excitation state can be written as $|\Psi_{\mathcal{S}}^{(2)}\rangle \propto \sum_{j<k} \hat{\sigma}_j^\dagger \hat{\sigma}_k^\dagger |G\rangle$ and decay with a rate $2(N-1)\gamma$. By contrast, for $k_0 d = n\pi$, a completely dark state is

$$|\Psi_{\mathcal{D}}^{(2)}\rangle = \frac{\sqrt{N-3}}{\sqrt{N-1}}\left((\mathcal{S}_1^\dagger)^2 - \frac{\sqrt{2}\mathcal{S}_1^\dagger \mathcal{S}_2^\dagger}{\sqrt{N-2}} + \frac{(\mathcal{S}_2^\dagger)^2}{N-3}\right)|G\rangle, \tag{7.7}$$

where a fraction $2(N-3)/(N-2)$ of the excitations is stored in the first two qubits with $\mathcal{S}_{1,2}$ defined above Eq. (7.2).

Subradiant states for two excitations are illustrated in Fig. 7.3. Figure 7.3(a) shows the minimal decay rate $\gamma_{\rm min}^{(2)}$ as a function of qubit number N and relative distance d. The decay rate changes with lattice constant and signals different types of dark states with qualitatively different spatial correlations $|\langle e_n e_m|\Psi\rangle|^2$, as shown in Figs. 7.3(b)-(d). For $k_0 d = (2n+1)\pi/2$ with $n \in \mathbb{N}$, correlations display a checkerboard-type pattern [233] due to the fact that coherent nearest-neighbor and dissipative next-nearest-neighbour interactions in Eq. (9.4) are zero. Figure 7.3(c) shows a typical state, described by a fermionic ansatz, where two-excitation states are composed of single-excitation subradiant states, as commonly found for multiple excitations [205, 232]. For a large number of qubits, $N50$ and $k_0 d = (6n-1)\pi/6$, another extremely subradiant two-excitation state emerges with dimerized spatial

correlations and a decay rate lower than any fermionic-type state [235]. These extended states are to be compared with Fig. 7.3(d), where the dark state $|\Psi_{\mathcal{D}}^{(2)}\rangle$ of Eq. (7.7) with $k_0 d = 2\pi n$ is shown for a 20-qubit chain. The spatial correlations of the dark state lead to easily accessible preparation as opposed to most other subradiant states with non-trivial spatial correlations. For instance, a (local) coherent drive with Rabi frequency $\Omega_{\mathrm{d}}(t)$ exciting two of the qubits drives the dark state with strength $\Omega_{\mathrm{d}}(t)\sqrt{N-3}/\sqrt{N-1}$ and subsequently a waveguide drive can be used to probe the preparation of the dark state, see also Fig. 7.2(b).

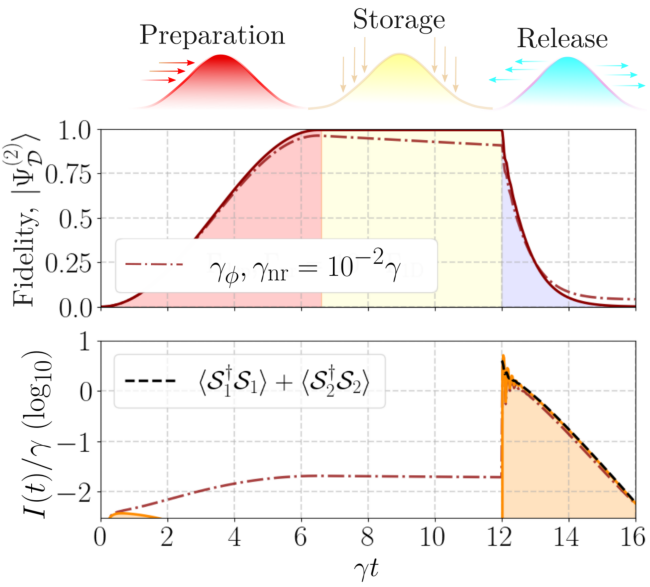

Figure 7.4: Protocol to prepare, store, and release two excitations using a chain of 16 qubits separated a distance $d = \lambda_0$. (a) A π-pulse drives the first two qubits into the dark state $|\Psi_{\mathcal{D}}^{(2)}\rangle$ where excitations are stored until $\gamma t = 12$, when they are released via a superradiant channel created by quickly detuning the last $N-2$ qubits by $\Delta_{\mathrm{q}} = 50\gamma$. (b) Fidelity $F = \langle \Psi_{\mathcal{D}}^{(2)} | \rho | \Psi_{\mathcal{D}}^{(2)} \rangle$ to prepare the dark state for an ideal case (solid line) compared to a case with dephasing and non-radiative damping $\gamma_{\mathrm{dep}}, \gamma_{\mathrm{nr}} = 10^{-2}\gamma$ (dashed-dotted). (c) The field radiated into the waveguide displays a sharp peak in intensity $I(t) = \langle \hat{E}^\dagger \hat{E} \rangle(t)$ after release and negligible values during preparation and storage. A beating in intesity appears as the excitation oscillates between initial and final qubits during release [see $\hat{\mathcal{S}}_{1,2}$ in Eq. (7.2)]. Emission with (dashed-dotted) and without interference term $2\mathrm{Re}\langle \mathcal{S}_1^\dagger \mathcal{S}_2 \rangle$ (black dashed). Here, the π-pulse has a Gaussian temporal profile of duration 8γ at FWHM and reaches a peak Rabi frequency 0.25γ at $t_0 = 3\gamma^{-1}$.

Two-Photon Storage and Release.—Building on the above results we establish a simple protocol for storing and releasing two excitations into a waveguide. The protocol starts with N qubits in the ground state that are driven into the dark state $|\Psi_{\mathcal{D}}^{(2)}\rangle$ by a coherent pulse on the first two qubits. The two excitations remain stored for a time τ after which the last $N-2$ qubits are detuned by $\Delta_{\mathrm{q}}(N-2)\gamma$ to transfer most of the two excitations into the product state $|e_1e_2\rangle$. This is illustrated in Fig. 7.4 for a 16-qubit chain with and without imperfections. The coherent drive $\hat{\mathcal{H}}_{\mathrm{d}}(t) = \Omega_{\mathrm{d}}(t)(\hat{\sigma}_1^\dagger + \hat{\sigma}_2^\dagger + h.c.)$ prepares the state $|\Psi_{\mathcal{D}}^{(2)}\rangle$. Then, at $\gamma t = 12$, the last 14 qubits are detuned by $\Delta_{\mathrm{q}} = 50\gamma$ from the resonance frequency ω_0 to initiate the decay of excitations. The radiated intensity $I(t) = \langle \hat{E}^\dagger \hat{E}\rangle(t)$, equivalently expressed as $\langle \mathcal{S}_1^\dagger \mathcal{S}_1\rangle + \langle \mathcal{S}_2^\dagger \mathcal{S}_2\rangle + 2\mathrm{Re}\langle \mathcal{S}_1^\dagger \mathcal{S}_2\rangle$ is negligible until a sharp pulse of emission appears after the detuning is turned on.

7.5 Superconducting circuit implementation

Due to near-perfect mode matching, superconducting qubits in a 1D transmission line [214, 249–251] are an ideal platform for realizing these ideas. Here, we focus on the implementation with transmon qubits capacitively coupled to a common coplanar waveguide as shown schematically in Fig. 10.1(c). Similar to Ref. [252], the distance d between the qubits on chip is fixed but changing the frequency at which the transmon qubits emit effectively changes their separation. This ensures that we can satisfy $d \sim \lambda_0$, as well as tune qubits on and off resonance via on-chip flux lines. Weakly-coupled control lines realize the drive $\hat{\mathcal{H}}_{\mathrm{d}}(t)$ and allow to selectively excite the single qubits respectivley in-situ, and thus prepare dark states [247]. Non-radiative decay rates γ_{nr} and dephasing rates γ_ϕ for superconducting qubits are usually multiple orders of magnitude smaller than typical couplings to the waveguide γ, see the SI [248]. The achievable parameters are easily sufficient to realize the protocol demonstrated in Fig. 7.4 with $\sim 99\%$ fidelity for the dark state preparation.

7.6 Conclusions

Motivated by state of the art implementations of waveguide-coupled superconducting qubits, we introduced and studied a theoretical model of the properties and excitation pathways of multi-excitation dark states. Due to the symmetry and (practically infinite-range) all to all coupling, such system possesses almost degenereate manifolds of multi-excitation states radiatively decoupled from the waveguide if the qubits are positioned at wavelength distance. These states allow to absorb and store multiple photons simultaneously [248], while localizing the majority of the excitation energy in just a handful of qubits. This contrasts with typical free space subradiant states, where each excitation is maximally delocalized. Their localized nature facilitates the preparation of these states via local addressing of individual qubits, which is currently

available in state of the art implementations. The system and the proposed protocol also allows for controlled storage and release of multiple photons into the waveguide, pointing towards possible applications for non-classical multi-photon sources or a tailored memory for a quantum repeater. As the projected numbers for experimental realizations seem favorable, we expect to inspire efforts in various quantum simulation platforms including superconducting circuits or Rydberg arrays [211, 253]. Similarly, optical waveguide systems [218] and atoms, which are tweezer trapped in optical resonators [254], can be envisaged as an alternative setup.

R.H. and H.R. acknowledge funding from the Austrian Science Fund (FWF) doctoral college DK-ALM W1259-N27 and the FET OPEN Network Cryst3 funded by the European Union (EU) via Horizon 2020. T. H-D. acknowledges financial support from the Lise Meitner programme of the Austrian Science Fund (FWF), project M3347. AAG gratefully acknowledges support from the Air Force Office of Scientific Research through their Young Investigator Prize (grant No. 21RT0751), the National Science Foundation through their CAREER Award (No. 2047380), the A. P. Sloan foundation, and the David and Lucile Packard foundation. G.K. acknowledges funding by the European Research Council (ERC) under the European Union's Horizon 2020 research and innovation program (714235).

7.7 Supplemental material

7.7.1 Master Equation Derivation

In this Appendix, we present the approximations used to derive the superradiant master equation, the theoretical starting point for our work. The derivation is standard and follows from the conventional picture of a system coupled linearly to a one-dimensional bath formed of harmonic oscillators [28, 29].

The evolution of bath and system is described by the Hamiltonian

$$\begin{aligned}
\mathcal{H} &= \mathcal{H}_\mathrm{b} + \mathcal{H}_\mathrm{s} + \mathcal{H}_\mathrm{int}\,, \\
\mathcal{H}_\mathrm{b} &= \hbar \sum_s \int_0^\infty d\omega \omega b_s^\dagger(\omega) b_s^\dagger(\omega)\,, \\
\mathcal{H}_\mathrm{int} &= \hbar \sum_{n,s} \int d\omega \lambda_{n,s}(\omega) \left(b_s(\omega) + b_s^\dagger(\omega)\right)\left(c_n + c_n^\dagger\right)\,,
\end{aligned} \tag{7.8}$$

where $b_s(\omega)$ are boson annihilation operators for bath modes of frequency ω propagating along the $s = \pm$ directions, and c_n are system operators for the nth qubit. The coupling strength $\lambda_{n,s}(\omega)$ depends on the field amplitude evaluated at the qubit position x_n, with $\lambda_{n,s}(\omega) \propto \exp[-is\omega x_n/c]$. This rather general coupling can accurately describe atoms coupled to an electromagnetic environment under the electric dipole approximation or transmon qubits capacitively coupled to a transmission line. We restrict to the

two-level approximation where system operators become $\hat{c}_n = \hat{\sigma}_n$ and the system Hamiltonian is

$$\mathcal{H}_{\rm s} = \sum_n \omega_0 \sigma_n^\dagger \sigma_n \,. \tag{7.9}$$

In an interaction picture with respect to the free Hamiltonians $\mathcal{H}_{\rm b}$ and $\mathcal{H}_{\rm s}$ the density operator for bath plus system $\chi(t)$ follows the equation $i\hbar\dot{\tilde{\chi}} = [\tilde{\mathcal{H}}_{\rm int}, \tilde{\chi}]$. This differential equation gives way to an integral equation

$$i\hbar\dot{\rho} = -\frac{1}{\hbar^2}\int_0^t d\tau [\tilde{\mathcal{H}}_{\rm int}(t), [\tilde{\mathcal{H}}_{\rm int}(t-\tau), \tilde{\chi}(t-\tau)]] \tag{7.10}$$

where bath variables have been traced out to obtain the density matrix of the array ρ. In writting Eq. (7.10) we have assumed that system and bath are uncorrelated at an initial time.

Equation (7.10) describes the self-consistent evolution of system and bath, it thus accounting for the correlations that rise between the two. The description can be simplified for a large bath weakly coupled to the qubits $\omega_0 \gg \lambda_{n,s}(\omega_0)$ and with a smooth frequcy spectrum around the qubit resonance frequency. Futher simplification follows if we consider that the array is sufficiently small so that the only changes in a qubit as a free bath mode propagates from one end of the array to the other are given by the qubits free evolution [31, 255]. Under these conditions it is possible to make the Born-Markov approximation. This approximation neglects the correlations that arise between field and bath and sets the correlation time of the environment as the shortest time-scale of the system [28]. The upper limit in the temporal integral can be extended to infinity once this approximation has been made. After performing the temporal integral, summing over left- and right-propagating modes of the bath, and eliminating non-resonant terms under the rotating-wave approximation [256], Eq. (7.10) takes the form

$$\dot{\rho} = -i(\mathcal{H}_{\rm eff}\rho - \rho\mathcal{H}_{\rm eff}) + \sum_{n,m}\gamma\cos k_0|x_n - x_m|\sigma_m\rho\sigma_n^\dagger \,,$$

where

$$\mathcal{H}_{\rm eff} = \sum_{n,m}\tfrac{1}{2}\gamma(\sin k_0|x_n - x_m| - i\cos k_0|x_n - x_m|)\sigma_n^\dagger\sigma_m + \sum_n \Delta_{\rm rad}\sigma_n^\dagger\sigma_n \tag{7.11}$$

with decay rate $\gamma = \pi|\lambda_{n,s}(\omega_0)|^2$ and radiative frequency shift $\Delta_{\rm rad}$ [256]. By moving to an interaction picture with respect to $\Delta_{\rm rad}$ we recover Eq. (1) in the main text.

7.7.2 M-Excitation Dark State

Given a linear chain of N qubits at multiples of λ_0 separation coupled to a 1D waveguide we show the generalization of the dark state presented in the main text to

M excitations, given $M \leq N/2$. Assuming identical waveguide couplings γ for all qubits, the single- and two-excitation dark states can be extended to arbitrary excitations by using the condition that it has to be a combination of the symmetric operators $\mathcal{S}_1^\dagger = \sum_{j=1}^{M} \hat{\sigma}_j^\dagger/\sqrt{M}$ and $\mathcal{S}_2^\dagger = \sum_{j=M+1}^{N} \hat{\sigma}_j^\dagger/\sqrt{N-M}$, namely $c_k(\mathcal{S}_1^\dagger)^{M-k}(\mathcal{S}_2^\dagger)^k$, with $k \in \{0, ..., M\}$. Consequently the eigenvalue equation $\hat{\mathcal{H}}_{\text{eff}}|\Psi_{\mathcal{D}}^{(M)}\rangle = 0|\Psi_{\mathcal{D}}^{(M)}\rangle$ leads to a system of $M+1$ equations, which can be solved. Alternatively the Gram-Schmidt procedure can be applied with the initial eigenstate being the symmetric $M-$excitation eigenstate up to normalization $|\Psi_{\mathcal{S}}^{(M)}\rangle \propto (\sqrt{M}\mathcal{S}_1^\dagger + \sqrt{N-M}\mathcal{S}_2^\dagger)^M|G\rangle$ with decay rate $\gamma_{\mathcal{S}} = M(N-M+1)\gamma$. The general expression for the $M-$excitation dark state reads

$$\begin{aligned}\Big|\Psi_{\mathcal{D}}^{(M)}\Big\rangle = &\sqrt{\frac{(N-2M+1)!(N-2M)!}{(N-M+1)!(N-M)!}} \\ &\times \sum_{k=0}^{M}(-1)^k \binom{N-M-k}{M-k}\Big[\sqrt{M}\mathcal{S}_1^\dagger\Big]^{M-k}\Big[\sqrt{N-M}\mathcal{S}_2^\dagger\Big]^k \Big|G\Big\rangle. \end{aligned} \tag{7.12}$$

This is the unique dark state which involves the operators $\mathcal{S}_1$, $\mathcal{S}_2$ and is orthogonal to $|\Psi_{\mathcal{S}}^{(M)}\rangle$. The cases for $M = 1, 2$ are already shown in the main text, the dark state for $M = 3$ excitations is given by

$$\Big|\Psi_{\mathcal{D}}^{(3)}\Big\rangle = \sqrt{\frac{N-5}{N-2}}\left[\frac{\sqrt{3}(\mathcal{S}_1^\dagger)^3}{2} - \frac{3(\mathcal{S}_1^\dagger)^2\mathcal{S}_2^\dagger}{2\sqrt{N-3}} + \frac{\sqrt{3}\mathcal{S}_1^\dagger(\mathcal{S}_2^\dagger)^2}{N-4} - \frac{\sqrt{N-3}(\mathcal{S}_2^\dagger)^3}{(N-4)(N-5)}\right]\Big|G\Big\rangle. \tag{7.13}$$

Given the expression for the M-excitation dark state, the excited state population in the first M qubits is expressed as

$$\sum_{j=1}^{M}\langle\Psi_{\mathcal{D}}^{(M)}|\hat{\sigma}_j^\dagger\hat{\sigma}_j|\Psi_{\mathcal{D}}^{(M)}\rangle = \frac{N-2M+1}{N-2M+2}. \tag{7.14}$$

The choice of letting the first M qubits be excited is arbitrary as, for a qubit separation of multiples of λ_0, any M of the N qubits can be excited in order to prepare the dark state $|\Psi_{\mathcal{D}}^{(M)}\rangle$. Also, by letting the distace be odd multiples of $\lambda_0/2$, the same results as above hold, in which case the symmetric operators are replaced by anti-symmetric operators with alternating sign between consecutive qubits. One more note on the orthogonality of the single-excitation dark state $|\Psi_{\mathcal{D}}^{(1)}\rangle$ of the main text: let us define another equally valid dark state $|\tilde{\Psi}_{\mathcal{D}}^{(1)}\rangle = 1/\sqrt{N}(\sqrt{N-1}\hat{\sigma}_N^\dagger - \mathcal{S}_2^\dagger)|G\rangle$, where $\mathcal{S}_2^\dagger$ creates the symmetric superposition for the first $N-1$ qubits. It follows that these two dark states are nearly orthogonal for large N, namely, $|\langle\tilde{\Psi}_{\mathcal{D}}^{(1)}|\Psi_{\mathcal{D}}^{(1)}\rangle| = 1/(N-1)$.

7.7.3 Bright/Dark Subspaces

In this section we explain the possible excitation/decay paths for the highly degenerate effective Hamiltonian at multiples of λ_0 qubit separation in more detail, in particular

to understand the transmission properties if a certain dark state is prepared. Using the language of Dicke superradiance for collective spins, the symmetric collapse operator for all qubits, $\mathcal{S} = (\sqrt{M}\mathcal{S}_1 + \sqrt{N-M}\mathcal{S}_2)/\sqrt{N}$ is in the angular momentum representation for the sum of N spin 1/2 subsystems and defines lowering/raising operations on the Dicke states, $\mathcal{S}|N/2, m\rangle \propto |N/2, m-1\rangle$ and $\mathcal{S}^\dagger|N/2, m\rangle \propto |N/2, m+1\rangle$ where states are generally expressed as $|m, s\rangle$ with the quantum numbers s running from 0 or 1/2 to $N/2$ and m from $-s$ to s. The Dicke states are explicitly given by the symmetric M-excitation states $|\Psi_{\mathcal{S}}^{(M)}\rangle$ with a decay rates $M(N-M+1)\gamma$ and are shown in Fig. 7.5. There are additional bright states, for instance $|N/2-1, m\rangle$ with a $(N-1)$-fold degeneracy and decay rates $(M-1)(N-M)\gamma$. For multiples of λ_0 separation, the Dicke limit, jumps between different excitation manifolds can only be achieved with the symmetric operator $\mathcal{S}$ and a waveguide drive on resonance with the qubit transition frequency ω_0 that excites all qubits equally can be expressed as

$$\hat{\mathcal{H}}_{\mathrm{wg}}(t) = \Omega_{\mathrm{wg}}(t)\Big(\sqrt{M}\mathcal{S}_1^\dagger + \sqrt{N-M}\mathcal{S}_2^\dagger + h.c.\Big), \tag{7.15}$$

where the qubit chain is partitioned into M and $N-M$ qubit arrays respectively, and $\Omega_{\mathrm{d}}(t)$ is the time dependent Rabi frequency which can be pulsed or continuous. The waveguide drive can now connect Dicke states with the same quantum number m shown as vertical red arrows in Fig. 7.5 but is not able to access the completely dark state manifold which requires some asymmetry that is provided here by a coherent drive on a single or multiple qubits, $\hat{\mathcal{H}}_{\mathrm{d}}(t) = \Omega_{\mathrm{d}}(t)\sum_m(\hat{\sigma}_m^\dagger + \hat{\sigma}_m)$, with the requirement that only up to $N-1$ qubits are driven, in order to have non-zero overlap with the dark state manifold. This way, the every dark state (up to the $N/2$-excitation manifold) can be driven. Alternatively, the single-excitation dark state $|\Psi_{\mathcal{D}}^{(1)}\rangle$ can be prepared by driving a single qubit, subsequently $|\Psi_{\mathcal{D}}^{(2)}\rangle$ can be prepared by driving another qubit and so on up to $|\Psi_{\mathcal{D}}^{(N/2)}\rangle$ as shown in Fig. 7.5. On the other hand, for instance, the waveguide drive in Eq. (7.15) drives the single-excitation dark state $|\Psi_{\mathcal{D}}^{(1)}\rangle$ to the two-excitation bright state

$$|\Psi^{(2)}\rangle = \sqrt{\frac{2}{3}}\Big(\hat{\sigma}_1^\dagger\mathcal{S}_2^\dagger - \frac{\sqrt{N-1}}{N-2}(\mathcal{S}_2^\dagger)^2\Big)|G\rangle, \tag{7.16}$$

which decays with a rate $(N-2)\gamma$ and is observable in the transmission spectrum. The symmetric single excitation state $|\Psi_{\mathcal{S}}^{(1)}\rangle$ is driven to the symmetric two-excitation Dicke state with the superradiant decay rate $2(N-1)\gamma$. All states shown in Fig. 7.5 except the symmetric Dicke states $|\Psi_{\mathcal{S}}^{(M)}\rangle$, the ground state $|g\rangle^{\otimes N}$ and the totally inverted state $|e\rangle^{\otimes N}$ are elements of a subspace with degeneracy $d_M = \binom{N}{N-M} - \binom{N}{N-M-1}$.

The driving strength (for instance from the single- to the two-excitation dark state) is given by

$$\langle\Psi_{\mathcal{D}}^{(2)}|\hat{\mathcal{H}}_{\mathrm{d}}|\Psi_{\mathcal{D}}^{(1)}\rangle/\Omega_{\mathrm{d}}(t) = \frac{\sqrt{N-3}}{\sqrt{N}}\left(1 + \frac{1}{\sqrt{(N-1)(N-2)}}\right), \tag{7.17}$$

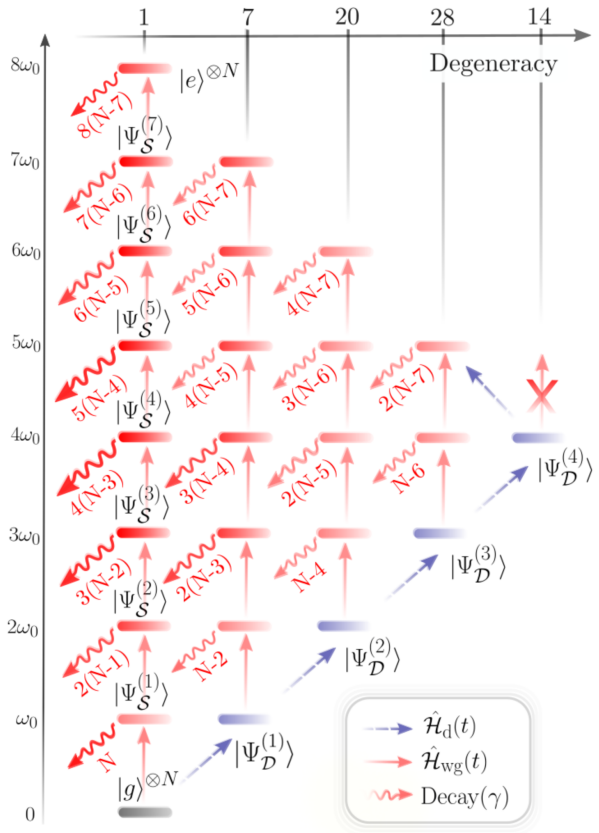

Figure 7.5: Energy level diagram for $N = 8$ qubits with multiples of λ_0 separation featuring a coherent drive $\hat{\mathcal{H}}_{\mathrm{d}}(t)$ on individual qubits and a waveguide drive $\hat{\mathcal{H}}_{\mathrm{wg}}(t)$ exciting all qubits symmetrically. The symmetric Dicke states $|\Psi_{\mathcal{S}}^{(M)}\rangle$ decay with the superradiant rate $M(N-M+1)\gamma$ which a maximum at $M = N/2$. Dark states exist for $M \leq N/2$ and $|\Psi_{\mathcal{D}}^{(M)}\rangle$, which resides in the dark subspace with M excitations, can be efficiently prepared by driving M qubits. The state can be probed via a symmetric waveguide drive on all qubits which excites it into a bright manifold with decay rate $(N-2M)\gamma$. Qubits prepared in the state $|\Psi_{\mathcal{D}}^{(N/2)}\rangle$ lead to complete transmission, as there is no bright manifold above with the same s quantum number. In between symmetric Dicke states and the dark state manifold are bright state manifolds with finite decay rates which are connected by a symmetric excitation to the excitation manifold below. Each subspace has a certain degeneracy which is shown on the top and note that there is no mixing between states from different excitation manifolds due to the absence of collective dephasing (no imperfections).

where the coherent drive only excites the second qubit and the single-excitation dark state has the majority of the excited state population in the first qubit.

7.7.4 Effect of Disorder, Imperfections and Non-Identical Waveguide Couplings

The above results can be generalized to non-identical waveguide couplings, in particular we assume the first qubit is coupled with rate γ_1 and the remaining qubits with rate γ_2. Here we show this actually enhances the effect studied so far, that is, an even higher fraction of the excited state population is concentrated in the first qubit and the driving strength of the dark state is equally enhanced. The single-excitation symmetric state can now be written as

$$|\Psi_{\mathcal{S}}^{(1)}\rangle = \frac{1}{\sqrt{\gamma_1 + (N-1)\gamma_2}}\left(\sqrt{\gamma_1}\hat{\sigma}_1^\dagger + \sqrt{(N-1)\gamma_2}\mathcal{S}_2^\dagger\right)\Big|G\Big\rangle, \tag{7.18}$$

where the populations in the individual qubits is not equally distributed since the different couplings lead to a redistribution of the excitation. The dark state obtains is readily found to be

$$|\Psi_{\mathcal{D}}^{(1)}\rangle = \frac{1}{\sqrt{\gamma_1 + (N-1)\gamma_2}}\left(\sqrt{(N-1)\gamma_2}\hat{\sigma}_1^\dagger - \sqrt{\gamma_1}\mathcal{S}_2^\dagger\right)\Big|G\Big\rangle. \tag{7.19}$$

The amount of population in the first qubit for the dark state is given by $(N-1)\gamma_2/(\gamma_1 + (N-1)\gamma_2)$ and in particular for $\gamma_2 \gg \gamma_1$ most is stored in the first qubit even for small N. It follows that the dark state can be prepared even more efficiently given that $\gamma_1 < \gamma_2$.

The two-excitation dark state, with the first two qubits having a coupling rate γ_1, is given by

$$|\Psi_{\mathcal{D}}^{(2)}\rangle = \frac{1}{\sqrt{\alpha}}\left(\frac{\sqrt{\gamma_1\gamma_2}}{\gamma_1}(\mathcal{S}_1^\dagger)^2 + \frac{\sqrt{\gamma_1\gamma_2}}{\gamma_2(N-2)}(\mathcal{S}_2^\dagger)^2 - \frac{\sqrt{2}}{\sqrt{N-1}}\mathcal{S}_1^\dagger\mathcal{S}_2^\dagger\right)\Big|G\Big\rangle, \tag{7.20}$$

with

$$\alpha = \frac{\gamma_2^2(N-1)(N-2) + 2\gamma_1\gamma_2(N-2) + 2\gamma_1^2}{\gamma_1\gamma_2(N-2)}. \tag{7.21}$$

The case of a single qubit interacting with a chain of qubits in the collective symmetric state can also be realized with two-level atoms in free space. In this analogy the first qubit is placed at the center of a ring of subwavelength-spaced two-level emitters where, due to permutational ring symmetry, only the symmetric mode of the ring couples to the central emitter [257]. The ring plays the role of an antenna

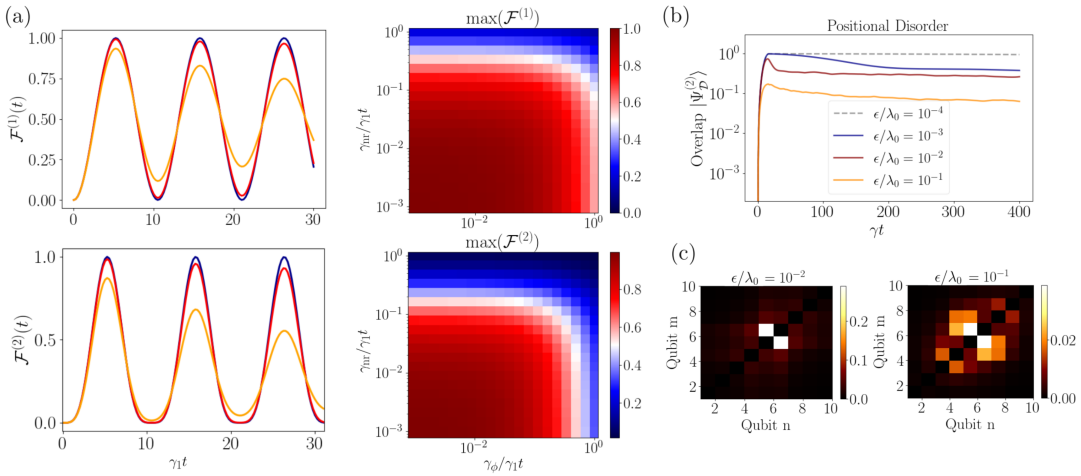

Figure 7.6: (a) Dark state preparation under dephasing and non-radiative decay for $N = 6$ qubits with $\gamma_2 = 20\gamma_1$ for either the last 4 or last 5 qubits and $d = \lambda_0$ and under continuous driving with Rabi frequency $\Omega_\mathrm{d}/\gamma_1$=0.3 for either the first or the first two qubits. The time evolution of the fidelity with the target state $\mathcal{F}^{(M)}(t) = \langle\Psi_\mathcal{D}^{(M)}|\rho(t)|\Psi_\mathcal{D}^{(M)}\rangle$ is shown. Blue, red and orange lines correspond to dephasing rates (i) $\gamma_\phi = 0$, (ii) $\gamma_\phi = 0.01\gamma_1$, (iii) $\gamma_\phi = 0.1\gamma_1$ respectively, with γ_nr=0. Also shown is the maximal fidelity for preparing the one- or two-excitation dark state $|\Psi_\mathcal{D}^{(M)}\rangle$ in the presence of non-radiative loss and dephasing rates γ_nr and γ_ϕ. (b) Influence of classical position disorder ϵ/λ_0 on the two-excitation dark state preparation with a rectangular driving pulse on the central two qubits and decay rate of the dark state for identical waveguide couplings γ in a chain of $N = 10$ qubits. The disorder is assumed to be following a normal distribution of standard deviation ϵ and 200 random configurations for each value of ϵ are considered. (c) The averaged spatial correlation $|\langle e_n e_m|\Psi(t)\rangle|^2$ is shown at $\gamma t = 20$ for the disordered arrays in (b).

focusing most of the incoming radiation into the central emitter, equivalent to driving $N-1$ qubits in the waveguide scenario.

In a realistic scenario both dephasing γ_ϕ and excitation loss γ_{nr} into channels other than the waveguide are present and affect the fidelities of driving the one- and two-excitation dark state as well as their lifetimes. The non-waveguide decay and dephasing are included as uncorrelated terms in the Lindbladian and the master equation for arbitrary distances obtains the form

$$\dot{\hat{\rho}} = -i[\hat{\mathcal{H}}_{\mathrm{eff}}, \hat{\rho}] + \sum_{m,n} \Gamma_{m,n} \hat{\sigma}_m \hat{\rho} \hat{\sigma}_n^\dagger + \gamma_{\mathrm{nr}} \sum_m \hat{\sigma}_m \hat{\rho} \hat{\sigma}_m^\dagger + 2\gamma_\phi \sum_m \hat{\sigma}_m^\dagger \hat{\sigma}_m \hat{\rho} \hat{\sigma}_m^\dagger \hat{\sigma}_m, \quad (7.22)$$

and the effective Hamiltonian in the interaction picture is given by

$$\hat{\mathcal{H}}_{\mathrm{eff}} = \sum_{m,n} \Big(J_{m,n} - i\frac{\Gamma_{m,n}}{2} \Big) \hat{\sigma}_m^\dagger \hat{\sigma}_n - i\frac{\gamma_{\mathrm{nr}} + 2\gamma_\phi}{2} \sum_m \hat{\sigma}_m^\dagger \hat{\sigma}_m. \quad (7.23)$$

For instance in Fig. 7.6(a) the influence of individual qubit dephasing and non-radiative decay on the dark state preparation fidelity is shown for non-identical waveguide couplings. A high preparation fidelity is prevailing even under considerable individual dephasing and decay, which in state-of-the-art laboratories working with superconducting qubits can be held below $10^{-2}\gamma_1$ for both. In Fig. 7.6(b) the two-excitation dark state preparation and decay rate are shown for various degrees of classical position disorder. Each qubit is randomly displaced around its multiple of λ_0 position by a normal distribution of standard deviation ϵ. The overlap with $|\Psi_{\mathcal{D}}^{(2)}\rangle$ is plotted after performing an average over disorder realizations which is confined along the 1D chain axis. The number of disorder realizations is 200 and in Fig. 7.6(c) the averaged spatial correlation $|\langle e_n e_m|\Psi(t)\rangle|^2$ is shown after the overlap reached the maximum value. For quantum platforms in the microwave regime e.g. superconducting transmon qubits, the positional disorder can be kept well below 10^{-4} but even other platforms like atoms trapped along a nanofiber exhibit small positional disorder.

Frequency disorder might be a further complication which introduces finite lifetimes to the dark state and decreases the preparation fidelity. Specifically for superconducting circuits this can be remedied by additionally adding flux bias lines, which ensures that we can tune the frequency of all qubits on resonance. Although this means there is an overhead of one control line per qubit, which should be fine for systems up to e.g. 10-15 qubits or potentially even more. Another point is that with increasing qubit number N, the resilience to frequency disorder increases as, on the one hand, the linewidth of the symmetric state scales with N allowing for more detuned remaining qubits. On the other hand with more qubits it is more likely that at least a handful are closer to resonanance with each other, thereby allowing them to combine into a dark state.

7.7.5 Multilevel Nature of the Transmon Qubit

For the specific platform of superconducting transmon qubits the involved quantum emitters are inherently anharmonic and due to the multilevel nature it is necessary to model each emitter as a multilevel quantum emitter to capture the full richness of possible quantum states. So far we assumed a large enough anharmonicity U between the first and second excited state in each transmon and therefore neglected the second excited state to recover the two-level qubit. Here we show that the results obtained above still prevail in the case of small U and even the harmonic oscillator case $U = 0$. Let us first begin to write down the effective Hamiltonian for N transmons, which is given by

$$\hat{\mathcal{H}}_{\text{eff}} = \sum_{m,n} \Big(J_{m,n} - i\frac{\Gamma_{m,n}}{2} \Big) \hat{a}_m^\dagger \hat{a}_n - \frac{U}{2} \sum_m \hat{n}_m (\hat{n}_m - \mathbb{I}), \tag{7.24}$$

whereas the Lindbladian retains the same form as in the qubit case. The bosonic operator $\hat{a}_m^\dagger$ creates an excitation on the site m and $\hat{n}_j$ is the number operator of the site m. For many-body dynamics the anharmonicity U serves as an on-site interaction and the weaker the anharmonicity, the closer the system resembles the harmonic oscillator. For arbitrary U the transmons generally behave like anharmonic oscillators but assuming only a single excitation is present in the system, the single-excitation dark and bright states have the same form as in the qubit case with the exchange $\hat{\sigma}_m \leftrightarrow \hat{a}_m$. The completely symmetric state with two excitations can be written as

$$|\Phi_{\mathcal{S}}^{(2)}\rangle = \frac{\sqrt{2}}{N} \sum_{n,m} \hat{a}_n^\dagger \hat{a}_m^\dagger |G\rangle = \frac{\sqrt{2}}{N} \Big((\hat{a}_1^\dagger)^2 + \sqrt{N-1}\hat{a}_1^\dagger \mathcal{S}_2^\dagger + (N-1)(\mathcal{S}_2^\dagger)^2 \Big) |G\rangle, \tag{7.25}$$

with the superradiant decay rate $2N\gamma$ which is larger than the superradiant rate of the two-excitation symmetric Dicke state. The two-excitation dark state with two excitations per site and the majority of the excitation in the first transmon is given by

$$|\Phi_{\mathcal{D}}^{(2)}\rangle = \frac{\sqrt{2}}{N} \Big((\hat{a}_1^\dagger)^2 - 2\sqrt{N-1}\hat{a}_1^\dagger \mathcal{S}_2^\dagger + (\mathcal{S}_2^\dagger)^2 \Big) |G\rangle, \tag{7.26}$$

with the fraction $2(N-1)/N$ of the population in the first transmon and $N\sigma^{ge}2$. As before, any transmon is equally valid to store the majority of the population and which one is determined whether or not it is excited by an external drive. The other possible dark state involving superpositions of symmetric states in the sub-arrays is equivalent to the two-excitation dark state for the qubit case $|\Psi_{\mathcal{D}}^{(2)}\rangle$ with the exchange $\hat{\sigma}_m^\dagger \leftrightarrow \hat{a}_m^\dagger$ in $\mathcal{S}_1^\dagger$ and $\mathcal{S}_2^\dagger$ respectively. Assuming that the first two transmons are driven by an external drive, the general dark state for arbitrary anharmonicities U is a superposition of the aforementioned dark states, namely $c_1|\Psi_{\mathcal{D}}^{(2)}\rangle + c_2|\Phi_{\mathcal{D}}^{(2)}\rangle$. Notably, the state $|\Phi_{\mathcal{D}}^{(2)}\rangle$ acquires a energy shift as well coming from the onsite interaction term in the Hamiltonian and has to be taking into account while driving the quibts externally. This shows that the effect described for the qubit case extends to the transmonic regime with the collective dark and bright states having a slightly modified

distribution in the populations due to their multilevel structure. Typical values for the anharmonicity are $U \sim 200 - 300$ MHz whereas the waveguide decay rate γ is in the range of $1 - 100$ MHz.

8 Publication

Physical Review Research **4**(033116), (2022)

Cooperative subwavelength molecular quantum emitter arrays

R. Holzinger[1], S. A. Oh[2], M. Reitz[2], H. Ritsch[1] and C. Genes[2]

[1]*Institut für Theoretische Physik, Universität Innsbruck, Technikerstrasse 21, A-6020 Innsbruck, Austria*
[2]*Max Planck Institute for the Science of Light, Staudtstrasse 2, D-91058 Erlangen, Germany*

Dipole-coupled subwavelength quantum emitter arrays respond cooperatively to external light fields as they may host collective delocalized excitations (a form of excitons) with super- or subradiant character. Deeply subwavelength separations typically occur in molecular ensembles, where in addition to photon-electron interactions, electron-vibron couplings and vibrational relaxation processes play an important role. We provide analytical and numerical results on the modification of super- and subradiance in molecular rings of dipoles including excitations of the vibrational degrees of freedom. While vibrations are typically considered detrimental to coherent dynamics, we show that molecular dimers or rings can be operated as platforms for the preparation of long-lived dark superposition states aided by vibrational relaxation. In closed ring configurations, we extend previous predictions for the generation of coherent light from ideal quantum emitters to molecular emitters, quantifying the role of vibronic coupling onto the output intensity and coherence.

DOI: 10.1103/PhysRevResearch.4.033116

8.1 Introduction

Structured subwavelength arrays of quantum emitters allow for the coherent hopping of excitations via the near-field coupling of neighbouring dipoles [165, 258–260]. In addition, they exhibit correlated spontaneous emission and support super- and subradiant collective modes, which can be exploited to control the interaction with

impinging light. Possible applications range from the design of highly reflective quantum metasurfaces [10, 261, 262] to the engineering of platforms showing robust transport of excitation in topological quantum optics [263, 264] and of high-fidelity photon storage devices for quantum information processing [50, 58, 168]. Moreover, quantum emitter rings have been proposed to act as coherent light sources on the nanoscale [143].

While subwavelength separations are not easily achieved in standard quantum optics setups, molecular aggregates (i.e., arrays of identical molecules) can feature deeply subwavelength separations on the nanometer scale, while retaining the electronic structure of the individual dipole transitions [265]. They can be artificially synthesized in a wide variety of forms such as one dimensional chains or two dimensional films and can also be found in nature, in particular in the photosynthetic light-harvesting complexes of plants and bacteria [177, 259, 266]. For example, long-lived electronic quantum coherence in a light-harvesting protein (the Fenna-Matthews-Olson complex) has been experimentally observed [267] and theoretically tackled [266]. The downside of such systems is the much more complex structure, which introduces coupling of electronic degrees of freedom with intra- and inter-molecular vibrations. While it is well established that the strong coherent near-field interactions give rise to delocalized exciton states (of the so-called Frenkel excitons) in molecular aggregates [23, 268], the characterization of the accompanying collective dissipation is usually not fully taken into account in such systems as vibronic couplings and induced dephasing are considered to dominate the dynamics, especially at high temperatures. It is therefore interesting and timely to characterize cooperative dissipative effects in the presence of vibrations, a task which involves an extension of previously developed methods to describe electron-photon-phonon interactions on an individual dipole basis [18, 269]. Moreover, the addition of localized gain, renders molecular emitter arrays as possible candidates for the realization of nanoscale coherent light sources as recently introduced for pure quantum emitters [143]. As an alternative (or addition) to strong near-field coupling, a modified material response of a molecular ensemble can also be obtained by collective strong coupling of the ensemble to a cavity which creates similar delocalized excitaton states among the molecules which are then hybridized with the cavity mode. The field of molecular polaritonics has recently emerged as a platform for observing strong modifications of material properties such as charge and energy transport or chemical reactivity [270–273].

In this work, we perform analytical and numerical studies of cooperative radiative properties of molecular arrays with particular emphasis on ring configurations, where we treat the vibronic coupling and electron-photon interactions on equal footing. Our treatment combines two approaches, a master equation approach, where the thermal environment of the vibrational degrees of freedom is traced out and a quantum Langevin equations approach, where the time evolution of both electronic and vibrational operators are fully considered. As a first important step, we elucidate the influence of vibronic couplings on the scaling of collective emission rates: modifications for the case of molecular systems originate from the Franck-Condon factors, which lead to a decay of the electronic coherence via coupling to several states of the vibrational

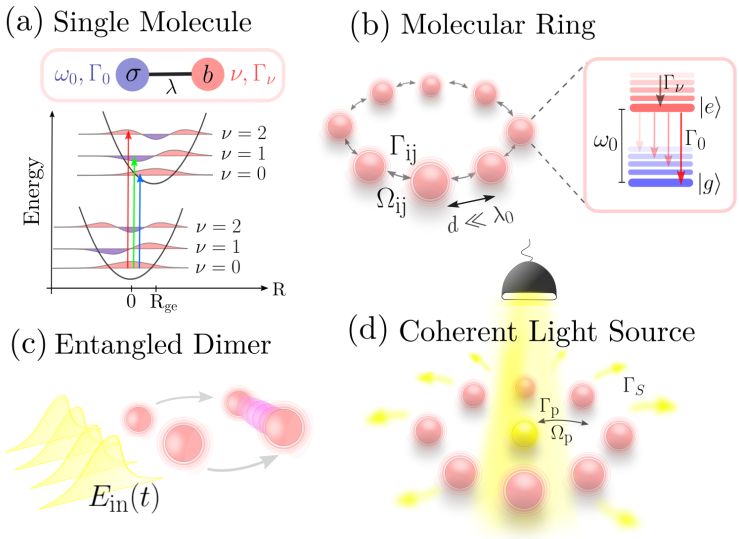

Figure 8.1: (a) The equilibrium mismatch R_{ge} between the ground and excited state electronic potential landscapes along a given nuclear coordinate leads to the standard Franck-Condon physics with a branching of transitions into different vibrational levels. The electron-vibron coupling is schematically represented by the link, at coupling strength λ, between an electronic transition operator σ and a bosonic vibrational mode operator b. (b) Schematics of a molecular ring where mutual interactions are mediated by the electromagnetic vacuum at coherent/incoherent rates Ω_{ij} and Γ_{ij}. The inset shows branching of electronic transitions between the manifolds of vibrational levels. (c) Preparation of an entangled molecular dimer with subwavelength separation $d \ll_0$ via an impinging short laser pulse. (d) Schematics of a molecular nanoscale light source where the central gain molecule is incoherently pumped and coherently coupled to the symmetric eigenmode of the ring molecules. The ring provides an effective resonator enhancement leading to the emission of coherent laser light.

degrees of freedom and the vibrational thermal environment.

Analytical results can be derived and understood more easily by a transformation to a collective electronic basis, which involves a single bright (symmetric) state and many more dark (antisymmetric) state of typically superradiant and subradiant character respectively. This basis allows a simplified understanding of how standard scenarios, such as Dicke superradiance and the band structure of dipole-dipole induced transport of excitations, are modified by the electron-vibron interactions.

While vibronic couplings are generally seen as detrimental in the efforts of controlling electronic coherence with light modes, here we present a generic vibronic dimer model, where bipartite long-lived entanglement is even engineered owing to

vibrational relaxation. The system involves a nanometer spaced molecular dimer, where two chromophores exchange energy but not charge. Under favorable conditions, unidirectional flow of population for a driven symmetric collective state is directed into a robust, entangled antisymmetric state, via a process similar to the Förster resonance energy transfer occurring in acceptor/donor configurations.

The same transformation to a collective basis proves useful in the understanding of molecular nanorings illuminated by incoherent light sources, as recently proposed for the design of nanoscale coherent light sources [143]. In such systems, symmetric collective states are almost fully responsible for the generation of emitted light, which greatly aids our analytical and numerical analysis, allowing for a great reduction of the relevant Hilbert space dimension and therefore for numerical results with a reasonably sized molecular nano-rings, where each electronic transition is coupled to at least one own phonon mode.

The paper is organized as follows: Sec. 9.2 introduces the open system dynamics formalism for molecules including electron-photon and electron-vibron interactions. In the following we describe super- and subradiance both in the Dicke limit of closely spaced ensembles, for population inverted systems, and also in the weak excitation for arbitrarily spaced chains and rings. We then introduce a particular case of nanoscale sized molecular dimers, where vibrationally induced couplings between collective symmetric and antisymmetric electronic states allow for the addressing of long-lived dark entangled states. The symmetric/antisymmetric collective basis is then generalized to the ring geometry with particular relevance to molecular nanoring lasers. We also provide analytical and numerical results for the scaling of intensity and second order correlation functions of coherent light emitted by an incoherently pumped nanoscale molecular ring.

8.2 Model

We consider $\mathcal{N}$ identical molecular quantum emitters, each involving electronic transitions between two potential landscapes, with minima slightly shifted from each other along a nuclear coordinate. This mismatch of the electronic potential energy landscapes in the ground and excited states gives rise to the electron-vibron coupling, as depicted in Fig. 10.1(a). External drive of electronic transitions is accompanied, in consequence, by the excitation of the motion of the nuclei, depicted as eigenstates of a harmonic potential in Fig. 10.1(a). The electronic transition for molecule j (index running between 1 and $\mathcal{N}$) is at frequency splitting ω_0 ($\hbar = 1$) and described by the collapse operator $\sigma_j = |g\rangle_j \langle e|_j$ and its Hermitian conjugate. The vibrational degree of freedom is at frequency ν and is described by a bosonic operator b_j satisfying the commutation relations $\left[b_j, b_j^\dagger\right] = 1$. The vibronic coupling is illustrated in Fig. 10.1(a) as a link between the electronic and vibration operator with magnitude characterized by the Huang-Rhys factor λ^2. The electronic and vibrational degrees of freedom are subject to loss quantified by the spontaneous emission rate Γ_0 and by the vibrational relaxation

rate Γ_ν, respectively. A standard Jablonski diagram of radiative and non-radiative processes involving two electronic states with their corresponding vibrational manifold is illustrated in the inset of Fig. 10.1(b). This complex competition of transitions shows that molecules are typically inefficient quantum emitters as they do not possess closed transitions. Furthermore, we will consider rings of $\mathcal{N}$ molecules, as illustrated in Fig. 10.1(b), with ring radius r and interparticle separation $d = 2r \sin 2\pi/\mathcal{N}$. Their close separation brings into play cooperative effects such as near field dipole-dipole interactions and collective spontaneous emission, quantified by the distance dependent rates Ω_{ij} and Γ_{ij}, which are mediated by the quantum electromagnetic vacuum.

The free Hamiltonian for the ensemble of $\mathcal{N}$ molecules $\mathcal{H}_0 = \sum_j h_0^{(j)}$ is obtained as a sum over each particle's free Hamiltonian

$$h_0^{(j)} = \left(\omega_0 + \lambda^2\nu\right) \sigma_j^\dagger \sigma_j + \nu b_j^\dagger b_j, \tag{8.1}$$

which sees a vibronic shift $\lambda^2\nu$ added to the electronic bare transition frequency (which will later cancel out after a polaron transformation – see supplemental material. The index j runs from 1 to $\mathcal{N}$ for the ring configuration which will be used in the next section to derive cooperative radiative emission properties of molecular ensembles. Later we will incorporate an additional index p to describe the situation depicted in Fig. 10.1(d), which sees the realization of a molecular nanoscale light source with a gain molecule implanted in the center of the ring.

The vibronic coupling Hamiltonian [20] is now added as a sum $\mathcal{H}_{\text{Hol}} = \sum_j h_{\text{Hol}}^{(j)}$ over all particles, where

$$h_{\text{Hol}}^{(j)} = -\lambda\nu\sigma_j^\dagger\sigma_j(b_j^\dagger + b_j). \tag{8.2}$$

The Holstein Hamiltonian listed above assumes identical molecules and is a minimal model for electron-vibron interactions derivable from first principles [18] (see the supplemental material).

For closely spaced quantum emitters, near-field dipole-dipole interactions at rates $\Omega_{jj'}$ are added, which are strongly dependent on their interseparation (with a standard $|\vec{r}_j - \vec{r}_{j'}|^{-3}$ dependence in the near field region) and relative orientation of transition dipoles [19] (see the supplemental material for exact expressions). This can be listed as

$$\mathcal{H}_{\text{d-d}} = \textstyle\sum_{j\neq j'} \Omega_{jj'}\sigma_j^\dagger\sigma_{j'} \tag{8.3}$$

and describes an excitation transfer via a virtual photon exchange. Notice that by definition the diagonal terms Ω_{jj} vanish.

To the coherent dynamics one can then add the effects of infinite reservoirs in an open system dynamics described by a master equation (for the system's density operator ρ) in the form

$$\partial_t\rho = i[\rho, \mathcal{H}] + \mathcal{L}[\rho], \tag{8.4}$$

where the total Hamiltonian is $\mathcal{H} = \mathcal{H}_0 + \mathcal{H}_{\text{Hol}} + \mathcal{H}_{\text{d-d}}$. The dissipative, incoherent dynamics stemming from the coupling of the electronic and vibrational degrees of freedom to their baths in thermal equilibrium, is included in the Lindblad part as

a superoperator (an operator acting on density operators). A standard, diagonal superoperator in Lindblad form [14, 16, 62, 274–276] is defined as

$$\mathcal{L}_{\gamma}[\rho] = \frac{\gamma_{\mathcal{O}}}{2}\left[2\mathcal{O}\rho(t)\mathcal{O}^{\dagger} - \mathcal{O}^{\dagger}\mathcal{O}\rho(t) - \rho(t)\mathcal{O}^{\dagger}\mathcal{O}\right], \tag{8.5}$$

and describes decay at generic rate $\gamma_{\mathcal{O}}$ through a single channel with a generic collapse operator $\mathcal{O}$. The radiative dynamics stemming from the coupling of electronic transitions to the electromagnetic vacuum is, however, not in diagonal Lindblad form [43] but achieves the following expression

$$\mathcal{L}_{e}[\rho] = \sum_{j,j'} \frac{\Gamma_{jj'}}{2}\left[2\sigma_{j}\rho\sigma_{j'}^{\dagger} - \sigma_{j}^{\dagger}\sigma_{j'}\rho - \rho\sigma_{j}^{\dagger}\sigma_{j'}\right]. \tag{8.6}$$

A simple diagonalization of the matrix of decay rates suffices to bring the expression above into standard Lindblad form and to see the emergence of $\mathcal{N}$ collective dissipation channels. The second contribution to $\mathcal{L}[\rho]$ stems from the non-radiative loss of vibrational excitation and is in standard Lindblad form with rate Γ_{ν} for all molecules and collapse operators b_j. This is an approximated model, as some care has to be taken regarding the correct collapse operator since the vibronic coupling can be strong ($\lambda \sim 1$) and the vibrational relaxation is typically much faster than the spontaneous emission.

8.3 Radiative properties of vibronically coupled emitters

The non-standard form of the radiative dissipation leads to cooperative effects which show the imprint of superradiance and subradiance. For ideal quantum emitters, such effects are well understood [43] and analytically tackled e.g. in Ref. [19]. However, the vibronic coupling appearing in the Hamiltonian in Eq. (9.1) changes these effects considerably. We will focus on two distinct situations: i) inverted ensembles, where the dynamics is followed on the whole Bloch sphere and ii) the single excitation manifold, relevant under weak excitation conditions. We will make use of both an individual site basis (described by operators σ_j), as well as a collective basis, where symmetric and antisymmetric combinations of the σ_j operators will be defined. We first show that vibrations lead to a degradation of the superradiant pulse emission in the Dicke limit. Then we analyze the symmetric/antisymmetric dynamics to show that both dissipative dynamics and vibronic effects lead to couplings among collective states of different symmetries. In the single excitation subspace, states of different symmetry do not couple via dissipative effects, allowing the derivation of a band structure describing the dispersion of excitations tunneling between molecules via the near field dipole-dipole interactions; this behavior is only changed owing to vibronic effects.

8.3.1 Dissipation under vibronic coupling

Let us first review a few details on the vibronic coupling following the description in Ref. [18]. For a single molecule indexed by j, the Holstein Hamiltonian can be diagonalized via a level-dependent polaron transformation $\mathcal{U}_j^\dagger = |g\rangle_j \langle g|_j + \mathcal{D}_j^\dagger |e\rangle_j \langle e|_j$ with the standard displacement operator defined as

$$\mathcal{D}_j = e^{-i\sqrt{2}\lambda p_j} = e^{\lambda(b_j^\dagger - b_j)}. \tag{8.7}$$

In the polaron-displaced basis, the Holstein Hamiltonian $h_0^{(j)} + h_{\mathrm{Hol}}^{(j)}$ becomes diagonal

$$\tilde{h}^{(j)} = \mathcal{U}_j^\dagger (h_0^{(j)} + h_{\mathrm{Hol}}^{(j)}) \mathcal{U}_j = \omega_0 \sigma_j^\dagger \sigma_j + \nu b_j^\dagger b_j \tag{8.8}$$

and has simple eigenvectors $|g; n\rangle_j$ and $|e; n\rangle_j$. The eigenvectors in the bare, original basis can be found by inverting the polaron transformation $|g; n\rangle_j$ and $\mathcal{D}\,|e; n\rangle_j$. The important property we have used is the transformation of the Pauli matrices under the vibrational displacement $\mathcal{U}_j^\dagger \sigma_j \mathcal{U}_j = \sigma_j \mathcal{D}_j$. The dressed operators describe polarons, i.e. hybrid electronic-vibrational operators. Furthermore we assume a thermal state with the average occupancy $\bar{n} = [\exp(\hbar\nu/(k_B T)) - 1]^{-1}$ (where k_B is the Boltzmann constant). The partial trace over the vibronic displacement operators at temperature T is therefore given by

$$\langle \mathcal{D}_j \mathcal{D}_{j'}^\dagger \rangle_T = e^{-\lambda^2(1+2\bar{n})(1-\delta_{jj'})}. \tag{8.9}$$

Note that at $T = 0$ the above trace reduces simply to $\langle \mathcal{D}_j \mathcal{D}_{j'}^\dagger \rangle_{T=0} = \exp[-\lambda^2(1-\delta_{jj'})]$ giving unity on a given molecule but a reduction by the Franck-Condon factor $e^{-\lambda^2}$ for a two molecule term.

We can now apply the polaron transformation with an operator $\mathcal{U}^\dagger = \prod_j \mathcal{U}_j^\dagger$ such as to diagonalize the whole vibronic Hamiltonian. We are however left with the polaron transformed dipole-dipole interaction as well as a polaron transformed Lindblad term, which describes dissipation via polaron collapse operators

$$\tilde{\mathcal{L}}_e[\rho] = \sum_{j,j'} \frac{\Gamma_{jj'}}{2} \left[2\sigma_j \mathcal{D}_j \rho \mathcal{D}_{j'}^\dagger \sigma_{j'}^\dagger - \{\mathcal{D}_j^\dagger \sigma_j^\dagger \sigma_{j'} \mathcal{D}_{j'}, \rho\} \right], \tag{8.10}$$

where the last term denotes an anticommutator. We will then make the assumption that the vibrations are in a thermal state and that the electronic and vibrational states factorize. This leads to a renormalization of the dipole-dipole interaction $\Omega_{jj'}^\lambda = \Omega_{jj'} e^{-\lambda^2(1+2\bar{n})}$ as well as renormalized off-diagonal (or mutual) decay rates as evident from the polaron transformed Lindblad term

$$\tilde{\mathcal{L}}_e[\rho] = \sum_{jj'} e^{-\lambda^2(1+2\bar{n})(1-\delta_{jj'})} \frac{\Gamma_{jj'}}{2} \Big[2\sigma_j \rho \sigma_{j'}^\dagger - \{\sigma_j^\dagger \sigma_{j'}, \rho\} \Big]. \tag{8.11}$$

Notice that for large λ or large thermal occupancies, the off-diagonal elements of the Lindblad term above (corresponding to cooperative emission) vanish, leading to the disappearance of any subradiant or superradiant behavior and the recovery of the independent decay behavior.

8.3.2 Dynamics on the Bloch sphere

We will first analyze the standard Dicke superradiance phenomenon extended to the case of molecules, i.e. for a vibronic coupling characterized by a non-zero Huang-Rhys factor $\lambda = 0$. To this end, we will make use of a Bloch sphere representation for the collective spin of the system as illustrated in Fig. 9.2(a). We use of a non-standard angular momentum representation for the sum of $\mathcal{N}$ spin 1/2 subsystems where a collective collapse operator is introduced as a symmetric combination $\mathcal{S} = \sum_j \sigma_j/\sqrt{\mathcal{N}}$. The Cartesian components are $\mathcal{S}_z = \sum_j \sigma_j^{(z)}$, $\mathcal{S}_x = \mathcal{S} + \mathcal{S}^\dagger$ and $\mathcal{S}_y = -i(\mathcal{S} - \mathcal{S}^\dagger)$. Common eigenstates of the total spin vector $\vec{\mathcal{S}}$ and $\mathcal{S}_z$ are then denoted by $|s, m\rangle$ where the quantum number s runs 0 or 1/2 to $\mathcal{N}/2$ and m from $-s$ to s. In the symmetric subspace the so-called Dicke states arise denoted by $|\mathcal{N}/2, m\rangle$ and obtained by fixing s to its maximal value $\mathcal{N}/2$. The action of the lowering/raising operators on the Dicke states is $\mathcal{S}|\mathcal{N}/2, m\rangle = \alpha_m^{(-)}|\mathcal{N}/2, m-1\rangle$ and $\mathcal{S}^\dagger|\mathcal{N}/2, m\rangle = \alpha_m^{(+)}|\mathcal{N}/2, m+1\rangle$ where the coefficients are

$$\alpha_m^{(\pm)} = \frac{1}{\sqrt{\mathcal{N}}}\sqrt{(\mathcal{N}/2 \mp m)(\mathcal{N}/2 \pm m + 1)}. \tag{8.12}$$

In the Dicke limit ($d = 0$) and in the absence of vibrations ($\lambda = 0$), the Lindblad term in Eq. (8.11) can be immediately diagonalized as a single loss channel with collapse operator $\mathcal{S}$ at superradiant rate $\mathcal{N}\Gamma_0$. This is no longer when $\lambda \neq 0$ or $d > 0$ or both, as population spills outside the symmetric subspace towards the interior of the Bloch sphere. This behavior can be easily understood in a collective basis, where additional $\mathcal{N} - 1$ antisymmetric operators are introduced

$$\mathcal{A}_k = \frac{1}{\sqrt{\mathcal{N}}}\sum_{j=1}^{\mathcal{N}} \sigma_j e^{2\pi i j k/\mathcal{N}}, \quad \text{for} \quad k \in \{1, ..., \mathcal{N} - 1\}, \tag{8.13}$$

under the requirement that they are orthogonal to the $\mathcal{S}$ operator (this can be done more generally, for example, via a Gram-Schmidt algorithm). The Hamiltonian can be easily diagonalized in terms of collective operators giving

$$\mathcal{H} = \omega_{\mathcal{S}}^\lambda \mathcal{S}^\dagger \mathcal{S} + \sum_{k=1}^{\mathcal{N}-1} \omega_k^\lambda \mathcal{A}_k^\dagger \mathcal{A}_k. \tag{8.14}$$

This is based on the orthonormality condition $\sum_{k=1}^{\mathcal{N}} e^{2\pi i k(j-j')/\mathcal{N}} = \mathcal{N}\delta_{jj'}$ and on the cyclic symmetry of the ring allowing to write any sums $\sum_{j' \neq j} e^{2\pi i k(j'-j)/\mathcal{N}}\Omega_{jj'} = \sum_{j'=2}^{\mathcal{N}} e^{2\pi i k(j'-1)/\mathcal{N}}\Omega_{1j'}$. The modified eigenenergies are given by $\omega_{\mathcal{S}}^\lambda = \omega_0 + \sum_{j=2}^{\mathcal{N}} \Omega_{1j}^\lambda$, for the symmetric states and

$$\omega_k^\lambda = \omega_0 + \sum_{j=2}^{\mathcal{N}} \Omega_{1j}^\lambda e^{2\pi i (j-1) k/\mathcal{N}}, \tag{8.15}$$

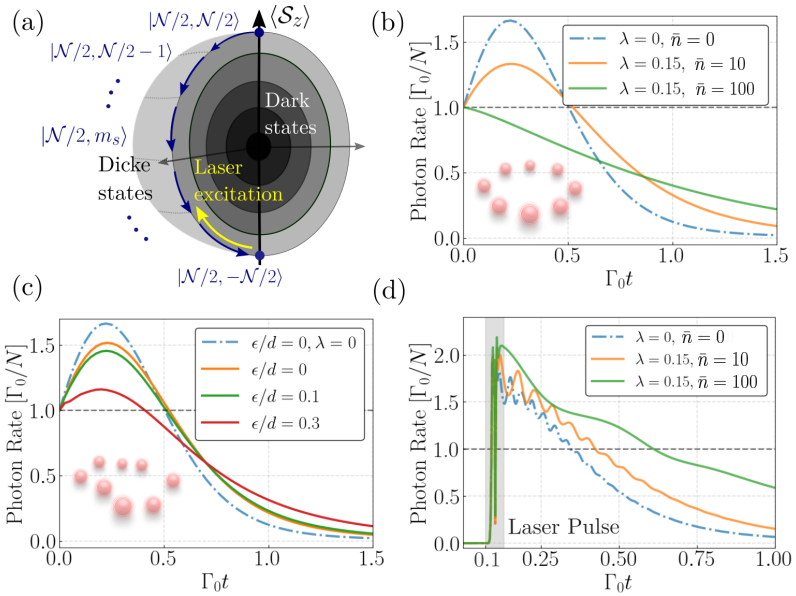

Figure 8.2: (a) Illustration of the collective Bloch sphere for $\mathcal{N}$ emitters. The symmetric subspace is spanned by $\mathcal{N}+1$ Dicke states, while the inside of the sphere is spanned by antisymmetric states. (b) Superradiant decay for an initially fully inverted ring of $\mathcal{N} = 8$ molecules with their vibrational degree of freedom in thermal equilibrium at various temperatures. (c) Scaling of the superradiant pulse intensity for a fully inverted system of molecules in the ring configuration, as a function of increasing positional disorder ϵ and with vibronic coupling $\lambda = 0.15$ (d) Time dependence of the intensity of emission for a ring of $\mathcal{N} = 8$ molecules driven by a laser pulse with the frequency matched to the symmetric state resonance $\omega_\ell = \omega_\mathcal{S}$. The inter-molecular separation in all plots is $d = 0.04_0$ and the dipoles are linearly polarized perpendicular to the plane of the ring. Parameters are fixed to $\eta = 260\Gamma_0, t_0 = 0.1/\Gamma_0$ and $\tau = 0.1/\Gamma_0$.

for the set of antisymmetric combinations.

The thermally averaged Lindblad term from Eq. (8.11) can now be split into $\mathcal{N}$ decay channels: a symmetric one with loss rate $\Gamma^\lambda_\mathcal{S}(d)$ and $\mathcal{N}-1$ antisymmetric channels with rates $\Gamma^\lambda_k(d)$. These can be expressed as

$$\Gamma^\lambda_{\mathcal{S},k}(d) = \Gamma_0 \left[1 - e^{-\lambda^2(1+2\bar{n})}\right] + \Gamma^{\lambda=0}_{\mathcal{S},k}(d) e^{-\lambda^2(1+2\bar{n})}, \tag{8.16}$$

in terms of the bare rates for zero vibronic coupling $\Gamma^{\lambda=0}_\mathcal{S}(d) = \sum_{j=1}^{\mathcal{N}} \Gamma_{1j}(d)$ and $\Gamma^{\lambda=0}_k(d) = \sum_{j=1}^{\mathcal{N}} \Gamma_{1j}(d) e^{i2\pi(j-1)k/\mathcal{N}}$. Notice that for zero distance and no vibronic couplings, we recover the Dicke superradiance effect with rate $\mathcal{N}\Gamma_0$. For larger distances this is effect is reduced; additional reduction appears for nonzero vibronic coupling and temperature. Finally, for large λ or $\bar{n}$, a complete washout of superradiance occurs

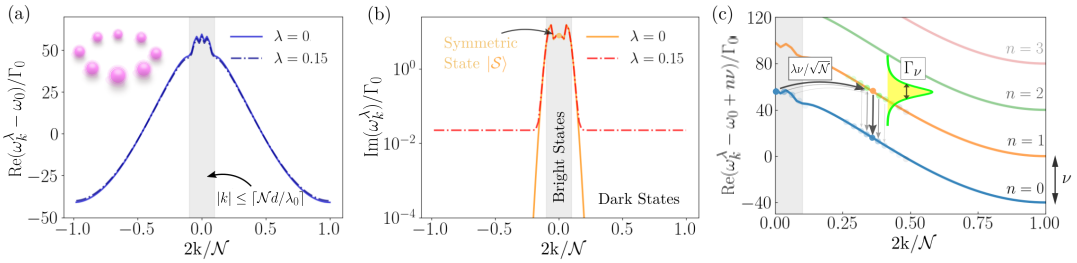

Figure 8.3: (a) Single-excitation dispersion relation in the first Brillouin zone for a ring of $\mathcal{N} = 100$ transversely polarized molecules at zero temperature with nearest-neighbour separation $d = 0.05_0$. Bright states enclosed by the shaded region are characterized by a mode number $|k| \leq \lceil \mathcal{N}d/_0 \rceil$ whereas the region beyond is occupied by dark states. (b) Bright states feature a finite decay rate with the symmetric state located at $k = 0$. For $d \ll_0$ the dark state decay rates are approximately given by $\Gamma_k^\lambda \sim (1 - e^{-\lambda^2})\Gamma_0$ whereas the bright state decay rate approaches $\Gamma_\mathcal{S}^\lambda \sim \Gamma_0 + e^{-\lambda^2}(\mathcal{N} - 1)\Gamma_0$. (c) Dispersion curves in the full vibrational Hilbert space (for $\lambda = 0.15$). States with n vibrational energy quanta are shifted by $n\nu$ with respect to the zero-vibrational states. Vibrations lead to coherent population transfer from bright states with lower vibrational quantum state excitation to dark states with higher vibrational quantum state excitation, at a coupling strength $\lambda\nu/\sqrt{\mathcal{N}}$. The process is followed by non-radiative vibrational relaxation into the dark state with zero vibrations at a rate $\Gamma_\nu \gg \Gamma_0$.

and the first term in the expression above indicates the independent rate Γ_0 for both symmetric and antisymmetric states.

For a better understanding of the coupling between states of different symmetries, we now perform an analysis in the full Hilbert space, i.e. without tracing over the thermal bath. Instead, intuitive understanding is offered by an additional transformation to a collective basis for the vibrational degrees of freedom as well, introduced via

$$Q_k = \frac{1}{\sqrt{\mathcal{N}}} \sum_{j=1}^{\mathcal{N}} e^{2\pi i j k/\mathcal{N}} (b_j + b_j^\dagger), \tag{8.17}$$

where $k \in \{1, ..., \mathcal{N}\}$ (with $k = \mathcal{N}$ corresponding to the symmetric vibrational mode) and with the momentum quadratures satisfying $[Q_k, P_{k'}] = 2i\delta_{kk'}$. An interaction term emerges, coupling the symmetric state to the antisymmetric manifold

$$\mathcal{H}_{\text{int}}^{\mathcal{SA}} = -\frac{\lambda\nu}{\sqrt{\mathcal{N}}} \sum_{k=1}^{\mathcal{N}-1} (Q_k \mathcal{S}^\dagger \mathcal{A}_k + h.c.), \tag{8.18}$$

via the position quadratures of the collective vibrations. This coupling is responsible for the spilling of population into the interior of the Bloch sphere even when fully

symmetric driving for the system takes place. The effect will be useful in order to understand the dynamics of the coherent nanoscale source analyzed in Sec. 8.5. In addition, couplings within the antisymmetric states manifold emerge via

$$\mathcal{H}_{\text{int}}^{\mathcal{A}\mathcal{A}} = -\frac{\lambda\nu}{\sqrt{\mathcal{N}}}\sum_{k\neq k'}^{\mathcal{N}-1}(Q_{k-k'}\mathcal{A}_k^\dagger\mathcal{A}_{k'} + h.c.). \tag{8.19}$$

This Hamiltonian shows a redistribution of energy within the whole manifold of antisymmetric states. In the mesoscopic limit, a very large number of such states exist, leading to a quick energy loss from the symmetric subspace to all other subspaces orthogonal to it. This observation could constitute the basis for an effective theory as developed in Ref. [277], which allows for the derivation of an effective unidirectional Markovian loss dynamics for the symmetric operator.

Let us now numerically illustrate the Dicke superradiant behavior for a tightly packed system of emitters and check the analytically obtained results. We depart now from the ideal case of zero separation, and consider a ring of $\mathcal{N} = 8$ molecules with a separation of $d = 0.04_0$. The inclusion of the inherent coherent dipole-dipole interactions leads to a shift of the collective symmetric state which we effectively target in the numerical simulations. These results are illustrated in Fig. 9.2(b) as a function of the environmental temperature for $\lambda = 0.15$. One can clearly observe the washing out of the standard Dicke superradiant pulsed decay, plotted as the intensity of the emitted pulse as a function of time. In the large temperature limit, the independent decay behavior is recovered, signaling that temperature effects hinder the build up of two-particle correlations necessary for the emergence of superradiant behavior. In Fig. 9.2(c), some robustness to positional disorder is observed where each molecule is randomly displaced around its equilibrium position by a normal distribution of standard deviation ϵ. The trajectories are plotted after performing an average over 100 disorder realizations with $\lambda = 0.15$.

Finally, we numerically illustrate time dynamics under resonant laser drive ($\omega_\ell = \omega_{\mathcal{S}}$), modeled by a pulsed excitation with electric field amplitude

$$E_{\text{in}}(t) = \Omega_\ell(t)\sum_{j=1}^{\mathcal{N}}\left(e^{-i\vec{k}_\ell\cdot\vec{r}_j}e^{i\omega_\ell t}\sigma_j + e^{i\vec{k}_\ell\cdot\vec{r}_j}e^{-i\omega_\ell t}\sigma_j^\dagger\right). \tag{8.20}$$

The laser pulse is considered to be impinging from the xy-plane with a linear polarization $\hat{e}_z$ coinciding with the dipole orientation of the molecules. The time dependence is a Gaussian envelope of the form $\Omega_\ell(t) = \eta\,\exp[-(t-t_0)^2/\tau^2]$, with maximum amplitude η and duration τ and the wave vector of the laser is assumed to be $\vec{k}_\ell = k_0\hat{e}_x$. The situation is depicted in Fig. 9.2(d) and shows that superradiant emission is reached even at large temperatures, via the properly tailored pulsed, resonant addressing. In fact, vibronic coupling not only leads to an increase of possible states reachable by the laser which in the Dicke regime ($d \ll_0$) would otherwise be prohibited, but additionally decreases the dephasing stemming from the coherent dipole-dipole interaction and thereby leads to an increased photon emission after the pulse is switched off. Let us

now use our approach to compare our results to analytical predictions [39, 278] which show that superradiant decay of a fully inverted ensemble of two-level emitters can be predicted purely by the geometry of the system by observing that a positive slope of the total emitted intensity $\sum_{ij}\Gamma_{ij}\langle\sigma_i^\dagger\sigma_j\rangle(t)$ at $t=0$ is a good criterion for superradiant emission. The condition derived in these references reads $\sum_{k=1}^{\mathcal{N}}\Gamma_k^2 > 2\mathcal{N}\Gamma_0^2$, where Γ_k are the collective decay rates corresponding in our case to a fixed distance d and zero vibronic coupling. This can be immediately translated to the case of $\mathcal{N}$ identical molecules, where the factor $\exp[-\lambda^2(1+2\bar{n})]$ is crucial, leading to the following condition for the emergence of superradiant decay

$$\sum_{k=1}^{\mathcal{N}}\left(\Gamma_k^{\lambda=0}\right)^2 > \frac{1+e^{-2\lambda^2(1+2\bar{n})}}{e^{-2\lambda^2(1+2\bar{n})}}\mathcal{N}\Gamma_0^2. \tag{8.21}$$

This shows that with increasing temperature and/or vibronic coupling the condition for superradiance to occur is more difficult to meet and in the Dicke limit only one collective decay rate is non-zero and the inequality reduces to

$$\mathcal{N} > \frac{1+e^{-2\lambda^2(1+2\bar{n})}}{e^{-2\lambda^2(1+2\bar{n})}}, \tag{8.22}$$

which sets an upper bound of $\lambda^2(1+2\bar{n}) < \log(\mathcal{N}-1)/2$ for the Huang-Rhys factor λ^2. It then follows that for molecular systems at zero temperature and in the Dicke limit ($d/_0 = 0$), the criteria for the Huang-Rhys factor for which superradiant effects can still be observed is $\lambda^2 < \log(\mathcal{N}-1)/2$.

8.3.3 Dynamics in the single excitation subspace

The single excitation subspace is especially relevant for the case of mesoscopic systems of quantum emitters driven with a very weak excitation pulse. Dipole-dipole interactions induce tunneling behavior between neighboring emitters, allowing the understanding of the system's properties in terms of the band structure or dispersion relations for the propagation of collective excitations. Non-hermitian, dissipative effects such as superradiance and subradiance of such linear systems can also be understood in terms of the localization of collective states within or outside a light cone.

Restricting the Hilbert space to a single excitation, one can recast the Hamiltonian in Eq. (9.2) into the following non-Hermitian form (by disregarding the recycling term in the Lindbladian)

$$\mathcal{H} = \omega_0\sum_{j}^{\mathcal{N}}\sigma_j^\dagger\sigma_j + \sum_{jj'}^{\mathcal{N}}\Big[\Omega_{jj'}^{\lambda}(d) - i\frac{\Gamma_{jj'}^{\lambda}(d)}{2}\Big]\sigma_j^\dagger\sigma_{j'}. \tag{8.23}$$

As mentioned in the previous subsection, the collective basis offers a diagonalization of the dynamics. As opposed to the full Bloch sphere case, in the single excitation one can proceed with diagonalization of both coherent and incoherent parts by writing

$\mathcal{H} = \sum_{k=1}^{\mathcal{N}} \bar{\omega}_k^{\lambda} \mathcal{A}_k^{\dagger} \mathcal{A}_k$ where by definition the symmetric state operator corresponds to the case $\mathcal{S} = \mathcal{A}_{k=\mathcal{N}}$. The eigenenergies and the decay rates are given by the real and imaginary part of the complex eigenvalues

$$\bar{\omega}_k^{\lambda} = \omega_0 + \Omega_k^{\lambda}(d) - i\frac{\Gamma_k^{\lambda}(d)}{2}. \tag{8.24}$$

The excitations can be understood in terms of the quasimomentum $q = 2\pi k/(\mathcal{N}d)$, where due to the periodicity we can define the first Brillouin zone by the index $k = 0, \pm 1, ... \pm \lceil (N-1)/2 \rceil$ where $\lceil x \rceil$ denotes the ceiling function. Note that the center of the Brillouin zone $k = 0$ corresponds to the symmetric mode and the edges at $k_{\pm} = \pm\lceil (\mathcal{N}-1)/2 \rceil$ to the most subradiant modes with degenerate eigenvalues $\omega_{k_{\pm}}$. This can be understood from the wave equation $q^2 + q_{\perp}^2 = (2\pi/_0)^2$ which requires that for modes with $|q|\sigma^{ge} 2\pi/_0$, the radial electric field components are evanescent, i.e., exponentially decaying, and the excitation is guided along the ring. Modes inside the region $|q| \leq 2\pi/_0$ on the other hand have electric field components transverse to the ring and are therefore radiating energy away into the vacuum.

In Fig. 9.3(a) the dispersion relation for a ring of $\mathcal{N} = 100$ molecules is shown for the cases with and without vibronic coupling λ. The region defined by the integer number $|k|\sigma^{ge}\lceil \mathcal{N}d/_0 \rceil$ is occupied by dark states as shown in Fig. 9.3(b) whose decay rates (for a fixed k) are decreasing exponentially with the number of emitters for $\lambda = 0$ [58]. For molecules with a non-zero vibronic coupling λ the exponential scaling gets strongly modified and the decay rates for eigenstates with mode number k are approximately given by $\Gamma_k^{\lambda}/\Gamma_0 \sim (1 - e^{-\lambda^2})$.

While Figs. 9.3(a) and (b) show the real and imaginary parts of the dispersion relation using the reduced Hamiltonian, one can also discuss the dispersion relation in the collective basis including vibrations. The term in Eq. (9.5) illuminates the fact that the presence of vibrations causes a coherent transfer of population between the symmetric mode $\mathcal{S}$ and the dark modes $\mathcal{A}_k$. The coupling strength between the symmetric mode in the vibrational ground state and a dark mode with one vibrational excitation is given by $\lambda\nu/\sqrt{\mathcal{N}}$ which is illustrated in Fig. 9.3(c). Since the vibrational relaxation rate Γ_{ν} is fast compared to the timescale $1/\Gamma_0$ of the electronic decay rate, the population relaxes quickly to the dark state with no vibrational quanta. In general the coupling strength between $\mathcal{S}$ with n vibrations and mode $\mathcal{A}_k$ with $n+1$ vibrations is given by $\langle \mathcal{S}, n | \mathcal{H} | \mathcal{A}_k, n+1 \rangle = \sqrt{(n+1)/\mathcal{N}}\lambda\nu$ where the Hamiltonian includes the vibrational degrees of freedom and in particular the terms in Eq. (9.5)-(8.19) which mediate the coherent transfer. The rate of transfer for a ring geometry is derived in section 8.4 and generally the large vibrational linewidth $\Gamma_{\nu} \gg \Gamma_0$ will create resonances between multiple modes thereby enhancing the population transfer to the dark state manifold.

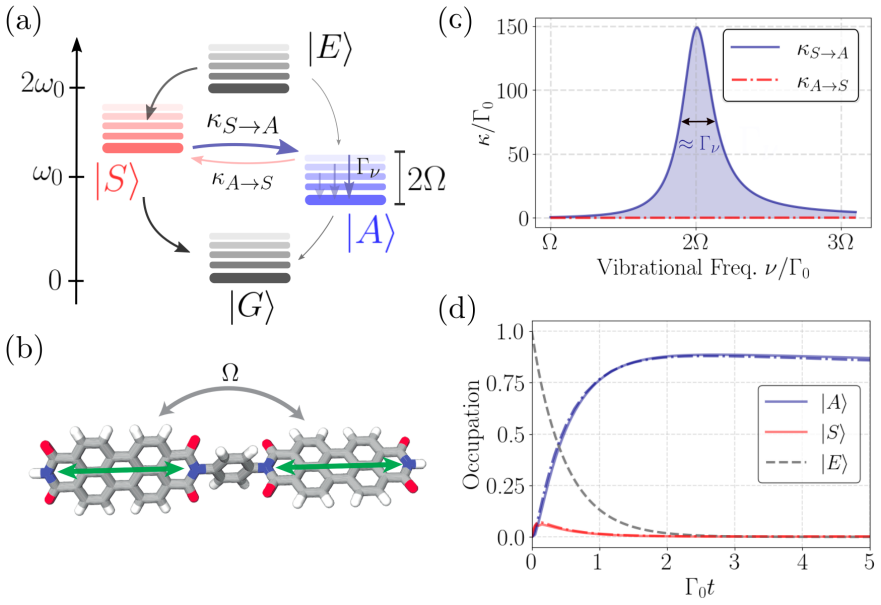

Figure 8.4: (a) Energy diagram showing population transfer between symmetric (superradiant) and antisymmetric (subradiant) collective states via their mutual coupling to the vibrational bath. (b) Illustration of a molecular dimer where two identical chromophores are separated by an insulating bridge. Energy transfer between the two chromophores can take place via near field coupling on length on the order of nanometers. The situation depicted here shows in-plane dipoles (resulting in $\Omega < 0$). (c) Energy transfer rates between the symmetric and antisymmetric dimer state as a function of the vibrational frequency. (d) Time evolution of a fully inverted molecular dimer. The fully excited state decays exponentially via the symmetric state which transfers energy to the antisymmetric state. The analytical results in dashed-dotted lines show a good agreement. Parameters are $\nu = 2\Omega, d =_0 /40, \Gamma_\nu = 30\Gamma_0, \lambda = 0.1, \Omega(d) \approx 191.1\Gamma_0$ and polarization perpendicular to dimer axis.

8.4 Subradiant state preparation in molecular dimers and rings

Molecular dimers are ideal for the study of dipole-dipole induced energy shifts at very small separations and for the study of the interplay between electronic and vibrational quantum superpositions [279]. In such compounds, two chromophores are linked by insulating bridges which do not allow for charge migration and do not shift the bare electronic transitions. In Ref. [280], an experimental study of molecular dimers shows the possibility to control the inter-chromophoric distance from 1.3 nm to 2.6 nm while keeping the orientation of each chromophore dipole fixed. Previous theoretical studies have focused mainly on the purely coherent interactions and have neglected the effects

of vibrational relaxation and collective spontaneous emission [281–283].

Here, we show that the coupling between symmetric (bright) and antisymmetric (dark) collective states in a vibronic dimer, combined with the vibrational relaxation can lead to an efficient preparation of long-lived quantum entangled states of the two chromophores (see Fig. 8.4). The mechanism is reminiscent of the process of FRET (Förster resonance energy transfer) between donor and acceptor molecules, where coherent energy exchanges followed by quick vibrational relaxation can lead to a unidirectional flow of energy.

The model is described by the free Hamiltonians $h_0^{(1)} + h_0^{(2)}$ to which we add $h_{\text{Hol}}^{(2)} + h_{\text{Hol}}^{(2)}$ and the two-particle term $\mathcal{H}_{\text{d-d}} = \Omega(\sigma_1^\dagger\sigma_2 + \sigma_2^\dagger\sigma_1)$ describing excitation exchange between the two chromophores via the near field dipole-dipole coupling. We make use of the collective basis representation with $\mathcal{S} = (\sigma_1+\sigma_2)/\sqrt{2}$ as the symmetric operator and a single antisymmetric, orthogonal operator $\mathcal{A} = (\sigma_1 - \sigma_2)/\sqrt{2}$. We define collective vibrational quadratures $Q_\pm = (q_1 \pm q_2)/\sqrt{2}$ and $P_\pm = (p_1 \pm p_2)/\sqrt{2}$ as well. The free Hamiltonian of electronic and vibrational degrees of freedom then can be expressed as

$$\mathcal{H}_0^{\text{dim}} = \omega_{\mathcal{S}}\mathcal{S}^\dagger\mathcal{S} + \omega_{\mathcal{A}}\mathcal{A}^\dagger\mathcal{A} + \frac{\nu}{4}\sum_{k=\pm}(Q_k^2 + P_k^2), \tag{8.25}$$

where the collective states frequencies $\omega_{\mathcal{S}} = \tilde{\omega}_0 + \Omega - \lambda\nu Q_+/\sqrt{2}$ and $\omega_{\mathcal{A}} = \tilde{\omega}_0 - \Omega - \lambda\nu Q_+/\sqrt{2}$ become now operators which include the symmetric vibrational coordinate. The energy scheme of the dimer is presented in Fig. 8.4(a) showing vibrationally-dressed collective electronic states. While in the absence of motion the symmetric and antisymmetric states are orthogonal to each other, this is no longer the case when vibrations are included allowing for transitions between them. The vibrational degrees of freedom then couple the two states via the relative motion coordinate Q_-

$$\mathcal{H}_{\text{int}}^{\text{dim}} = -\frac{\lambda\nu}{\sqrt{2}}Q_-(\mathcal{S}^\dagger\mathcal{A} + \mathcal{A}^\dagger\mathcal{S}), \tag{8.26}$$

such that the total dimer Hamiltonian expresses as $\mathcal{H}_0^{\text{dim}} + \mathcal{H}_{\text{int}}^{\text{dim}}$. The interaction term in Eq. (8.26) can mediate transfer of excitation between the bright and dark state through the annihilation or creation of a vibrational quantum of the relative motion coordinate. Under the assumption that the vibrational relaxation is fast as compared to the coherent coupling $\Gamma_\nu \gg \lambda\nu$ as well as all other decay rates, a perturbative set of rate equations for the populations $p_= \langle\dagger\rangle$ and $p_= \langle\dagger\rangle$ can be obtained (for derivation see Appendix 8.7.3)

$$\dot{p} = -(\Gamma_+\kappa_\rightarrow)p_+\kappa_\rightarrow p_, \tag{8.27a}$$

$$\dot{p} = -(\Gamma_+\kappa_\rightarrow)p_+\kappa_\rightarrow p_, \tag{8.27b}$$

with transfer rate from the symmetric to antisymmetric state

$$\kappa_\rightarrow = \frac{\lambda^2\nu^2\Gamma_\nu/2}{(\Gamma_\nu/2)^2 + (2\Omega - \nu)^2}. \tag{8.28}$$

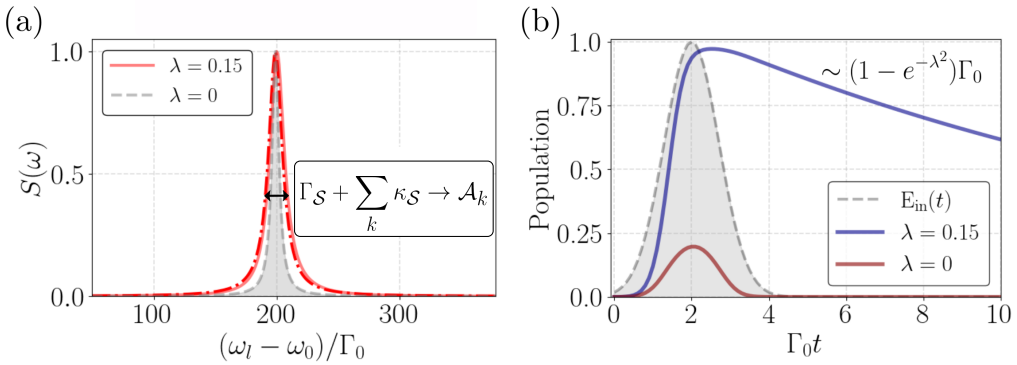

Figure 8.5: (a) Absorption spectrum in steady state for a ring with $\mathcal{N} = 7$ molecules with the linewidth of the symmetric state broadened by the sum of the energy transfer rates to the dark state manifold. The dashed-dotted line is a Lorentzian with linewidth given by $\Gamma_S + \sum_k \kappa_{S\to\mathcal{A}_k}$ and maximum at $\omega_\ell = \omega_0 + \Omega_S^{\lambda=0}$. (b) Laser pulse with a Gaussian time profile as in Eq. (8.20) with $\eta = 2.5\ \Gamma_0, t_0 = 2/\Gamma_0, \tau = 1/\Gamma_0$. The laser frequency ω_ℓ is tuned to the superradiant mode $k = 0$. The single excitation manifold is populated almost with unity and decays with a subradiant rate $\sim \Gamma_0(1 - e^{-\lambda^2})$ afterwards. Further parameters for both plots are $d =_0 /30, \Gamma_\nu = 100\Gamma_0, \lambda = 0.15, \nu = 120\Gamma_0$.

The transfer from the antisymmetric to symmetric state $\kappa_{\to}$ has a similar expression, however with a term $(2\Omega + \nu)$ present in the denominator. For $\Omega > 0$ the resonance condition is given by $2\Omega = \nu$ leading to unidirectional transfer from the symmetric to the antisymmetric state while the back transfer is off-resonant and therefore suppressed [see Fig. 8.4(c)]. In Fig. 8.4(d) we plot the time dynamics of a dimer initialized in the fully excited state $|E\rangle$ under this resonance condition. Initial decay to the symmetric state is followed immediately by a rapid transfer to the antisymmetric state, causing only a small temporary population in the symmetric state and a large accumulation of population in the antisymmetric state. Remarkably, this can lead to a near-unity population in the antisymmetric state even for moderate vibronic coupling strengths λ. Since vibrational frequencies are on the order of $\nu/2\pi \sim 10\,\mathrm{THz}$ and the spontaneous emission rate is on the order of $\Gamma_0/2\pi \sim 10\,\mathrm{MHz}$, this resonance condition requires dipole-dipole shifts on the order of $\sim 10^6\,\Gamma_0$ which can be achieved by dimers with nm separations.

Let us finally remark that the dark state preparation scheme described here for the dimer can be extended to configurations of many molecules in the ring configuration. To this end we have performed numerical simulations showing the drive of collective states which are not accessible via direct illumination but are populated via the incoherent, vibrationally mediated transfer. In Fig. 8.5(a), the enhanced absorption profile for a ring of $\mathcal{N} = 7$ molecules signals the transfer of population from the symmetric, laser accessible collective state to a number of initially dark states. The

increase in the linewidth is simply given by the sum of all transfer rates to the dark state manifold which are obtained as a generalization of the dimer result

$$\sum_k \kappa_{\mathcal{S}\to\mathcal{A}_k} = \sum_k \frac{\lambda^2\nu^2\Gamma_\nu/2}{(\Gamma_\nu/2)^2 + (\Omega_\mathcal{S} - \Omega_{\mathcal{A}_k} - \nu)^2}. \tag{8.29}$$

In Fig. 8.5(b) the total population is shown following a pulsed excitation with the laser frequency tuned to the superradiant mode. The numerical fit shows that most population is trapped into dark states with an effective overall decay constant equal to $\Gamma_0(1 - e^{-\lambda^2})$, as predicted in Sec. 8.3.3.

8.5 Molecular coherent light sources

The formalism developed in the previous section allows us to tackle platforms such as molecular nano-rings illuminated by incoherent light, as recently advanced in Ref. [143]. It has been suggested that these might act as natural filters with coherent light as output. The situation is illustrated in Fig. 10.1(d): an incoherently pumped (at rate η_p) central emitter couples to the waveguide-like light modes supported by the ring of surrounding $\mathcal{N}$ emitters. While the treatment in Ref. [143] has been restricted to ideal, identical two level systems and strongly relied on numerical evidence, we aim here at providing a deeper analytical understanding and the natural extension to more complex, molecular quantum emitters. Our analysis is based on simplifications brought on by the transition from the bare basis to the collective basis.

We will make use of results in the following section and notice that the central pump molecule is solely coupled to the symmetric combination of the ring molecules with the Hamiltonian

$$\mathcal{H}_p = \omega_p\sigma_p^\dagger\sigma_p + \sqrt{\mathcal{N}}\Omega_p^\lambda(d)\left[\sigma_p^\dagger\mathcal{S} + \mathcal{S}^\dagger\sigma_p\right]. \tag{8.30}$$

As the symmetric operator creates delocalized excitations over the whole ring, the coupling above benefits from the collective enhancement with $\sqrt{\mathcal{N}}$ multiplying the dipole-dipole exchange rate $\Omega_p^\lambda(d)$ which is dependent on the ring radius $r = d/[2\sin(2\pi/\mathcal{N})]$. Notice that the effect of vibrations has already been taken into account by the renormalization of any dipole-dipole coherent and incoherent exchanges with the Huang-Rhys factor (denoted by the index λ). The effect is mainly detrimental as the coherent coupling between the pump emitter and the waveguide emitters is scaled down both with λ and with temperature.

The dissipative part of the master equation governing the whole system's evolution includes the usual terms characterizing the decay of the ring molecules, adding to the diagonal decay of the pump molecule and the mutual incoherent coupling between pump and ring molecules of the form

$$\mathcal{L}_p[\rho] = \frac{\sqrt{\mathcal{N}}\Gamma_p^\lambda(d)}{2}\Big[2\mathcal{S}\rho\sigma_p^\dagger + 2\sigma_p\rho\mathcal{S}^\dagger - \{\mathcal{S}^\dagger\sigma_p + \sigma_p^\dagger\mathcal{S}, \rho\}\Big], \tag{8.31}$$

where $\Gamma_p^\lambda(d)$ the incoherent coupling between the pump molecule and each of the ring molecules. In addition, incoherent pump is modeled as an inverted spontaneous emission process: this is in Lindblad form but with a collapse operator $\sigma_p^\dagger$ and rate η_p

$$\mathcal{L}_{\eta_p}[\rho] = \frac{\eta_p}{2}\Big[2\sigma_p^\dagger\rho\sigma_p - \{\sigma_p\sigma_p^\dagger, \rho\}\Big]. \tag{8.32}$$

To characterize the emission properties of the system, one makes use of both the

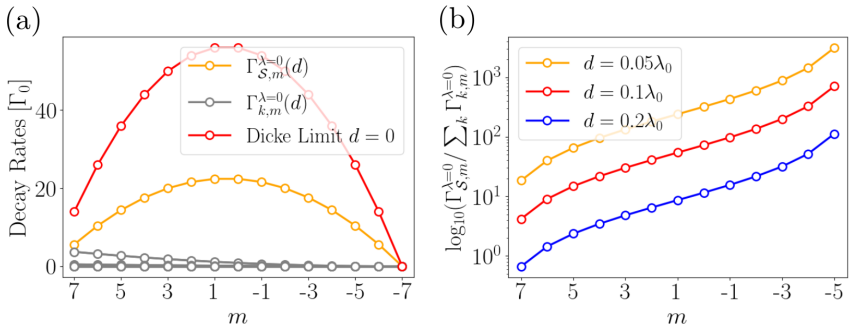

Figure 8.6: (a) State dependent decay rates via symmetric and antisymmetric loss channels for the ring configuration of $\mathcal{N} = 14$ emitters placed in in the xy-plane with separation $d = 0.1_0$ and dipole polarization in the z-direction. A comparison with the full Dicke limit is provided. (b) The ratio between the state dependent symmetric decay rate and the sum of the dark decay rates as a function of the inversion quantum number m. It can be seen that loss of excitations takes place mainly via the symmetric decay channel even at distances of the order $d = 0.2_0$.

emitted light intensity $\mathcal{I}_{\text{out}}$ as well as of the $g^{(2)}$-function at zero time delay. We proceed by using the definitions from Ref. [143] in the uncoupled basis before performing our analysis in the alternative collective basis. The intensity in the bare, uncoupled basis is a sum over the following terms $\mathcal{I}_{\text{out}} = \sum_{jj'}^{\mathcal{N}+1}\Gamma_{jj'}^\lambda\langle\sigma_j^\dagger\sigma_{j'}\rangle$, where now the sum extends to the additional site which is the pump molecule. In the collective basis this can be expressed as

$$\begin{aligned}\mathcal{I}_{\text{out}} = \Gamma_{\mathcal{S}}^\lambda(d)\langle\mathcal{S}^\dagger\mathcal{S}\rangle + \sum_{k=1}^{\mathcal{N}-1}\Gamma_k^\lambda(d)\langle\mathcal{A}_k^\dagger\mathcal{A}_k\rangle \\ + 2\sqrt{\mathcal{N}}\Gamma_p^\lambda(d)\text{Re}\langle\mathcal{S}^\dagger\sigma_p\rangle + \Gamma_0\langle\sigma_p^\dagger\sigma_p\rangle.\end{aligned} \tag{8.33}$$

For small inter-emitter separation $d \ll_0$ the ring contribution can be expressed purely in terms of the symmetric mode as decay into antisymmetric states is negligible $\Gamma_k^\lambda(d)/\Gamma_0 \ll 1$. This can be easily justified by computing the branching of loss rates from a given symmetric state $|\mathcal{N}/2, m\rangle$ into the symmetric manifold and outside of it, into any dark decay channel k by via the Lindbladian in Eq. (8.5). One obtains the state dependent decay rates $\Gamma_{k,m}^{\lambda=0}(d) = \alpha_m^{(-)2}\Gamma_k^{\lambda=0}(d)/(\mathcal{N}-1)$ and the state dependent

decay into the symmetric channel $\Gamma^{\lambda=0}_{\mathcal{S},m}(d) = \alpha^{(-)2}_m \Gamma^{\lambda=0}_{\mathcal{S}}(d)$. In Fig. 8.6 we plot these rates as a function of the quantum number m as well as the ratio $\Gamma^{\lambda=0}_{\mathcal{S},m}/\sum_k \Gamma^{\lambda=0}_{k,m}$ to show that the restriction of the dynamics to the symmetric subspace is a good approximation for small but still finite distances.

Moreover, this approximation is also well justified under weak excitation conditions

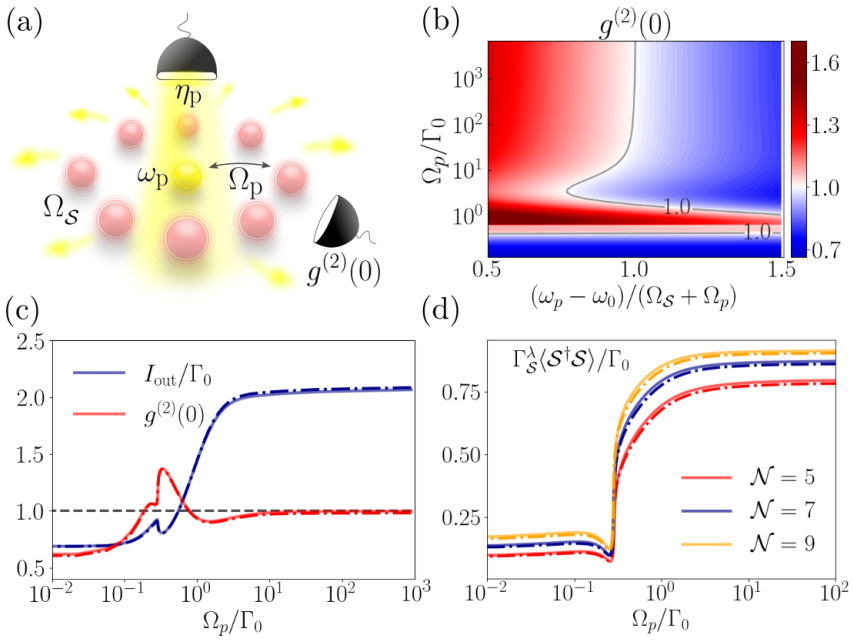

Figure 8.7: (a) Molecular ring acting as a waveguide coupled to a central, incoherently pumped molecule, at electronic transition frequency ω_p optimally adjusted to fit a waveguide resonance $\omega_0 + \Omega^{\lambda=0}_{\mathcal{S}} + \Omega^{\lambda=0}_p$. (b) The $g^{(2)}(0)$-function in the case of $\mathcal{N} = 5$ ring emitter in the absence of vibronic coupling for various tunings ω_p and coupling strengths Ω_p for $\eta_p = 3\Gamma_0$. (c) A cut along the optimal resonance frequency ω_p showing the steady state emission rate alongside the $g^{(2)}(0)$-function for $\eta_p = 3\Gamma_0, r = 0.05_0$. (d) Steady state photon emission for $\eta_p = \Gamma_0$ taking only the symmetric ring contribution in Eq. (8.33) into account. A clear threshold for the ring emission emerges at a coupling strength $\Omega^{\lambda=0}_p/\Gamma_0 \approx 1$. The dashed-dotted lines represent $\lambda = 0.15$ and the continuous lines $\lambda = 0$ in all plots.

and with small vibronic couplings. The reason is transparent from Eq. (8.30) which shows that the incoherent pump of the central molecules feeds only the symmetric mode which, in the single excitation regime can only decay back to the ground state, thus not allowing to trap population into robust, antisymmetric states. This is no longer true at higher excitations and in the presence of strong vibronic coupling, where antisymmetric collapse operators can bring population out of the symmetric manifold.

In Fig. 8.7(d) we illustrate the intensity of emitted light taking only the symmetric ring mode into account, namely $\Gamma_{\mathcal{S}}^{\lambda}(d)\langle\mathcal{S}^{\dagger}\mathcal{S}\rangle$ as a function of the coupling strength with a threshold at $\Omega_p^{\lambda}(d) \approx \Gamma_0$ after which the emission intensity is sharply increasing. While analytical calculations are possible for a wide range of parameters, the results are cumbersome; we therefore restrict here to the simplified case with $\Gamma_p^{\lambda} = 0$ (for full set of equations see the supplemental material):

$$\langle\mathcal{S}^{\dagger}\mathcal{S}\rangle = \frac{\mathcal{N}\bar{\Gamma}\eta_p{\Omega_p^{\lambda}}^2}{\Gamma_{\mathcal{S}}^{\lambda}(\Gamma_0+\eta_p)\left[\left(\bar{\Gamma}/2\right)^2+{\Omega_{\mathcal{S}}^{\lambda}}^2\right]+\bar{\Gamma}^2\mathcal{N}{\Omega_p^{\lambda}}^2}, \tag{8.34}$$

where $\bar{\Gamma} = \Gamma_0 + \eta_p + \Gamma_{\mathcal{S}}^{\lambda}$. The situation is relevant for the ideal geometry chosen in Ref. [143] which insured a maximal coherent coupling between the pumped, central emitter while allowing for the mutual dissipative coupling to vanish.

In order to characterize statistics of the emitted light, the second order correlation function with zero time delay is used which is defined via the electric field radiated by an ensemble of dipole emitters [62]. Due to the symmetrical ring geometry, the $g^{(2)}$-function in steady state at a detection distance $|r| \gg_0$ in the plane of the ring can be expressed purely in terms of the electronic transition operators as [143]

$$g^{(2)}(0) = \frac{\sum_{ijkl}^{\mathcal{N}+1}\langle\sigma_i^{\dagger}\sigma_j^{\dagger}\sigma_k\sigma_l\rangle}{\left(\sum_{ij}^{\mathcal{N}+1}\langle\sigma_i^{\dagger}\sigma_j\rangle\right)^2} = \frac{4\mathcal{N}\langle\mathcal{S}^{\dagger}\mathcal{S}\sigma_p^{\dagger}\sigma_p\rangle + 4\mathcal{N}^{\frac{3}{2}}\mathrm{Re}\langle\mathcal{S}^{\dagger}\mathcal{S}^{\dagger}\mathcal{S}\sigma_p\rangle + \mathcal{N}^2\langle\mathcal{S}^{\dagger}\mathcal{S}^{\dagger}\mathcal{S}\mathcal{S}\rangle}{\left(\mathcal{N}\langle\mathcal{S}^{\dagger}\mathcal{S}\rangle + 2\sqrt{\mathcal{N}}\mathrm{Re}\langle\mathcal{S}^{\dagger}\sigma_p\rangle + \langle\sigma_p^{\dagger}\sigma_p\rangle\right)^2}. \tag{8.35}$$

A second order correlation function equal to unity is used as a figure of merit for coherent light emission and in Fig. 8.7(b) it is shown that an optimal resonance frequency $\omega_p = \omega_0 + \Omega_{\mathcal{S}}^{\lambda=0} + \Omega_p^{\lambda=0}$ for the central molecule leads to coherent light emission in particular in the strong coupling regime $\Omega_p^{\lambda=0} \gg \Gamma_0$. Setting the optimal resonance frequency for the pumped molecule, Fig. 8.7(c) shows the total steady state intensity alongside the $g^{(2)}(0)$ as a function of the coupling strength where the sudden increase of intensity stems from the ring contribution as shown in Fig. 8.7(d). This sudden increase originates from a coupling strength which attains the same magnitude as the incoherent loss rate into the vacuum modes Γ_0 of the pumped molecule. Consequently, in the strong coupling regime the majority of the excitation in the center is coherently transfered to the ring.

8.6 Conclusions

We have provided a largely analytical approach to the description of light-matter cooperativity in molecular arrays, where subwavelength emitter-emitter separations lead to the occurrence of a strong coherent and incoherent collective response. The effect of molecular vibrations has been incorporated via the Holstein Hamiltonian, that

describes vibronic coupling between electronic and nuclear degrees of freedom. In a first step, we have identified analytical scaling laws which characterize phenomena such as super- and subradiance in molecular rings. The ring configuration, as characterized by periodic boundary conditions, allow for the natural extension to mesoscopic systems. For the situation of Dicke superradiance, we find that a collective basis description provides insight into how the superradiant pulse intensity is lost into antisymmetric, dark channels coupled via vibrations. In the low excitation regime, we have analyzed the open system band diagram and found the imprint of the vibrational coupling on both energy and loss rate bands. For molecular dimers, in which case near field couplings are considerably large, we have shown that long-lived bipartite entanglement at the level of electronic degrees of freedom can be produced via dissipative effects such as vibrational relaxation. For incoherently pumped, nanoscale coherent light sources, we have provided analytical results supplementing the results in Ref. [143] and an extension to molecular emitters.

Acknowledgments – We acknowledge fruitful discussions with Christian Sommer. We acknowledge financial support from the Max Planck Society and the Deutsche Forschungsgemeinschaft (DFG, German Research Foundation) – Project-ID 429529648 – TRR 306 QuCoLiMa ("Quantum Cooperativity of Light and Matter"). M. R. acknowledges financial support from the International Max Planck Research School - Physics of Light (IMPRS-PL). R. H. acknowledges funding from the Austrian Science Fund (FWF) doctoral college DK-ALM W1259-N27.

8.7 Supplemental material

8.7.1 Vibronic coupling

Let us justify the form of the Holstein Hamiltonian in Eq. (9.1) by following a first-principle derivation for a single nuclear coordinate R of effective mass μ. We assume that, along the nuclear coordinate, the equilibria for ground (coordinate R_g , state vector $|g\rangle$) and excited (coordinate R_e and state vector $|e\rangle$) electronic orbitals are different. Assuming equilibrium positions R_g and R_e for the potential surfaces of electronic ground and excited states, one can write the total molecular Hamiltonian describing both electronic and vibrational dynamics as

$$\mathcal{H}_{\mathrm{mol}} = \left[\omega_0 + \frac{\hat{P}^2}{2\mu} + \frac{1}{2}\mu\nu^2\left(\hat{R} - R_e\right)^2\right]\sigma^\dagger\sigma + \left[\frac{\hat{P}^2}{2\mu} + \frac{1}{2}\mu\nu^2\left(\hat{R} - R_g\right)^2\right]\sigma\sigma^\dagger, \quad (8.36)$$

where μ is the reduced mass of the vibrational mode. The kinetic and potential energies are written in terms of the position $\hat{Q}$ and momentum operator $\hat{P}$ describing the nuclear coordinate under consideration, with commutation $[\hat{Q}, \hat{P}] = i$. Introducing oscillations around the equilibria $\hat{Q} = \hat{R} - R_{\mathrm{g}}$ and subsequently $\hat{R} - R_{\mathrm{e}} = \hat{Q} + R_{\mathrm{g}} - R_{\mathrm{e}} =: \hat{Q} - R_{\mathrm{ge}}$

we obtain

$$\mathcal{H}_{\mathrm{mol}} = \frac{\hat{P}^2}{2\mu} + \frac{1}{2}\mu\nu^2\hat{Q}^2 + \omega_0\sigma^\dagger\sigma - \mu\nu^2\hat{Q}R_{\mathrm{ge}}\sigma^\dagger\sigma + \frac{1}{2}\mu\nu^2R_{\mathrm{ge}}^2\sigma^\dagger\sigma. \tag{8.37}$$

We can now rewrite the momentum and position operators in terms of bosonic operators $\hat{Q} = q_{\mathrm{zpm}}(b^\dagger + b)$, $\hat{P} = ip_{\mathrm{zpm}}(b^\dagger - b)$. The bosonic operators satisfy the usual commutation relation $[b, b^\dagger] = 1$ and the zero-point motion displacement and momentum are defined as $q_{\mathrm{zpm}} = 1/\sqrt{2\mu\nu}$ and $p_{\mathrm{zpm}} = \sqrt{\mu\nu/2}$. Reexpressing the terms above yields the Holstein Hamiltonian [20]

$$\mathcal{H}_{\mathrm{mol}} = (\omega_0 + \lambda^2\nu)\sigma^\dagger\sigma + \nu b^\dagger b - \lambda\nu(b^\dagger + b)\sigma^\dagger\sigma. \tag{8.38}$$

The dimensionless vibronic coupling strength λ is given by $\lambda = \mu\nu R_{\mathrm{ge}}q_{\mathrm{zpm}}$ (λ^2 is called the Huang-Rhys factor and is typically on the order of $\sim 0.01 - 1$).

The polaron transformation

The Holstein Hamiltonian can be diagonalized via a level-dependent polaron transformation $\mathcal{U}^\dagger = |g\rangle\langle g| + \mathcal{D}^\dagger|e\rangle\langle e|$ with the standard displacement operator $\mathcal{D} = e^{-i\sqrt{2}\lambda p} = e^{\lambda(b^\dagger - b)}$. In the polaron-displaced basis, the Holstein Hamiltonian becomes $\tilde{\mathcal{H}}_{\mathrm{mol}} = \mathcal{U}^\dagger\mathcal{H}_{\mathrm{mol}}\mathcal{U} = \omega_0\sigma^\dagger\sigma + \nu b^\dagger b$ and has simple eigenvectors $|g;n\rangle$ and $|e;n\rangle$. The eigenvectors in the bare, original basis can be found by inverting the polaron transformation $|g;n\rangle$ and $\mathcal{D}|e;n\rangle$. The polaron-transformed probe Hamiltonian is then expressed as $\tilde{\mathcal{H}}_\ell = i\eta(\sigma^\dagger\mathcal{D}^\dagger e^{-i\omega_\ell t} - \sigma\mathcal{D}e^{i\omega_\ell t})$. One can now look for selection rules applying to processes such as stimulated emission and absorption induced by the external optical drive. To this end, we focus on absorption (as emission is similar) by assuming an initial state $|g;0\rangle$ in the displaced basis and asking for the probability of exciting the system to state $|e;n\rangle$. This is easily computed to lead to

$$P_{\mathrm{abs}}(n) = |\langle e;n|\sigma^\dagger\mathcal{D}^\dagger|g;0\rangle|^2 = e^{-\lambda^2}\frac{\lambda^{2n}}{n!}, \tag{8.39}$$

which is the expected Poissonian distribution leading to the Franck-Condon principle for molecular transitions. For dissipative radiative processes, we notice that the Lindblad collapse operator is also transformed to the polaron one $\sigma\mathcal{D}$ such that spontaneous emission follows the same Poissionian distribution in taking the electronic state from $|e;0\rangle$ to $|g;n\rangle$.

Thermal averaging of vibrational effects

Assuming a thermal state for the vibrational modes we are going to calculate the trace of a single vibrational displacement operator $\mathcal{D}^\dagger = e^{-\lambda^2/2} e^{-\lambda b^\dagger} e^{\lambda b}$:

$$\begin{aligned}\langle \mathcal{D}^\dagger \rangle_T &= \mathrm{Tr}[\mathcal{D}^\dagger \rho_{\mathrm{th}}] = e^{-\lambda^2/2} \mathrm{Tr}[e^{-\lambda b^\dagger} e^{\lambda b} \rho_{\mathrm{th}}] = \\ &= e^{-\lambda^2/2} \sum_{n=0}^{\infty} e^{-\beta\nu n}(1 - e^{-\beta\nu}) \langle n| \sum_{m,l} \frac{(-\lambda^m)\lambda^l}{m!l!} (b^\dagger)^m b^l |n\rangle \\ &= e^{-\lambda^2/2} \sum_{n=0}^{\infty} e^{-\beta\nu n}(1 - e^{-\beta\nu}) \sum_{m=0}^{n} \frac{(-\lambda^2)^m}{m!} \binom{n}{m} \\ &= e^{-\lambda^2/2}(1 - e^{-\beta\nu}) \sum_{m=0}^{\infty} \frac{(-\lambda^2)^m}{m!} \sum_{n=m}^{\infty} e^{-\beta\nu n} \binom{n}{m},\end{aligned} \tag{8.40}$$

where we made use of the sum identity $\sum_{i=k}^{n} \sum_{j=k}^{i} a_{i,j} = \sum_{j=k}^{n} \sum_{i=j}^{n} a_{i,j}$ in the last step. Additionally making use of the binomial identity $\sum_{n=k}^{\infty} \binom{n}{k} y^n = \frac{y^k}{(1-y)^{k+1}}$ one readily obtains

$$\langle \mathcal{D}^\dagger \rangle_T = e^{-\lambda^2/2} \sum_{m=0}^{\infty} \frac{(-\lambda^2)^m}{m!} \frac{e^{-\beta\nu m}}{(1 - e^{-\beta\nu})^m} = e^{-\lambda^2/2(1+2\bar{n})} = e^{-\frac{\lambda^2}{2} \coth\left(\frac{\hbar\nu}{2k_B T}\right)}. \tag{8.41}$$

8.7.2 Vacuum mediated coherent and incoherent coupling rates

The vacuum mediated dipole-dipole interactions for an electronic transition at wavelength $_0$ (corresponding wave vector $k = 2\pi/_0$) between an identical pair of emitters separated by r_{ij} is

$$\Omega_{ij} = \frac{3}{4}\Gamma_0 \left[(1 - 3\cos^2\theta) \left(\frac{\sin(kr_{ij})}{(kr_{ij})^2} + \frac{\cos(kr_{ij})}{(kr_{ij})^3} \right) - \sin^2\theta \frac{\cos(kr_{ij})}{(kr_{ij})} \right]. \tag{8.42}$$

The quantity θ is the angle between the dipole moment $\mathbf{d}$ and the vector $\mathbf{r}_{ij}$. The associated collective decay is quantified by the following mutual decay rates

$$\Gamma_{ij} = \frac{3}{2}\Gamma_0 \left[(1 - 3\cos^2\theta) \left(\frac{\cos(kr_{ij})}{(kr_{ij})^2} - \frac{\sin(kr_{ij})}{(kr_{ij})^3} \right) + \sin^2\theta \frac{\sin(kr_{ij})}{(kr_{ij})} \right]. \tag{8.43}$$

8.7.3 Vibrationally mediated energy transfer rates in the collective basis

The Holstein Hamiltonian rewritten in a collective basis both for the electronic as well as the vibrational degrees of freedom has the following form

$$\mathcal{H}^{\mathrm{dim}} = \omega_{\mathcal{S}}(Q_+)\mathcal{S}^\dagger\mathcal{S} + \omega_{\mathcal{A}}(Q_+)\mathcal{A}^\dagger\mathcal{A} - \frac{\lambda\nu}{\sqrt{2}} Q_-(\mathcal{S}^\dagger\mathcal{A} + \mathcal{A}^\dagger\mathcal{S}) + \nu \sum_{k=\pm} b_k^\dagger b_k, \tag{8.44}$$

where the energies of the collective state frequencies depend on the symmetric vibrational coordinate $\omega_{\mathcal{S}}(Q_+) = \omega_0 + \lambda^2\nu + \Omega - \lambda\nu Q_+/\sqrt{2}$ and $\omega_{\mathcal{A}}(Q_+) = \omega_0 + \lambda^2\nu - \Omega - \lambda\nu Q_+/\sqrt{2}$. We note that the Q_+-dependent shifts can be removed by the collective polaron transforms $\mathcal{U}_{\mathcal{S}} = e^{i\lambda P_+ \mathcal{S}^\dagger\mathcal{S}/\sqrt{2}}$ and $\mathcal{U}_{\mathcal{A}} = e^{i\lambda P_+ \mathcal{A}^\dagger\mathcal{A}/\sqrt{2}}$ which transform the symmetric nuclear coordinates as

$$\mathcal{U}_{\mathcal{S}} Q_+ \mathcal{U}_{\mathcal{S}}^\dagger = Q_+ + \sqrt{2}\lambda\mathcal{S}^\dagger\mathcal{S}, \tag{8.45a}$$

$$\mathcal{U}_{\mathcal{A}} Q_+ \mathcal{U}_{\mathcal{A}}^\dagger = Q_+ + \sqrt{2}\lambda\mathcal{A}^\dagger\mathcal{A}, \tag{8.45b}$$

and lead to a renormalization of the state energies $\tilde{\omega}_{\mathcal{A}} = \omega_0 + \lambda^2\nu/2 + \Omega$ and $\tilde{\omega}_{\mathcal{S}} = \omega_0 + \lambda^2\nu/2 - \Omega$. The equations of motion for the operators are given by

$$\dot{\mathcal{S}} = -\Big[i\tilde{\omega}_+ \frac{\Gamma}{2}\Big]\mathcal{S} + \frac{i\lambda\nu}{\sqrt{2}} Q_- \mathcal{A} + \sqrt{\Gamma}\mathcal{S}_{\text{in}}, \tag{8.46a}$$

$$\dot{\mathcal{A}} = -\Big[i\tilde{\omega}_+ \frac{\Gamma}{2}\Big]\mathcal{A} + \frac{i\lambda\nu}{\sqrt{2}} Q_- \mathcal{S} + \sqrt{\Gamma}\mathcal{A}_{\text{in}}, \tag{8.46b}$$

where $\mathcal{S}_{\text{in}} = (\sigma_{1,\text{in}} + \sigma_{2,\text{in}})/\sqrt{2}$ and $\mathcal{A}_{\text{in}} = (\sigma_{1,\text{in}} - \sigma_{2,\text{in}})/\sqrt{2}$ are the collective noise terms which we will neglect from now on as they do not contribute to the transfer process.

To calculate the transfer rate from the symmetric state to the antisymmetric state we assume some initial population in the symmetric state and no population in the antisymmetric state, additionally we assume that the symmetric state decays independently and formally integrate

$$\mathcal{S}(t) = S(0)e^{-(i\tilde{\omega}_+\Gamma/2)t}, \tag{8.47a}$$

$$\mathcal{A}(t) = A(0)e^{-i(\tilde{\omega}_+\Gamma/2)t} + \frac{i\lambda\nu}{\sqrt{2}}\int_0^t dt' e^{-i(\tilde{\omega}_+\Gamma/2)(t-t')} Q_-(t')\mathcal{S}(t'), \tag{8.47b}$$

and for the expectation value of the populations we get

$$\langle\dot{\mathcal{S}^\dagger\mathcal{S}}\rangle = -\Gamma_{\langle\mathcal{S}^\dagger\mathcal{S}\rangle} - \sqrt{2}\lambda\nu\,\text{Im}\langle\mathcal{S}^\dagger\mathcal{A}Q_-\rangle, \tag{8.48a}$$

$$\langle\dot{\mathcal{A}^\dagger\mathcal{A}}\rangle = -\Gamma_{\langle\mathcal{A}^\dagger\mathcal{A}\rangle} - \sqrt{2}\lambda\nu\,\text{Im}\langle\mathcal{A}^\dagger\mathcal{S}Q_-\rangle. \tag{8.48b}$$

Therefore, the term $-\sqrt{2}\lambda\nu\,\text{Im}\langle\mathcal{A}^\dagger\mathcal{S}Q_-\rangle$ will be responsible for population transfer from the symmetric to the antisymmetric state at a rate $\kappa_{\mathcal{S}\to\mathcal{A}}$ and we can calculate

$$\begin{aligned}-\sqrt{2}\lambda\nu\langle\mathcal{A}^\dagger\mathcal{S}Q_-\rangle &= -i\lambda^2\nu^2\int_0^t dt' e^{-\epsilon_(t-t')}\langle Q_-(t')Q_-(t)\rangle\langle\mathcal{S}^\dagger(0)\mathcal{S}(0)\rangle e^{-\epsilon'_t}e^{-\epsilon^*_t} \\ &= -i\lambda^2\nu^2\langle\mathcal{S}^\dagger(0)\mathcal{S}(0)\rangle\frac{e^{-\Gamma_t} - e^{-((\Gamma_\nu+\Gamma_-\Gamma_)/2+i(\omega_-\omega_-\nu))t}}{(\Gamma_\nu+\Gamma_-\Gamma_)/2 + i(\omega_-\omega_-\nu)},\end{aligned} \tag{8.49}$$

where we used the fact, that the expectation values for $\mathcal{S}$ and Q_- factorize and defined $\epsilon_= - (\Gamma_/2 - i\tilde{\omega}_)$ and $\epsilon_= - (\Gamma_/2 - i\tilde{\omega}_)$. The correlations for Q_- are evaluated

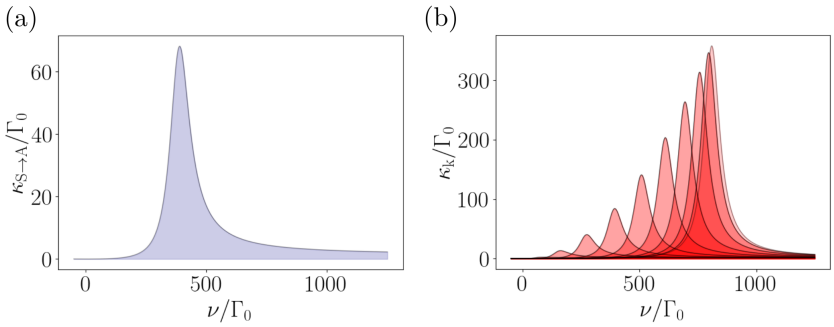

Figure 8.8: (a) Transfer rate from the symmetric to the antisymmetric state for a molecular dimer as a function of the vibronic frequency. The maximum transfer occurs at the resonance $\nu = \Omega_S^\lambda - \Omega_A^\lambda$. (b) Transfer rates for a molecular ring of $\mathcal{N} = 20$ molecules from the symmetric state with mode number $k = 0$ to the $\mathcal{N}-1$ dark states. Resonances occur at $\nu = \Omega_S^\lambda - \Omega_k^\lambda$ for $k = 1, ..., \lceil(\mathcal{N}-1)/2\rceil$ and the range of vibrational frequencies at which transfer to the dark state manifold occur is increasing with $\mathcal{N}$ as well as the linewidth of the vibrational resonance Γ_ν. Parameters are $d = 0.025_0,\ \Gamma_\nu = 100\Gamma_0,\ \lambda = 0.15$ and the dipole polarization is chosen perpendicular to the ring plane.

assuming free evolution of the vibrations (to lowest order) and zero temperature for the vibrational modes:

$$\langle Q_-(t')Q_-(t)\rangle = \frac{1}{2}\Big(\langle b_1(t')b_1^\dagger(t)\rangle + \langle b_2(t')b_2^\dagger(t)\rangle\Big) = e^{-(\Gamma_\nu/2-i\nu)(t-t')}. \tag{8.50}$$

In the case of a fast vibrational relaxation rate $\Gamma_\nu \gg \Gamma_,\Gamma$ the transfer rate can be written as:

$$\kappa_{\mathcal{S}\to\mathcal{A}} = \frac{\lambda^2\nu^2}{2}\frac{\Gamma_\nu + \Gamma_-\Gamma}{\frac{(\Gamma_\nu+\Gamma_-\Gamma^2_)}{4} + (\omega_-\omega_-\nu)^2}. \tag{8.51}$$

The transfer rate from the antisymmetric to the symmetric state can be calculated similarly, assuming initial population in the antisymmetric state:

$$\kappa_{\mathcal{A}\to\mathcal{S}} = \frac{\lambda^2\nu^2}{2}\frac{\Gamma_\nu + \Gamma_-\Gamma}{\frac{(\Gamma_\nu+\Gamma_-\Gamma^2_)}{4} + (\omega_-\omega_-\nu)^2}. \tag{8.52}$$

Generalization to $\mathcal{N}$ molecules

The generalization to an arbitrary number of molecules is straightforward by first writing the full Hamiltonian in a collective basis for both the electronic as well as the vibrational modes.

$$\mathcal{H}_{\text{coll}} = \omega_{\mathcal{S}}(Q_{\mathcal{N}})\mathcal{S}^{\dagger}\mathcal{S} + \sum_{k=1}^{\mathcal{N}-1} \omega_k(Q_{\mathcal{N}})\mathcal{A}_k^{\dagger}\mathcal{A}_k \\ - \frac{\lambda\nu}{\sqrt{\mathcal{N}}} \sum_{k=1}^{\mathcal{N}-1} (Q_k \mathcal{S}^{\dagger}\mathcal{A}_k + h.c.) - \frac{\lambda\nu}{\sqrt{\mathcal{N}}} \sum_{k\neq k'}^{\mathcal{N}-1} (Q_{k-k'}\mathcal{A}_k^{\dagger}\mathcal{A}_{k'} + h.c.) + \nu \sum_{k=1}^{\mathcal{N}} b_k^{\dagger} b_k, \tag{8.53}$$

where the energies of the collective states are shifted by the contribution of the symmetric vibrational mode $\omega_k(Q_{\mathcal{N}}) = \omega_0 + \lambda^2\nu + \Omega_k - \lambda\nu Q_{\mathcal{N}}/\sqrt{\mathcal{N}}$ for $k = 1, \ldots, \mathcal{N}$. Similarly to the dimer case, the $Q_{\mathcal{N}}$-dependent energy shifts can be removed by the collective polaron transformation $\prod_{k=1}^{\mathcal{N}} \mathcal{U}_{\mathcal{A}_k} = \prod_{k=1}^{\mathcal{N}} e^{i\lambda P_{\mathcal{N}} \mathcal{A}_k^{\dagger}\mathcal{A}_k/\sqrt{\mathcal{N}}}$ which leads to a renormalization of the collective state energies as $\tilde{\omega}_k = \omega_0 + \lambda^2\nu/2 + \Omega_k$. The crucial term is however the coupling between the symmetric states and the dark state manifold. Similar to the molecular dimer case we assume initial population in the symmetric state and solve the Heisenberg equations of motion neglecting the noise terms

$$\dot{\mathcal{S}} = -i\tilde{\omega}_{\mathcal{S}}\mathcal{S} - \frac{\Gamma_{\mathcal{S}}}{2}\mathcal{S} + \frac{i\lambda\nu}{\sqrt{\mathcal{N}}} \sum_{k=1}^{\mathcal{N}-1} Q_k \mathcal{A}_k, \tag{8.54a}$$

$$\dot{\mathcal{A}}_k = -i\tilde{\omega}_k\mathcal{A}_k - \frac{\Gamma_k}{2}\mathcal{A}_k + \frac{i\lambda\nu}{\sqrt{\mathcal{N}}} Q_k^{\dagger}\mathcal{S} + \frac{i\lambda\nu}{\sqrt{\mathcal{N}}} \sum_{k'\neq k}^{\mathcal{N}-1} Q_{k-k'}\mathcal{A}_{k'}. \tag{8.54b}$$

After solving for the population $\langle \mathcal{S}^{\dagger}\mathcal{S} \rangle(t)$ and tracing out the vibrational modes one finds transfer rates $\kappa_{\mathcal{S}\to\mathcal{A}_k}$ between the symmetric state and the dark state manifold:

$$\kappa_{\mathcal{S}\to\mathcal{A}_k} = \frac{\lambda^2\nu^2}{2} \frac{\Gamma_\nu + \Gamma_k - \Gamma_{\mathcal{S}}}{\frac{(\Gamma_\nu + \Gamma_k - \Gamma_{\mathcal{S}})^2}{4} + (\Omega_{\mathcal{S}} - \Omega_k - \nu)^2}. \tag{8.55}$$

9 Preprint

Scaling law for Kasha's rule in photoexcited subwavelength molecular aggregates

R. Holzinger[1], N. S. Bassler[2], H. Ritsch[1] and C. Genes[2]

[1] *Institut für Theoretische Physik, Universität Innsbruck, Technikerstrasse 21, A-6020 Innsbruck, Austria*

[2] *Max Planck Institute for the Science of Light, Staudtstrasse 2, D-91058 Erlangen, Germany*

We study the photophysics of molecular aggregates from a quantum optics perspective, with emphasis on deriving scaling laws for the fast non-radiative relaxation of collective electronic excitations, referred to as Kasha's rule. At deep subwavelength separations, quantum emitter arrays exhibit an energetically broad manifold of collective states with delocalized electronic excitations originating from near field dipole-dipole exchanges between the aggregate's monomers. Photoexcitation with visible light addresses almost exclusively symmetric collective states, which for an arrangement known as H-aggregate, have the highest energies (hypsochromic shift). The extremely fast subsequent non-radiative relaxation via intramolecular vibrational modes then populates lower energy, subradiant states which results in the effective inhibition of fluorescence. Our treatment allows for the derivation of an approximate linear scaling law of this relaxation process with the number of available low energy vibrational modes and reveals its direct proportionality to the dipole-dipole interaction strength between neighbouring monomers.

DOI: 10.48550/arXiv.2304.10236

9.1 Introduction

Molecular aggregates [265, 284, 285] are self-ordered arrangements of monomers with a strong optical transition dipole strength. Owing to the dense packing of monomers within the aggregate, at the level of tens of nanometers, thus much below an optical

wavelength and despite inhomogeneous broadening and separation disorder, they exhibit delocalized excitons [286]. This allows strong coupling to external light modes, resulting in collectively modified fluorescence rates. Following the discovery of J- and H-aggregates in the 1930s by Scheibe [287] and Jelley [288] their standard understanding is based on the original approach introduced by Kasha in the 1960s [21]. Currently, J-aggregates are widely employed in light-matter coupling experiments aiming at the modification of material properties via the manipulation of the electromagnetic vacuum mode density around electronic resonances [289].

In quantum optics, there is a growing interest in the cooperative behavior of subwavelength matter systems [19], confined to regions comparable to the typical wavelength λ of visible light. Implementation platforms include synthetic systems such as atoms in optical lattices, vacancy centers, quantum dots, etc., strongly building on the seminal work of Dicke [2] in the 1950s. Dicke predicted that the rate of radiative emission from indistinguishable electronic systems, such as a number $\mathcal{N}$ of atoms placed within a volume much smaller than λ^3, scales quadratically with particle number $\mathcal{N}$. This phenomenon, called Dicke superradiance [4, 47], is accompanied by the closely related effect of subradiance, where the emission rate of collective states can be much lower than that of an isolated single quantum emitter [290]. Subradiance holds many promises towards applications of robust quantum state design or in quantum metrology and sensing [19, 58]. Moreover, the open system dynamics combined with the study of naturally occurring photosynthetic systems have triggered many investigations into providing design principles of subwavelength biomimetic systems [143, 259, 291, 292].

Such cooperative behavior can also be naturally studied in molecular aggregates even at room temperature [259]. First, their small overall dimensions means that under external illumination the light-matter interaction strength is collectively enhanced by a factor $\sqrt{\mathcal{N}}$ - the number of monomers, due to the increase in the oscillator strength. The symmetric superposition of the individual electronic excitation states exhibits the lowest energy for a head-to-tail arrangement, i.e. a J- aggregate [284]. Consequently, the symmetric state is protected against further vibrational relaxation and hence the J-aggregate's fluorescence is strongly increased. For the opposite case of parallel arrangement of the dipole moments (H-aggregate), i.e. the side-by-side configuration, fluorescence is inhibited due to vibrational relaxation to subradiant lower energy states. These states deplete the symmetric state, in this case situated on top of the energy band, in a process generally denoted as Kasha's rule. Consequently, fluorescence is decreased and the system can undergo other processes such as the singlet to triplet transition followed by intersystem crossing and subsequently radiative relaxation via phosphorescence. At close distances, not only the radiative emission is modified but the inherent near-field dipole-dipole interactions lead to observable energy shifts in the absorption peak tied to the symmetric state. It is shifted towards higher energies (bathochromic) for H-aggregates and to lower energy (hypsochromic) for J-aggregates when compared to the bare monomer's absorption peak [284, 285].

To shed some new light into some of these phenomena we follow here a quantum

optics inspired approach [18] to analyse the photophysics of molecular aggregates. The aim is to provide an analytical description of Kasha's rule taking into account dipole-dipole interactions, electron-vibron couplings and vibrational relaxation. Our treatment involves a formulation where $\mathcal{N}$ monomers in a linear chain configuration with separation d form an aggregate, as depicted in Fig. 10.1(a). Each monomer is described as a two level electronic quantum emitter with an intrinsic coupling to a number n of vibrational degrees of freedom (see Fig. 10.1(b)). The near-field dipole-dipole couplings between monomers leads to the possibility of excitation migration within the whole aggregate and thus to the creation of delocalized excitons. We characterize these delocalized states by their collective energy shifts, seen as an energy dispersion curve in Fig. 10.1(c) and by their radiative properties. Notice that for such small separations, the light cone basically includes a single state characterized by a quasi-momentum $q = 0$ (the symmetric superposition) while all other states fall outside this light cone [58]. Uniform illumination leads to the activation of the symmetric electronic superposition, which in turn can indirectly redistribute energy to a manifold of asymmetric, dark collective states. In the specific case of H-aggregates, the higher energetic symmetric state relaxes quickly via vibronically-aided processes to the bottom asymmetric states characterized by subradiance. This presents an effective reduction of fluorescence, thus favoring transitions to triplet states and thus phosphorescence. The mechanism is roughly depicted in Fig. 10.1(c) as the initial excitation slides down quickly to the bottom of the dispersion curve. Snapshots of this process in time are shown in Fig. 10.1(d) describing the time evolution of the excitation from the symmetric, quickly decaying collective state to the bottom asymmetric, robust electronic states. A perturbative treatment allows us to derive an analytical expression for this rate, revealing independence of the number of monomers and a linear scaling with the number of nuclear vibrations available for the dissipation of electronic energy into low energy vibrations. Moreover, the timescale of the process is set by the strength of the nearest neighbor dipole-dipole interaction.

The manuscript is structured as follows: we first introduce the model for $\mathcal{N}$ coupled molecular quantum emitters in Sec. 9.2. We then quickly review the transformation from the bare monomer basis to the collective aggregate basis as introduced formally in Ref. [22]. In Sec. 9.3 we derive rate equations for collective state populations and compare with numerical simulation for the specific case of H-aggregates.

9.2 Model

We consider a deep subwavelength ensemble of molecular quantum emitters in an equidistant chain configuration (see Fig. 10.1(a)) mimicking a molecular aggregate comprised of $\mathcal{N}$ identical monomers and with a typical inter-monomer distance d in the nm range. As photoexcitation is performed with light sources of wavelength $2\pi/k_0$ (with k_0 the wavevector) in the μm range, the condition $k_0 d \ll 1$ is fulfilled. Each monomer is assumed to undergo a single electronic transition which in turn is coupled

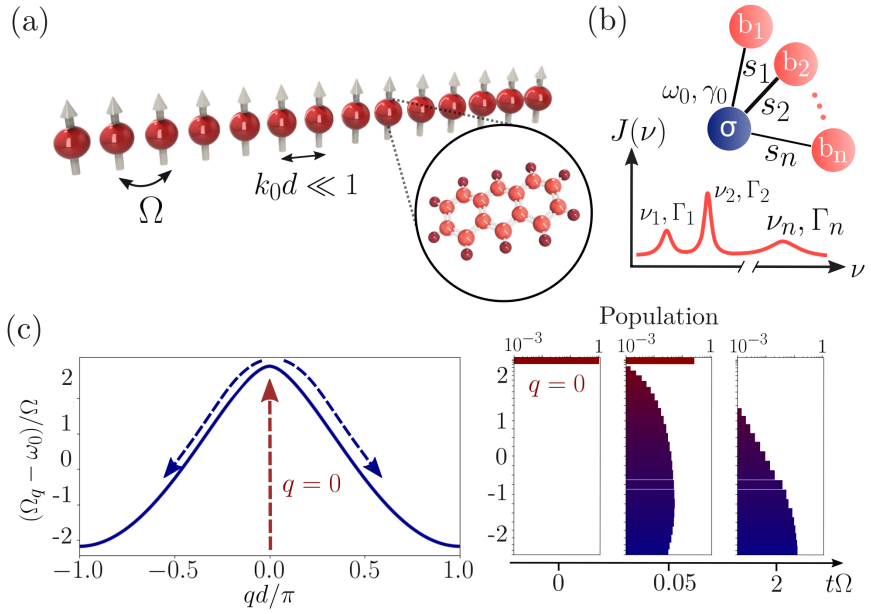

Figure 9.1: (a) Illustration of a tail-to-tail arrangement of monomer dipoles (H-aggregate configuration). With separations in the nm range, the condition $k_0 d \ll 1$ is fulfilled leading to strong near-field dipole-dipole interactions with nearest-neighbour strengths Ω. (b) Diagram describing electron-vibron interactions within each monomer. A single electronic transition operator σ is coupled to n vibrational mode operators b_m with frequencies ν_m, linewidths Γ_m and Huang-Rhys factors s_m, where m runs from 1 to n. (c) Energy band diagram for a mesoscopic chain as a function of the quasi-momentum q. Upon photoexcitation, only the symmetric state ($q = 0$) is initially populated. Subsequently, an almost instantaneous relaxation towards lower energy states takes place. On the right side, the population distribution of the collective excitation modes for $k_0 d = 0.0126$ is presented in snapshots at different times, showing that the electron-vibron coupling combined with vibrational relaxation leads to the migration of energy towards the lowest energy asymmetric modes. We have considered a large n spanning the range of frequencies from 0 to 4Ω, with $\Gamma_m = \nu_m/10$ and identical $s_m = 10^{-2}$.

to a n vibrational modes. Each vibrational mode has a frequency ν_m and relaxation rate Γ_m, where m runs from 1 to n. The monomer can undergo spontaneous emission at rate γ_0, owing to the coupling to the electromagnetic environment.

Electron-vibron interactions - For each monomer j, the electronic transition is at frequency splitting ω_0 ($\hbar = 1$) and is described by the collapse operator $\sigma_j = |g\rangle_j \langle e|_j$. The vibrational degrees of freedom are described by bosonic operators b_{jm} satisfying the

commutation relations $\left[b_{jm}, b^\dagger_{j'm'}\right] = \delta_{jj'}\delta_{mm'}$. The vibronic couplings are illustrated in Fig. 10.1(b) as links between the electronic and vibration operators with magnitude characterized by the Huang-Rhys factors s_m. The electronic and vibrational degrees of freedom are subject to loss quantified by the spontaneous emission rate γ_0 and by the vibrational relaxation rates Γ_m, respectively. The Hamiltonian for all $\mathcal{N}$ monomers is obtained as a sum over each particle's Hamiltonian

$$h^{(j)} = \bar{\omega}_0 \sigma_j^\dagger \sigma_j + \sum_{m=1}^{n} \nu_m \Big(b_{jm}^\dagger b_{jm} - \sqrt{s_m}\sigma_j^\dagger \sigma_j (b_{jm}^\dagger + b_{jm}) \Big). \tag{9.1}$$

Notice that the bare frequency is Stokes shifted $\bar{\omega}_0 = \omega_0 + \sum_m s_m \nu_m$. This shift will later be eliminated after a polaron transformation (see Apendix 8.7.1 for more details).

Collective electronic excitations - Dipole-dipole exchanges at rates $\Omega_{jj'}$ have a strong imprint at nm distances, owing to their scaling with the inverse cube of the particle separation $|\vec{r}_j - \vec{r}_{j'}|^{-3}$ in the near field region [19]. This can be listed in the Hamiltonian as

$$\mathcal{H}_{\text{d-d}} = \textstyle\sum_{j\neq j'} \Omega_{jj'} \sigma_j^\dagger \sigma_{j'} \tag{9.2}$$

and describes an excitation transfer between pairs of monomers via a virtual photon exchange. The coherent exchange is mediated by the dipole-dipole frequency shifts $\Omega_{jj'}$, which in units of the optical emission rate γ_0 are given by $\Omega_{jj'}/\gamma_0 = -3\pi/k_0 \; \vec{\mu}^* \cdot \text{Re}\, \boldsymbol{G}(\vec{r}_j, \vec{r}_{j'}, \omega_0) \cdot \vec{\mu}$, namely, proportional to the real part of the Green's tensor in free space (see Appendix 8.7.2). In the following we will consider the particular case of side-by-side arrangement, where all transition dipoles $\vec{\mu}$ are parallel to each other and perpendicular to the chain direction.

Radiative and vibrational loss - In a master equation formulation for the system density operator ρ written as $\partial_t \rho = i[\rho, \mathcal{H}] + \mathcal{L}[\rho]$ loss can be included via the Lindblad superoperator $\mathcal{L}_\gamma[\rho] = \gamma_\mathcal{O}/2 \left[2\mathcal{O}\rho(t)\mathcal{O}^\dagger - \mathcal{O}^\dagger\mathcal{O}\rho(t) - \rho(t)\mathcal{O}^\dagger\mathcal{O}\right]$, describing decay at generic rate $\gamma_\mathcal{O}$ through a single channel with a generic collapse operator $\mathcal{O}$. For vibrational loss, the collapse rate for each mode m is Γ_m and the corresponding collapse operator is $b_{jm} - \sqrt{s_m}\sigma_j^\dagger\sigma_j$. This form for the collapse operator is derived in analogy to the dissipative physics of optomechanical systems in the ultrastrong coupling regime [293]. The radiative loss is not in diagonal Lindblad form but achieves the following expression $\mathcal{L}_e[\rho] = \sum_{j,j'} \gamma_{jj'}/2 \left[2\sigma_j \rho \sigma_{j'}^\dagger - \sigma_j^\dagger \sigma_{j'} \rho - \rho \sigma_j^\dagger \sigma_{j'}\right]$. This form can be diagonalized and it shows the emergence of $\mathcal{N}$ independent decay channels, each corresponding to some collective electronic superposition state [19]. At very small separation, deep into the subwavelength regime, the fully symmetric superposition decays at a superradiant rate roughly equal to $\mathcal{N}\gamma_0$ while all other states have vanishingly small decay rates (which we will assume in the following to be exactly zero). This is by no means a limitation of our treatment as one can easily generalize this to the case of non-zero decay rates of the dark manifold [19, 22].

Collective basis formulation - The model can be better tackled in the collective basis, as has been previously considered in Ref. [22]. In the mesoscopic limit, where $\mathcal{N}$ is very large, the system illustrated in Fig. 10.1(a) can be considered translationally invariant and periodic boundary conditions can be invoked. Furthermore, in the deep subwavelength regime where $k_0 d \ll 1$, the eigenstates of the Hamiltonian in Eq. (9.2) are collective excitation states. A single symmetric mode can be distinguished with state vector obtained by the application of the symmetric operator $\mathcal{S}^\dagger = \sum_j \sigma_j^\dagger/\sqrt{\mathcal{N}}$ to the collective ground state. To a good approximation the system can be considered to be in the Dicke limit where a single superradiant emission rate roughly estimated by $\gamma_\mathcal{S} = \mathcal{N}\gamma_0$ characterizes this 'bright' state. In addition, the other orthogonal $\mathcal{N}-1$ asymmetric states are obtained via the application of asymmetric operators $\mathcal{A}_q = \sum_{j=1}^{\mathcal{N}} e^{iqjd}\sigma_j/\sqrt{\mathcal{N}}$ indexed by the quasi-momentum $q = 2\pi k/(\mathcal{N}d)$ obtained by a rescaling of the index of the mode $k = \pm 1, ..., \pm(\mathcal{N}-1)/2$ as used in Ref. [22] (for simplicity of notations, we restrict the discussion here to the $\mathcal{N}$ odd case). These states are non-radiative at such deep subwavelength molecular separations and we dub them therefore as 'dark' as they are situated outside the light cone.

The collective excitations are eigenstates of the dipole-dipole interaction Hamiltonian

$$\mathcal{H}_{\mathrm{d-d}}\mathcal{A}_q|g\rangle^{\otimes\mathcal{N}} = \Omega_q\mathcal{A}_q|g\rangle^{\otimes\mathcal{N}}, \tag{9.3}$$

where by definition we fix the symmetric shift $\Omega_\mathcal{S} \equiv \Omega_{q=0}$. With periodic boundary conditions imposed, in the mesoscopic limit, one can derive the collective shifts as $\Omega_q = 2\sum_j \Omega_{1j}\cos(q(j-1)d)$ [22, 58]. Further simplifications occur by considering the nearest neighbour approximation and the collective eigenenergies become $\Omega_q = 2\Omega\cos(qd)$, where the nearest-neighbour coupling is simply denoted by $\Omega \equiv \Omega_{12}$. The dipole-dipole Hamiltonian can now be recast in terms of the collective operators in the single excitation subspace

$$\mathcal{H}_{\mathrm{d-d}} = \Omega_\mathcal{S}\mathcal{S}^\dagger\mathcal{S} + \sum_{q\neq 0}\Omega_q\mathcal{A}_q^\dagger\mathcal{A}_q \tag{9.4}$$

which is derived by using the orthonormality condition $\sum_q e^{iqd(j-j')} = \mathcal{N}\delta_{jj'}$. Closely following the procedure introduced in Ref. [22], one can analyze the coupling between states of different symmetries via electron-vibron couplings by an additional transformation to a collective basis for the vibrational degrees of freedom as well. This is done by introducing collective vibrational modes $Q_q^{(m)} = \sum_{j=1}^{\mathcal{N}}(b_{m,j} + b_{m,j}^\dagger)e^{iqjd}/\sqrt{\mathcal{N}}$, with the momentum quadratures satisfying $[Q_q^{(m)}, P_q^{(m)}] = i$ and m labels the vibrational mode running from 1 to n. The Hamiltonian coupling the symmetric state to the dark state manifold is then given by

$$\mathcal{H}_{\mathrm{int}}^{\mathcal{SA}} = -\sum_{m=1}^{n}\sum_{q\neq 0}\frac{\sqrt{s_m}\nu_m}{\sqrt{\mathcal{N}}}\Big(Q_q^{(m)}\mathcal{S}^\dagger\mathcal{A}_q + \mathrm{h.c.}\Big), \tag{9.5}$$

via collective vibrations. This coupling is responsible for funneling population into the long lived dark state manifold after the initial driving of the fully symmetric

state under uniform illumination. This mechanism is fundamental to understand the dynamics associated with Kasha's rule which we tackle in Sec. 9.3. In addition, within the dark state manifold an all-to-all coupling Hamiltonian acts with the following form

$$\mathcal{H}_{\rm int}^{\mathcal{A}\mathcal{A}} = -\sum_{m=1}^{n}\sum_{q\neq q'}\frac{\sqrt{s_m}\nu_m}{\sqrt{\mathcal{N}}}\Big(Q^{(m)}_{q-q'}\mathcal{A}_q^\dagger\mathcal{A}_{q'} + \text{h.c.}\Big), \tag{9.6}$$

and the sum implies that $q, q' \neq 0$. This indicates that a redistribution of energy takes place within the whole manifold of dark states. After transforming the system Hamiltonian, the energies of the collective states are shifted by the contribution of the symmetric vibrational mode $-\sum_m \sqrt{s_m}\nu_m Q_0^{(m)}/\sqrt{\mathcal{N}}$. The energy shifts can be removed by the collective polaron transformation $U = \prod_q \prod_{m=1}^n e^{i\sqrt{s_m}/\sqrt{\mathcal{N}}P_0^{(m)}\mathcal{A}_q^\dagger\mathcal{A}_q}$ which leads to a renormalization of the collective state energies as $\bar{\omega}_q = \omega_0 + \sum_m s_m\nu_m/2 + \Omega_q$.

9.3 Photophysics of J- and H-aggregates

The crucial point in analyzing the photophysics of aggregates is their small dimension and the very small monomer-monomer separation with respect to the incoming optical excitation wavelength. This means that laser driving takes place by the excitation of the symmetric collective mode which leads to a rescaling of the Rabi driving with a factor of $\sqrt{\mathcal{N}}$: this can be seen equivalently as an increase of the oscillator strength by $\sqrt{\mathcal{N}}$, thus rendering aggregates of any kind as good candidates for strong light-matter coupling. In addition, the particularity of the subsequent aggregate electronic dynamics lies within the shape of the energy band. For example, J-aggregates present an energy band where the symmetric mode at $q = 0$ lies at the bottom of the band thus leading to a bathochromic frequency shift (to the left of the bare monomer frequency) and subsequently shows not only an enhanced absorption cross section but also enhanced fluorescence at a superradiant rate. In contrast, H-aggregates have the symmetric state located at the top of the energy band corresponding to a hypsochromic shift (to the right of the monomer bare frequency, see Fig. 9.2(c)). Most importantly, quick dynamics follows the optical excitation involving the relaxation of the collective state towards low energy dark states. This takes place owing to the Hamiltonian in Eq. (9.5) which couples the symmetric state to the manifold of asymmetric states via vibrational Huang-Rhys factors and which is followed by quick vibrational relaxation.

Analytical results. Rate equations. - Let us now derive an analytical expression for the timescale associated with Kasha's rule, for the relaxation of the collective symmetric state. We largely follow the derivation in Ref. [22] which we generalize here to incorporate the crucial aspect that many vibrational modes have to be taken into account. Under the assumption that the vibrational relaxation rates are fast compared to the coherent couplings and radiative loss rates, a set of rate equations for the populations of the symmetric state $p_{\mathcal{S}} = \langle\mathcal{S}^\dagger\mathcal{S}\rangle$ and all dark states $p_q = \langle\mathcal{A}_q^\dagger\mathcal{A}_q\rangle$ can

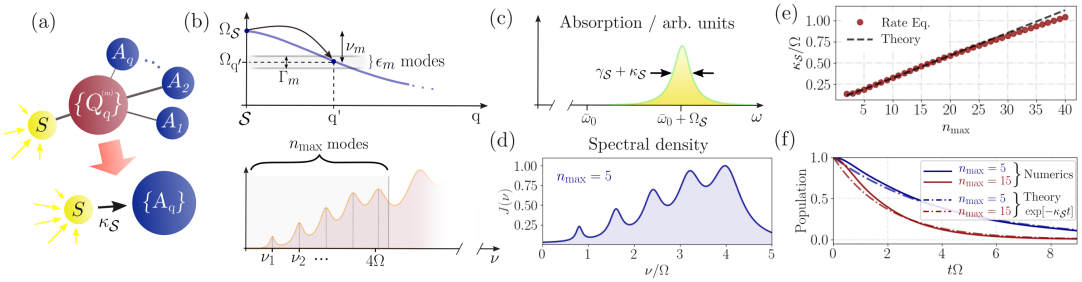

Figure 9.2: (a) The initially excited symmetric mode is linked to all asymmetric modes via collective vibrational modes $Q_q^{(m)}$. Elimination of the vibrational degrees of freedom reveals a unidirectional transfer of energy into the dark state manifold. (b) Diagram illustrating the transfer $\mathcal{S} \to q'$ into a number ϵ_m of asymmetric states located around a vibrational resonance ν_m (top). (Bottom) Only a limited number of vibrational modes, from 1 to $n_{\max}$ can efficiently mediate resonant transfer between the symmetric state and the dark manifold. These modes are within the 4Ω bandwidth. (c) Absorption profile of a H-aggregate, exhibiting a hypsochromic frequency shift to the right of the monomer resonance. (d) Vibrational spectral density for equidistantly spaced vibrational frequencies ν_m, with identical Huang-Rhys factors $s = 0.01$ and relaxation rates $\Gamma_m = \nu_m/10$. (e) Linear scaling of the transfer rate $\kappa_{\mathcal{S}}$ as a function of the number of vibrational modes, with the same parameters as in (d) and $\mathcal{N} = 20$ molecules at $k_0 d = 0.0126$ separation. The scaling law from Eq. (9.11) provides a very good fit to the rate equations in Eq. (9.8). (f) Time dynamics of 20 molecules initialized in the symmetric state. Numerical results in the single excitation manifold show excellent agreement with an exponential decay given by $e^{-\kappa_{\mathcal{S}} t}$, and governed by the analytical formula in Eq. (9.11) (Same parameters as in (d)-(e)).

be derived (see Appendix 9.5.1 for more details). The intermediate step is the tracing out the vibrational modes as introduced in Ref. [22] and illustrated in Fig. 9.2(a). With the definitions $\kappa_{\mathcal{S}}$ - total loss rate of the symmetric state, κ_q - loss rate for dark state q, $\kappa_{q\to\mathcal{S}}$ - incoherent repopulation rate from the dark to the bright state and $\kappa_{q'\to q}$ - incoherent rate for redistribution of energy within the dark state manifold, one can write

$$\dot{p}_{\mathcal{S}} = -(\gamma_{\mathcal{S}} + \kappa_{\mathcal{S}})p_{\mathcal{S}} + \sum_{q\neq 0} \kappa_{q\to\mathcal{S}} p_q, \tag{9.7a}$$

$$\dot{p}_q = -\kappa_q p_q + \sum_{q'\neq q} \kappa_{q'\to q} p_{q'}. \tag{9.7b}$$

The rate equations show that the symmetric state energy spills into the whole dark state manifold via rate $\kappa_{\mathcal{S}}$ and in addition, higher energy dark states spill into the lower

energy ones via κ_q. The quasi-unidirectionality of the process is ensured by the fact that, in this perturbative treatment, the coherent coupling between states is followed by quick vibrational relaxation, making the reverse process, governed by rates $\kappa_{q\to\mathcal{S}}$ and $\kappa_{q'\to q}$ from lower energy state to higher ones, very unlikely (as shown in Ref. [22] for the two monomer case). Mathematically, the condition is $\sqrt{s_m}\nu_m/\sqrt{\mathcal{N}} \ll \Gamma$. Analytically, one can get an expression for the transfer rate between the symmetric mode and any dark mode q mediated by vibrational mode m as

$$\kappa^{(m)}_{\mathcal{S}\to q} = \frac{2s_m\nu_m^2(\Gamma_m+\gamma_{\mathcal{S}})/\mathcal{N}}{(\Gamma_m+\gamma_{\mathcal{S}})^2+4(\Omega_{\mathcal{S}}-\Omega_q-\nu_m)^2} \tag{9.8}$$

and construct the total rate to all states spanned by the index q by summing $\kappa_{\mathcal{S}} = \sum_{m=1}^{n_{\max}}\sum_q \kappa^{(m)}_{\mathcal{S}\to q}$ over all vibrations up to an index $n_{\max}$ within the frequency interval covered by 4Ω where the electronic collective states are positioned in energy. Moreover, we will consider the standard underdamped harmonic oscillator model for the molecular vibrations, i.e. the dissipation rate is much smaller than the resonance frequency for any mode $\Gamma_m \ll \nu_m$. Equivalently, one can state that the quality factor of any vibrational mode is much larger than unity $\nu_m/\Gamma_m \gg 1$.

In order to further proceed with analytical estimates, let us first make some comments regarding typical timescales. Given that vibrational relaxation is in the order of tens to hundreds of GHz while spontaneous emission is in the range of tens of MHz, a very quick non-radiative path from the symmetric to low energy asymmetric states can be achieved on ps timescales. For monomer separations in the nm range, expected near field shifts Ω in the range of 1 THz to tens of THz are expected. This means that only a few, low energy, molecular vibrations can fit in the window of 4Ω (see Fig. 9.2(b), bottom) and aid the relaxation process. This allows us to derive an approximate scaling law for $\kappa_{\mathcal{S}}$ as a function of a given number of vibrational modes $n_{\max}$ that can efficiently mediate the relaxation of the symmetric state into the dark state manifold.

We proceed by first consider a given vibrational mode m and asking for the condition that this mode can transfer excitation from the symmetric mode to any of the dark states. This procedure is illustrated in Fig. 9.2(b) (top). We notice that with the condition that $\Gamma_m \ll \nu_m$ (it is also implied that $\gamma_{\mathcal{S}} \ll \nu_m$ even for large $\mathcal{N}$) the resonance condition requires that the states to which resonant transfer can take place are only in the vicinity of the mode q fulfilling $\Omega_q = \Omega_{\mathcal{S}} - \nu_m$. Of course, in this case one can immediately observe that any modes with $\nu_m > 4\Omega$ cannot take part in this transfer. Assuming a constant density of all $\mathcal{N}$ collective states spread within the interval 4Ω, we can then estimate that a number of approximately $\epsilon_m = \Gamma_m\mathcal{N}/(4\Omega)$ states fall close to the resonance $\Omega_q = \Omega_{\mathcal{S}} - \nu_m$, i.e. within the linewidth Γ_m. Summing over all these contributions gives the total rate for all transitions mediated by mode m to states close to q as

$$\sum_q \kappa^{(m)}_{\mathcal{S}\to q} \approx \frac{\epsilon_m}{\mathcal{N}}\frac{2s_m\nu_m^2}{(\Gamma_m+\gamma_{\mathcal{S}})}. \tag{9.9}$$

The next step is the summation over all possible relaxation paths that participate

in the transfer giving thus an estimate for the total rate

$$\kappa_{\mathcal{S}} \approx \sum_{m=1}^{n_{\max}} \frac{\Gamma_m}{2\Omega} \frac{s_m \nu_m^2}{(\Gamma_m + \gamma_{\mathcal{S}})}. \tag{9.10}$$

In order to estimate the sum above, knowledge of the particular nature of the monomer's frequencies, Huang-Rhys factors and vibrational relaxation rates is necessary. However, while later we will numerically investigate random distributions of frequencies and Huang-Rhys factors, we aim first at deriving a simple scaling law. To this end we will proceed by making some simplifying assumptions, among which the first is that the vibrational spectrum is equally spaced in the interval from 0 up to 4Ω. We denote the frequency of mode m by $\nu_m = m4\Omega/n_{\max}$. Let us also consider that all Huang-Rhys factors are equal to s (later we compare with a randomized distribution with an average s). Moreover, we neglect the contribution of $\gamma_{\mathcal{S}}$ as it is much smaller than Γ_m (this should be typically very well fulfilled as γ_0/Γ_m is expected to be around 10^{-5}).

Summing over all vibrational modes within the interval of 4Ω gives us an approximated scaling law

$$\kappa_{\mathcal{S}} \approx \frac{4s\Omega}{3} \frac{(n_{\max}+1)(2n_{\max}+1)}{n_{\max}}. \tag{9.11}$$

The result shows independence of the total number of monomers $\mathcal{N}$ and a quasi linear dependence on the total number of available low frequency vibrational modes which can resonantly participate in Kasha's relaxation process from the high energy symmetric state to the bottom of the dark state manifold. Notice that the predicted timescale is dictated by the nearest neighbor dipole-dipole coupling strength Ω which in turn depends on the inverse cube of the monomer-monomer separation. In a first step, we can estimate that the analytical scaling is in very good agreement with the results of the rate equations, as seen in Fig. 9.2(e). The distribution of vibrational modes and their spectral density is shown in Fig. 9.2(d). However, the important test of validity will be performed against numerical simulations of the full Hamiltonian and loss processes.

Comparison to numerics - The previously derived rate equations are obtained in the limit where the quickest timescale in the system is set by the rates Γ_m and for smaller than unity Huang-Rhys factors. The validity of this approach can be easily checked against numerical simulations restricted to the single excitation subspace of the total Hamiltonian in Eqs. (9.1) and (9.2). We therefore perform simulations in the single excitation subspace and follow the time evolution of the system assuming unit population of the symmetric state at the initial time $t = 0$. As Γ_m is larger than the coherent rates, any excitation of a vibration is followed by quick relaxation, justifying the assumption that any double excitation can be neglected.

The basis set is picked as a tensor product $|j\rangle \otimes |j'\rangle^{(m)}$ where by definition $|j\rangle = |g, g, ...e_j, ...\rangle$ - only emitter j excited electronically and $|j'\rangle = |0, 0, ...1_{j'}, ...\rangle^{(m)}$ - only mode m in emitter j' has one vibrational excitation. Instead of solving the master

equation directly, one can use the quantum jump formalism to evaluate single stochastic quantum trajectories using the Monte Carlo wave function method (MCWF). The advantage is that instead of describing the state of the quantum system by a density matrix of size $\mathcal{N}^4 \times n^2$ the stochastic method only requires state vectors of size $\mathcal{N}^2 \times n$. This is somewhat counteracted by the stochastic nature of the formalism which makes it necessary to repeat the simulation until the wanted accuracy is reached. However, in most scenarios, especially for higher dimensional quantum systems, the necessary number of repetitions is much smaller than the system size $\mathcal{N}^2 \times n$ and therefore using the MCWF method is advantageous (see Appendix 9.5.2 for more details). For the simulation we write

$$|\Psi\rangle = \sum_{j,j'=1}^{\mathcal{N}} \sum_{m=1}^{n} \alpha_{jj'}^{(m)} |g, g, ...e_j, ...\rangle \otimes |0, 0, ...1_{j'}, ...\rangle^{(m)}, \tag{9.12}$$

with coefficients $\alpha_{jj'}^{(m)}$ and where the first part refers to the electronic excitation of molecule j and the second part to the excitation of the m-th vibrational mode of molecule j'.

In a first step, we compare the numerical results with the analytical scaling of Eq. (9.11), for an equidistant vibrational spectrum, in Fig. 9.2(f). A very good agreement is obtained showing that the time evolution of the symmetric state is well reproduced by an exponential decay following $e^{-\kappa_{\mathcal{S}} t}$. In the next step we pick a set of randomly drawn vibrational frequencies $\nu_1, ...\nu_{n_{\max}}$ in the window 0 to 4Ω and Huang-Rhys factors $s_1, ...s_{n_{\max}}$ in the interval $[0, 0.2]$ (with an average $s = 0.1$). The results plotted in Fig. 9.3(a) show that a good fit is obtained with the simplified result of Eq. (9.11) which assumes evenly spaced vibrational frequencies and a Huang-Rhys factor at the level of the distribution average $s = 0.1$. Furthermore, an average of the numerical results over 200 random realizations predicts an excellent agreement to the linear fit predicted by Eq. (9.11).

Effects of frequency disorder - Let us now proceed with analyzing the effect of frequency disorder. As aggregates are immersed in solvents and usually under room temperature conditions, they are expected to present a large inhomogeneous broadening, at the level of THz. We consider a distribution of the $\mathcal{N}$ monomer frequencies around ω_0 such that the frequency of each monomer becomes $\omega_0 + \delta_j$ where δ_j is randomly drawn from a distribution of width $\delta\omega$. In the collective basis, the symmetric state couples to any asymmetric state and acquires a shift as well [294]. The coupling of $\mathcal{S}$ to a state q mediated by disorder is simply given by the Fourier transform of the distribution

$$\delta_q = \frac{1}{\sqrt{\mathcal{N}}} \sum_{j=1}^{\mathcal{N}} e^{iqjd} \delta_j, \tag{9.13}$$

while the shift of the collective state $\delta_{\mathcal{S}} = 1/\sqrt{\mathcal{N}} \sum_{j=1}^{\mathcal{N}} \delta_j$ is the average of the distribution, thus close to zero. According to Ref. [294], disorder induced couplings

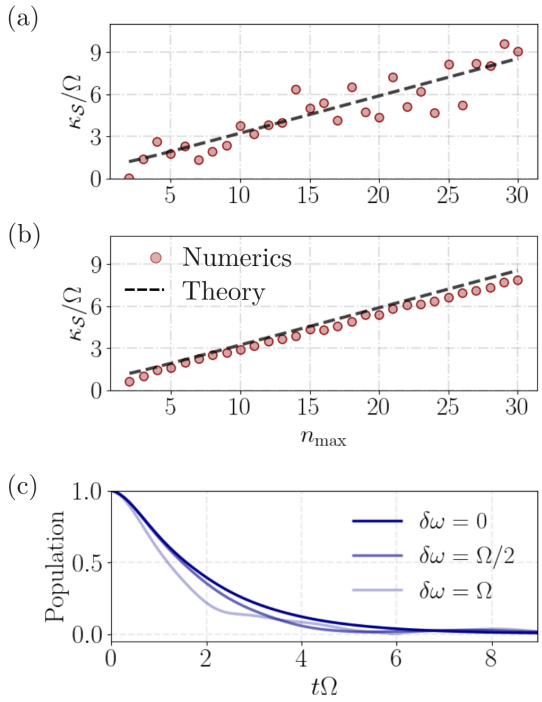

Figure 9.3: (a) Numerical results for κ_S plotted against increasing $n_{\max}$ for a randomly drawn set of vibrational frequencies $\nu_1, ...\nu_{n_{\max}}$ in the window 0 to 4Ω and Huang-Rhys factors $s_1, ...s_{n_{\max}}$ in the interval $[0, 0.2]$. The fit is performed with the analytical scaling in Eq. (9.11) for evenly spaced vibrational frequencies and Huang-Rhys factor at the level of the distribution average $s = 0.1$. (b) Further comparison of the analytical scaling from Eq. (9.11) with an average over 200 random realizations shows almost perfect agreement. (c) Decay of the initial symmetric state population under the influence of random static frequency disorder with fluctuation $\delta\omega$ around ω_0. Further parameters in all plots: $\mathcal{N} = 20$ molecules, $k_0 d = 0.0126$, $\Gamma_m = \nu_m/10$, $\Omega \approx 3.759 \times 10^5 \gamma_0$.

introduce an additional loss channel, thus slightly increasing the Kasha rate. This is indeed consistent with numerical simulations shown in Fig. 9.3(c) where the dynamics of the symmetric state without disorder and with considerable disorder at $\delta\omega = \Omega$ and $\delta\omega = 2\Omega$ are compared. The upshot is that the analytically derived loss rate holds well even for considerable disorder levels.

9.4 Conclusions

Molecular aggregates are a perfect showcase of cooperative phenomena as their photophysics is naturally characterized by coherent and incoherent effects brought

on by the positioning of individual monomers in the near field of each other. Effects widely explored in quantum optics, such as Dicke superradiance and subradiance, naturally occur in the theoretical description of such compounds, albeit in the presence of more complex, additional interactions between electrons and a vast number of molecular vibrations. We have provided a theoretical approach to the dynamics of collective electronic states making the connection, at the analytical and numerical level, with the physical mechanism introduced long ago by Kasha, stating that photon emission (fluorescence or phosphorescence) occurs in appreciable yield only from the lowest excited state of a given multiplicity. Our analytical conclusions predict that the Kasha loss rate from the symmetric, high energy, optically addressable state to the lower energy states of an H-aggregate is roughly independent of the number of monomers but strongly dependent on the number of low energy vibrational modes which can be excited and then dissipate the accumulated energy afterwards.

Further investigations will focus on aspects such as the role of quantum coherence in such systems. An important direction is the application of the methods presented in this manuscript to photosynthetic systems under various conditions of illumination, ranging from spatially and time coherent laser light to spatially and time incoherent light sources.

Acknowledgments

We acknowledge financial support from the Max Planck Society and the Deutsche Forschungsgemeinschaft (DFG, German Research Foundation) – Project-ID 429529648 – TRR 306 QuCoLiMa ("Quantum Cooperativity of Light and Matter"). R. H. acknowledges funding from the Austrian Science Fund (FWF) doctoral college DK-ALM W1259-N27. We acknowledge fruitful discussions with Michael Reitz and Johannes Feist. The numerical simulations were performed with the open-source framework QuantumOptics.jl [295].

9.5 Supplemental material

9.5.1 Deriving rate equations

Starting from the Holstein Hamiltonian in Eqs. (9.4)-(9.6) for $\mathcal{N}$ identical molecules with n vibrational modes each. The Heisenberg equations for the collective electronic modes are given by

$$\dot{\mathcal{S}} = -i\Big(\Omega_{\mathcal{S}} - \frac{\gamma_{\mathcal{S}}}{2}\Big)\mathcal{S} + \frac{i\sqrt{s}_m\nu_m}{\sqrt{\mathcal{N}}}\sum_{m=1}^{n}\sum_{q} Q_q^{(m)}\mathcal{A}_q + \text{noise}, \tag{9.14a}$$

$$\dot{\mathcal{A}}_q = -i\Omega_q\mathcal{A}_q + \sum_{m=1}^{n}\frac{i\sqrt{s_m}\nu_m}{\sqrt{\mathcal{N}}}\Big(Q_q^{(m)\dagger}\mathcal{S} + \sum_{q'\neq q} Q_{q-q'}^{(m)}\mathcal{A}_{q'}\Big) + \text{noise}. \tag{9.14b}$$

The collective noise terms will be neglected from now on as they do not contribute to the transfer process.

To calculate the transfer rate from the symmetric state to the antisymmetric states we assume some initial population in the symmetric state and no population in the antisymmetric states, additionally we assume that the symmetric state decays independently and formally integrate

$$\mathcal{S}(t) = S(0)e^{-(i\Omega_+\gamma/2)t}, \tag{9.15a}$$

$$\mathcal{A}_q(t) = A_q(0)e^{-i\Omega_q t} + \sum_{m=1}^{n}\frac{i\sqrt{s_m}\nu_m}{\sqrt{\mathcal{N}}}\int_0^t dt' e^{-i\Omega_q(t-t')}\Big(Q_q^{(m)}(t')\mathcal{S}(t') + \sum_{q'\neq q} Q_{q-q'}^{(m)}(t')\mathcal{A}_{q'}(t')\Big), \tag{9.15b}$$

and for the expectation value of the populations we get

$$\dot{\langle\mathcal{S}^\dagger\mathcal{S}\rangle} = -\gamma_{\langle\mathcal{S}^\dagger\mathcal{S}\rangle} - \sum_{m=1}^{n}\sum_{q}\frac{2\sqrt{s_m}\nu_m}{\sqrt{\mathcal{N}}}\,\mathrm{Im}\langle\mathcal{S}^\dagger\mathcal{A}_q Q_q^{(m)}\rangle, \tag{9.16a}$$

$$\dot{\langle\mathcal{A}_q^\dagger\mathcal{A}_q\rangle} = -\sum_{m=1}^{n}\frac{2\sqrt{s_m}\nu_m}{\sqrt{\mathcal{N}}}\,\mathrm{Im}\Big(\langle\mathcal{A}_q^\dagger\mathcal{S}Q_q^{(m)}\rangle + \sum_{q'\neq q}\langle\mathcal{A}_q^\dagger\mathcal{A}_{q'}Q_{q'-q}^{(m)}\rangle\Big). \tag{9.16b}$$

Therefore the terms $-2\sqrt{s}_m\nu_m/\sqrt{\mathcal{N}}\,\mathrm{Im}\langle\mathcal{A}_q^\dagger\mathcal{S}Q_q^{(m)}\rangle$ will be responsible for population transfer from the symmetric to the antisymmetric state with quasi-momentum q at a rate $\kappa_{\mathcal{S}\to q}^{(m)}$. We can calculate the rates explicitly up to order $\mathcal{O}(s_m\nu_m^2)$ and assuming that correlations between vibronic and electronic operators factorize.

$$\begin{aligned}
&-2\sqrt{s}_m\nu_m/\sqrt{\mathcal{N}}\langle\mathcal{A}_q^\dagger\mathcal{S}Q_q^{(m)}\rangle \\
&= -is_m\nu_m^2\int_0^t dt' e^{-\Omega_q(t-t')}\langle Q_q^{(m)}(t')Q_q^{(m)}(t)\rangle\langle\mathcal{S}^\dagger(0)\mathcal{S}(0)\rangle e^{-\epsilon_t'}e^{-\epsilon_t^*} \\
&= -is_m\nu_m^2\langle\mathcal{S}^\dagger(0)\mathcal{S}(0)\rangle\frac{e^{-\gamma_t} - e^{-((\Gamma_m+\gamma_)/2+i(\Omega_-\Omega_q-\nu_m))t}}{(\Gamma_m+\gamma_)/2 + i(\Omega_-\Omega_q-\nu_m)},
\end{aligned} \tag{9.17}$$

where we defined $\epsilon_= - (\gamma_/ 2 - i\Omega_)$ and used the fact that different vibrational modes are uncorrelated at all times, i.e. $\langle Q_q^{(m')}(t') Q_q^{(m)}(t)\rangle = 0$ for $m' \neq m$. The correlations for $Q_q^{(m)}$ are evaluated assuming free evolution of the vibrations (to lowest order) and zero temperature for the vibrational modes:

$$\langle Q_q^{(m)}(t') Q_q^{(m)}(t)\rangle = \frac{1}{\mathcal{N}} \sum_{j=1}^{\mathcal{N}} \langle b_{jm}(t') b_{jm}^\dagger(t)\rangle = e^{-(\Gamma_m/2 - i\nu_m)(t-t')}. \tag{9.18}$$

The transfer rate can be written as

$$\kappa_{\mathcal{S}\to q}^{(m)} = \frac{2 s_m \nu_m^2 (\Gamma_m + \gamma_{\mathcal{S}})/\mathcal{N}}{(\Gamma_m + \gamma_{\mathcal{S}})^2 + 4(\Omega_{\mathcal{S}} - \Omega_q - \nu_m)^2}, \tag{9.19}$$

given fast vibrational relaxation rates $\Gamma_m \gg \gamma$ compared to the electronic decay rates.

9.5.2 Single excitation subspace

The numerical diagonalization and subsequent time dynamics are evaluated in the single-excitation sector for both the electronic and vibrational degrees of freedom. This allows to rewrite the effective Hamiltonian in non-hermitian form as ($\hbar = 1$)

$$\mathcal{H}_{\text{eff}} = \sum_{j=1}^{\mathcal{N}} \Big(h^{(j)} + \sum_{j'=1}^{\mathcal{N}} \Big(\Omega_{jj'} - i\frac{\gamma_{jj'}}{2} \Big) \sigma_j^\dagger \sigma_{j'} - \frac{i}{2} \sum_{m=1}^{n} \Gamma_m \mathcal{O}_{jm}^\dagger \mathcal{O}_{jm} \Big), \tag{9.20}$$

where $h^{(j)}$ is defined in Eq. (9.1) and $\mathcal{O}_{jm} = b_{jm} - \sqrt{s_m}\sigma_j^\dagger \sigma_j$. The dynamics of the electron-vibron density matrix ρ can be described by a von Neumann equation of the form

$$i\frac{\mathrm{d}}{\mathrm{d}t}\rho(t) = [\mathcal{H}_{\text{eff}}\rho - \rho\mathcal{H}_{\text{eff}}], \tag{9.21}$$

and the expectation value of observable $\mathcal{O}$ becomes $\bar{\mathcal{O}} = \mathrm{tr}(\rho\mathcal{O})$. However, instead of solving the von Neumann equation directly, one can use the quantum jump formalism to evaluate single stochastic quantum trajectories using the Monte Carlo wave function method (MCWF). For large numbers of trajectories, the statistical average then approximates the result of the Master equation. The huge advantage is that instead of describing the state of the quantum system by a density matrix of size $\mathcal{N}^4 \times n^2$ these trajectories work in terms of state vectors of size $\mathcal{N}^2 \times n$. This is somewhat counteracted by the stochastic nature of the formalism which makes it necessary to repeat the simulation until the wanted accuracy is reached. It turns out, however, that for many cases, especially for high dimensional quantum systems, the necessary number of repetitions is much smaller than the system size $\mathcal{N}^2 \times n$ and therefore using the MCWF method is advantageous.

The system size stems from the fact, that in the single excitation subspace for both electronic and vibronic modes a general state vector can be written as

$$|\Psi\rangle = \sum_{j=1}^{\mathcal{N}} \alpha_{jj'}^{(m)} |g, g, ...e_j, ...\rangle \otimes \sum_{m=1}^{n} \sum_{j'=1}^{\mathcal{N}} |0, 0, ...1_{j'}, ...\rangle^{(m)}, \tag{9.22}$$

with coefficients $\alpha_{jj'}^{(m)}$ and where the first part refers to the electronic excitation of molecule j and the second part to the excitation of the m-th vibrational mode of molecule j'. Thus, the single excitation assumption substantially reduces the Hilbert space dimension from $2^{\mathcal{N}} \times n_{\text{cut}}^{\mathcal{N}} \times n$ to $\mathcal{N}^2 \times n$ (where n_{cut} is the cut-off of the Fock space dimension for the vibrational modes), allowing the simulation of mesoscopic numbers of molecules.

10 Publication

Nanomaterials, 13(5), 851, (2023)

Optical Properties of Concentric Nanorings of Quantum Emitters

V. Scheil[1], R. Holzinger[1], M. Moreno-Cardoner[1] and H. Ritsch[1]

[1] *Institut für Theoretische Physik, Universität Innsbruck, Technikerstrasse 21, A-6020 Innsbruck, Austria*

A ring of sub-wavelength spaced dipole-coupled quantum emitters features extraordinary optical properties when compared to a one-dimensional chain or a random collection of emitters. One finds the emergence of extremely subradiant collective eigenmodes similar to an optical resonator, which feature strong 3D sub-wavelength field confinement near the ring. Motivated by structures commonly appearing in natural light harvesting complexes (LHCs), we extend these studies to stacked multi ring ring geometries. We predict that using double rings allows to engineer significantly darker and better confined collective excitations over a broader energy band compared to the single ring case. These enhance weak field absorption and low loss excitation energy transport. For the specific geomtry of the three rings appearing in the natural LH2 light harvesting antenna we show that the coupling between the lower double ring structure and the higher energy blue shifted single ring is very close to a critical value for the actual size of the molecule. This creates collective excitations with contributions from all three rings, which is a vital ingredient for efficient and fast coherent interring transport. This geometry thus should also prove useful for the design of sub-wavelength weak field antennae.

DOI: 10.3390/nano13050851

10.1 Introduction

The optical properties of a quantum emitter, such as its excitation lifetime and transition frequency, are strongly modified when it is placed close to a second emitter, due to vacuum fluctuations that mediate dipole-dipole interactions between them.

As a remarkable example, the decay rate of a collection of emitters separated by subwavelength distances can be enhanced or suppressed, leading to the well known phenomena of superradiance or subradiance, respectively [1,2,5,115]. These phenomena are expected to be strongly enhanced in ordered subwavelength arrays of emitters, where maximal interference of the scattered fields can be observed [9, 50, 58, 61, 116, 117, 119, 120, 122–129, 131–136, 168].

Among the different array geometries, a ring-shaped structure formed by regularly placed emitters has very special optical properties. It has been shown before [50, 58, 116], that a linear chain of emitters whose inter-particle distance is smaller than half of the light wavelength supports collective modes that can guide light and are extremely subradiant with the excitation lifetime increasing polynomially with the atom number. The lifetime limitation arises from photon scattering off the ends of the chain. Remarkably, by joining the ends of the chain to form a closed ring, the lifetime can be exponentially increased with atom number [58, 165, 184].

Such extraordinary optical properties can be exploited for applications including efficient energy transfer, single photon sources or light harvesting [296, 297]. We have previously shown [165, 184], that tailoring the geometry, orientation and distance between two such nanorings allows for lossless and high fidelity transport of subradiant excitations, as if the two rings were two coupled nano-scale ring resonators. Besides subradiant states confining and guiding light, these nanorings also feature radiant modes whose corresponding electromagnetic field is strongly focused at its center. By placing an extra emitter at its center, these modes can be exploited to create a nano-scale coherent light source with a spectral line width which is strongly suppressed compared to the single atom decay rate [143]. In this case the collective optical modes of the ring play the role of the cavity modes and the central atom acts as the gain medium when incoherently pumped. Furthermore, if the central emitter is absorptive, the system can be tailored to achieve a strong absorption cross section way beyond the single atom case, while the outer ring behaves as a parabolic mirror when illuminated externally by a coherent light field [298].

In this work, we analyse in detail how the optical properties of two or more of these nanorings are modified when they are stacked in a concentric way. Note that this system is radically different compared to the case previously studied of two rings coupled side by side [165, 184], as it preserves some rotational symmetry. The study of this geometry is strongly motivated by the abundant presence in nature of highly efficient photosynthetic complexes sharing a similar stacked structure [176, 299]. In particular, the active core photosynthetic apparatus of certain bacteria is formed by chromophores, featuring an optical dipole transition, which are arranged symmetrically forming a complex structure of stacked concentric coupled nanorings. Some of these units are specialized in transforming the absorbed energy into chemical energy (LH1), while a larger number of them (LH2 and LH3) do not have a reaction center but efficiently capture and funnel light towards the LH1 units.

In this system, coherence effects between the chromophores have already shown to

play a crucial role in the energy transfer and light harvesting [300–302]. A natural question is whether collective decay, i.e., superradiance and subradiance, plays an essential role in this process, and whether nature chooses a particular geometry in order to optimize its effects. In this work, we aim at shedding light on this question, by analyzing the optical properties and exciton dynamics in realistic structures. Furthermore, similar mechanisms could be in principle exploited for artificial light harvesting. Proving these concepts could be already possible using state-of-the-art experimental setups, such as neutral atoms trapped in optical lattices, optical tweezer arrays, microwave coupled superconducting q-bits or solid-state quantum dots [172, 173].

The paper is organized as follows. We first introduce the theoretical framework to describe a system of dipole-dipole interacting quantum emitters, and demonstrate that a structure of coupled symmetric nanorings can be described in a particularly simple form in terms of Bloch eigenmodes. Next, we summarize the optical properties of single nanorings, which can exhibit special radiating properties. We then move to study the case of two coupled nanorings, displaying two energy bands. Thereafter, we apply a similar analysis to elucidate the radiating properties of a realistic natural light-harvesting complex (LH2), which contains a closely double ring structure with a shifted third ring at higher resonance frequencies. Studying this geometry we find that the rings geometry and size is critically close to the case where the energy bands of all rings overlap to for common superradiant exciton states.

10.2 Bloch Eigenmodes

Let us consider first a ring-shaped array (or regular polygon) of N identical two-level quantum emitters with minimum inter-particle distance d. The emitters possess a single narrow optical dipole transition around the frequency ω_0 with dipole orientation $\hat{\boldsymbol{\wp}}_i = \sin\theta\cos\phi\,\hat{e}_{\phi,i} + \sin\theta\sin\phi\,\hat{e}_{r,i} + \cos\theta\,\hat{e}_z$ $(i = 1, \ldots, N)$, where $\hat{e}_z$ and $\hat{e}_{r,i(\phi,i)}$ denote unit vectors along the vertical and radial (tangential) direction defined with respect to the emitter i, respectively [see Fig. 10.1(a)]. In this work we will then consider a configuration where two or more of these rings are stacked concentrically around the $\hat{z}$-axis [see Fig. 10.1(b)].

All the emitters are dipole-dipole interacting via the electromagnetic field vacuum fluctuations. After integrating out the optical degrees of freedom in the Born-Markov approximation [43], the atomic reduced density matrix is governed by the master equation $\dot{\rho} = -i[H, \rho] + \mathcal{L}[\rho]$ $(\hbar \equiv 1)$, with the dipole-dipole Hamiltonian

$$H = \sum_{ij;i\neq j} \Omega_{ij} \hat{\sigma}_i^{ge} \hat{\sigma}_j^{eg}, \tag{10.1}$$

and Lindblad operator

$$\mathcal{L}[\rho] = \frac{1}{2} \sum_{i,j} \Gamma_{ij} \left(2\hat{\sigma}_i^{ge} \rho \hat{\sigma}_j^{eg} - \hat{\sigma}_i^{eg} \hat{\sigma}_j^{ge} \rho - \rho \hat{\sigma}_i^{eg} \hat{\sigma}_j^{ge} \right), \tag{10.2}$$

with i and j running over all dipoles. The coherent Ω_{ij} and dissipative Γ_{ij} dipole-dipole couplings can be written in terms of the Green's tensor $\mathbf{G}(\mathbf{r}, \omega_0)$ in free space:

$$\Omega_{ij} = -\frac{3\pi\Gamma_0}{k_0} \operatorname{Re}\left\{\hat{\boldsymbol{\wp}}_i^* \cdot \mathbf{G}(\mathbf{r}_i - \mathbf{r}_j, \omega_0) \cdot \hat{\boldsymbol{\wp}}_j\right\}, \tag{10.3}$$

$$\Gamma_{ij} = \frac{6\pi\Gamma_0}{k_0} \operatorname{Im}\left\{\hat{\boldsymbol{\wp}}_i^* \cdot \mathbf{G}(\mathbf{r}_i - \mathbf{r}_j, \omega_0) \cdot \hat{\boldsymbol{\wp}}_j\right\}, \tag{10.4}$$

where $\mathbf{r}_i$ is the position of the i-th dipole and $\mathbf{G}(\mathbf{r}, \omega_0)$ is given by

$$\mathbf{G}(\mathbf{r}, \omega_0) = \frac{e^{ik_0 r}}{4\pi k_0^2 r^3}\left[(k_0^2 r^2 + ik_0 r - 1)\mathcal{I} - (k_0^2 r^2 + 3ik_0 r - 3)\frac{\mathbf{r} \otimes \mathbf{r}^{\mathrm{T}}}{r^2}\right]. \tag{10.5}$$

Here, $k_0 = \omega_0/c = 2\pi/\lambda$ is the wavenumber associated with the atomic transition, λ the transition wavelength, and $\Gamma_0 = |\boldsymbol{\wp}|^2 k_0^3/3\pi\epsilon_0$ is the decay rate of a single emitter with dipole moment strength $|\boldsymbol{\wp}|$.

The scattered electromagnetic field can be also retrieved from a generalized input-output relation [58, 127] once the atomic coherences are known:

$$\mathbf{E}^+(\mathbf{r}) = \frac{|\boldsymbol{\wp}|k_0^2}{\epsilon_0} \sum_i \mathbf{G}(\mathbf{r} - \mathbf{r}_i, \omega_0) \cdot \hat{\boldsymbol{\wp}}_i \hat{\sigma}_i^{ge}. \tag{10.6}$$

Motivated by realistic conditions in natural light harvesting complexes, this work focuses on the linear optical properties and response of the system at low light conditions. Therefore, we will restrict our study to the case where at most a single excitation is present in the system. In this situation, the first term in the Lindblad operator Eq.(10.2) (also known as recycling term) only modifies the ground state population and it is not relevant for the observables of interest (e.g. scattered fields or excitation population). The remaining terms in the equation can be recast as an effective non-Hermitian Hamiltonian:

$$H_{\text{eff}} = \sum_{ij}\left(\Omega_{ij} - i\frac{\Gamma_{ij}}{2}\right)\hat{\sigma}_i^{eg}\hat{\sigma}_j^{ge}. \tag{10.7}$$

with $\Omega_{ii} = 0$. In this situation, the dynamics of the system can then be fully understood in terms of the collective modes defined by the eigenstates of H_{eff}. Each of these modes have associated a complex eigenvalue, whose real and imaginary parts correspond to the frequency shift and decay rate of the collective mode, respectively. As we will see next, for a symmetric ring-shaped structure these modes have a particularly simple form as they correspond to Bloch functions.

10.3 Bloch Eigenmodes in Rotationally Symmetric Ring Structures

We will consider here ring structures possessing an $N-$fold rotational symmetry, similarly to those arising in certain natural light harvesting complexes [176, 299]. In

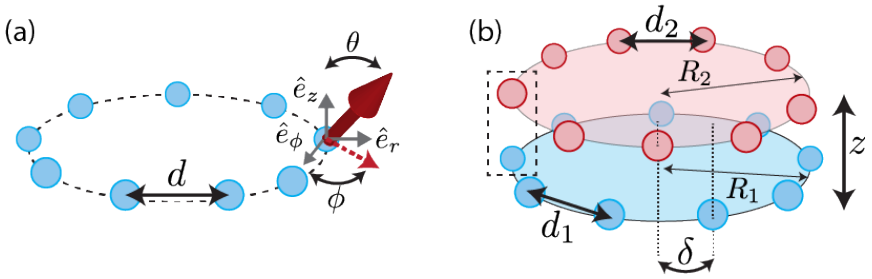

Figure 10.1: **(a)** Schematics of a single ring with lattice constant d. Each emitter features an optical dipole moment (indicated by the red solid arrow) with orientation $\hat{\boldsymbol{\wp}} = \sin\theta\cos\phi\,\hat{e}_\phi + \sin\theta\sin\phi\,\hat{e}_r + \cos\theta\,\hat{e}_z$, where θ and ϕ are the polar and azimuth angle, respectively. The vertical, radial and tangential unit vectors are indicated by $\hat{e}_z$, $\hat{e}_r$ and $\hat{e}_\theta$, respectively. The red dashed arrow denotes the projection of the dipole onto the ring plane. **(b)** Double ring structure: two rings of radius R_1 and R_2 and lattice constants d_1 and d_2 are stacked concentrically and separated by the vertical distance z. The two rings are in general rotated by an angle δ. The dashed-line rectangle encloses the two sites (one from each of the rings) forming a possible unit cell (see main text).

this case, as we will see, the eigenmodes corresponding to the single excitation manifold will be of the Bloch form, i.e., delocalized states with well defined angular momentum m. The N-fold rotational symmetry enables defining N different unit cells (for an example, see Fig. 10.1), which will be denoted by $j = 1, \cdots, N$. Each cell contains in general d dipoles with given orientations $\hat{\boldsymbol{\wp}}_{j\alpha}$ with $\alpha = 1, \cdots, d$. We can then rewrite Eq.(10.7) as

$$H_{\text{eff}} = \sum_{i,j=1}^{N} \sum_{\alpha,\beta=1}^{d} G_{ij}^{\alpha\beta}\, \hat{\sigma}_{i\alpha}^{eg} \hat{\sigma}_{j\beta}^{ge}, \tag{10.8}$$

with $G_{ij}^{\alpha\beta} \equiv \hat{\boldsymbol{\wp}}_{i\alpha}^{*} \cdot \mathbf{G}(\mathbf{r}_{i\alpha} - \mathbf{r}_{j\beta}) \cdot \hat{\boldsymbol{\wp}}_{j\beta}$. We note that a structure consisting of several coupled concentric rings with the same emitter number, each ring being rotationally symmetric, can also be described within this model. In this case, the unit cell contains one site of each of the rings, and it has as many components as rings are. In the following, we demonstrate that the eigenmodes of the coupled structure are of the Bloch form. The symmetry of the system imposes that the position and polarization vectors associated with dipole $i\alpha$ transform under a rotation $\mathcal{U}$ of angle $2\pi/N$ (around the $\hat{z}-$axis) according to $\mathbf{r}_{i\alpha} \to \mathcal{U}\mathbf{r}_{i\alpha} = \mathbf{r}_{i+1\alpha}$ and $\hat{\boldsymbol{\wp}}_{i\alpha} \to \mathcal{U}\hat{\boldsymbol{\wp}}_{i\alpha} = \hat{\boldsymbol{\wp}}_{i+1\alpha}$. By noting that $\mathbf{G}$ is a tensor containing terms proportional to the identity and to $\mathbf{r}_{i\alpha} \otimes \mathbf{r}_{j\beta}^{\mathrm{T}}$, and thus it transforms under the same rotation as $\mathbf{G}(\mathbf{r}_{i\alpha} - \mathbf{r}_{j\beta}) \to \mathcal{U}\mathbf{G}(\mathbf{r}_{i\alpha} - \mathbf{r}_{j\beta})\mathcal{U}^{\dagger} = \mathbf{G}(\mathbf{r}_{i+1,\alpha} - \mathbf{r}_{j+1,\beta})$, we can then conclude that $G_{ij}^{\alpha\beta} = G_{i+1,j+1}^{\alpha\beta}$. Thus, this coupling matrix can be relabelled as $G_{i+1,j+1}^{\alpha\beta} \equiv G_{\ell}^{\alpha\beta}$, with $\ell = j - i$ ($\ell = 0, \cdots, N-1$), as it is

a periodic function only depending on the difference between the two indices i and j. This property allows to write the Hamiltonian Eq.(10.8) in terms of Bloch modes as follows:

$$\begin{aligned} H_{\text{eff}} &= \sum_{i}^{N} \sum_{\ell=0}^{N-1} \sum_{\alpha,\beta=1}^{d} G_{\ell}^{\alpha\beta} \hat{\sigma}_{i\alpha}^{eg} \hat{\sigma}_{i+\ell,\beta}^{ge} \\ &= \sum_{m} \sum_{\alpha,\beta=1}^{d} \tilde{G}_{m}^{\alpha\beta} \hat{\sigma}_{m\alpha}^{eg} \hat{\sigma}_{m\beta}^{ge}, \end{aligned} \tag{10.9}$$

where $\tilde{G}_{m}^{\alpha\beta} \equiv \sum_{\ell=0}^{N-1} e^{i2\pi m\ell/N} G_{\ell}^{\alpha\beta}$, and we have defined the creation and annihilation operators of a collective Bloch mode with well defined angular momentum m:

$$\hat{\sigma}_{m\alpha}^{eg(ge)} = \frac{1}{\sqrt{N}} \sum_{\ell=0}^{N-1} e^{(-)i2\pi m\ell/N} \hat{\sigma}_{\ell\alpha}^{eg(ge)}.$$

Here, the periodicity of the wavefunction under a 2π rotation imposes m to be an integer value, and thus, N linearly independent eigenstates can be constructed by choosing $m = 0, \pm 1, \pm 2, \cdots, \lceil \pm (N-1)/2 \rceil$, where $\lceil \cdot \rceil$ is the ceiling function. Eq.(10.9) is not yet in its full diagonal form (except if the unit cell contains a single dipole), but it already tells us that the angular momentum is a good quantum number. For each value of m, the eigenmodes consist in general of a superposition of each excited dipole in the unit cell and it can be easily found by diagonalizing the $d \times d$ complex $\tilde{G}_{m}^{\alpha\beta}$ matrix, leading to $\hat{H}_{\text{eff}} = \sum_{m,\lambda} (\Omega_{m\lambda} - i\Gamma_{m\lambda}/2)\, \hat{\sigma}_{m\lambda}^{eg} \hat{\sigma}_{m\lambda}^{ge}$. Here, $\Omega_{m\lambda}$ ($\Gamma_{m\lambda}$) is the real (imaginary) part of the eigenvalue associated with Bloch mode m and λ, whereas $\hat{\sigma}_{m\lambda}^{eg}$ is the corresponding creation operator.

10.4 Results

10.4.1 Optical properties of a single nano-ring

Let us first summarize some of the most relevant optical properties for a single ring with N dipoles, i.e., the case where the unit cell contains just a single dipole. As previously shown in [165, 184] the optical properties of the ring strongly depend on the size of the ring compared to the light wavelength and on the dipole orientations. In the following, we focus on two different limiting regimes: a dense large ring (quasi linear chain) and a small ring (Dicke limit).

Dense and large ring case (quasi-linear chain limit)

A large ring with a large number of emitters locally resembles a linear array, and can support optical modes which do not propagate into the three-dimensional space

but are rather confined and guided through the array. These modes correspond to spin-waves (Bloch modes) whose quasi-momentum along the chain is larger than the light wavenumber k_0. This leads to an evanescent field along the transverse directions to the array. In the very large ring case, one can identify the linear momentum $k_z \leftrightarrow 2\pi m/Nd$, and the condition $k_z > k_0$ sets the value of the angular momentum of the guided subradiant modes to be mm_0, with $m_0 = Nd/\lambda$ associated with the light line. Moreover, such states can only exist if $d < \lambda/2$, as the maximum value of k_z (or equivalently m) is given by the boundary of the first Brillouin zone.

Despite these similarities, a striking difference between linear and closed ring configurations is the scaling of the subradiant decay rates with emitter number. Indeed, by closing the ends of the open chain in a ring structure losses can be strongly reduced, leading to an exponential suppression of the decay rates with atom number, in contrast to the polynomial suppression for the linear chain.

On the other hand, the modes for which mm_0 are in general radiant. The angular momentum of the brightest state however, strongly depends on the polarization direction of the atoms. In Fig. 10.2(a) we have plotted the collective decay rates versus m, for a ring of $N = 100$ emitters and different polarization orientations $\hat{\boldsymbol{\wp}}_i = \{\hat{e}_z, \hat{e}_{r,i}, \hat{e}_{\phi,i}\}$. For comparison, we also plot the result for an infinitely long linear chain with the same lattice constant (solid line). Clearly, in this regime, the radial and transverse (tangential) polarization decay rates tend to those for the perpendicularly (longitudinally) polarized linear chain, with maximally bright modes close to the light line $m = m_0$ ($m = 0$).

Besides studying the radiative properties, it is also interesting to analyse the sign of the frequency shifts in the collective modes arising due to dipole-dipole interactions. Figure 10.2(c) shows the frequency shifts corresponding to Fig. 10.2(a). We find that the symmetric $m = 0$ mode has a positive (negative) shift when the dipoles are aligned transversely (longitudinally). This is not so surprising when thinking of interacting classical static dipoles which repel (attract) each other if they are aligned in parallel (in a head-to-tail configuration). Note also that in this regime the bright states are always energetically lower than the guided subradiant modes.

Small ring case (Dicke limit)

We now focus on a different regime where the ring diameter is small compared to the light wavelength, i.e., $R\lambda/2$ (Dicke limit). This regime will be relevant in the study of natural light harvesting complexes, given the small inter-particle distances which are few orders of magnitude smaller than the light wavelength. In this case, the emitters radiate as if they were a single dipole with effective moment strength and decay rate

$$\hat{\boldsymbol{\wp}}_{m,\text{eff}} = N^{-1/2} \sum_{\ell} e^{i2\pi m\ell/N} \hat{\boldsymbol{\wp}}_{\ell}, \qquad \Gamma_m = |\hat{\boldsymbol{\wp}}_{m,\text{eff}}|^2 \Gamma_0. \tag{10.10}$$

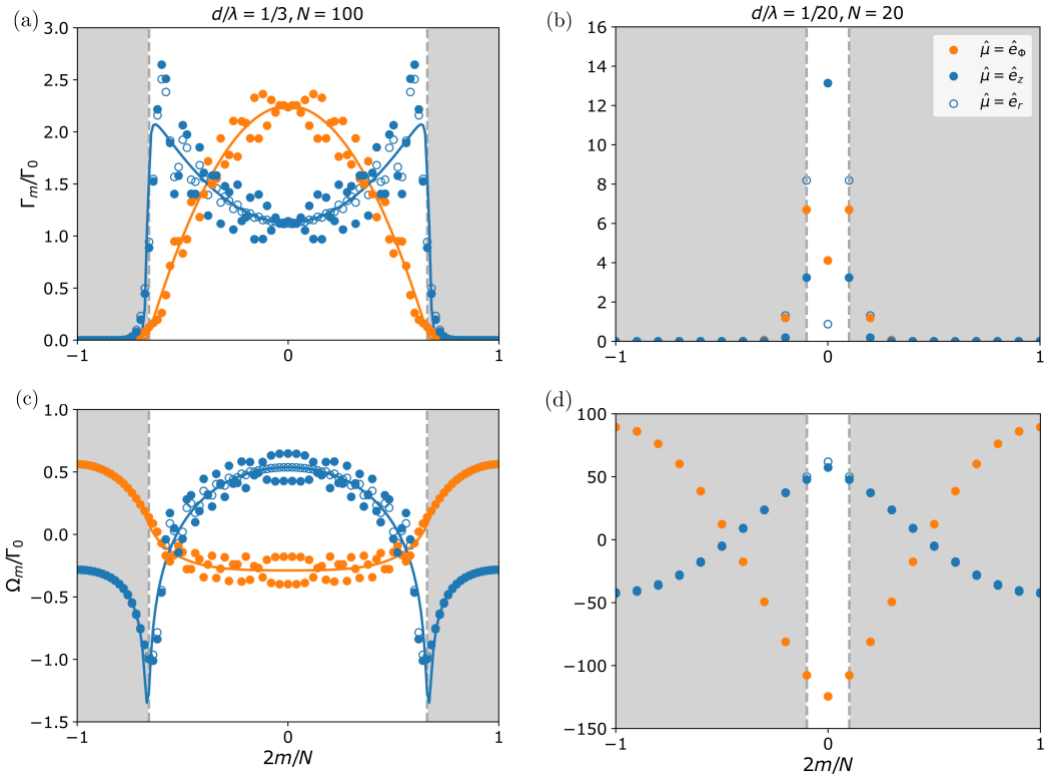

Figure 10.2: Single Ring Optical Properties. **(a)-(b)** Collective decay rates Γ_m and **(c)-(d)** frequency shifts Ω_m versus angular momentum m, depending on polarization orientation (blue open, blue solid and orange are for transverse, radial and tangential polarization, respectively). Left panels correspond to a large ring with $d/\lambda = 1/3$ and $N = 100$. For comparison, solid lines show the result for an infinite linear chain with transverse (blue) and longitudinal (orange) polarization. Right panels are for $d/\lambda = 0.05$ and $N = 20$ (Dicke regime). In this case there are only one (two) bright modes at $m = 0$ ($m = \pm 1$) for transverse (tangential and radial) polarization. For tangential polarization the bright (dark) modes are energetically low (high), whereas the opposite behavior is found for radial and transverse polarization.

From this expression, one can then easily see that for transverse polarization only the mode with $m = 0$ has a non-vanishing value of the effective dipole moment $\hat{\boldsymbol{\wp}}_{m,\text{eff}} = \sqrt{N}\hat{e}_z$, and thus it is bright and decaying at rate $\Gamma_{m=0} \sim N\Gamma_0$. Instead for tangential or radial polarization there are two bright modes $m = \pm 1$ with $\hat{\boldsymbol{\wp}}_{m,\text{eff}} = \sqrt{N/2}\,(\hat{e}_x \pm i\hat{e}_y)$ and $\Gamma_{m=\pm 1} \sim N\Gamma_0/2$. The remaining modes are dark with vanishing effective dipole moment and $\Gamma_m \to 0$. Figure 10.2(c) shows the decay rates for a ring in this regime ($d/\lambda = 0.05$, $N = 20$) with different polarization orientations $\hat{\boldsymbol{\wp}}_i = \{\hat{e}_z, \hat{e}_{r,i}, \hat{e}_{\phi,i}\}$. Moreover, note that in general, a ring with polarization $\hat{\boldsymbol{\wp}}_i =$

$\cos\theta\cos\phi\,\hat{e}_{\phi,i} + \cos\theta\sin\phi\,\hat{e}_{r,i} + \sin\theta\,\hat{e}_z$ $(i = 1, \ldots, N)$ will have three different bright modes $m = 0, \pm 1$ with decay rates $\Gamma_{m=0} = N\Gamma_0 \sin^2\theta$ and $\Gamma_{\pm 1} = (N\Gamma_0/2)\cos^2\theta$.

In this limit, the collective frequency shifts also acquire a particularly simple cosinusoidal form. Indeed, in this regime the interactions Ω_{ij} between first neighbouring sites dominate, and one can approximate

$$\Omega_m \approx N^{-1} \sum_{\ell} \left(\Omega_{\ell,\ell+1} e^{i2\pi m/N} + \Omega_{\ell,\ell-1} e^{-i2\pi m/N} \right) = 2\Omega_d \cos\left(2\pi m/N\right), \qquad (10.11)$$

where we use again the discrete rotational symmetry of the ring. Here the sign and strength of first-neighbour coupling Ω_d strongly depends on the polarization direction. For the same general polarization as before,

$$\Omega_d = -(3\Gamma_0/4k_0^3 d^3)\left[\cos^2\theta(3\cos^2\phi - \sin^2(\pi/N)) - 1\right] \qquad (10.12)$$

[184]. Therefore, the bright modes will be energetically high (low) for transverse / radial (tangential) polarization, as it is shown in Fig. 10.2(d) for the same parameters as before. Moreover, for polarization angles $\cos\theta \approx 1/\sqrt{3}\cos\phi$ and large number of emitters, a nearly degenerated flat band emerges, with frequency shifts that basically vanish [184].

Finally, it is also possible to evaluate the electromagnetic field generated by one of these eigenmodes, by using Eq.(10.6). The result will strongly depend on the angular momentum m, polarization orientation, and size of the ring. For the ring geometry, we find that strongly subradiant modes radiate with very low intensity basically along the ring plane, while the field is evanescent in the transverse direction, as shown in the top row of Fig. 10.6 and Fig. 10.7 for a ring of $N = 9$ tangentially polarized emitters and $m = 4$. Instead, the brightest modes (which in this case correspond to $m = \pm 1$) exhibit a strong field at the center of the ring and propagates also transversally to the ring plane, as shown in the same figures.

10.4.2 Optical properties of two coupled nano-rings

We now analyze the case of two rings of radius R_1 and R_2 that are arranged concentrically and separated by a vertical distance Z. In general, we will also allow in the model a general rotation of angle $\delta \in [0, 2\pi/N)$ of one of the rings around the $\hat{z}$-axis (see Fig. 10.1). In this case the unit cell consists of only two dipoles ($d = 2$).

Coupled identical non-rotated rings ($\delta = 0$)

We first focus on the case of two identical rings ($R_1 = R_2$) concentrically stacked on top of each other and with no rotation angle δ. Because the two rings are identical, and due to $\delta = 0$, the matrix $\tilde{G}_m^{\alpha\beta}$ is complex symmetric, and the eigenmodes of Eq.(10.8)

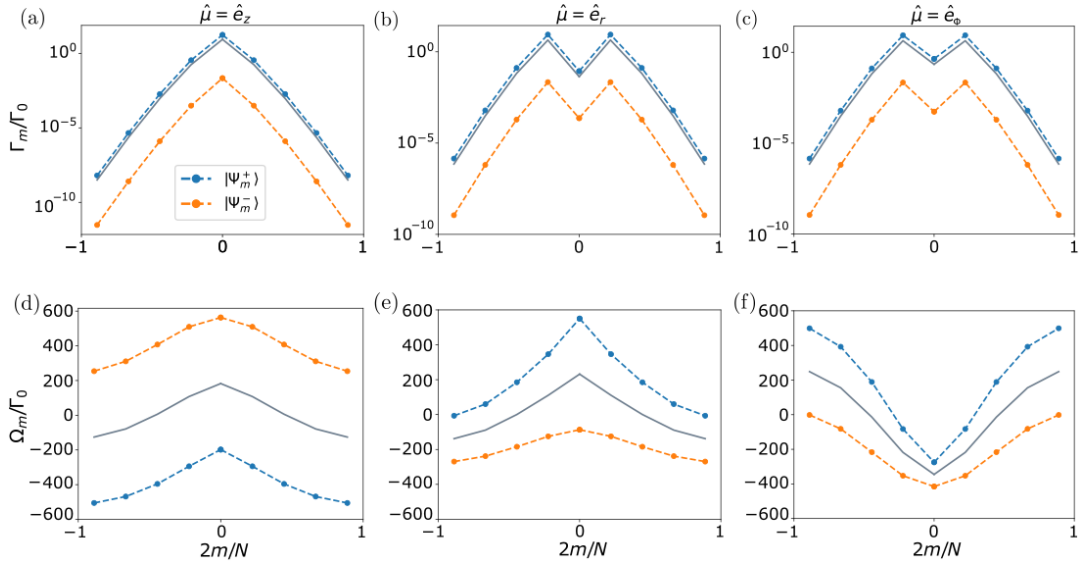

Figure 10.3: Two coupled identical non-rotated nanorings ($\delta = 0$). **(a)-(c)** Collective decay rates Γ_m and **(d)-(f)** frequency shifts Ω_m versus angular momentum m, for two coupled rings of $N = 9$ emitters each and $R/\lambda = 0.05$. The blue (orange) dashed lines denote the symmetric (anti-symmetric) eigenmodes. For comparison, the single ring solution for the same parameters is shown (grey solid line). The two rings are separated by the vertical distance $Z = 0.5R$, and the emitters have transverse, radial or tangential polarization (left, middle or right panels, respectively). For transverse (radial and tangential) polarization the symmetric band is lower (higher) in energy.

can be chosen as the symmetric and the anti-symmetric superposition of Bloch states corresponding to each ring with well defined angular momentum m, which will be denoted as $|\Psi_m^\pm\rangle = (|m,1\rangle \pm |m,2\rangle)/\sqrt{2}$ (with $|m\alpha\rangle \equiv \hat{\sigma}_{m\alpha}^{eg}|g\rangle$). The corresponding collective frequency shifts and decay rates are then simply given by $\Omega_m^\pm = \Omega_m \mp \Omega_m^{\text{inter}}$ and $\Gamma_m^\pm = \Gamma_m \pm \Gamma_m^{\text{inter}}$, where Ω_m and Γ_m are the frequency shift and decay rate corresponding to a single ring, whereas $\Omega_m^{\text{inter}} = \text{Re}[\tilde{G}_m^{12}]$ and $\Gamma_m^{\text{inter}} = -2\text{Im}[\tilde{G}_m^{12}]$ are the dispersive and dissipative inter-ring couplings, respectively.

In Fig. 10.3 we plot for two rings in the Dicke regime ($R/\lambda = 0.05$) and separated by vertical distance $Z = 0.5R$ the decay rates and frequency shifts of the two emerging bands: symmetric $|\Psi_m^+\rangle$ (orange line) and anti-symmetric $|\Psi_m^-\rangle$ (blue line). For comparison, we overlay the result for two independent rings (grey line). We find that, regardless of the emitters polarization, the anti-symmetric solution is always more subradiant than the symmetric one. Moreover the darkest state is $\Psi_{\max[m]}^-$, i.e., the anti-symmetric superposition of the darkest state of a single ring. Looking at the frequency shifts, we find that the behavior with angular momentum m is similar to that for the single ring case, but shifted in energy. In particular, the symmetric band

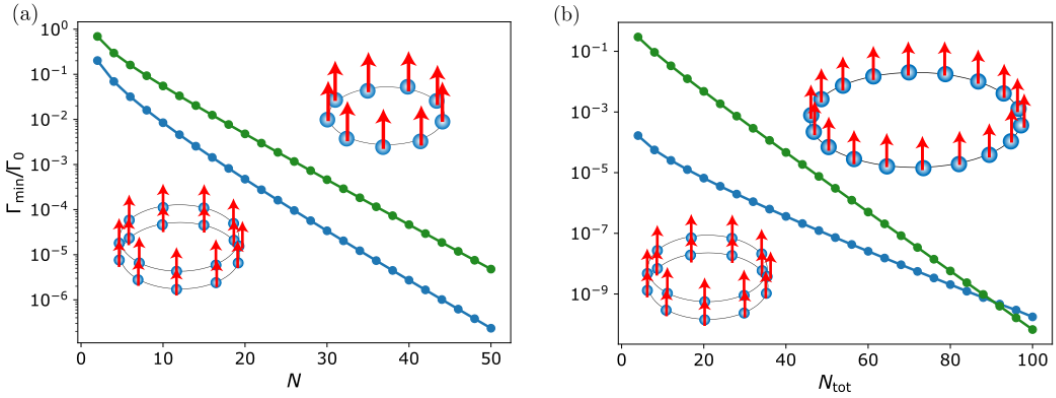

Figure 10.4: Two coupled identical non-rotated nanorings ($\delta = 0$). Scaling of the most subradiant eigenmode decay rate for two coupled rings (blue) with $Z/\lambda = 0.009$ versus the atom number N of each of the rings. For comparison, we overlay the most subradiant decay rate for a single ring of N atoms (**a**) and a single ring of $N_{\text{tot}} = 2N$ atoms (**b**) (green) with fixed inter-particle distance $d/\lambda = 1/3$ and transverse polarization. Similar results are found in case of tangential polarization.

is shifted to lower energies (higher energies) for transverse (tangential and radial) polarization of the emitters. This fundamental difference in the energy shift sign can be intuitively understood in analogy to the energy of two interacting static dipoles. For the case with transverse polarization, two closer emitters from the two different rings are in a tail-to-head configuration, thus decreasing its total energy if they are in phase. Instead, for the case of tangential and radial polarization the emitters polarization is parallel, increasing its energy when they have the same phase. In conclusion, these results show that the polarization of the emitters can fundamentally modify the optical properties of the emerging bands and determine the ordering of states in energy, something which is relevant in the excitation transfer between the different energy bands. In particular the energy transfer in photosynthetic processes involving dipole interacting chromophores is understood via H- and J-aggregation. In J-aggregates, neighboring chromophores are oriented in a head-to-tail arrangement, resulting in a negative coherent nearest-neighbor coupling Ω_d and the positioning of the optically allowed ($m = 0$) Bloch mode at the bottom of the energy band, whereas for H-aggregates the orientation is parallel and the symmetric ($m = 0$) mode is positioned at the top of the energy band. Another interesting property of this system is the scaling of the most subradiant state decay rate with the atom number N. For a fixed inter-particle distance d/λ, we show in Fig. 10.4(a) the decay rate of the most subradiant state of two coupled rings of N emitters each, compared to that of a single ring of N emitters (left panel). We observe that, in addition to a lower decay rate, the double ring structure shows always a stronger exponential suppression with the atom number compared to a single ring of the same size and interparticle distance

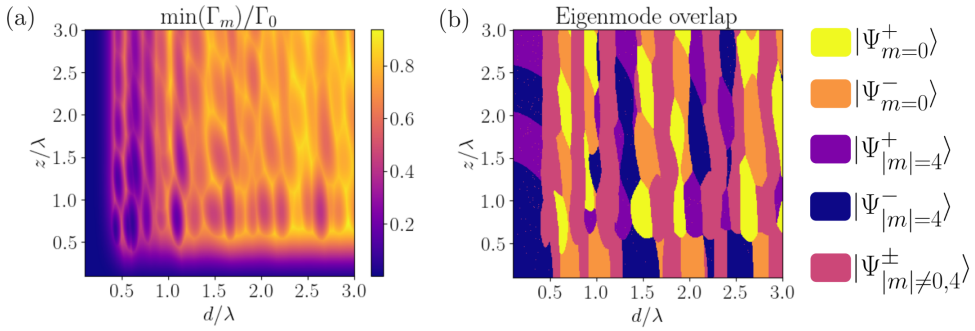

Figure 10.5: Two coupled identical non-rotated nanorings ($\delta = 0$). (a) Most subradiant decay rate of two coupled rings with $N = 9$ emitters and transverse polarization, as a function of ring constant d/λ and inter-ring distance z/λ. Subradiant states can exist even beyond the threshold $d/\lambda < 1/2$ and $z/\lambda < 1/2$ due to destructive wave interference. **(b)** Overlap of the most subradiant eigenmode with the Bloch waves corresponding to angular momentum $|m|$. The Bloch waves of each ring can form symmetric and antisymmetric superpositions and it can be seen, that at various distances the symmetric superposition of $m = 0$ Bloch waves can be subradiant. The parameters are identical to (a) and the overlap oscillates when varying the ring parameters, as soon as $d, z\lambda/2$.

d. In Fig. 10.4(b) we also compare the double-ring result but with a single ring of $2N$ emitters and the same density. We find that in this case, for small inter-ring distances z and ring atom number N, the coupling between the two rings is still strong enough to lead to more subradiance compared to the single ring case with the same total number of atoms. However, if N is too large, then the single ring will always support the most subradiant state, as the curvature and therefore losses will experience a strong suppression as the system approaches an infinite linear chain, for which it is known that the decay rates are exactly zero. For this threshold the exponential suppression with N overcomes the coupling effect between the two rings. Interestingly, the most subradiant decay rate does not show a monotonic behavior with the lattice constant d/λ or the inter-ring distance z/λ. In 10.5(a) we plot the most subradiant decay rate versus these two ratios. We observe that the decay rate oscillates due to wave interference and that there can still exist subradiance beyond the values $d/\lambda = 1/2$ and $z/\lambda = 1/2$. As previously discussed, such subradiant state is always the anti-symmetric superposition of two Bloch waves of well defined angular momentum m. For small rings such that $d/\lambda < 1/2$, the most subradiant state always corresponds to the superposition of the two most subradiant states, i.e., $|m| = \lceil (N-1)/2 \rceil$. However, for $d/\lambda > 1/2$ the value of m that produces the most subradiant state periodically varies. This behavior is shown in 10.5(b), where we have plotted the overlap of the Bloch waves of particular absolute value of the angular momentum. Additionally

the Bloch waves can be in a symmetric or antisymmetric superposition and even the symmetric superposition of the symmetric $m = 0$ modes can lead to subradiance at various distances.

We finally discuss the striking differences in the field patterns generated by the eigenmodes $|\Psi_m^{\pm}\rangle$, with $m = 0, 1, 4$. In Fig. 10.6 and Fig. 10.7 we plot (middle and bottom rows) the field intensity as a function of real space position, for two identical coupled concentric rings of $N = 9$ emitters with tangential polarization, lattice constant $d/\lambda = 0.1$ and separated by a vertical distance $Z/\lambda = 0.2$. For comparison, we have added in the top row the result for a single ring with the same parameters. We find that the symmetric superposition shows a pattern which is very similar to the single ring case. The brightest mode ($m = 1$ in this case) shows an enhanced field intensity along the central axis of the rings. In the symmetric mode, the field is enhanced in the region between the two rings, whereas in the anti-symmetric superposition, it shows a striking different pattern with suppressed field in the region between the two rings.

Coupled unequal rings with rotation ($\delta \neq 0$)

We now consider the more general case where the two rings can have different radius and are rotated by an angle δ. Note that in this case the matrix describing the single excitation manifold $\tilde{G}_m^{\alpha\beta}$ is in general not complex symmetric. However, for the equal radius case ($R_1 = R_2$) in the Dicke regime, the off-diagonal elements satisfy $\tilde{G}_m^{\alpha\beta} = (\tilde{G}_m^{\beta\alpha})^*$ ($\alpha \neq \beta$). This leads to eigenmodes of the form $|\Psi_m^{\pm}\rangle = (|m, 1\rangle \pm e^{i\eta} |m, 2\rangle)/\sqrt{2}$ with $\eta = \text{atan}\left[\text{Im}\tilde{G}_m^{12}/\text{Re}\tilde{G}_m^{12}\right]$.

The behavior of the eigenmodes and eigenvalues with the rotation angle δ is not trivial and strongly depends on the polarization orientation and inter-particle distances. For transverse polarization and a small vertical separation between the rings ($Z = 0.1R$, $R/\lambda = 0.05$ we find a value of $\delta_c \sim 0.15$ for which the frequencies of the two eigenmodes with $m = \lceil (N-1)/2 \rceil$ feature an avoided level crossing. Interestingly, at this point the nature of the state changes. While for $\delta < \delta_c$ the highest energy state is radiant with $\eta \sim 0$, for $\delta > \delta_c$ the highest energy state becomes subradiant with $\eta \sim \pi$. These features are shown in Fig. 10.11 (top panels) and disappear for too small value of Z. Similar results can be found for other values of m. Moreover, the decay rate of the most subradiant state presents a broad minimum around π/N and with $\eta \sim \pi/2$, i.e., when the sites of the second ring lie exactly in between those of the first ring. At this point and because the interparticle distances are larger, the frequency shifts are also smaller.

Similar results can be found for other polarization orientations and also when varying the relative radius between the two rings. As an example, we show in Fig. 10.11 (bottom panels) the same analysis for two co-planar rings ($Z = 0$) with tangential polarization and $R_1 = 0.9R_2$. As it can be seen in the figure, in this case there is also an avoided level crossing (inset) at value $\delta_c \sim 0.07$, where the state of the

highest energy state changes to be subradiant. As in the previous case, we find also the broad minimum around $\delta \sim \pi/N$, where the frequency shifts almost vanish. It is worth noting that in the natural light harvesting complex LH2 (see next section) the dipoles of the B850 band are arranged in a similar configuration with rotation angle $\delta \sim \pi/N$. An intriguing question is whether this is an accidental coincidence or whether the broad minimum emerging in the decay rate, which is thus robust against small fluctuations in the emitters position, can play a relevant role in the energy transfer and the light harvesting processes.

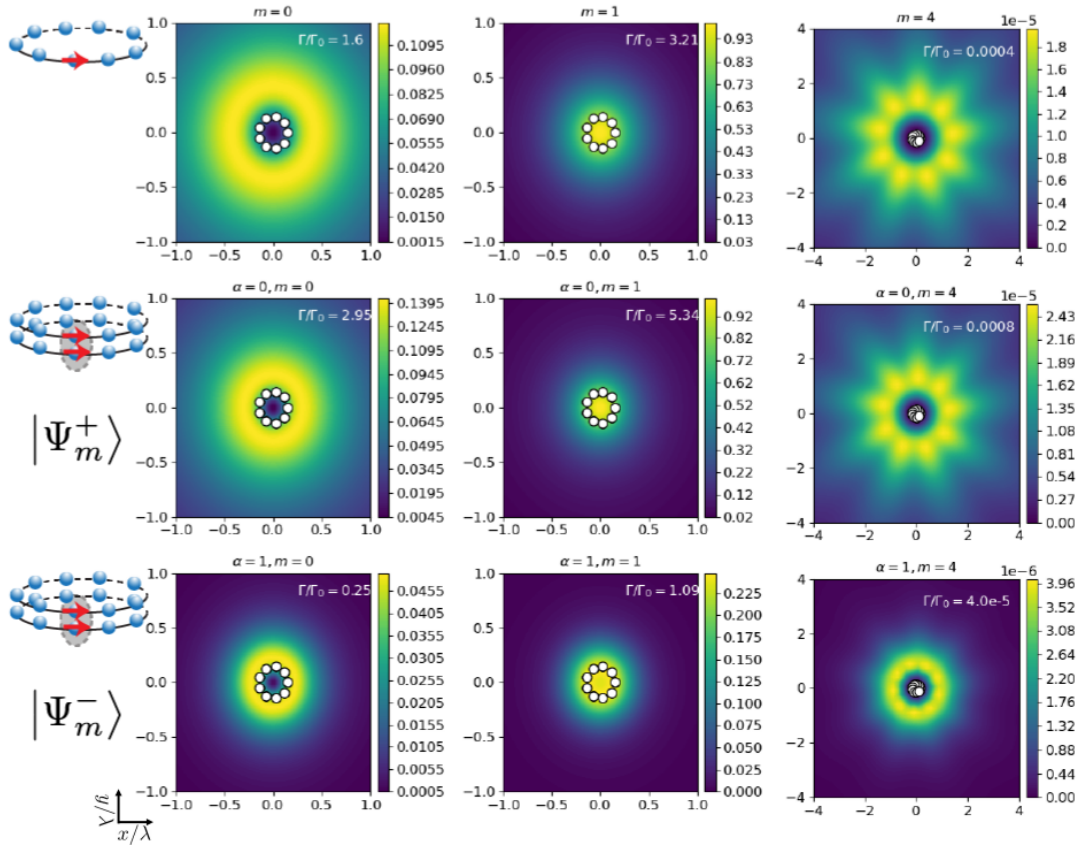

Figure 10.6: Two coupled identical non-rotated nanorings ($\delta = 0$). Field intensity pattern versus real space coordinates in units of the transition wavelength λ (cut at $z = 6R$) generated by the eigenmodes with $m = 0, 1, 4$ as indicated in the panels. Middle and bottom rows correspond to the symmetric and anti-symmetric eigenmodes, respectively. Top panels are for the single ring, for comparison. ($N = 9$, $d/\lambda = 0.1$, $Z/\lambda = 0.2$, tangential polarization.)

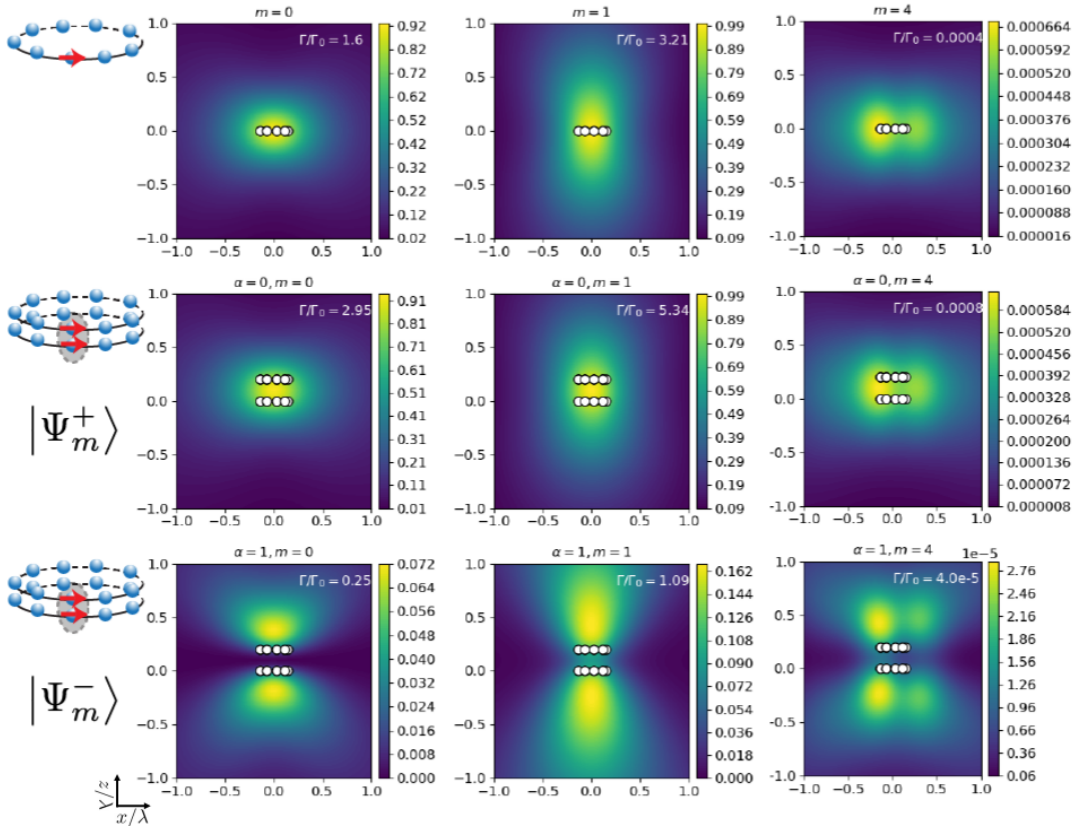

Figure 10.7: Two coupled identical non-rotated nanorings ($\delta = 0$). Field intensity pattern versus real space coordinates (cut at $y = 6R$) generated by the eigenmodes with $m = 0, 1, 4$ as indicated in the panels. Middle and bottom rows correspond to the symmetric and anti-symmetric eigenmodes, respectively. Top panels are for the single ring, for comparison. ($N = 9$, $d/\lambda = 0.1$, $Z/\lambda = 0.2$, tangential polarization.)

10.4.3 B850 and B800 bands in LH2

As already anticipated, the study of the optical properties of two (or more) coupled nanorings is motivated by the existence of similar structures in nature that enable efficient light harvesting and energy transfer [160, 176–181, 189–193]. Indeed, while most biological systems are soft and disordered, photosynthetic complexes in certain purple bacteria exhibit crystalline order. The complexes are composed by antenna units that show a n-fold symmetry [179] which in turn, are arranged forming a maximally packed hexagonal pattern [202]. Purple bacteria are among the oldest living organisms and most efficient in turning sunlight into chemical usable energy. One of the most common species (Rhodopseudomonas Acidophila) contains two well differentiated types of complexes: a larger one containing the reaction center where the energy conversion takes place (LH1), and a second one (LH2) which is more abundant and

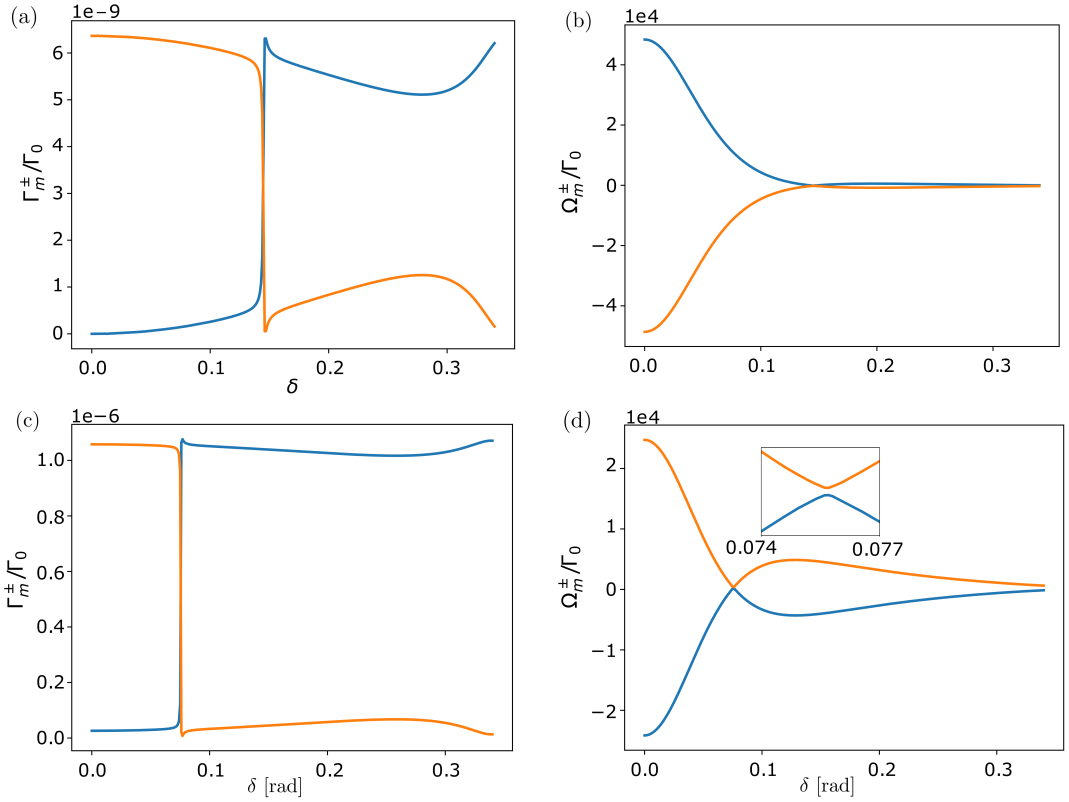

Figure 10.8: Two coupled rotated nanorings ($\delta \neq 0$). **(Top panels)** Two identical nanorings ($R = 0.05\lambda$) with transverse dipole orientation separated by a vertical distance $Z = 0.1R$, depending on the rotation angle $\delta \in [0, 2\pi/18]$: **(a)** decay rate and **(b)** frequency shift of the two eigenmodes with $m = \lceil (N-1)/2 \rceil$. An avoided level crossing emerges at $\delta \sim 0.15$, where the highest energy level changes from being subradiant to radiant, and from being antisymmetric to symmetric. **(Bottom panels)** Two coplanar unequal nanorings ($Z = 0$) with radius $R_1 = 0.05\lambda$ and $R_2 = 0.9R_1$ and tangential dipole orientation, depending on the rotation angle δ: **(c)** decay rate and **(d)** frequency shift of the two eigenmodes with $m = \lceil (N-1)/2 \rceil$. Similarly as before, an avoided level crossing (shown amplified in the inset) emerges at $\delta \sim 0.07$, where the highest energy level changes from being radiant to subradiant, and from being symmetric to anti-symmetric.

whose main role is the absorption of photons and efficient subsequent energy transfer towards the LH1 units. The two complexes are formed by the same light-absorbing pigments: carotenoids (absorbing wavelengths ranging from 400 to 550 nanometers) and bacteriochlorophyl-a (BChla, absorbing in the red and infrared). The BChla features a two-level optical dipole transition around $800 - 875$ nanometers (depending

on the complex). These pigments are sustained by a hollow cylinder of apoproteins whose diameter is few tens of $\mathring{A}$.

Here we will focus on the LH2 complex and the optical properties displayed by the BChla. Early x-ray crystallography data [299] together with subsequent molecular dynamics simulations suggests a ring structure with 9-fold symmetry. This structure consists of a ring of 9 emitters maximally absorbing at 800 nm (the so-called $B800$ band) concentrically arranged and coupled to another two-component ring with 9-fold symmetry (with a total of 18 emitters) maximally absorbing at 850 nm (the so-called $B850$ band). The dipoles orientation also preserves the 9-fold rotational symmetry and are mostly contained in the plane of the ring, except for a small vertical component (see inset in Fig. 10.9). Therefore, the whole structure can be regarded as a ring of 9−unit cells of 3 components (denoted by purple, blue and yellow in the figure).

In the following, we analyse the eigenmodes and collective optical properties of the two bands ($B800$ and $B850$) using the parameters extracted from [179]. This analysis can be relevant for the understanding of the efficient energy transfer between the $B800$ and the $B850$ bands, but also for energy transfer between the LH2 and the LH1 units. Taking into account that the lifetime of the excited state in the BChla is of the order of nanoseconds, the energy transfer process is expected to occur at a much faster time scale. Figure 10.9 shows and compares the decay rates and frequency shifts of the collective eigenmodes as a function of the angular momentum quantum number m, considering the rings are uncoupled (left) or coupled (right). The dispersive couplings between the two components of the $B850$ band (denoted by yellow and blue in the figure) are very large due to the small inter-particle distances, and of the order of $10^6\Gamma$ (being $\Gamma \sim 25$ MHz the estimated decay rate of the excited state in the dipole transition). This leads to the emergence of a two-band structure with large frequency splitting where the two components of the $B850$ ring strongly hybridize: a higher energy band which is mostly subradiant, and a lower energy band containing only two bright modes at $m = \pm 1$. For completeness, we show in Fig. 10.10 the excited state population of each of the components for the coupled system eigenmodes. Clearly, the excitation is delocalized over the two components of the ring.

In the inset of Fig. 10.10 we show the small contributions of the lower double ring configuration to the excited state population of the third band. A similar behavior emerges in case of the first and second band, where the $B800$ ring gives a non-vanishing contribution to the population of the first and second band.

In contrast, the coupling between the $B850$ and $B800$ band (indicated by purple in the plot) is ten times smaller (of the order $10^5\Gamma$), whereas the energy transition difference is of the order of $10^7\Gamma$, and therefore, the $B800$ band remains mostly decoupled. However, it is worth noting that after the $B850$ bands are coupled, the higher energy band lies close to the $B800$ band.

Finally let us point out a very special property of the naturally occurring geometry. Indeed it can be seen that the actual geometry is very close to the critical transition point, where the up shifted eigenstate energies of the lower double ring just overlap

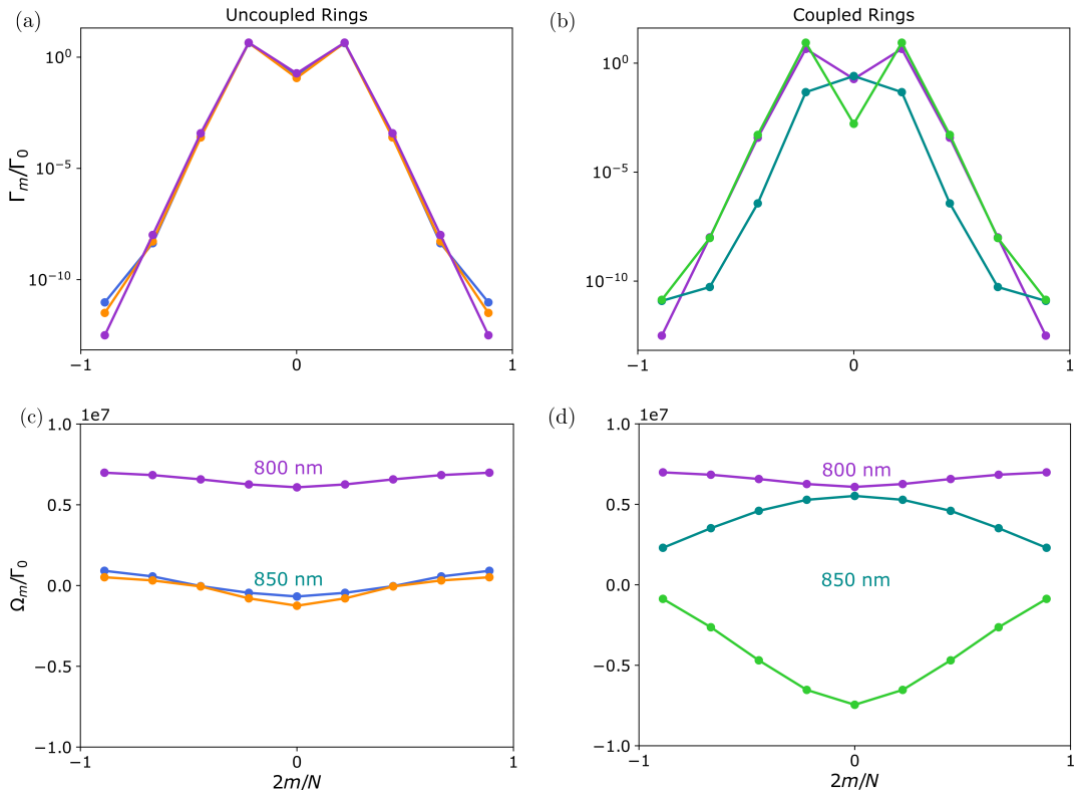

Figure 10.9: LH2 dipole configuration. **(a)-(b)** Collective decay rates and **(c)-(d)** frequency shifts as a function of angular momentum index m for the LH2 structure (B800 and B850 bands) parameterized according to [179]. Left and Right panels correspond to uncoupled and coupled rings, respectively. The B850 band consists of a two-component unit cell ring with 9-fold symmetry (denoted by blue and orange), whereas the B800 band is a single component ring with 9-fold symmetry (denoted by violet). The B800 ring is far in energy and thus only couples very weakly to the B850 rings. However, the two components of the B850 band are strongly coupled, due to the reduced inter-particle distance, what leads to a broad dispersion in the frequency shifts. Two bands emerge: a darker band which is higher in energy and close to the B800 band, and a brighter band (with two bright modes corresponding to $m = \pm 1$) which is lower in energy. This band structure is relevant for the excitation energy transfer occurring between the B800 and B850 bands.

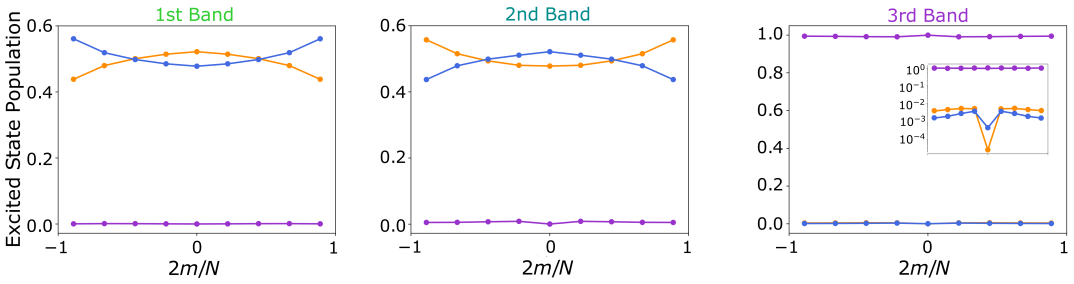

Figure 10.10: LH2 dipole configuration. Individual ring occupation propabilities for each of the three eigenmodes as a function of angular momentum index m. Blue and yellow correspond to the two B850 rings (as indicated in Fig. 10.9), whereas violet is the occupation of the B800 ring. Each panel is a different eigenmode, indicated with the same code color as in Fig. 10.9.

with the upper ring energies. For this in Fig. 10.11 we plot the corresponding exciton energies as function of the overall size of the molecule, where we only consider small size variations $R_{\alpha,i} = \alpha R_i$ around the actually measured size. We see that closely below the value of $\alpha = 1$ the energy bands cross and eigenstates appear which posses similar contributions of all three rings. Close to this resonance condition any excitation in one of the rings is thus coherently transported to the other rings in short time. Interestingly the crossing point depends on the angular index m shifting further away from $\alpha = 1$ with growing m. From this sensity behaviour one could expect tune-ability of the ring properties via the local refractive index or small deformations of the complex.

10.5 Conclusions

Our calculations show that structures involving multiple concentric rings exhibit strongly modified exciton properties and in particular, feature extremely subradiant states with sub-wavelength confined fields. For two identical rings at close enough distances, we find that the anti-symmetric superposition of the individual ring radiative modes, which inherits the angular symmetry of the setup, is always more subradiant than the corresponding symmetric combination. In particular, the most subradiant states are obtained by choosing the individual ring darkest eigenmodes. We have shown that the spontaneous emission of such states decays faster with the emitter number compared to the single ring case. Moreover, important radiative properties, such as the ordering in frequency of the optical modes, can be controlled via a relative rotation or size differences of two otherwise identical rings. For instance, we find that by modifying these parameters, the highest energy level changes from being subradiant to superradiant. When we apply our model to the specific geometry of the triple ring LH2 structure including the natural distances, energy shifts and dipole polarization, we

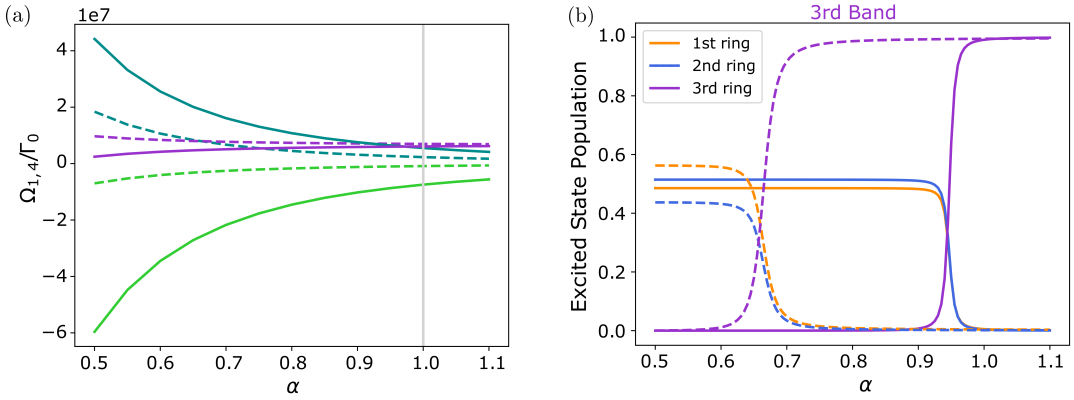

Figure 10.11: LH2 dipole configuration. **(a)** Frequency shift and **(b)** ring occupation probabilities for the third band as function of the overall size of the molecule at the $m = 1, 4$ mode. The size of ring i is varied via $R_{\alpha,i} = \alpha R_i$ around the actual size ($\alpha = 1$). Solid (dashed) lines correspond to the $m = 1$ ($m = 4$) mode. The color code is equivalent to the one in Fig. 10.9. Dependent on the mode m the second and third band as well as the excited state populations cross at $\alpha_c < 1$. For systems with $\alpha < \alpha_c$, the third band is occupied by the B850 ring whereas for $\alpha > \alpha_c$ it is occupied by the B800 ring.

find most of the collective modes are extremely dark. Most interestingly the collective energy shifts from the lower double B850 ring structure, for which the interparticle distances are very small, is of the order of the 50 nm energy shift of the upper ring, so that the energy spectrum spans almost the full gap between the rings. More specifically, two bands emerge due to the strong coupling between the two B850 components. A subradiant band which is higher in energy and close to the B800 band, and a brighter band which is much lower in energy. The realistic dipole orientations and distances lead to only two bright modes corresponding to a quasi-symmetric superposition of the angular momentum $m = 1$ and $m = -1$ modes. This emerging band structure could be helpful for any phonon induced collective energy transfer processes, which are, of course, beyond our model here, but which we plan to explore in future work.

Acknoledgements

Conceptualization, M.M-C., R.H., H.R; formal analysis, M.M-C. and V.S.; investigation, V.S., M.M-C.; writing—original draft preparation, V.S.,M.M-C., R.H., H.R; writing—review and editing, M.M-C.,V.S., R.H., H.R; visualization, V.S., R.H. and M.M-C.; supervision, H.R.; project administration, H.R.; funding acquisition, H.R. All authors have read and agreed to the published version of the manuscript."

V. S., R.H. and H.R. acknowledge funding from the Austrian Science Fund (FWF) doctoral college DK-ALM W1259- N27 and the FET OPEN Network Cryst3 funded by the European Union (EU) via Horizon 2020.

11 Conclusions and Outlook

At the onset of this thesis, we gave a compact introduction to the quantum optical framework necessary to follow the research presented in the following chapters. We laid out numerous studies, which demonstrate the usefulness of collectively interacting quantum emitters in various platforms. In the beginning, we explored the possibilities of dissipatively preparing long-lived subradiant states in atoms with an internal multi-level structure, featuring two excited states. Even though preparation is not straightforward without for instance applying magnetic fields to lift the degeneracy, there remains still a significant fraction of the excited state population in the atoms after long waiting times. After that, we focused on possible applications of the collective nature of interacting quantum emitters in free space. In particular, we analyzed the possibility of having a coherent light source with a spatial extent of less than a micrometer. Here the subradiant character of the system allowed us to realize a continuous source of coherent light with a linewidth that is below that of a single independent emitter. Next, we found that a chain of deeply subwavelength-spaced emitters can be utilized to implement a continuous single-photon source, with directional emission and an emission rate larger than that of a single emitter. We showed, that if the extent of the ensemble exceeds a wavelength of light, the resulting emission obtains directionality and is focused in a narrow emission angle as opposed to emission into all directions for a single photon source in free space. We quantified the quantum character of the emitted light via the second order correlation function between the emitter coherences. Enhanced light-matter interactions in free-space can also be realized employing again a ring of quantum emitters. The geometry was initially inspired by natural light-harvesting complexes, which exhibit ring-shaped units acting as antennas for collecting sunlight. We showed, that a single ring, surrounding an emitter, can enhance the effective absorption rate of the central emitter by many times. Consequently, the central emitter can be engineered to have an additional trapping channel through which the light can be extracted. As yet another example for the extraordinary properties of cooperativity, we showed that in case of quantum emitters with a periodic infinite range interaction, as is the case for superconducting qubits coupled via one-dimensional transmission lines, one can realize a protocoll which, deterministically controls the storage and release of multiple photons simultaneously. Finally, we demonstrated that molecules with vibrational couplings, at finite temperatures can show collective effects such as super- and subradiance. In particular their extremely subwavelength spacing renders them ideal candidates for harnessing collective states. In particular, we showed how the vibrational degrees of freedom lead to a strong unidirectional transfer of the excitation energy between collective states with a decreasing energy gradient, known as

Kasha's rule. In summary, the collective nature of interacting quantum emitters can be harnessed to strongly modify light-matter interactions. Particularly intriguing to me is the persistence of these collective properties in the face of environmental influences, such as ambient temperature, disorder, dynamical dephasing and unwanted decay channels. Here I envision future research which explores possible design principles for artifical light collection, sensing, transport and trapping. As was shown in the above research, the tools are essentially in place and have to be combined in order to tackle potential problems such as understanding the natural design of bacterial light harvesting complexes. Such an understanding should turn out be extremely useful for quantum technological applications ranging from artifical solar cells to quantum sensors for medical applications. Harnessing collective effects in interacting quantum emitters hold the promise to push the boundaries of quantum technologies beyond what is currently possible. It is also intriguing to take inspiration from nature to design not only robust quantum devices, but devices that actually benefit from environmental influences, disorder and noise up to a limit of course. Long-term, devices that harness quantum features but are embedded in real-world applications will be superior if they can thrive under contact with the environment, as opposed to systems that demand pristine laboratory conditions or are robust but show diminished performance when interacting with the environment.

Bibliography

[1] M. Gross and S. Haroche, "Superradiance: An essay on the theory of collective spontaneous emission," *Physics Reports*, vol. 93, no. 5, pp. 301 – 396, 1982.

[2] R. H. Dicke, "Coherence in spontaneous radiation processes," *Phys. Rev.*, vol. 93, pp. 99–110, Jan 1954.

[3] M. O. Araújo, I. Krešić, R. Kaiser, and W. Guerin, "Superradiance in a large and dilute cloud of cold atoms in the linear-optics regime," *Phys. Rev. Lett.*, vol. 117, p. 073002, Aug 2016.

[4] G. Ferioli, A. Glicenstein, F. Robicheaux, R. T. Sutherland, A. Browaeys, and I. Ferrier-Barbut, "Laser-driven superradiant ensembles of two-level atoms near Dicke regime," *Phys. Rev. Lett.*, vol. 127, p. 243602, Dec 2021.

[5] W. Guerin, M. O. Araújo, and R. Kaiser, "Subradiance in a large cloud of cold atoms," *Physical Review Letters*, vol. 116, no. 8, p. 083601, 2016.

[6] I. H. Deutsch, "Harnessing the power of the second quantum revolution," *PRX Quantum*, vol. 1, p. 020101, Nov 2020.

[7] G. Kurizki, P. Bertet, Y. Kubo, K. Mølmer, D. Petrosyan, P. Rabl, and J. Schmiedmayer, "Quantum technologies with hybrid systems," *Proceedings of the National Academy of Sciences*, vol. 112, no. 13, pp. 3866–3873, 2015.

[8] M. Wallquist, K. Hammerer, P. Rabl, M. Lukin, and P. Zoller, "Hybrid quantum devices and quantum engineering," *Physica Scripta*, vol. 2009, no. T137, p. 014001, 2009.

[9] R. J. Bettles, S. A. Gardiner, and C. S. Adams, "Cooperative eigenmodes and scattering in one-dimensional atomic arrays," *Phys. Rev. A*, vol. 94, p. 043844, Oct 2016.

[10] J. Rui, D. Wei, A. Rubio-Abadal, S. Hollerith, J. Zeiher, D. M. Stamper-Kurn, C. Gross, and I. Bloch, "A subradiant optical mirror formed by a single structured atomic layer," *Nature*, vol. 583, no. 7816, p. 369, 2020.

[11] G. D. Scholes, "Long-range resonance transfer in molecular systems," *Annual Review of Physical Chemistry*, vol. 54, no. 1, p. 57, 2003. PMID: 12471171.

[12] J. Cao, R. J. Cogdell, D. F. Coker, H.-G. Duan, J. Hauer, U. KleinekathÃ¶fer, T. L. C. Jansen, T. ManÄal, R. J. D. Miller, J. P. Ogilvie, V. I. Prokhorenko, T. Renger, H.-S. Tan, R. Tempelaar, M. Thorwart, E. Thyrhaug, S. Westenhoff, and D. Zigmantas, "Quantum biology revisited," *Science Advances*, vol. 6, no. 14,

p. eaaz4888, 2020.

[13] S. Krämer, D. Plankensteiner, L. Ostermann, and H. Ritsch, "Quantumoptics.jl: A Julia framework for simulating open quantum systems," *Comput. Phys. Commun.*, vol. 227, pp. 109–116, 2018.

[14] D. Walls and G. Milburn, *Quantum Optics*. Springer Study Edition, Springer Berlin Heidelberg, 2012.

[15] C. Gardiner *et al.*, *Handbook of stochastic methods*, vol. 4. Springer Berlin, 1985.

[16] M. Scully and M. Zubairy, *Quantum Optics*. Cambridge University Press, 1997.

[17] D. F. Walls and G. Milburn, *Quantum optics*. Springer-Verlag Berlin, 2006.

[18] M. Reitz, C. Sommer, and C. Genes, "Langevin approach to quantum optics with molecules," *Phys. Rev. Lett.*, vol. 122, p. 203602, May 2019.

[19] M. Reitz, C. Sommer, and C. Genes, "Cooperative quantum phenomena in light-matter platforms," *PRX Quantum*, vol. 3, p. 010201, Jan 2022.

[20] T. Holstein, "Studies of polaron motion: Part I. The molecular-crystal model," *Annals of Physics*, vol. 8, no. 3, p. 325, 1959.

[21] M. Kasha, "Energy transfer mechanisms and the molecular exciton model for molecular aggregates(1, 2). 1963," *Radiat. Res.*, vol. 178, pp. AV27–34, Aug 1963.

[22] R. Holzinger, S. A. Oh, M. Reitz, H. Ritsch, and C. Genes, "Cooperative subwavelength molecular quantum emitter arrays," *Phys. Rev. Res.*, vol. 4, p. 033116, Aug 2022.

[23] G. D. Scholes and G. Rumbles, "Excitons in nanoscale systems," *Nature Materials*, vol. 5, pp. 683–696, Sep 2006.

[24] X. Huang, W. Yuan, A. Holman, M. Kwon, S. J. Masson, R. Gutierrez-Jauregui, A. Asenjo-Garcia, S. Will, and N. Yu, "Metasurface holographic optical traps for ultracold atoms," *Progress in Quantum Electronics*, vol. 89, p. 100470, 2023.

[25] S. Baier, M. J. Mark, D. Petter, K. Aikawa, L. Chomaz, Z. Cai, M. Baranov, P. Zoller, and F. Ferlaino, "Extended bose-hubbard models with ultracold magnetic atoms," *Science*, vol. 352, no. 6282, pp. 201–205, 2016.

[26] S. Scheuring and J. N. Sturgis, "Atomic force microscopy of the bacterial photosynthetic apparatus: plain pictures of an elaborate machinery," *Photosynthesis research*, vol. 102, pp. 197–211, 2009.

[27] A. Tiranov, V. Angelopoulou, C. J. van Diepen, B. Schrinski, O. A. D. Sandberg, Y. Wang, L. Midolo, S. Scholz, A. D. Wieck, A. Ludwig, *et al.*, "Collective super- and subradiant dynamics between distant optical quantum emitters," *Science*, vol. 379, no. 6630, pp. 389–393, 2023.

[28] M. Gross and S. Haroche, "Superradiance: An essay on the theory of collective

spontaneous emission," *Physics Reports*, vol. 93, no. 5, pp. 301–396, 1982.

[29] M. J. Collett and C. W. Gardiner, "Squeezing of intracavity and traveling-wave light fields produced in parametric amplification," *Phys. Rev. A*, vol. 30, pp. 1386–1391, Sep 1984.

[30] H. J. Carmichael, *Statistical Methods in Quantum Optics 1: Master Equations and Fokker-Planck Equations*. Springer-Verlag Berlin Heidelberg, 1999.

[31] K. Lalumière, B. C. Sanders, A. F. van Loo, A. Fedorov, A. Wallraff, and A. Blais, "Input-output theory for waveguide qed with an ensemble of inhomogeneous atoms," *Phys. Rev. A*, vol. 88, p. 043806, Oct 2013.

[32] J. D. Jackson, *Classical electrodynamics*. John Wiley & Sons, 2007.

[33] A. Asenjo-Garcia, M. Moreno-Cardoner, A. Albrecht, H. J. Kimble, and D. E. Chang, "Exponential improvement in photon storage fidelities using subradiance and "selective radiance" in atomic arrays," *Phys. Rev. X*, vol. 7, p. 031024, Aug 2017.

[34] A. Asenjo-Garcia, J. D. Hood, D. E. Chang, and H. J. Kimble, "Atom-light interactions in quasi-one-dimensional nanostructures: A green's-function perspective," *Phys. Rev. A*, vol. 95, p. 033818, Mar 2017.

[35] K. Lalumière, B. C. Sanders, A. F. van Loo, A. Fedorov, A. Wallraff, and A. Blais, "Input-output theory for waveguide qed with an ensemble of inhomogeneous atoms," *Phys. Rev. A*, vol. 88, p. 043806, Oct 2013.

[36] D. E. Chang, L. Jiang, A. V. Gorshkov, and H. J. Kimble, "Cavity QED with atomic mirrors," *New Journal of Physics*, vol. 14, p. 063003, jun 2012.

[37] M. Moreno-Cardoner, D. Plankensteiner, L. Ostermann, D. E. Chang, and H. Ritsch, "Subradiance-enhanced excitation transfer between dipole-coupled nanorings of quantum emitters," *Phys. Rev. A*, vol. 100, p. 023806, Aug 2019.

[38] J. A. Needham, I. Lesanovsky, and B. Olmos, "Subradiance-protected excitation transport," *New Journal of Physics*, vol. 21, p. 073061, jul 2019.

[39] S. J. Masson and A. Asenjo-Garcia, "Universality of dicke superradiance in arrays of quantum emitters," 2021.

[40] G. Ferioli, A. Glicenstein, F. Robicheaux, R. T. Sutherland, A. Browaeys, and I. Ferrier-Barbut, "Laser-driven superradiant ensembles of two-level atoms near Dicke regime," *Phys. Rev. Lett.*, vol. 127, p. 243602, Dec 2021.

[41] P. A. M. Dirac, "The quantum theory of the emission and absorption of radiation," *Proc. R. Soc. Lond. A Math. Phys. Sci.*, vol. 114, no. 767, pp. 243–265, 1927.

[42] V. Weisskopf, "Probleme der neueren quantentheorie des elektrons," *Naturwissenschaften*, vol. 23, no. 37, pp. 631–637, 1935.

[43] R. Lehmberg, "Radiation from an N-atom system. I. General formalism," *Phys. Rev. A*, vol. 2, no. 3, p. 883, 1970.

[44] R. Lehmberg, "Radiation from an n-atom system. ii. spontaneous emission from a pair of atoms," *Physical Review A*, vol. 2, no. 3, p. 889, 1970.

[45] Z. Ficek, R. Tanaś, and S. Kielich, "Quantum beats and superradiant effects in the spontaneous emission from two nonidentical atoms," *Physica A: Statistical Mechanics and its Applications*, vol. 146, no. 3, pp. 452–482, 1987.

[46] G. Agarwal and A. K. Patnaik, "Vacuum-induced coherences in radiatively coupled multilevel systems," *Physical Review A*, vol. 63, no. 4, p. 043805, 2001.

[47] M. Gross and S. Haroche, "Superradiance: An essay on the theory of collective spontaneous emission," *Physics Reports*, vol. 93, no. 5, p. 301, 1982.

[48] M. Lukin, S. Yelin, and M. Fleischhauer, "Entanglement of atomic ensembles by trapping correlated photon states," *Physical Review Letters*, vol. 84, no. 18, p. 4232, 2000.

[49] C.-W. Chou, H. De Riedmatten, D. Felinto, S. Polyakov, S. Van Enk, and H. J. Kimble, "Measurement-induced entanglement for excitation stored in remote atomic ensembles," *Nature*, vol. 438, no. 7069, p. 828, 2005.

[50] D. Plankensteiner, L. Ostermann, H. Ritsch, and C. Genes, "Selective protected state preparation of coupled dissipative quantum emitters," *Sci. Rep.*, vol. 5, p. 16231, 2015.

[51] C. Cabrillo, J. I. Cirac, P. Garcia-Fernandez, and P. Zoller, "Creation of entangled states of distant atoms by interference," *Physical Review A*, vol. 59, no. 2, p. 1025, 1999.

[52] J.-M. Raimond, M. Brune, and S. Haroche, "Manipulating quantum entanglement with atoms and photons in a cavity," *Reviews of Modern Physics*, vol. 73, no. 3, p. 565, 2001.

[53] M. Eibl, N. Kiesel, M. Bourennane, C. Kurtsiefer, and H. Weinfurter, "Experimental realization of a three-qubit entangled w state," *Physical review letters*, vol. 92, no. 7, p. 077901, 2004.

[54] X. Zou, K. Pahlke, and W. Mathis, "Generation of an entangled four-photon w state," *Physical Review A*, vol. 66, no. 4, p. 044302, 2002.

[55] M. Fleischhauer and M. D. Lukin, "Quantum memory for photons: Dark-state polaritons," *Physical Review A*, vol. 65, no. 2, p. 022314, 2002.

[56] T. Chaneliere, D. Matsukevich, S. Jenkins, S.-Y. Lan, T. Kennedy, and A. Kuzmich, "Storage and retrieval of single photons transmitted between remote quantum memories," *Nature*, vol. 438, no. 7069, p. 833, 2005.

[57] V. V. Temnov and U. Woggon, "Superradiance and subradiance in an inhomogeneously broadened ensemble of two-level systems coupled to a low-q cavity," *Physical Review Letters*, vol. 95, no. 24, p. 243602, 2005.

[58] A. Asenjo-Garcia, M. Moreno-Cardoner, A. Albrecht, H. J. Kimble, and D. E.

Chang, "Exponential improvement in photon storage fidelities using subradiance and "selective radiance" in atomic arrays," *Phys. Rev. X*, vol. 7, p. 031024, 2017.

[59] S. L. Bromley, B. Zhu, M. Bishof, X. Zhang, T. Bothwell, J. Schachenmayer, T. L. Nicholson, R. Kaiser, S. F. Yelin, M. D. Lukin, A. M. Rey, and J. Ye, "Collective atomic scattering and motional effects in a dense coherent medium," *Nature Communications*, vol. 7, no. 1, p. 11039, 2016.

[60] D. Bhatti, R. Schneider, S. Oppel, and J. von Zanthier, "Directional dicke subradiance with nonclassical and classical light sources," *Physical review letters*, vol. 120, no. 11, p. 113603, 2018.

[61] M. Hebenstreit, B. Kraus, L. Ostermann, and H. Ritsch, "Subradiance via entanglement in atoms with several independent decay channels," *Physical Review Letters*, vol. 118, no. 14, p. 143602, 2017.

[62] C. Gardiner and P. Zoller, *Quantum noise: a handbook of Markovian and non-Markovian quantum stochastic methods with applications to quantum optics*, vol. 56. Springer Science & Business Media, 2004.

[63] Z. Ficek and R. Tanaś, "Entangled states and collective nonclassical effects in two-atom systems," *Phys. Rep.*, vol. 372, no. 5, pp. 369 – 443, 2002.

[64] G. Moy, J. Hope, and C. Savage, "Born and markov approximations for atom lasers," *Physical Review A*, vol. 59, no. 1, p. 667, 1999.

[65] "See suplemental material,"

[66] S. Krämer, L. Ostermann, and H. Ritsch, "Optimized geometries for future generation optical lattice clocks," *EPL (Europhysics Letters)*, vol. 114, p. 14003, apr 2016.

[67] L. Ostermann, D. Plankensteiner, H. Ritsch, and C. Genes, "Protected subspace ramsey spectroscopy," *Physical Review A*, vol. 90, no. 5, p. 053823, 2014.

[68] D. Plankensteiner, C. Sommer, M. Reitz, H. Ritsch, and C. Genes, "Enhanced collective purcell effect of coupled quantum emitter systems," 2018.

[69] M. Moreno-Cardoner, D. Plankensteiner, L. Ostermann, D. E. Chang, and H. Ritsch, "Subradiance-enhanced excitation transfer between dipole-coupled nanorings of quantum emitters," *Phys. Rev. A*, vol. 100, p. 023806, Aug 2019.

[70] M. Brune, J. Raimond, P. Goy, L. Davidovich, and S. Haroche, "Realization of a two-photon maser oscillator," *Physical review letters*, vol. 59, no. 17, p. 1899, 1987.

[71] J. McKeever, A. Boca, A. D. Boozer, J. R. Buck, and H. J. Kimble, "Experimental realization of a one-atom laser in the regime of strong coupling," *Nature*, vol. 425, no. 6955, pp. 268–271, 2003.

[72] L. Davidovich, J. Raimond, M. Brune, and S. Haroche, "Quantum theory of a two-photon micromaser," *Physical Review A*, vol. 36, no. 8, p. 3771, 1987.

[73] H. Walther, "The single atom maser and the quantum electrodynamics in a cavity," *Physica Scripta*, vol. 1988, no. T23, p. 165, 1988.

[74] K. An, J. J. Childs, R. R. Dasari, and M. S. Feld, "Microlaser: A laser with one atom in an optical resonator," *Physical review letters*, vol. 73, no. 25, p. 3375, 1994.

[75] O. Astafiev, K. Inomata, A. Niskanen, T. Yamamoto, Y. A. Pashkin, Y. Nakamura, and J. S. Tsai, "Single artificial-atom lasing," *Nature*, vol. 449, no. 7162, pp. 588–590, 2007.

[76] G. Rastelli and M. Governale, "Single atom laser in normal-superconductor quantum dots," *Phys. Rev. B*, vol. 100, p. 085435, Aug 2019.

[77] M. Löffler, G. M. Meyer, and H. Walther, "Spectral properties of the one-atom laser," *Phys. Rev. A*, vol. 55, pp. 3923–3930, May 1997.

[78] D. Meschede, H. Walther, and G. Müller, "One-atom maser," *Physical review letters*, vol. 54, no. 6, p. 551, 1985.

[79] Y. Mu and C. M. Savage, "One-atom lasers," *Phys. Rev. A*, vol. 46, pp. 5944–5954, Nov 1992.

[80] T. Pellizzari and H. Ritsch, "Photon statistics of the three-level one-atom laser," *Journal of Modern Optics*, vol. 41, no. 3, pp. 609–623, 1994.

[81] T. Salzburger, P. Domokos, and H. Ritsch, "Theory of a single-atom laser including light forces," *Physical Review A*, vol. 72, no. 3, p. 033805, 2005.

[82] D. Meiser, J. Ye, D. Carlson, and M. Holland, "Prospects for a millihertz-linewidth laser," *Physical review letters*, vol. 102, no. 16, p. 163601, 2009.

[83] D. Meiser and M. Holland, "Steady-state superradiance with alkaline-earth-metal atoms," *Phys. Rev. A*, vol. 81, no. 3, p. 033847, 2010.

[84] S. Bedoui, M. Lopes, W. Nicolazzi, S. Bonnet, S. Zheng, G. Molnár, and A. Bousseksou, "Triggering a phase transition by a spatially localized laser pulse: Role of strain," *Phys. Rev. Lett.*, vol. 109, p. 135702, Sep 2012.

[85] T. Maier, S. Krämer, L. Ostermann, and H. Ritsch, "A superradiant clock laser on a magic wavelength optical lattice," *Opt. Express*, vol. 22, pp. 13269–13279, 2014.

[86] C. Hotter, D. Plankensteiner, L. Ostermann, and H. Ritsch, "Superradiant cooling, trapping, and lasing of dipole-interacting clock atoms," *Optics express*, vol. 27, no. 22, pp. 31193–31206, 2019.

[87] M. T. Manzoni, M. Moreno-Cardoner, A. Asenjo-Garcia, J. V. Porto, A. V. Gorshkov, and D. E. Chang, "Optimization of photon storage fidelity in ordered atomic arrays," *New Journal of Physics*, vol. 20, no. 8, p. 083048, 2018.

[88] D. Barredo, S. De Léséleuc, V. Lienhard, T. Lahaye, and A. Browaeys, "An atom-by-atom assembler of defect-free arbitrary two-dimensional atomic arrays,"

Science, vol. 354, no. 354, pp. 1021–1023, 2016.

[89] D. Barredo, V. Lienhard, S. de Léséleuc, T. Lahaye, and A. Browaeys, "Synthetic three-dimensional atomic structures assembled atom by atom," *Nature*, vol. 561, pp. 79–82, Sep 2018.

[90] Y. Wang, S. Shevate, T. M. Wintermantel, M. Morgado, G. Lochead, and S. Whitlock, "Preparation of hundreds of microscopic atomic ensembles in optical tweezer arrays," 2019.

[91] A. Blais, R.-S. Huang, A. Wallraff, S. M. Girvin, and R. J. Schoelkopf, "Cavity quantum electrodynamics for superconducting electrical circuits: An architecture for quantum computation," *Physical Review A*, vol. 69, no. 6, p. 062320, 2004.

[92] J. D. Hood, A. Goban, A. Asenjo-Garcia, M. Lu, S.-P. Yu, D. E. Chang, and H. Kimble, "Atom–atom interactions around the band edge of a photonic crystal waveguide," *Proceedings of the National Academy of Sciences*, vol. 113, no. 38, pp. 10507–10512, 2016.

[93] *See Supplemental Material at [URL will be inserted by publisher] for a discussion of the Green's Function, the symmetric subspace and the scaling behaviour.*

[94] L. Mandel and E. Wolf, *Optical Coherence and Quantum Optics*. Cambridge University Press, 1995.

[95] H. Carmichael, *An open systems approach to quantum optics: lectures presented at the Université Libre de Bruxelles, October 28 to November 4, 1991*, vol. 18. Springer Science & Business Media, 2009.

[96] A. Boca, R. Miller, K. M. Birnbaum, A. D. Boozer, J. McKeever, and H. J. Kimble, "Observation of the vacuum Rabi spectrum for one trapped atom," *Phys. Rev. Lett.*, vol. 93, no. 23, p. 233603, 2004.

[97] B. le Feber, F. Prins, E. De Leo, F. T. Rabouw, and D. J. Norris, "Colloidal-quantum-dot ring lasers with active color control," *Nano letters*, vol. 18, no. 2, pp. 1028–1034, 2018.

[98] J. D. Hunter, "Matplotlib: A 2D graphics environment," *Comput. Sci. Eng.*, vol. 9, no. 3, pp. 90–95, 2007.

[99] G. Leuchs, "Photon statistics, antibunching and squeezed states," in *Frontiers of nonequilibrium statistical physics*, pp. 329–360, Springer, 1986.

[100] H. J. Kimble, M. Dagenais, and L. Mandel, "Photon antibunching in resonance fluorescence," *Physical Review Letters*, vol. 39, no. 11, p. 691, 1977.

[101] H. Paul, "Photon antibunching," *Reviews of Modern Physics*, vol. 54, no. 4, p. 1061, 1982.

[102] M. Collett, D. Walls, and P. Zoller, "Spectrum of squeezing in resonance fluorescence," *Optics communications*, vol. 52, no. 2, pp. 145–149, 1984.

[103] D. Walls and P. Zoller, "Reduced quantum fluctuations in resonance fluorescence,"

Physical Review Letters, vol. 47, no. 10, p. 709, 1981.

[104] M. K. Tey, Z. Chen, S. A. Aljunid, B. Chng, F. Huber, G. Maslennikov, and C. Kurtsiefer, "Strong interaction between light and a single trapped atom without the need for a cavity," *Nature Physics*, vol. 4, pp. 924–927, 2008.

[105] N. Bruno, L. C. Bianchet, V. Prakash, N. Li, N. Alves, and M. W. Mitchell, "Maltese cross coupling to individual cold atoms in free space," *Opt. Express*, vol. 27, pp. 31042–31052, Oct 2019.

[106] H. Takahashi, A. Wilson, A. Riley-Watson, F. Oručević, N. Seymour-Smith, M. Keller, and W. Lange, "An integrated fiber trap for single-ion photonics," *New Journal of Physics*, vol. 15, no. 5, p. 053011, 2013.

[107] M. Hennrich, A. Kuhn, and G. Rempe, "Transition from antibunching to bunching in cavity qed," *Physical review letters*, vol. 94, no. 5, p. 053604, 2005.

[108] S. Wolf, S. Richter, J. von Zanthier, and F. Schmidt-Kaler, "Light of two atoms in free space: Bunching or antibunching?," *Phys. Rev. Lett.*, vol. 124, p. 063603, Feb 2020.

[109] E. Ressayre and A. Tallet, "Holstein-primakoff transformation for the study of cooperative emission of radiation," *Physical Review A*, vol. 11, no. 3, p. 981, 1975.

[110] A. Kuzmich, K. Mølmer, and E. Polzik, "Spin squeezing in an ensemble of atoms illuminated with squeezed light," *Physical review letters*, vol. 79, no. 24, p. 4782, 1997.

[111] J. Rui, D. Wei, A. Rubio-Abadal, S. Hollerith, J. Zeiher, D. M. Stamper-Kurn, C. Gross, and I. Bloch, "A subradiant optical mirror formed by a single structured atomic layer," *Nature*, vol. 583, pp. 369–374, 2020.

[112] W. S. Bakr, J. I. Gillen, A. Peng, S. Fölling, and M. Greiner, "A quantum gas microscope for detecting single atoms in a Hubbard-regime optical lattice," *Nature*, vol. 462, no. 7269, pp. 74–77, 2009.

[113] J. F. Sherson, C. Weitenberg, M. Endres, M. Cheneau, I. Bloch, and S. Kuhr, "Single-atom-resolved fluorescence imaging of an atomic Mott insulator.," *Nature*, vol. 467, no. 7311, pp. 68–72, 2010.

[114] C. Weitenberg, M. Endres, J. F. Sherson, M. Cheneau, P. Schau, T. Fukuhara, I. Bloch, and S. Kuhr, "Single-spin addressing in an atomic Mott insulator," *Nature*, vol. 471, no. 7338, pp. 319–325, 2011.

[115] P. Solano, P. Barberis-Blostein, F. K. Fatemi, L. A. Orozco, and S. L. Rolston, "Super-radiance reveals infinite-range dipole interactions through a nanofiber," *Nature Communications*, vol. 8, no. 1, pp. 1–7, 2017.

[116] H. Zoubi and H. Ritsch, "Bright and dark excitons in an atom-pair–filled optical lattice within a cavity," *EPL (Europhysics Letters)*, vol. 82, no. 1, p. 14001, 2008.

[117] D. Porras and J. I. Cirac, "Collective generation of quantum states of light by entangled atoms," *Physical Review A*, vol. 78, no. 5, pp. 1–14, 2008.

[118] M. O. Scully, "Collective lamb shift in single photon dicke superradiance," *Physical Review Letters*, vol. 102, no. 14, p. 143601, 2009.

[119] S. D. Jenkins and J. Ruostekoski, "Controlled manipulation of light by cooperative response of atoms in an optical lattice," *Physical Review A*, vol. 86, no. 3, pp. 1–5, 2012.

[120] S. D. Jenkins and J. Ruostekoski, "Metamaterial transparency induced by cooperative electromagnetic interactions," *Physical Review Letters*, vol. 111, no. 14, pp. 1–5, 2013.

[121] M. O. Scully, "Single photon subradiance: quantum control of spontaneous emission and ultrafast readout," *Physical Review Letters*, vol. 115, no. 24, p. 243602, 2015.

[122] R. J. Bettles, S. A. Gardiner, and C. S. Adams, "Cooperative ordering in lattices of interacting two-level dipoles," *Phys. Rev. A*, vol. 92, p. 063822, Dec 2015.

[123] A. González-Tudela, C.-L. Hung, D. E. Chang, J. I. Cirac, and H. J. Kimble, "Subwavelength vacuum lattices and atomâatom interactions in two-dimensional photonic crystals," *Nature Photonics*, vol. 9, pp. 320–325, apr 2015.

[124] R. Sutherland and F. Robicheaux, "Collective dipole-dipole interactions in an atomic array," *Physical Review A*, vol. 94, no. 1, p. 013847, 2016.

[125] R. J. Bettles, S. A. Gardiner, and C. S. Adams, "Enhanced optical cross section via collective coupling of atomic dipoles in a 2D array," *Phys. Rev. Lett.*, vol. 116, p. 103602, Mar 2016.

[126] E. Shahmoon, D. S. Wild, M. D. Lukin, and S. F. Yelin, "Cooperative resonances in light scattering from two-dimensional atomic arrays," *arxiv:1610.00138*, 2016.

[127] A. Asenjo-Garcia, J. D. Hood, D. E. Chang, and H. J. Kimble, "Atom-light interactions in quasi-1d nanostructures: a green's function perspective," *Phys. Rev. A*, vol. 95, p. 033818, 2017.

[128] J. Ruostekoski and J. Javanainen, "Arrays of strongly coupled atoms in a one-dimensional waveguide," *Physical Review A*, vol. 96, no. 3, p. 033857, 2017.

[129] D. Chang, J. Douglas, A. González-Tudela, C.-L. Hung, and H. Kimble, "Colloquium: Quantum matter built from nanoscopic lattices of atoms and photons," *Reviews of Modern Physics*, vol. 90, no. 3, p. 031002, 2018.

[130] F. Cottier, R. Kaiser, and R. Bachelard, "Role of disorder in super-and subradiance of cold atomic clouds," *Physical Review A*, vol. 98, no. 1, p. 013622, 2018.

[131] A. Piñeiro Orioli and A. M. Rey, "Dark states of multilevel fermionic atoms in doubly filled optical lattices," *Physical Review Letters*, vol. 123, no. 22, p. 223601,

2019.

[132] Y. X. Zhang and K. Mølmer, "Theory of Subradiant States of a One-Dimensional Two-Level Atom Chain," *Physical Review Letters*, vol. 122, no. 20, p. 203605, 2019.

[133] D. Kornovan, N. Corzo, J. Laurat, and A. Sheremet, "Extremely subradiant states in a periodic one-dimensional atomic array," *Physical Review A*, vol. 100, no. 6, p. 063832, 2019.

[134] Y.-X. Zhang, C. Yu, and K. Mølmer, "Subradiant bound dimer excited states of emitter chains coupled to a one dimensional waveguide," *Physical Review Research*, vol. 2, no. 1, pp. 1–9, 2020.

[135] Y.-X. Zhang, "Universal scaling of decay rates of emitter arrays in the subradiant states," 2020.

[136] A. Piñeiro Orioli and A. M. Rey, "Subradiance of multilevel fermionic atoms in arrays with filling n >= 2," *Phys. Rev. A*, vol. 101, p. 043816, Apr 2020.

[137] R. J. Bettles, M. D. Lee, S. A. Gardiner, and J. Ruostekoski, "Quantum and nonlinear effects in light transmitted through planar atomic arrays," *Communications Physics*, vol. 3, aug 2020.

[138] S. D. Jenkins, J. Ruostekoski, N. Papasimakis, S. Savo, and N. I. Zheludev, "Many-body subradiant excitations in metamaterial arrays: Experiment and theory," *arXiv preprint arXiv:1611.01509*, 2016.

[139] L. Henriet, J. S. Douglas, D. E. Chang, and A. Albrecht, "Critical open-system dynamics in a one-dimensional optical-lattice clock," *Physical Review A*, vol. 99, no. 2, pp. 1–20, 2019.

[140] E. Shahmoon, D. S. Wild, M. D. Lukin, and S. F. Yelin, "Cavity quantum optomechanics with an atom-array membrane," *arXiv preprint arXiv:2006.01973*, 2020.

[141] E. Shahmoon, M. D. Lukin, and S. F. Yelin, "Quantum optomechanics of a two-dimensional atomic array," *Physical Review A*, vol. 101, p. 06383, 2020.

[142] T. Bienaimé, N. Piovella, and R. Kaiser, "Controlled dicke subradiance from a large cloud of two-level systems," *Phys. Rev. Lett.*, vol. 108, p. 123602, Mar 2012.

[143] R. Holzinger, D. Plankensteiner, L. Ostermann, and H. Ritsch, "Nanoscale coherent light source," *Phys. Rev. Lett.*, vol. 124, p. 253603, Jun 2020.

[144] L. Williamson, M. O. Borgh, and J. Ruostekoski, "Superatom picture of collective nonclassical light emission and dipole blockade in atom arrays," *Physical review letters*, vol. 125, no. 7, p. 073602, 2020.

[145] L. Williamson and J. Ruostekoski, "Optical response of atom chains beyond the limit of low light intensity: The validity of the linear classical oscillator model,"

Physical Review Research, vol. 2, no. 2, p. 023273, 2020.

[146] S. J. van Enk and H. J. Kimble, "Single atom in free space as a quantum aperture," *Phys. Rev. A*, vol. 61, p. 051802, Mar 2000.

[147] D. Goncalves, M. W. Mitchell, and D. E. Chang, "Strong quantum correlations of light emitted by a single atom in free space," *ArXiv preprint arXiv:2004.01993*, 2020.

[148] M. D. Lee, S. D. Jenkins, and J. Ruostekoski, "Stochastic methods for light propagation and recurrent scattering in saturated and nonsaturated atomic ensembles," *Phys. Rev. A*, vol. 93, p. 063803, Jun 2016.

[149] E. Wientjes, J. Renger, A. G. Curto, R. Cogdell, and N. F. Van Hulst, "Strong antenna-enhanced fluorescence of a single light-harvesting complex shows photon antibunching," *Nature communications*, vol. 5, no. 1, pp. 1–7, 2014.

[150] J. P. Clemens, L. Horvath, B. C. Sanders, and H. J. Carmichael, "Shot-to-shot fluctuations in the directed superradiant emission from extended atomic samples," *Journal of Optics B: Quantum and Semiclassical Optics*, vol. 6, pp. S736–S741, jul 2004.

[151] J. P. Clemens, L. Horvath, B. C. Sanders, and H. J. Carmichael, "Collective spontaneous emission from a line of atoms," *Phys. Rev. A*, vol. 68, p. 023809, Aug 2003.

[152] R. Wagner and J. P. Clemens, "Fidelity of quantum teleportation based on spatially and temporally resolved spontaneous emission," *J. Opt. Soc. Am. B*, vol. 27, pp. A73–A80, Jun 2010.

[153] S. J. Masson, I. Ferrier-Barbut, L. A. Orozco, A. Browaeys, and A. Asenjo-Garcia, "Many-body signatures of collective decay in atomic chains," *Phys. Rev. Lett.*, vol. 125, p. 263601, Dec 2020.

[154] H. Zoubi and H. Ritsch, "Metastability and directional emission characteristics of excitons in 1d optical lattices," *EPL (Europhysics Letters)*, vol. 90, p. 23001, apr 2010.

[155] K. E. Ballantine and J. Ruostekoski, "Subradiance-protected excitation spreading in the generation of collimated photon emission from an atomic array," *Phys. Rev. Research*, vol. 2, p. 023086, Apr 2020.

[156] K. E. Ballantine and J. Ruostekoski, "Radiative toroidal dipole and anapole excitations in collectively responding arrays of atoms," *Phys. Rev. Lett.*, vol. 125, p. 063201, Aug 2020.

[157] C. D. Parmee and J. Ruostekoski, "Signatures of optical phase transitions in superradiant and subradiant atomic arrays," *Communications Physics*, vol. 3, p. 205, Nov 2020.

[158] J. P. Philbin, J. Kelly, L. Peng, I. Coropceanu, A. Hazarika, D. V. Talapin, X. M. Eran Rabani, and P. Narang, "Room temperature single-photon super-

fluorescence from a single epitaxial cuboid nano-heterostructure," 2021.

[159] C. Groiseau, A. E. J. Elliott, S. J. Masson, and S. Parkins, "Deterministic single-atom source of quasi-superradiant n-photon pulses," 2020.

[160] J. Pruchyathamkorn, W. J. Kendrick, A. T. Frawley, A. Mattioni, F. Caycedo-Soler, S. F. Huelga, M. B. Plenio, and H. L. Anderson, "A complex comprising a cyanine dye rotaxane and a porphyrin nanoring as a model light-harvesting system," *Angewandte Chemie International Edition*, vol. 59, no. 38, pp. 16455–16458, 2020.

[161] W. R. Dalacu D, Poole PJ, "Nanowire-based sources of non-classical light," *Nanotechnology*, vol. 30, Jun 2019.

[162] S. J. Masson and A. Asenjo-Garcia, "Atomic-waveguide quantum electrodynamics," *Phys. Rev. Research*, vol. 2, p. 043213, Nov 2020.

[163] T. Shi, D. E. Chang, and J. I. Cirac, "Multiphoton-scattering theory and generalized master equations," *Phys. Rev. A*, vol. 92, p. 053834, Nov 2015.

[164] R. J. Thompson, G. Rempe, and H. J. Kimble, "Observation of normal-mode splitting for an atom in an optical cavity," *Phys. Rev. Lett.*, vol. 68, pp. 1132–1135, Feb 1992.

[165] M. Moreno-Cardoner, D. Plankensteiner, L. Ostermann, D. E. Chang, and H. Ritsch, "Subradiance-enhanced excitation transfer between dipole-coupled nanorings of quantum emitters," *Phys. Rev. A*, vol. 100, p. 023806, Aug 2019.

[166] J. Cremer, D. Plankensteiner, M. Moreno-Cardoner, L. Ostermann, and H. Ritsch, "Polarization control of radiation and energy flow in dipole-coupled nanorings," *New Journal of Physics*, vol. 22, p. 083052, aug 2020.

[167] A. Asenjo-Garcia, H. J. Kimble, and D. E. Chang, "Optical waveguiding by atomic entanglement in multilevel atom arrays," *Proceedings of the National Academy of Sciences*, vol. 116, no. 51, pp. 25503–25511, 2019.

[168] P.-O. Guimond, A. Grankin, D. Vasilyev, B. Vermersch, and P. Zoller, "Subradiant bell states in distant atomic arrays," *Physical Review Letters*, vol. 122, no. 9, p. 093601, 2019.

[169] Z. Wang, H. Li, W. Feng, X. Song, C. Song, W. Liu, Q. Guo, X. Zhang, H. Dong, D. Zheng, *et al.*, "Controllable switching between superradiant and subradiant states in a 10-qubit superconducting circuit," *Physical Review Letters*, vol. 124, no. 1, p. 013601, 2020.

[170] M. Mirhosseini, E. Kim, X. Zhang, A. Sipahigil, P. B. Dieterle, A. J. Keller, A. Asenjo-Garcia, D. E. Chang, and O. Painter, "Cavity quantum electrodynamics with atom-like mirrors," *Nature*, vol. 569, no. 7758, pp. 692–697, 2019.

[171] A. F. van Loo, A. Fedorov, K. LalumiÃ¨re, B. C. Sanders, A. Blais, and A. Wallraff, "Photon-mediated interactions between distant artificial atoms,"

Science, vol. 342, no. 6165, pp. 1494–1496, 2013.

[172] J. Vukajlovic-Plestina, W. Kim, V. G. Dubrovski, G. TütüncüoÄlu, M. Lagier, H. Potts, M. Friedl, and A. Fontcuberta i Morral, "Engineering the size distributions of ordered gaas nanowires on silicon," *Nano Letters*, vol. 17, no. 7, pp. 4101–4108, 2017.

[173] M. Y. Swinkels, A. Campo, D. Vakulov, W. Kim, L. Gagliano, S. E. Steinvall, H. Detz, M. De Luca, A. Lugstein, E. Bakkers, A. Fontcuberta i Morral, and I. Zardo, "Measuring the optical absorption of single nanowires," *Phys. Rev. Applied*, vol. 14, p. 024045, 2020.

[174] S. Mahmoodian, G. Calajó, D. E. Chang, K. Hammerer, and A. S. Sørensen, "Dynamics of many-body photon bound states in chiral waveguide QED," *Physical Review X*, vol. 10, no. 3, p. 31011, 2019.

[175] J. Perczel, J. Borregaard, D. E. Chang, S. F. Yelin, and M. D. Lukin, "Topological Quantum Optics Using Atomlike Emitter Arrays Coupled to Photonic Crystals," *Physical Review Letters*, vol. 124, no. 8, p. 83603, 2020.

[176] S. Bourne Worster, C. Stross, F. M. W. C. Vaughan, N. Linden, and Manby, "Structure and Efficiency in Bacterial Photosynthetic Light Harvesting," *Journal of Physical Chemistry Letters*, vol. 10, no. 23, pp. 7383–7390, 2019.

[177] R. J. Cogdell, A. Gall, and J. Köhler, "The architecture and function of the light-harvesting apparatus of purple bacteria: From single molecules to in vivo membranes," *Quarterly Reviews of Biophysics*, vol. 39, no. 3, pp. 227–324, 2006.

[178] T. Mirkovic, E. E. Ostroumov, J. M. Anna, R. Van Grondelle, Govindjee, and G. D. Scholes, "Light absorption and energy transfer in the antenna complexes of photosynthetic organisms," *Chemical Reviews*, vol. 117, no. 2, pp. 249–293, 2017.

[179] D. Montemayor, E. Rivera, and S. J. Jang, "Computational Modeling of Exciton-Bath Hamiltonians for Light Harvesting 2 and Light Harvesting 3 Complexes of Purple Photosynthetic Bacteria at Room Temperature," *Journal of Physical Chemistry B*, vol. 122, no. 14, pp. 3815–3825, 2018.

[180] F. Caycedo-Soler, C. A. Schroeder, C. Autenrieth, A. Pick, R. Ghosh, S. F. Huelga, and M. B. Plenio, "Quantum redirection of antenna absorption to photosynthetic reaction centers," *The journal of physical chemistry letters*, vol. 8, no. 24, pp. 6015–6021, 2017.

[181] S. J. Jang and B. Mennucci, "Delocalized excitons in natural light-harvesting complexes," *Rev. Mod. Phys.*, vol. 90, p. 035003, 2018.

[182] H. H. Jen, M. S. Chang, and Y. C. Chen, "Cooperative light scattering from helical-phase-imprinted atomic rings," *Scientific Reports*, vol. 8, no. 1, pp. 1–12, 2018.

[183] J. A. Needham, I. Lesanovsky, and B. Olmos, "Subradiance-protected excitation

transport," *New Journal of Physics*, vol. 21, no. 7, p. 073061, 2019.

[184] J. Cremer, D. Plankensteiner, M. Moreno-Cardoner, L. Ostermann, and H. Ritsch, "Polarization control of radiation and energy flow in dipole-coupled nanorings," *New Journal of Physics*, vol. 22, no. 8, 2020.

[185] G. Alber, J. Bernád, M. Stobińska, L. Sánchez-Soto, and G. Leuchs, "Qed with a parabolic mirror," *Physical Review A*, vol. 88, no. 2, p. 023825, 2013.

[186] M. Sondermann and G. Leuchs, *Book chapter in "Engineering the Atom-Photon Interaction"*. Springer, 2015.

[187] V. Sundström, T. Pullerits, and R. van Grondelle, "Photosynthetic light-harvesting:â reconciling dynamics and structure of purple bacterial lh2 reveals function of photosynthetic unit," *The Journal of Physical Chemistry B*, vol. 103, no. 13, pp. 2327–2346, 1999.

[188] L. Janosi, I. Kosztin, and A. DamjanoviÄ, "Theoretical prediction of spectral and optical properties of bacteriochlorophylls in thermally disordered lh2 antenna complexes," *The Journal of Chemical Physics*, vol. 125, no. 1, p. 014903, 2006.

[189] G. D. Scholes and G. R. Fleming, "On the mechanism of light harvesting in photosynthetic purple bacteria:â b800 to b850 energy transfer," *The Journal of Physical Chemistry B*, vol. 104, no. 8, pp. 1854–1868, 2000.

[190] S. Jang, M. D. Newton, and R. J. Silbey, "Multichromophoric förster resonance energy transfer," *Phys. Rev. Lett.*, vol. 92, p. 218301, May 2004.

[191] Y. C. Cheng and R. J. Silbey, "Coherence in the b800 ring of purple bacteria lh2," *Phys. Rev. Lett.*, vol. 96, p. 028103, Jan 2006.

[192] S. Jang, M. D. Newton, and R. J. Silbey, "Multichromophoric förster resonance energy transfer from b800 to b850 in the light harvesting complex 2:â evidence for subtle energetic optimization by purple bacteria," *The Journal of Physical Chemistry B*, vol. 111, no. 24, pp. 6807–6814, 2007. PMID: 17439170.

[193] A. Olaya-Castro, C. F. Lee, F. F. Olsen, and N. F. Johnson, "Efficiency of energy transfer in a light-harvesting system under quantum coherence," *Phys. Rev. B*, vol. 78, p. 085115, Aug 2008.

[194] D. Plankensteiner, C. Sommer, H. Ritsch, and C. Genes, "Cavity antiresonance spectroscopy of dipole coupled subradiant arrays," *Physical Review Letters*, vol. 119, no. 9, p. 093601, 2017.

[195] R. G. Saer and R. E. Blankenship, "Light harvesting in phototrophic bacteria: structure and function," *Biochemical Journal*, vol. 474, no. 13, pp. 2107–2131, 2017.

[196] M. M.-C. et al., "See supplemental material."

[197] K. D. Higgins, S. C. Benjamin, T. M. Stace, G. J. Milburn, B. W. Lovett, and E. M. Gauger, "Superabsorption of light via quantum engineering," *Nature*

Communications, vol. 5, pp. 1–7, 2014.

[198] P.-O. Guimond, B. Vermersch, M. Juan, A. Sharafiev, G. Kirchmair, and P. Zoller, "A unidirectional on-chip photonic interface for superconducting circuits," *npj Quantum Information*, vol. 6, no. 1, pp. 1–12, 2020.

[199] J. Cosgrove and M. A. Borowitzka, "Chlorophyll fluorescence terminology: an introduction," in *Chlorophyll a fluorescence in aquatic sciences: methods and applications*, pp. 1–17, Springer, 2010.

[200] W. Kühlbrandt, "Structure and function of bacterial light-harvesting complexes," *Structure*, vol. 3, no. 6, pp. 521–525, 1995.

[201] X. Hu, A. Damjanović, T. Ritz, and K. Schulten, "Architecture and mechanism of the light-harvesting apparatus of purple bacteria," *Proceedings of the National Academy of Sciences*, vol. 95, no. 11, pp. 5935–5941, 1998.

[202] L. Cleary, H. Chen, C. Chuang, R. J. Silbey, and J. Cao, "Optimal fold symmetry of lh2 rings on a photosynthetic membrane," *Proceedings of the National Academy of Sciences*, vol. 110, no. 21, pp. 8537–8542, 2013.

[203] G. Facchinetti, S. D. Jenkins, and J. Ruostekoski, "Storing Light with Subradiant Correlations in Arrays of Atoms," *Physical Review Letters*, vol. 117, no. 24, pp. 1–5, 2016.

[204] R. Holzinger, M. Moreno-Cardoner, and H. Ritsch, "Nanoscale continuous quantum light sources based on driven dipole emitter arrays," *arXiv preprint arXiv:2103.02416*, 2021.

[205] A. Asenjo-Garcia, M. Moreno-Cardoner, A. Albrecht, H. J. Kimble, and D. E. Chang, "Exponential improvement in photon storage fidelities using subradiance and "selective radiance" in atomic arrays," *Phys. Rev. X*, vol. 7, p. 031024, Aug 2017.

[206] M. Moreno-Cardoner, D. Plankensteiner, L. Ostermann, D. E. Chang, and H. Ritsch, "Subradiance-enhanced excitation transfer between dipole-coupled nanorings of quantum emitters," *Phys. Rev. A*, vol. 100, p. 023806, Aug 2019.

[207] S. J. Masson and A. Asenjo-Garcia, "Atomic-waveguide quantum electrodynamics," *Phys. Rev. Research*, vol. 2, p. 043213, Nov 2020.

[208] R. Gutiérrez-Jáuregui and A. Asenjo-Garcia, "Directional transport along an atomic chain," *Phys. Rev. A*, vol. 105, p. 043703, Apr 2022.

[209] M. Moreno-Cardoner, D. Goncalves, and D. E. Chang, "Quantum nonlinear optics based on two-dimensional rydberg atom arrays," *Phys. Rev. Lett.*, vol. 127, p. 263602, Dec 2021.

[210] I. S. Madjarov, A. Cooper, A. L. Shaw, J. P. Covey, V. Schkolnik, T. H. Yoon, J. R. Williams, and M. Endres, "An atomic-array optical clock with single-atom readout," *Phys. Rev. X*, vol. 9, p. 041052, Dec 2019.

[211] M. A. Norcia, A. W. Young, W. J. Eckner, E. Oelker, J. Ye, and A. M. Kaufman, "Seconds-scale coherence on an optical clock transition in a tweezer array," *Science*, vol. 366, no. 6461, pp. 93–97, 2019.

[212] M. Moreno-Cardoner, R. Holzinger, and H. Ritsch, "Efficient nano-photonic antennas based on dark states in quantum emitter rings," *Opt. Express*, vol. 30, pp. 10779–10791, Mar 2022.

[213] R. Holzinger, M. Moreno-Cardoner, and H. Ritsch, "Nanoscale continuous quantum light sources based on driven dipole emitter arrays," *Applied Physics Letters*, vol. 119, no. 2, p. 024002, 2021.

[214] M. Mirhosseini, E. Kim, X. Zhang, A. Sipahigil, P. B. Dieterle, A. J. Keller, A. Asenjo-Garcia, D. E. Chang, and O. Painter, "Cavity quantum electrodynamics with atom-like mirrors," *Nature*, vol. 569, pp. 692–697, May 2019.

[215] M. T. Manzoni, M. Moreno-Cardoner, A. Asenjo-Garcia, J. V. Porto, A. V. Gorshkov, and D. E. Chang, "Optimization of photon storage fidelity in ordered atomic arrays," *New Journal of Physics*, vol. 20, p. 083048, aug 2018.

[216] K. E. Ballantine and J. Ruostekoski, "Quantum single-photon control, storage, and entanglement generation with planar atomic arrays," *PRX Quantum*, vol. 2, p. 040362, Dec 2021.

[217] D. F. Kornovan, N. V. Corzo, J. Laurat, and A. S. Sheremet, "Extremely subradiant states in a periodic one-dimensional atomic array," *Phys. Rev. A*, vol. 100, p. 063832, Dec 2019.

[218] N. V. Corzo, J. Raskop, A. Chandra, A. S. Sheremet, B. Gouraud, and J. Laurat, "Waveguide-coupled single collective excitation of atomic arrays," *Nature*, vol. 566, pp. 359–362, Feb 2019.

[219] B. Olmos, G. Buonaiuto, P. Schneeweiss, and I. Lesanovsky, "Interaction signatures and non-gaussian photon states from a strongly driven atomic ensemble coupled to a nanophotonic waveguide," *Phys. Rev. A*, vol. 102, p. 043711, Oct 2020.

[220] T. Orell, M. Zanner, M. L. Juan, A. Sharafiev, R. Albert, S. Oleschko, G. Kirchmair, and M. Silveri, "Collective bosonic effects in an array of transmon devices," *Phys. Rev. A*, vol. 105, p. 063701, Jun 2022.

[221] X.-L. Chu, V. Angelopoulou, P. Lodahl, and N. Rotenberg, "Sub-radiant states for imperfect quantum emitters coupled by a nanophotonic waveguide," 2022.

[222] Y. He, L. Ji, Y. Wang, L. Qiu, J. Zhao, Y. Ma, X. Huang, S. Wu, and D. E. Chang, "Geometric control of collective spontaneous emission," *Phys. Rev. Lett.*, vol. 125, p. 213602, Nov 2020.

[223] O. Rubies-Bigorda, V. Walther, T. L. Patti, and S. F. Yelin, "Photon control and coherent interactions via lattice dark states in atomic arrays," *Phys. Rev. Research*, vol. 4, p. 013110, Feb 2022.

[224] R. J. Bettles, S. A. Gardiner, and C. S. Adams, "Cooperative eigenmodes and scattering in one-dimensional atomic arrays," *Phys. Rev. A*, vol. 94, p. 043844, Oct 2016.

[225] V. Paulisch, H. J. Kimble, and A. González-Tudela, "Universal quantum computation in waveguide QED using decoherence free subspaces," *New Journal of Physics*, vol. 18, p. 043041, apr 2016.

[226] A. Asenjo-Garcia, H. J. Kimble, and D. E. Chang, "Optical waveguiding by atomic entanglement in multilevel atom arrays," *Proceedings of the National Academy of Sciences*, vol. 116, no. 51, pp. 25503–25511, 2019.

[227] A. González-Tudela, V. Paulisch, H. J. Kimble, and J. I. Cirac, "Efficient multiphoton generation in waveguide quantum electrodynamics," *Phys. Rev. Lett.*, vol. 118, p. 213601, May 2017.

[228] R. Holzinger, L. Ostermann, and H. Ritsch, "Subradiance in multiply excited states of dipole-coupled v-type atoms," *EPL (Europhysics Letters)*, vol. 128, p. 44001, jan 2020.

[229] O. Rubies-Bigorda, S. Ostermann, and S. F. Yelin, "Generating multi-excitation subradiant states in incoherently excited atomic arrays," 2022.

[230] Q.-M. Chen, Y.-x. Liu, L. Sun, and R.-B. Wu, "Tuning the coupling between superconducting resonators with collective qubits," *Phys. Rev. A*, vol. 98, p. 042328, Oct 2018.

[231] A. González-Tudela, V. Paulisch, D. E. Chang, H. J. Kimble, and J. I. Cirac, "Deterministic generation of arbitrary photonic states assisted by dissipation," *Phys. Rev. Lett.*, vol. 115, p. 163603, Oct 2015.

[232] Y.-X. Zhang and K. Mølmer, "Theory of subradiant states of a one-dimensional two-level atom chain," *Phys. Rev. Lett.*, vol. 122, p. 203605, May 2019.

[233] A. Albrecht, L. Henriet, A. Asenjo-Garcia, P. B. Dieterle, O. Painter, and D. E. Chang, "Subradiant states of quantum bits coupled to a one-dimensional waveguide," *New Journal of Physics*, vol. 21, p. 025003, feb 2019.

[234] L. Henriet, J. S. Douglas, D. E. Chang, and A. Albrecht, "Critical open-system dynamics in a one-dimensional optical-lattice clock," *Phys. Rev. A*, vol. 99, p. 023802, Feb 2019.

[235] Y.-X. Zhang, C. Yu, and K. Mølmer, "Subradiant bound dimer excited states of emitter chains coupled to a one dimensional waveguide," *Phys. Rev. Research*, vol. 2, p. 013173, Feb 2020.

[236] B. Bakkensen, Y.-X. Zhang, J. Bjerlin, and A. S. SÃ¸rensen, "Photonic bound states and scattering resonances in waveguide qed," 2021.

[237] Y.-L. L. Fang, H. Zheng, and H. U. Baranger, "One-dimensional waveguide coupled to multiple qubits: photon-photon correlations," *EPJ Quantum Technology*, vol. 1, p. 3, Jan 2014.

[238] J. Zhong, N. A. Olekhno, Y. Ke, A. V. Poshakinskiy, C. Lee, Y. S. Kivshar, and A. N. Poddubny, "Photon-mediated localization in two-level qubit arrays," *Phys. Rev. Lett.*, vol. 124, p. 093604, Mar 2020.

[239] A. S. Sheremet, M. I. Petrov, I. V. Iorsh, A. V. Poshakinskiy, and A. N. Poddubny, "Waveguide quantum electrodynamics: collective radiance and photon-photon correlations," 2021.

[240] A. V. Poshakinskiy and A. N. Poddubny, "Dimerization of many-body subradiant states in waveguide quantum electrodynamics," *Phys. Rev. Lett.*, vol. 127, p. 173601, Oct 2021.

[241] A. V. Poshakinskiy, J. Zhong, Y. Ke, N. A. Olekhno, C. Lee, Y. S. Kivshar, and A. N. Poddubny, "Quantum hall phases emerging from atom–photon interactions," *npj Quantum Information*, vol. 7, p. 34, Feb 2021.

[242] S. D. Jenkins, J. Ruostekoski, N. Papasimakis, S. Savo, and N. I. Zheludev, "Many-body subradiant excitations in metamaterial arrays: Experiment and theory," *Phys. Rev. Lett.*, vol. 119, p. 053901, Aug 2017.

[243] Y. Ke, A. V. Poshakinskiy, C. Lee, Y. S. Kivshar, and A. N. Poddubny, "Inelastic scattering of photon pairs in qubit arrays with subradiant states," *Phys. Rev. Lett.*, vol. 123, p. 253601, Dec 2019.

[244] S. J. Masson, I. Ferrier-Barbut, L. A. Orozco, A. Browaeys, and A. Asenjo-Garcia, "Many-body signatures of collective decay in atomic chains," *Phys. Rev. Lett.*, vol. 125, p. 263601, Dec 2020.

[245] N. Fayard, L. Henriet, A. Asenjo-Garcia, and D. E. Chang, "Many-body localization in waveguide quantum electrodynamics," *Phys. Rev. Research*, vol. 3, p. 033233, Sep 2021.

[246] J. Zhong and A. N. Poddubny, "Classification of three-photon states in waveguide quantum electrodynamics," *Phys. Rev. A*, vol. 103, p. 023720, Feb 2021.

[247] M. Zanner, T. Orell, C. M. F. Schneider, R. Albert, S. Oleschko, M. L. Juan, M. Silveri, and G. Kirchmair, "Coherent control of a multi-qubit dark state in waveguide quantum electrodynamics," *Nature Physics*, vol. 18, pp. 538–543, May 2022.

[248] "See supplemental material at." `URL_will_be_inserted_by_publisher`, . for a general description of the M-excitation dark state, the dynamics between the bright- and dark state manifolds, the effect of positional disorder, imperfections and the multilevel nature of the transmon.

[249] O. Astafiev, A. M. Zagoskin, A. A. Abdumalikov, Y. A. Pashkin, T. Yamamoto, K. Inomata, Y. Nakamura, and J. S. Tsai, "Resonance fluorescence of a single artificial atom," *Science*, vol. 327, no. 5967, pp. 840–843, 2010.

[250] T. Hönigl-Decrinis, R. Shaikhaidarov, S. de Graaf, V. Antonov, and O. Astafiev, "Two-level system as a quantum sensor for absolute calibration of power," *Phys.*

Rev. Applied, vol. 13, p. 024066, Feb 2020.

[251] J. D. Brehm, R. Gebauer, A. Stehli, A. N. Poddubny, O. Sander, H. Rotzinger, and A. V. Ustinov, "Slowing down light in a qubit metamaterial," 2022.

[252] A. F. van Loo, A. Fedorov, K. LalumiÃ¨re, B. C. Sanders, A. Blais, and A. Wallraff, "Photon-mediated interactions between distant artificial atoms," *Science*, vol. 342, no. 6165, pp. 1494–1496, 2013.

[253] E. Kuznetsova, S. T. Rittenhouse, H. R. Sadeghpour, and S. F. Yelin, "Rydberg-atom-mediated nondestructive readout of collective rotational states in polar-molecule arrays," *Phys. Rev. A*, vol. 94, p. 032325, Sep 2016.

[254] N. Sauerwein, F. Orsi, P. Uhrich, S. Bandyopadhyay, F. Mattiotti, T. Cantat-Moltrecht, G. Pupillo, P. Hauke, and J.-P. Brantut, "Engineering random spin models with atoms in a high-finesse cavity," 2022.

[255] R. H. Lehmberg, "Radiation from an n-atom system. i. general formalism," *Phys. Rev. A*, vol. 2, pp. 883–888, Sep 1970.

[256] G. S. Agarwal, "Rotating-wave approximation and spontaneous emission," *Phys. Rev. A*, vol. 7, pp. 1195–1197, Mar 1973.

[257] R. Holzinger, D. Plankensteiner, L. Ostermann, and H. Ritsch, "Nanoscale coherent light source," *Phys. Rev. Lett.*, vol. 124, p. 253603, Jun 2020.

[258] T. Brixner, R. Hildner, J. Köhler, C. Lambert, and F. Würthner, "Exciton transport in molecular aggregates–from natural antennas to synthetic chromophore systems," *Advanced Energy Materials*, vol. 7, no. 16, p. 1700236, 2017.

[259] A. Mattioni, F. Caycedo-Soler, S. F. Huelga, and M. B. Plenio, "Design principles for long-range energy transfer at room temperature," *Phys. Rev. X*, vol. 11, p. 041003, Oct 2021.

[260] W. Popp, D. Brey, R. Binder, and I. Burghardt, "Quantum dynamics of exciton transport and dissociation in multichromophoric systems," *Annual review of physical chemistry*, vol. 72, pp. 591–616, 2021.

[261] J. Perczel, J. Borregaard, D. E. Chang, H. Pichler, S. F. Yelin, P. Zoller, and M. D. Lukin, "Photonic band structure of two-dimensional atomic lattices," *Physical Review A*, vol. 96, no. 6, p. 063801, 2017.

[262] O. Rubies-Bigorda, V. Walther, T. L. Patti, and S. F. Yelin, "Photon control and coherent interactions via lattice dark states in atomic arrays," *Phys. Rev. Research*, vol. 4, p. 013110, Feb 2022.

[263] J. Perczel, J. Borregaard, D. Chang, H. Pichler, S. F. Yelin, P. Zoller, and M. D. Lukin, "Topological quantum optics in two-dimensional atomic arrays," *arXiv:1703.04849*, 2017.

[264] R. J. Bettles, J. Minar, C. S. Adams, I. Lesanovsky, and B. Olmos, "Topological properties of a dense atomic lattice gas," *Phys. Rev. A*, vol. 96, p. 041603, Oct

2017.

[265] S. K. Saikin, A. Eisfeld, S. Valleau, and A. Aspuru-Guzik, "Photonics meets excitonics: natural and artificial molecular aggregates," *Nanophotonics*, vol. 2, no. 1, pp. 21–38, 2013.

[266] A. Ishizaki and G. R. Fleming, "Quantum coherence in photosynthetic light harvesting," *Annual Review of Condensed Matter Physics*, vol. 3, no. 1, pp. 333–361, 2012.

[267] T. Brixner, J. Stenger, H. Vaswani, R. Blankenship, and G. Fleming, "Two-dimensional spectroscopy of electronic couplings in photosynthesis," *Nature*, vol. 434, no. 1, p. 625, 2005.

[268] H. DeVoe, "Optical properties of molecular aggregates. I. classical model of electronic absorption and refraction," *J. Chem. Phys*, vol. 41, no. 2, pp. 393–400, 1964.

[269] M. Reitz, C. Sommer, B. Gurlek, V. Sandoghdar, D. Martin-Cano, and C. Genes, "Molecule-photon interactions in phononic environments," *Phys. Rev. Research*, vol. 2, p. 033270, Aug 2020.

[270] E. Orgiu, J. George, J. Hutchison, E. Devaux, J. F. Dayen, B. Doudin, F. F. Stellacci, C. Genet, J. Schachenmayer, C. Genes, G. Pupillo, P. Samori, and T. W. Ebbesen, "Conductivity in organic semiconductors hybridized with the vacuum field," *Nat. Mater.*, vol. 14, p. 1123, 2015.

[271] X. Zhong, T. Chervy, L. Zhang, A. Thomas, J. George, C. Genet, J. Hutchinson, and T. W. Ebbesen, "Energy transfer between spatially separated entangled molecules," *Angew. Chem.*, vol. 56, p. 9034, 2017.

[272] J. A. Hutchison, T. Schwartz, C. Genet, E. Devaux, and T. W. Ebbesen, "Modifying chemical landscapes by coupling to vacuum fields," *Angew. Chem. Int. Ed.*, vol. 51, no. 7, p. 1592, 2012.

[273] F. Herrera and J. Owrutsky, "Molecular polaritons for controlling chemistry with quantum optics," *J. Chem. Phys.*, vol. 152, no. 10, p. 100902, 2020.

[274] H. P. Breuer and F. Petruccione, *The Theory of Open Quantum Systems*. Oxford University Press, 2002.

[275] U. Weiss, *Quantum Dissipative Systems*. Series in modern condensed matter physics, World Scientific, 1999.

[276] W. Vogel and D. Welsch, *Quantum Optics*. Wiley, 2006.

[277] C. Sommer, M. Reitz, F. Mineo, and C. Genes, "Molecular polaritonics in dense mesoscopic disordered ensembles," *Phys. Rev. Research*, vol. 3, p. 033141, Aug 2021.

[278] F. Robicheaux, "Theoretical study of early-time superradiance for atom clouds and arrays," *Phys. Rev. A*, vol. 104, p. 063706, Dec 2021.

[279] A. Halpin, P. J. M. Johnson, R. Tempelaar, R. S. Murphy, J. Knoester, T. L. C. Jansen, and R. J. D. Miller, "Two-dimensional spectroscopy of a molecular dimer unveils the effects of vibronic coupling on exciton coherences," *Nature Chemistry*, vol. 6, pp. 196–201, Mar 2014.

[280] F. P. Diehl, C. Roos, A. Duymaz, B. Lunkenheimer, A. Köhn, and T. Basche, "Emergence of coherence through variation of intermolecular distances in a series of molecular dimers," *J. Phys. Chem. Lett*, vol. 5, p. 262, 2014.

[281] R. E. Merrifield, "Vibronic states of dimers," *Radiation Research*, vol. 20, p. 154, 1963.

[282] A. Eisfeld, L. Braun, W. T. Strunz, J. S. Briggs, J. Beck, and V. Engel, "Vibronic energies and spectra of molecular dimers," *The Journal of Chemical Physics*, vol. 122, no. 13, p. 134103, 2005.

[283] A. Chenu, N. Christensson, H. F. Kauffmann, and T. Mančal, "Enhancement of vibronic and ground-state vibrational coherences in 2D spectra of photosynthetic complexes," *Scientific Reports*, vol. 3, p. 2029, Jun 2013.

[284] N. J. Hestand and F. C. Spano, "Expanded theory of H- and J-molecular aggregates: The effects of vibronic coupling and intermolecular charge transfer," *Chemical Reviews*, vol. 118, no. 15, pp. 7069–7163, 2018.

[285] S. Ma, S. Du, G. Pan, S. Dai, B. Xu, and W. Tian, "Organic molecular aggregates: From aggregation structure to emission property," *Aggregate*, vol. 2, no. 4, p. e96, 2021.

[286] D. Abramavicius, B. Palmieri, D. V. Voronine, F. Sanda, and S. Mukamel, "Coherent multidimensional optical spectroscopy of excitons in molecular aggregates; quasiparticle versus supermolecule perspectives," *Chem. Rev.*, vol. 109, p. 2350, 2009.

[287] G. Scheibe, L. Kandler, and H. Ecker, "Polymerisation und polymere Adsorption als Ursache neuartiger Absorptionsbanden von organischen Farbstoffen," *Naturwissenschaften*, vol. 25, p. 75, 1937.

[288] E. E. Jelley, "Spectral absorption and fluorescence of dyes in the molecular state," *Nature*, vol. 138, p. 1009, 1936.

[289] F. J. Garcia-Vidal, C. Ciuti, and T. W. Ebbesen, "Manipulating matter by strong coupling to vacuum fields," *Science*, vol. 373, p. 6551, 2012.

[290] P. Weiss, M. O. AraÃºjo, R. Kaiser, and W. Guerin, "Subradiance and radiation trapping in cold atoms," *New Journal of Physics*, vol. 20, p. 063024, jun 2018.

[291] N. Killoran, S. F. Huelga, and M. B. Plenio, "Enhancing light-harvesting power with coherent vibrational interactions: A quantum heat engine picture," *J. Chem. Phys*, vol. 143, p. 155102, 2015.

[292] F. Caruso, A. W. Chin, A. Datta, S. F. Huelga, and M. B. Plenio, "Highly efficient energy excitation transfer in light-harvesting complexes: The fundamental role

of noise-assisted transport," *J. Chem. Phys*, vol. 131, p. 105106, 2009.

[293] D. Hu, S.-Y. Huang, J.-Q. Liao, L. Tian, and H.-S. Goan, "Quantum coherence in ultrastrong optomechanics," *Phys. Rev. A*, vol. 91, p. 013812, Jan 2015.

[294] C. Sommer, M. Reitz, F. Mineo, and C. Genes, "Molecular polaritonics in dense mesoscopic disordered ensembles," *Phys. Rev. Res.*, vol. 3, p. 033141, Aug 2021.

[295] S. Krämer, D. Plankensteiner, L. Ostermann, and H. Ritsch, "Quantumoptics.jl: A Julia framework for simulating open quantum systems," *Computer Physics Communications*, vol. 227, p. 109, 2018.

[296] A. Mattioni, F. Caycedo-Soler, S. F. Huelga, and M. B. Plenio, "Design principles for long-range energy transfer at room temperature," *Phys. Rev. X*, vol. 11, p. 041003, Oct 2021.

[297] F. Mattiotti, M. Sarovar, G. G. Giusteri, F. Borgonovi, and G. L. Celardo, "Efficient light harvesting and photon sensing via engineered cooperative effects," *New Journal of Physics*, vol. 24, p. 013027, jan 2022.

[298] M. Moreno-Cardoner, R. Holzinger, and H. Ritsch, "Efficient nano-photonic antennas based on dark states in quantum emitter rings," *Opt. Express*, vol. 30, pp. 10779–10791, Mar 2022.

[299] G. McDermott, S. M. Prince, A. A. Freer, A. M. Hawthornthwaite-Lawless, M. Z. Papiz, R. J. Cogdell, and N. W. Isaacs, "Crystal structure of an integral membrane light-harvesting complex from photosynthetic bacteria," *Nature*, vol. 374, no. 6522, pp. 517–521, 1995.

[300] S. Jang, M. D. Newton, and R. J. Silbey, "Multichromophoric förster resonance energy transfer," *Phys. Rev. Lett.*, vol. 92, p. 218301, May 2004.

[301] S. Jang and Y.-C. Cheng, "Resonance energy flow dynamics of coherently delocalized excitons in biological and macromolecular systems: Recent theoretical advances and open issues," *Wiley Interdisciplinary Reviews: Computational Molecular Science*, vol. 3, 01 2013.

[302] A. Mattioni, F. Caycedo-Soler, S. F. Huelga, and M. B. Plenio, "Design principles for long-range energy transfer at room temperature," *Phys. Rev. X*, vol. 11, p. 041003, Oct 2021.

List of Publications

- R. Holzinger, D. Plankensteiner, L. Ostermann and H. Ritsch, "Nanoscale Coherent Light Source ," *Physical Review Letters* , vol. 124, p. 253603, 2020.
- R. Holzinger, R. Gutierrez-Jauregui, T. Hönigl-Decrinis, G. Kirchmair, A. Asenjo-Garcia and H. Ritsch, "Control of Localized Multiple Excitation Dark States in Waveguide QED ," *Physical Review Letters* , vol. 129, p. 253601, 2022.
- R. Holzinger, S. A. Oh, M. Reitz, H. Ritsch and C. Genes, "Cooperative Subwavelength Molecular Quantum Emitter Arrays," *Physical Review Research* , vol. 4, p. 033116, 2022.
- R. Holzinger, D. Plankensteiner, L. Ostermann and H. Ritsch, "Nanoscale continuous quantum light sources based on driven dipole emitter arrays ," *Applied Physics Letters* , vol. 119, p. 024002, 2021.
- R. Holzinger, L. Ostermann and H. Ritsch, "Subradiance in Multiply Excited States of Dipole-Coupled V-Type Atom ," *Europhysics Letters* , vol. 128, p. 44001, 2019.
- M. Moreno-Cardoner, R. Holzinger and H. Ritsch, "Efficient Nano-Photonic Antennas via Dark States in Quantum Emitter Rings ," *Optics Express* , vol. 30, p. 10779-10791, 2022.
- V. Scheil, R. Holzinger, M. Moreno-Cardoner and H. Ritsch, "Optical Properties of Concentric Nanorings of Quantum Emitters ," *Nanomaterials* , vol. 13, p. 851, 2023.